DESIGN GROUND MOTIONS NEAR ACTIVE FAULTS

Jonathan D. Bray,[1] Adrian Rodriguez-Marek[2] and Joanne L. Gillie[3]

SUMMARY

Forward-Directivity (FD) in the near-fault region can produce intense, pulse-type motions that differ significantly from ordinary ground motions that occur further from the ruptured fault. Near-fault FD motions typically govern the design of structures built close to active faults so the selection of design ground motions is critical for achieving effective performance without costly over-design. Updated empirical relationships are provided for estimating the peak ground velocity (*PGV*) and period of the velocity pulse (T_v) of near-fault FD motions. *PGV* varies significantly with magnitude, distance, and site effects. T_v is a function of magnitude and site conditions with most of the energy being concentrated within a narrow-period band centred on the pulse period. Lower magnitude events, which produce lower pulse periods, might produce more damaging ground motions for the stiff structures more common in urban areas. As the number of near-fault recordings is still limited, fully nonlinear bi-directional shaking simulations are employed to gain additional insight. It is shown that site effects generally cause T_v to increase. Although the amplification of *PGV* at soil sites depends on site properties, amplification is generally observed even for very intense rock motions. At soft soil sites, seismic site response can be limited by the yield strength of the soil, but then seismic instability may be a concern.

FORWARD-DIRECTIVITY

Near-fault ground motions are significantly influenced by the rupture mechanism and slip direction relative to the site and by the permanent ground displacement at the site resulting from tectonic movement. When the rupture and slip direction relative to a site coincide, and a significant portion of the fault ruptures towards the site, the ground motion can exhibit the effects of forward-directivity (FD) [1]. Most of the energy in FD motions is concentrated in a narrow frequency band and is expressed as one or more high intensity velocity pulses oriented in the fault-normal direction. These intense velocity pulses can lead to severe structural damage.

Ground motions close to the surface rupture may also contain a significant permanent displacement, which is called fling-step, and this may lead to a high intensity velocity pulse in the direction of the fault displacement. Pulses from fling-step have different characteristics than FD pulses. Whereas FD is a dynamic phenomenon that produces no permanent ground displacement and hence two-sided velocity pulses, fling-step is a result of a permanent ground displacement that generates one sided velocity pulses. The development of design ground motions for a project site close to an active fault should account for these special aspects of near-fault ground motions. Fling-step considerations are discussed in [2]. In this paper, near-fault forward-directivity effects are addressed.

The effects of forward-directivity are generated because the velocity of the fault rupture front is only slightly less than the shear wave propagation velocity [1]. As the rupture front propagates from the focus of the event, a shear wave front is formed by the accumulation of the shear waves travelling ahead of the rupture front. When a site is located at one end of the fault and rupture initiates at the other end of the fault and travels towards the site, the arrival of the wave front is seen as a large pulse of motion that occurs near the beginning of the record. Thus, FD motions typically occur at sites near the end of a strike-slip fault when the rupture moves towards the site, and at sites located in the up-dip projection of a ruptured dip-slip fault (i.e., reverse or normal fault). The radiation pattern of the shear dislocation on the fault causes this large pulse of motion to be oriented in a direction perpendicular to the fault plane [1]. These effects are typically long-period in nature and are best observed in the velocity-time history. FD conditions produce ground motions that have large amplitude and short durations. However, if a site is located at one end of the fault and rupture propagates away from the site, the opposite effect is observed (i.e., backward-directivity), and the motion is characterized by longer duration and lower amplitude ground motions.

Some examples of near-fault FD motions are shown in Figure 1. The use of the velocity-trace plot shown at the right is useful, because FD motions typically exhibit a systematic difference between the fault-normal and fault-parallel components of motion. The fault-normal component is systematically more intense than the fault-parallel component of motion. It is important to remember that the average of the two components of motion is systematically more intense at long periods than ordinary motions as well. Hence, near-fault FD fault-normal components of motion are especially severe and potentially destructive.

[1] *Professor, Dept. of Civil and Environmental Engineering, University of California, Berkeley, CA 94720-1710, USA, email: bray@ce.berkeley.edu*

[2] *Associate Professor, Dept. of Civil and Environmental Engineering, Washington State University, PO Box 642910, Pullman, WA 99164-2910, USA*

[3] *HWA Geosciences, 19730 64th Avenue West, Suite 200, Lynnwood, WA 98036-5957, USA.*

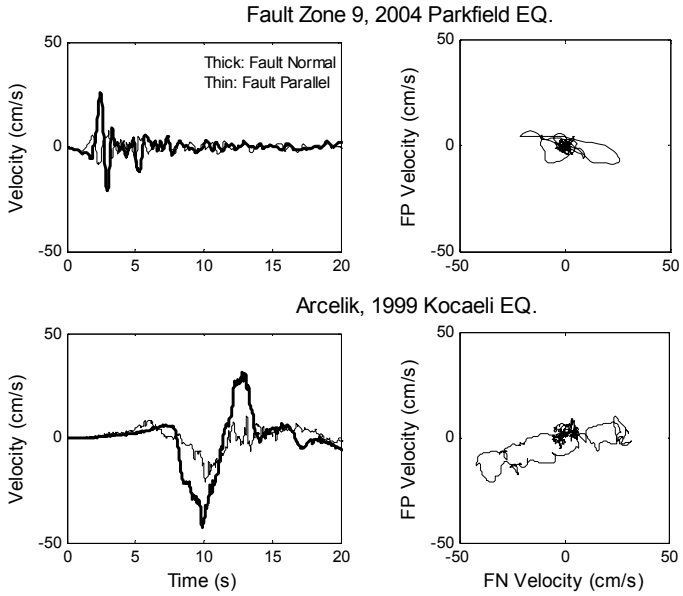

Figure 1: ***Fault normal (FN) and fault parallel (FP) horizontal velocity-time histories and velocity-traces for near-fault records from the 2004 Parkfield (M_w = 6.0) and the Kocaeli (M_w = 7.5) earthquakes.***

Pulse-type motions are critical in the design of structures in the near-fault zone. Two approaches have been used to account for near-fault ground motions in design. The frequency-domain approach uses empirical factors to modify acceleration response spectra for sites that are affected by forward-directivity effects [1, 3]. However, advanced dynamic analyses indicate that the amplitude, period, and number of significant pulses in the velocity-time history primarily control the performance of structures (e.g. [4, 5]). The alternative time-domain approach characterizes the FD motion through its velocity-time history (Figure 2), with its peak ground velocity (*PGV*), predominant pulse period (T_v), and number of significant velocity pulses (N_c). In this preferred approach, it is crucial that reliable estimates of *PGV* and T_v be obtained for near-fault FD motions.

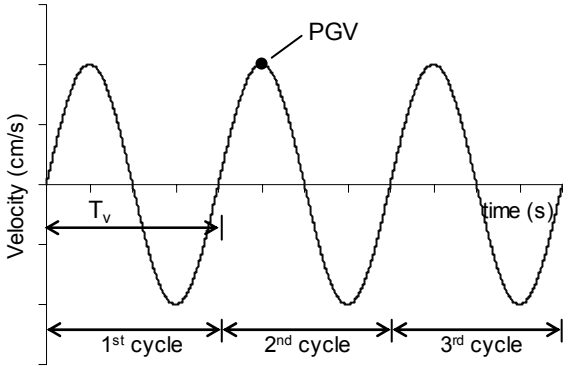

Figure 2: ***Simplified Velocity-Time History Showing Peak Ground Velocity (PGV), Period of the Velocity-Pulse (T_v), and number of significant cycles of motion (N_c).***

EMPIRICAL RELATIONSHIPS

Empirical ground motion relationships may be used to develop reasonable estimates of *PGV* and T_v for FD motions. A number of researchers have developed empirically based predictive relationships for these near-fault ground motion parameters (e.g. [6, 4, 7]). Most recently, Bray and Rodriguez-Marek [8] used a comprehensive database of FD ground motions to develop empirical relationships for *PGV* and T_v. This database was enhanced with FD records from recent earthquakes, and the relationships of Bray and Rodriguez-Marek [8] are updated in this paper.

Near-fault FD records were selected from the strong motion database of the Pacific Earthquake Engineering Research Center (http://peer.berkeley.edu/). Records with geometric conditions leading to FD were used. Records were selected if the ratio of fault-normal to fault-parallel spectral acceleration at a period of three seconds predicted by [1] was greater than one. Recordings not possessing at least some features of FD characteristics were excluded from the analysis. FD characteristics are positive fault-normal to fault-parallel response spectral ratios for long periods, and a reasonably well-defined velocity pulse in the fault-normal direction. The records are from shallow earthquakes ($M_w \geq 6$) in active tectonic regions at rupture distances (R = closest distance to the fault plane) less than 20 km. Fourteen near-fault records from four earthquakes (i.e., the 1986 Palm Springs, 2002 Denali, 2003 Bam, and 2004 Parkfield earthquakes) were added to the database of Bray and Rodriguez-Marek [8]. Three records from the 1999 Chi-Chi, Taiwan earthquake were processed to remove the fling-step present in the records by fitting a hyperbolic tangent function to the displacement-time history of the record and subsequently subtracting this motion from the time history (Rathje, pers. Comm. 2000). Ground motion sites were classified as either rock/shallow stiff soil (i.e., only 0 – 20 m of soil or weathered rock over competent rock) or soil (i.e., mostly stiff soil with shear wave velocity, V_s > 180 m/s). Soft soil and liquefiable sites were excluded. Additional details about the earthquakes, records, and fault-normal component orientation used are provided in [8] and [9].

The predictive relationships for *PGV* and T_v in this study (as well as the previous study by Bray and Rodriguez-Marek, [8]) include the influence of site conditions (i.e., "rock" or "soil") as well as earthquake moment magnitude (M_w) and the closest distance from the site to the ruptured fault (R). The empirical evidence clearly points to a systematic difference between near-fault FD motions recorded on rock and on soil sites. Ground motions recorded in soil tend to have longer pulse periods and larger *PGV*s than those recorded at rock sites [8]. An example of this is the set of ground motions recorded in Gilroy during the 1989 Loma Prieta earthquake as shown in Figure 3.

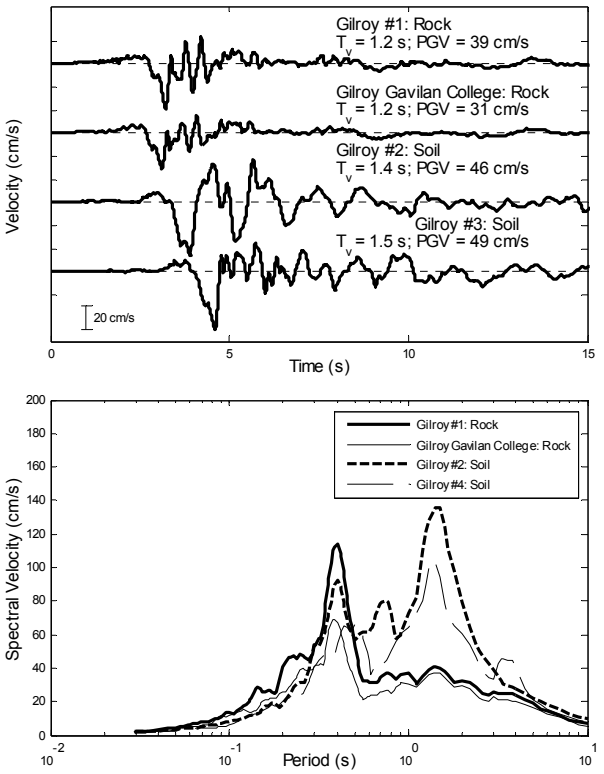

Figure 3: Recorded fault-normal motions during the 1989 Loma Prieta earthquake. Gilroy #1, Gavilan Coll., Gilroy #2, and Gilroy #3 have rupture distances of 11, 12, 13, and 14 km, resp. (modified from [8]).

Peak Ground Velocity

With the data for near-fault ground motions being restricted to relatively small source-to-site distances, the functional form of the model for estimating *PGV* can be simplified to:

$$\ln(PGV_{ij}) = a + b\,M_w + c\,\ln(R^2 + d^2) + \eta_i + \varepsilon_{ij} \qquad (1)$$

where PGV_{ij} is the peak ground velocity in units of cm/s of the j^{th} recording from the i^{th} event; M_w is moment magnitude of event i; R is rupture distance in km; and a, b, c, and d are regression parameters; and η_i and ε_{ij} represent the inter- and intra-event variations, respectively, obtained using the random effects model [10]. The inter-event and the intra-event error terms are assumed to be independent normally distributed random variables with variances τ^2 and σ^2, respectively. The standard error associated with the estimate of *PGV* is then

$$\sigma_{total}^2 = \tau^2 + \sigma^2 \qquad (2)$$

The functional form of Equation (1) for *PGV* as a function of distance results in a nearly zero slope at close distances to the fault, and it decreases linearly with the logarithm of distance at larger distances. The statistical analysis was performed on the entire dataset and then separately on the rock and soil motions. The parameters for Equation (1) are provided in Table 1.

Table1. Parameters for the PGV relationship (Equation 1).

Data Set	*a*	*b*	*c*	*d*	σ	τ	σ_{total}
All Motions	2.05	0.55	-0.39	5.00	0.37	0.24	0.44
Rock*	1.86	0.55	-0.39	5.00	-	-	0.40
Soil	2.11	0.55	-0.39	5.00	0.33	0.30	0.44

* Parameters had to be obtained using maximum likelihood.

Pulse Period

Somerville [6] provides justification for using self-similar scaling relationships to constrain fault parameters. The use of this scaling relationship indicates that the pulse period is about two times larger than the rise time of slip on a fault, which measures the duration of slip at a single point in the fault. From the mechanics of fault rupture, the rise time can be established as a lower bound for pulse period [6]. Because the logarithm of rise time is a linear function of moment magnitude, the use of a linear relationship between logarithm of rise time and magnitude is justified. Thus, the relationship used by [8] for pulse period is:

$$\ln(T_v)_{ij} = f + hM_w + \eta_i + \varepsilon_{ij} \qquad (3)$$

where $(T_v)_{ij}$ is the pulse period of the j^{th} recording from the i^{th} event; M_w is the moment magnitude of event i; f and h are regression parameters determined by the data through the random effects model; η_i is the inter-event term; and ε_{ij} represents the intra-event variations. The updated parameters for Equation (3) based on the regression analysis of the larger data included in this paper are provided in Table 2.

Table 2. Parameters for the relationship for velocity pulse period (Equation 3).

Data Set	*f*	*h*	σ	τ	σ_{total}
All Motions	-4.42	0.75	0.41	0.381	0.56
Rock	-6.37	1.00	0.46	0.29	0.55
Soil	-3.71	0.65	0.35	0.37	0.51

Number of Significant Cycles

The number of significant cycles of motion is defined as half the number of half-cycle (one-sided) velocity pulses that have an amplitude at least 50% of the peak ground velocity of the ground motion. Due to chaotic nature of fault rupture and the uncertainty in characterizing the details in the rupture process that determine the number of significant cycles, it is not possible at this time to develop a robust relationship for predicting this important parameter. However, an examination of FD records does provide useful insights.

Some earthquake events have a well-defined pulse sequence for nearly all of its near-fault motions. This might be expected for faults that have a relatively uniform slip distribution or earthquakes where slip is concentrated over a single zone. For these events, stations that are close to each other will likely be equidistant to regions of high slip. Moreover, path effects are minimized for stations in the near-fault region. However, for an earthquake with highly non-uniform slip, such as the 1994 Northridge earthquake, the type of pulse sequence observed depends on the instrument's distance relative to the asperities. Somerville [6] suggests that the number of half-sine pulses in the velocity time-history might be associated with the number of asperities in a fault rupture. Thus, details in the rupture process, such as the number of asperities of the fault and the slip distribution on the causative fault, determine the number of significant pulses in a FD motion.

Examination of the near-fault FD velocity-time histories included in this study does indicate that it is unlikely that a near-fault FD record will have more than two significant full cycles of motion. More than half of the FD records contained only one significant full cycle of motion (i.e., one two-sided velocity pulse). Hence, in developing design ground motions for use in projects, it is reasonable to select records that have

only one or two significant cycles of motion. It would be unnecessarily conservative to use simulated or modified ground motions records that have a large number of significant cycles of motion in their velocity-time history.

Although near-fault FD motions are more intense than ordinary records, they are shorter in duration. The seismic energy is compact, which leads to the high intensities, but also requires that the duration of significant shaking be short. Hence, it would also be unnecessarily conservative to use high intensity motions with long durations of strong shaking. It is more likely for near-fault FD motions to be at or below the median minus one standard deviation for significant duration.

Application into Probabilistic Seismic Hazard Analyses and Performance Based Design

Estimates of seismic hazard are usually made using Probabilistic Seismic Hazard Analyses (PSHA). PSHA predicts the mean annual rate of exceedance of a ground motion parameter (e.g., an *Intensity Measure*). These intensity measures, in turn, can be used to predict structural response in what is termed Performance Based Design (PBD). Equations (1) and (3) can be used in PSHA or in PBD for near-fault sites provided that the probability of occurrence of the pulse is known, and the cross correlation of PGV and T_v is also known. Thotong et al. [11] present a preliminary model for the probability of occurrence of a pulse. The correlation coefficient between $\ln(T_v)$ and $\ln(PGV)$ for the dataset used in this study is 0.24. The positive correlation coefficient implies that T_v increases as PGV increases, which is an expected outcome. However, the residuals of T_v and PGV (i.e., the difference between measured values their estimated values using Equations 1 or 3) are uncorrelated.

SEISMIC SITE RESPONSE FOR FD MOTIONS

Analytical Framework

Site conditions were found to be potentially of great importance in discerning the characteristics of near-fault FD motions. It should not be surprising that site effects have the potential for significantly modifying the ground motion at a deep or soft soil site compared to that which occurs at depth in the bedrock. The importance of local site conditions has been highlighted in a large number of empirical and analytical studies and is reflected in most building codes (e.g., the 2006 *International Building Code* [12]).

There are not a sufficient number of rock and soil recordings in close proximity to each other that contain near-fault FD characteristics to allow a detailed empirical study of site effects. Instead, numerical simulations are utilized. In a study by Rodriguez-Marek and Bray [13], seismic site response is modelled by means of a time-domain finite element analysis using the fully nonlinear multi-axial total stress soil constitutive model of Borja and Amies [14]. Bi-directional shaking is imposed to explore the combined effects of the more intense fault-normal component and the less intense, but still important, fault-parallel component of motion. One-dimensional propagation of horizontal shear waves is modelled by a column of 8-node tri-linear brick elements, where each node is allowed to move in two horizontal directions. Stress-free boundary conditions are imposed at the top of the column, and viscous dashpots are placed at the base of the soil column to model the energy absorption of the elastic half-space [15]. The implementation of the constitutive model in the finite element code GeoFeap [16] is discussed in [17]. This seismic site response analysis procedure has been validated using field downhole array recordings and laboratory shaking table measurements [17].

Eight parameters are required to define the soil model. Elastic soil response is determined by the shear wave velocity (V_s) and Poisson's ratio (v), which is assumed to be 0.49 to approach a fully undrained behavior. The exponential interpolation function of Borja and Amies' model is defined by two model parameters and the kinematic hardening parameter of the bounding surface. Soil strength is defined by the radius of the bounding surface, R, which is given by 1.6 S_u, where S_u is the soil's undrained strength in triaxial compression. When the soil will not reach shear failure, the parameter R can be used as a curve fitting parameter. Energy dissipation is naturally produced by the constitutive model through hysteretic damping. At small strain levels, damping is incorporated through Rayleigh damping, which is fully defined by the equivalent damping ratio at small strains, ξ, and a frequency band where ξ is matched.

Nonlinear site response is performed for generalized soil profiles subject to simplified pulse-type input motions so that insights can be made regarding the effects of site conditions in the near-fault region. Studies by structural engineers have shown that these simplified representations are capable of capturing the salient response features of structures subjected to near-fault ground motions (e.g., [4, 5]). Bray and Rodriguez-Marek [8] developed a simplified representation of FD velocity-time histories using sine pulses in both the fault-normal and fault-parallel directions. Ground motions are fully defined by the period of each cycle, their corresponding amplitude, and the number of significant pulses (see Figure 2). The PGV is the largest amplitude of all cycles and the pulse period of the record, T_v, is defined as the period of the cycle with the largest amplitude. A series of input velocity-time histories were created by parsing together sequences of sine pulses. The amplitude and period of these ground motions were varied systematically. Pulse periods were varied from 0.6 s to 4.0 s, and pulse amplitudes from 75 to 300 cm/s.

Generalized Site Profiles

Three generalized site profiles were created to represent common site classes used in building codes (Very Stiff Soil, Stiff Soil, and Soft Soil; corresponding to 2006 IBC Site classes C, D, and E, respectively). The selected shear wave velocity profiles are obtained from an extensive database of shear wave velocity logs of sites located largely within California (Silva, pers. comm. 2000). The shear wave velocities for all three generalized site profiles are shown in Figure 4. Shear wave velocities at depth (where V_s data is scarce) for the Site D profile were obtained assuming that shear wave velocities are proportional to $(\sigma'_m(z))^n$, where σ'_m is the mean effective stress at depth z and n = 0.25 [18]. The soft clay profile (Site E) represents typical Bay Mud sites from the San Francisco Bay region. The density of the stiff soils was about 1.9 Mg/m^3; whereas the density of Holocene clay was 1.6 Mg/m^3. The profiles were placed on 3 m of weathered rock that in turn overlies a rock elastic half-space with a shear wave velocity of 1200 m/s and a density of 2.4 Mg/m^3. For Site D, the depth of the profile was varied from 30 to 200 m to study the effects of variations of depth to bedrock on site response.

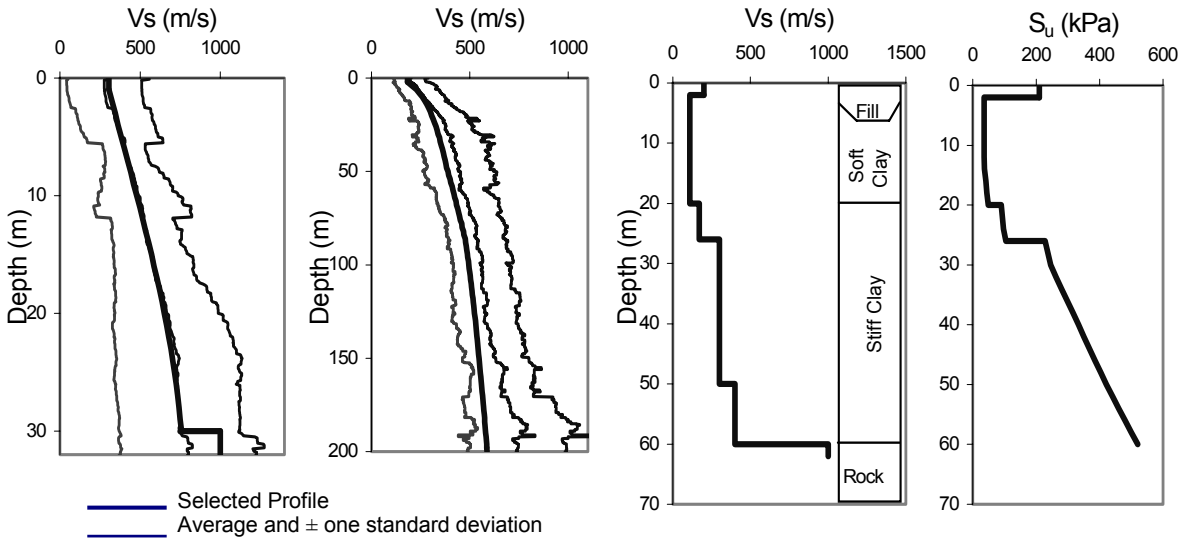

(a) Site C (b) Site D (c) Site E

Figure 4: ***Three generalized site profiles used in the dynamic analyses and representative values from a set of recorded V_s profiles in California (Silva, pers. Comm.) (from [13]).***

The strength profile of the clayey soils was developed using $S_u/\sigma_v' = 0.8$ for the stiff soils and $S_u/\sigma_v' = 0.3$ for the soft clay in the Site E profile. A lower bound of $S_u = 150$ kPa and $S_u = 25$ kPa were used for the stiff and soft clays, respectively. The static shear strength was multiplied by a factor of 1.4 to account for rate effects during the one primary cycle of rapid earthquake loading [19]. The nonlinear properties of the soil were obtained by matching the Borja and Amies [14] model to widely used strain-dependent shear modulus reduction and material damping relationships. The PI = 15 and PI = 30 curves of Vucetic and Dobry [20] were used for the stiff clay soils, and the curves of Isenhower and Stokoe [21] were used for the soft clays. Additional details are provided in [17].

Discussion of Results

The concept of an equivalent-linear "degraded site period" is still useful for interpreting the results of these nonlinear response analyses to intense near-fault FD motions. The degraded site period (T_s') is calculated as: $T_s' = 4H/V_s'$, where H is the soil depth and V_s' is the average effective shear wave velocity of the soil deposit using a shear modulus that is consistent with the effective shear strain induced in each layer of soil (i.e., $\gamma_{eff} = (n)\gamma_{max}$, where n is nearly 1.0 for pulse-type motions). The "degraded site period" increases with increasing soil depth, decreasing soil stiffness, and increasing soil nonlinearity resulting from more intense rock motions.

The largest amplification of *PGV* through a soil site occurs near its "degraded site period." The pulse period of the soil motion tends to approach the "degraded site period" when it is initially lower than the "degraded site period." Hence, input pulses that have lower periods undergo more elongation than those with higher periods. When the input velocity pulse period is higher than the "degraded site period," the soil deposit has a pseudo-rigid body response and pulse period is not affected. Although the stronger fault-normal component of near-fault FD motion is more critical, the fault-parallel component can also affect the response of a site. Larger fault-parallel component velocities lead to larger earthquake-induced shear strains, a softer response, and hence, a larger "degraded site period." Different shapes of the input pulse period also affect shear strain levels in the soil. Depending on the coincidence of fault-normal and fault-parallel peaks in velocity, motions can induce larger strains and result in higher degraded site periods [17].

Representative results are shown in Figure 5 for a set of bi-directional seismic site response analyses performed for a deep stiff soil site undergoing near-fault FD simplified half-cycle motions. For the relatively low pulse period input motion (Figure 5b), there is significant elongation of the pulse period due to the soil, but there is not amplification of the *PGV* as the input pulse period is not near the degraded period of the soil deposit. However, for the 2 s pulse period input motion (Figure 5a), there is significant amplification of the *PGV*, because it more closely coincides with the "degraded site period" of the deep, stiff soil deposit.

The relationship between output (PGV_{soil}) and input (PGV_{rock}) intensities for all site response analyses for the Stiff Soil profile (IBC Site D with soil depths ranging from 30 to 200 m) are shown in Figure 6. The ratio of PGV_{soil} to PGV_{rock} is generally between one and two. As a comparison to these analytical results, the results from an empirical study by Silva (pers. comm. 1998) exhibit a trend that is consistent with the results from these analyses. The computed amplification of *PGV* also agrees fairly well with the mid-period amplification factor for Site D in the 2006 IBC, suggesting that spectral amplification factors in the mid-period range ($T \sim 1$ s) are consistent with these *PGV* amplification factors. As indicated by the results shown in Figure 5, significant amplification still occurs for intense rock motions. Hence, the amount of nonlinearity in the amplification of *PGV* (or mid-period spectral acceleration amplification) is fairly minor for stiff soil profiles. Closer examination of the results in Figure 6 indicate that generally more amplification of *PGV* occurs for rock input motions with higher pulse periods and less amplification occurs for input motions with lower pulse periods.

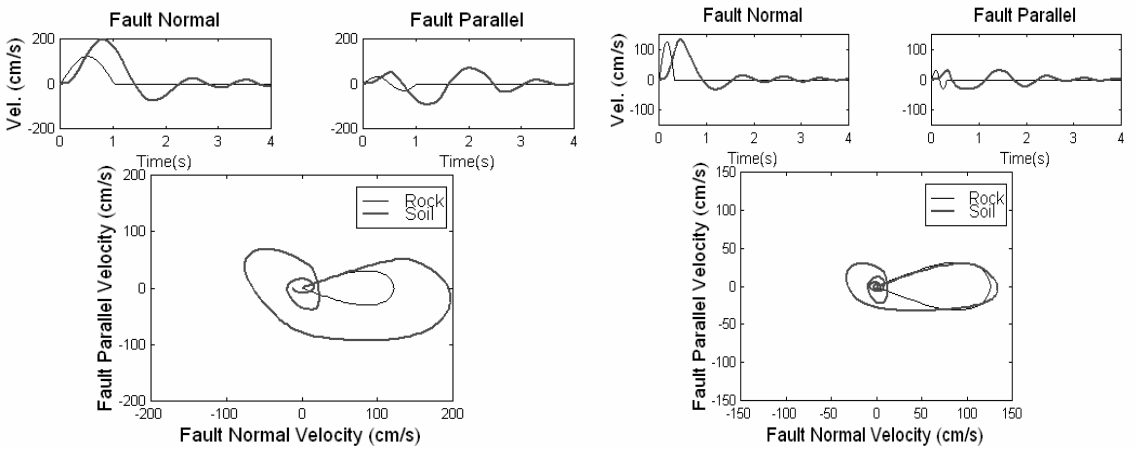

a) b)

Figure 5: ***Responses of a deep, stiff soil site to a half-sine-pulse input rock motion with PGV = 120 cm/s: (a) results for an input pulse period of 2.0 s, and (b) results for an input pulse period of 0.6 s.***

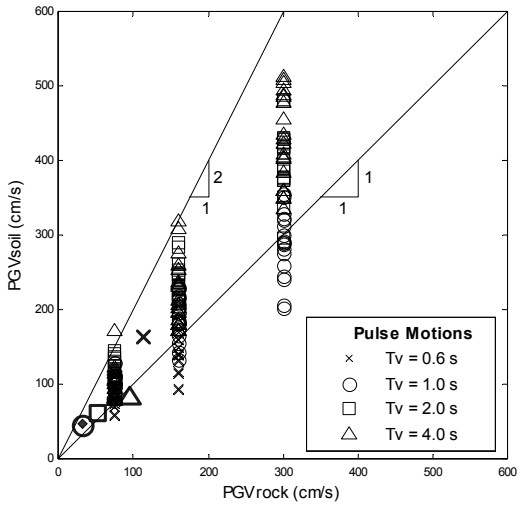

× Pacoima Dam, San Fernando EQ.

○ Gilroy Gavilan College, Loma Prieta EQ

□ Pacoima Dam Downstream, Northridge EQ

Δ KJMA, Kobe EQ

♦ Average for near-fault motions:
$M = 6 - 7$, $R < 10$ km (Silva, pers. comm. 1998) comm.)

Figure 6: ***Calculated PGV amplification at Stiff Clay profiles (see [17] for more details).***

Seismic site response analyses of the Soft Soil site (Site E) indicate that earthquake-induced shear stresses fully mobilized the dynamic strength of the soft clay for even relatively moderate near-fault motions. Thus, the soft soil deposit's low strength limits the site's peak seismic response. Significant variations in the shape of the soil's strain-dependent shear modulus reduction and material damping curves at intermediate strain levels do not affect the calculated *PGV* or T_v of the surface motion. Soil yielding leads to a significantly higher "degraded site period" with a significant amount of energy dissipation through plastic yielding. This leads to relatively more velocity period elongation at soft soil sites and greater attenuation of input rock PGV for intense rock motions than at stiff soil sites (Figure 7). This attenuation of pulse amplitude is not reflected in mid-period amplification factors in the 2006 IBC, because these factors are largely obtained from extrapolation of empirical site amplification factors for less intense motions and from equivalent-linear analyses that do not capture soil failure. Although seismic site response can be limited by the yield strength of soft soil, seismic instability effects must now be evaluated.

Seismic site response also affects the pulse period of the near-fault FD motion. Deep soil deposits with long degraded site periods tend to lengthen the pulse period of the input rock motion for all cases except when the rock pulse period is much greater than the degraded site period. Representative results for IBC 2006 Site D profiles are shown in Figure 8. The ratio of soil to rock pulse period may be as high as 2 for short pulse periods ($T_v < 1$ s), and this ratio approaches one as the input rock pulse period exceeds a few seconds. A greater amount of pulse period elongation occurs for very intense FD motions because of the greater nonlinearity in the seismic response of the soil at these intense levels of shaking. Hence, site effects are an important consideration in characterizing near-fault FD ground motions for use in design.

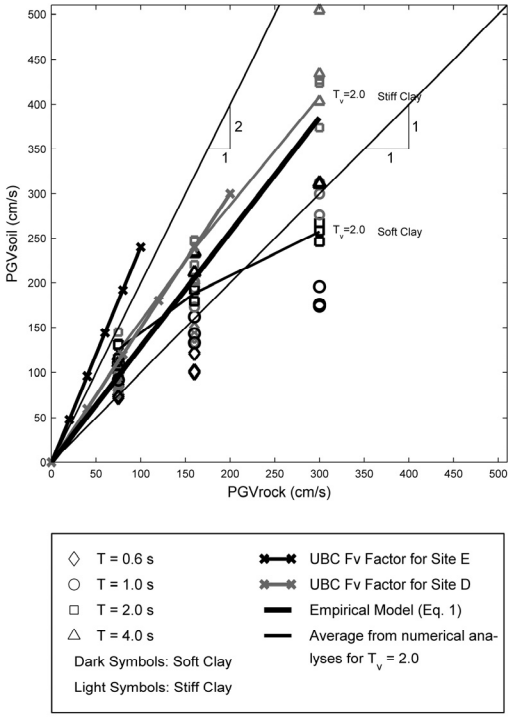

Figure 7: ***Results of seismic analyses of the Soft Clay and Stiff Clay profiles with soil depths of 60 m. Results are shown for various pulse shapes (see [17] for more details). Also shown for comparison are the mid-period amplification factors (F_v) from the 2006 IBC, and the predictions using the empirical model in Equation (1).***

Findings from Analytical Study

The characteristics of the near-fault FD motions at the surface of a soil deposit are primarily influenced by the characteristics of the input rock motion (i.e., its intensity, pulse period, and number of significant cycles) and the characteristics of the soil profile (i.e., soil type, stiffness, and depth to bedrock). Importantly, the *PGV* of the motion computed at the top of the soil is generally larger than the *PGV* of the rock input motion, with the exception of input motions with large intensities and short pulse periods. The T_v of the soil motion also systematically increases with increasing soil depth or increasing rock input motion intensity. Soil stiffness also affects the amplitude and period of input pulses. The largest amplification of *PGV* for the Very Stiff Soil profile (Site C) occurs for input motions with short pulse periods, whereas the largest amplification of *PGV* for the Stiff Soil profile (Site D) occurs at intermediate periods.

Site conditions play an important role in shaping the characteristics of near-fault FD motions at soil sites. Thus, the important influence of local soil conditions on FD motions should be considered when designing structures in the near-fault region. Site conditions affect the amplitude of the surface motion (i.e., its *PGV*) and its frequency content (i.e., its T_v). Fully nonlinear site-specific response analysis is required to capture the nonlinear response of soil deposits under the intense levels of shaking of FD motions. As guidance for this site-specific analysis, the likely range of site and intensity dependent amplification factors for *PGV* can be estimated using Figures 6 and 7, and the amount of pulse period elongation can be estimated using Figure 8.

CONCLUSIONS

Near-fault forward-directivity motions typically govern the design of structures built close to active faults. Hence, ground motions for use in evaluating designs in the near-fault region should be selected carefully to represent satisfactorily the unique nature of FD motions. Forward-directivity motions are often intense, pulse-type motions, which are significantly different from ordinary ground motions. These motions are best described by their velocity-time history, which requires estimation of its peak ground velocity (*PGV*), predominant pulse period (T_v), and number of significant velocity pulses (N_c).

Using recent FD motions, empirical relationships have been updated for estimating the *PGV* and T_v of near-fault FD motions. *PGV* varies significantly with magnitude, distance, and site effects. T_v is a function of magnitude and site conditions with most of the energy being concentrated within a narrow-period band centred on the pulse period. As lower magnitude events produce lower pulse periods, which better matches the low natural period of common buildings in urban areas, FD ground motions from these events have the potential to produce more damage than higher magnitude earthquakes in the near-fault region. Empirical relationships cannot be used at this time to predict N_c, because it depends on details of the rupture mechanism that cannot be known a priori. However, it is most likely that near-fault FD motions have only one or two significant cycles of motion. The compact FD wave form produces intense motions that are of short duration. Design near-fault FD velocity-time histories should not have a large number of significant cycles of motion.

Fully nonlinear bi-directional shaking simulations confirm indications from empirical evidence that site effects are important to consider in the near-fault region. It is shown that site effects generally cause T_v to increase, and that amplification of *PGV* depends on site properties, but amplification is generally observed even for very intense rock motions. At soft soil sites, seismic site response can be limited by the yield strength of the soil. In these cases, the seismic stability of the site and the building's foundation elements should be evaluated in terms of seismically induced permanent deformations.

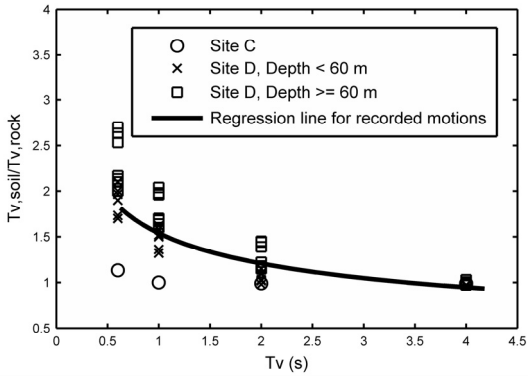

Figure 8: ***Pulse period of soil motion normalized by pulse period of rock motion vs. rock motion pulse period. Results are from seismic site response analyses for IBC 2006 Site C and D profiles. The heavy line represents the results from the Bray and Rodriguez-Marek (2004) regression of empirical records (modified from [13]).***

ACKNOWLEDGEMENTS

Financial support was provided by the Pacific Earthquake Engineering Research Center through Award 2011999 and by the David and Lucile Packard Foundation. The authors wish to thank Dr. Walter Silva of Pacific Engineering and Analysis for sharing his ground motion database and soil profile information. Professor Pestana of the University of California provided useful comments on the soil modelling.

REFERENCES

1 Somerville, P.G., Smith, N.F., Graves, R.W., and Abrahamson, N.A. (1997) "Modification of empirical strong ground motion attenuation relations to include the amplitude and duration effects of rupture directivity". *Seismological Research Letters*, **68**(1), 199-222.

2 Stewart, J.P., Chiou, S-J, Bray, J.D., Graves, R.W., Somerville, P.G., Abrahamson, N.A. (2001) "Ground Motion Evaluation Procedures For Performance-Based Design, PEER-2001/09". Pacific EQ Engrg. Research Center, Univ. of Calif., Berkeley, Sep., 229 pages.

3 Abrahamson, N.A. (2000) "Effects of rupture directivity on probabilistic seismic hazard analysis". *Proceedings, Sixth International Conference on Seismic Zonation*, Palm Springs, CA, Nov. 12-15.

4 Alavi, B., and Krawinkler, H. (2000) "Consideration of near-fault ground motion effects in seismic design". *Proceedings, 12th World Conf. on Earthquake Engineering.*, Auckland, New Zealand.

5 Sasani, M. and Bertero, V.V. (2000) "Importance of severe pulse-type ground motions in performance-based engineering: historical and critical review". *Proc., 12th World Conf. on EQ Engrg.*, Auckland, New Zealand.

6 Somerville, P.G. (1998) "Development of an improved ground motion representation for near-fault ground motions." *SMIP 98, Seminar on Utilization of Strong Motion Data*: Oakland, CA.

7 Mavroeidis, G.P., and Papageorgiou A.S. (2003) "A mathematical representation of near-fault ground motions." *Bulletin of the Seismological Society of America*, **93**(3), 1999-1131.

8 Bray, J.D., and Rodriguez-Marek, A., (2004) "Characterization of forward-directivity ground motions in the near-fault region." *Soil Dynamics and Earthquake Engineering*, **24**, 815-828.

9 Gillie J.L. (2005) *Nonlinear Response Spectra of Forward-Directivity Ground Motions*. MSc Thesis, Washington State University, Pullman, WA.

10 Abrahamson, N.A., and Youngs, R.R. (1992) "A stable algorithm for regression analyses using the random effects model". *Bulletin of the. Seismological Society of America*, **82**(1), 505-510.

11 Tothong P., Cornell C.A., and Baker J.W. (2007) "Explicit directivity-pulse inclusion in probabilistic seismic hazard analysis", *Earthquake Spectra*, **23** (4), 867-891.

12 International Code Council (2006) *International Building Code*, Country Club Hills, IL.

13 Rodriguez-Marek, A. and Bray, J.D. (2006) "Seismic site effects for near-fault forward directivity ground motions", *Journal of Geotechnical and Geoenvironmental Engineering*, ASCE, **132**(12), 1611-1620.

14 Borja, R.I., and Amies, A.P. (1994) "Multiaxial cyclic plasticity model for clays". *Journal of Geotechnical Engineering*, ASCE, **120**(6), 1051-1070.

15 Lysmer J.M., and Kuhlmeyer, A.M. (1969) "Finite dynamic model for infinite media". *Journal of the Engineering Mechanics Division*, ASCE, **95**(4) 859-877.

16 Espinoza R.D., Bray, J.D., Soga, K., and Taylor, R.L. (1995) *GeoFEAP: Geotechnical Finite Element Analysis Program, Report UCB/GT/95-05*, Dept. Civil Eng., Univ. of California, Berkeley.

17 Rodriguez-Marek, A. (2000) *Near-Fault Seismic Site Response*. Ph. D. Dissertation. Univ. of Calif., Berkeley.

18 Hardin, B. O., and Drnevich, V. P. (1972) "Shear modulus and damping in soils: measurements and parameter effects". *Journal of the Soil Mechanics and Foundation. Engineering*, ASCE, **98**(SM6), 603-624.

19 Lefebvre, G., and LeBoeuf, D., (1987) "Rate effects and cyclic loading of sensitive clays." *Journal of. Geotechnical Engineering*, ASCE, **113**(5), 476-489.

20 Vucetic, M., and Dobry, R. (1991) "Effect of Soil Plasticity on Cyclic Response". *Journal of. Geotechnical Engineering,* ASCE, **117**(1), 89-107.

21 Isenhower, W. M., and Stokoe, K. H. II, (1981) "Strain-rate dependent shear modulus of San Francisco Bay mud". *Inter. Conf. on Recent Advances in Geotechnical EQ Engineering.*, Univ. of Missouri, Rolla, 597-602.

Bulletin of the
Seismological Society of America

Vol. 81 October 1991 No. 5

THE 1989 LOMA PRIETA EARTHQUAKE AND ITS EFFECTS: INTRODUCTION TO THE SPECIAL ISSUE

By Thomas C. Hanks and Helmut Krawinkler

This special issue of the *Bulletin* consists of 33 articles dealing with the principal manifestations of the Loma Prieta earthquake (18 October 1989; **M** = 7.0) and its aftershocks. These articles span a wide range of scientific, engineering, and societal concerns and form the most recent addition to what promises to be a vast literature on the most important earthquake to occur in the United States since the 1906 San Francisco earthquake (**M** = 7.7). Interested readers of this special issue may wish to take note of the early contributions from the U.S. Geological Survey (1989, 1990) and the Earthquake Engineering Research Institute (1989, 1990); of the Governor's Board of Inquiry on the 1989 Loma Prieta Earthquake (Housner, 1990); of the 31 primarily seismological and geophysical studies in the July and August 1990 issues of *Geophysical Research Letters* (McNally and Ward, 1990); and of the probabilities for large earthquakes in the San Francisco Bay area, revised on the basis of the occurrence of the Loma Prieta earthquake (Working Group on California Earthquake Probabilities, 1990).

Even casual readers of this special issue will note that the Loma Prieta earthquake seems to have occurred on two different days. As any one of the hundred million or so viewers of the 1989 World Series knows, the Loma Prieta earthquake occurred at 5:04 p.m., Pacific Daylight Time (PDT), 17 October. This corresponds to 18 October 00:04, in Greenwich Mean Time (GMT). The engineering community, as a rule, does business according to local time, while seismologists and geophysicists generally adhere to GMT. Several different magnitudes are also associated with the Loma Prieta earthquake. The local magnitude M_L, the original magnitude scale of Richter (1935), is 6.7 (Uhrhammer and Bolt, this issue). As reported by the U.S. Geological Survey's National Earthquake Information Center (NEIC), the surface-wave magnitude M_s is 7.1. The (radiated) energy magnitude M_w of Kanamori (1977) is the same as the moment magnitude **M** of Hanks and Kanamori (1979) unless the earthquake stress drop is explicitly used in M_w. Numerous estimates of seismic moment M_0, both seismologic and geodetic, for the Loma Prieta earthquake may be found in this special issue (e.g., Beroza, Hartzell *et al.*, Marshall *et al.*, Snay *et al.*, Steidl *et al.*, Wald *et al.*, Wallace *et al.*), and most of them range from 2.5 to 3.5 $\times$ 10^{26} dyne-cm. For a "consensus M_0" = 3 $\times$ 10^{26} dyne-cm, **M** = 7.0.

More importantly, careful readers of this special issue will note that there seems to have been not just one Loma Prieta earthquake but four (at least): one expressed by the radiated field, perhaps 1A for frequencies >0.1 Hz (Beroza, Hartzell *et al.*, Steidl *et al.*, Wald *et al.*, this issue) and 1B for lower frequencies (Wallace *et al.*, this issue); a second to account for the aftershock distribution

and their focal mechanisms (Dietz and Ellsworth, 1990; Beck and Patton, this issue; Schwartz and Nelson, this issue); a third to explain horizontal displacements of the Earth's crust (Lisowski *et al.*, 1990; Snay *et al.*, this issue); and a fourth expressed as coseismic elevation data (Marshall *et al.*, this issue). Much work remains to reconcile these various models with one another in order to obtain a detailed but comprehensive model of the one earthquake that actually happened.

The Loma Prieta earthquake occurred in the Santa Cruz Mountains, which separate the San Francisco Bay area to the north from Santa Cruz on the northern margin of Monterey Bay to the south (Fig. 1). The principal tectonic player in this area is the San Andreas fault, which ruptured in the 1906 San Francisco earthquake, although documented surface evidence for this in the area of Figure 1 is very sparse (Prentice and Schwartz, this issue). If the Loma Prieta earthquake indeed occurred on the San Andreas fault, a yet arguable proposition, why did it not rupture the well-developed surface trace of the San Andreas fault? Ponti and Wells (this issue) describe in detail the ground ruptures and fissures that developed in the Summit Road area southwest of the San Andreas fault but attribute them primarily to shaking-induced, gravita-

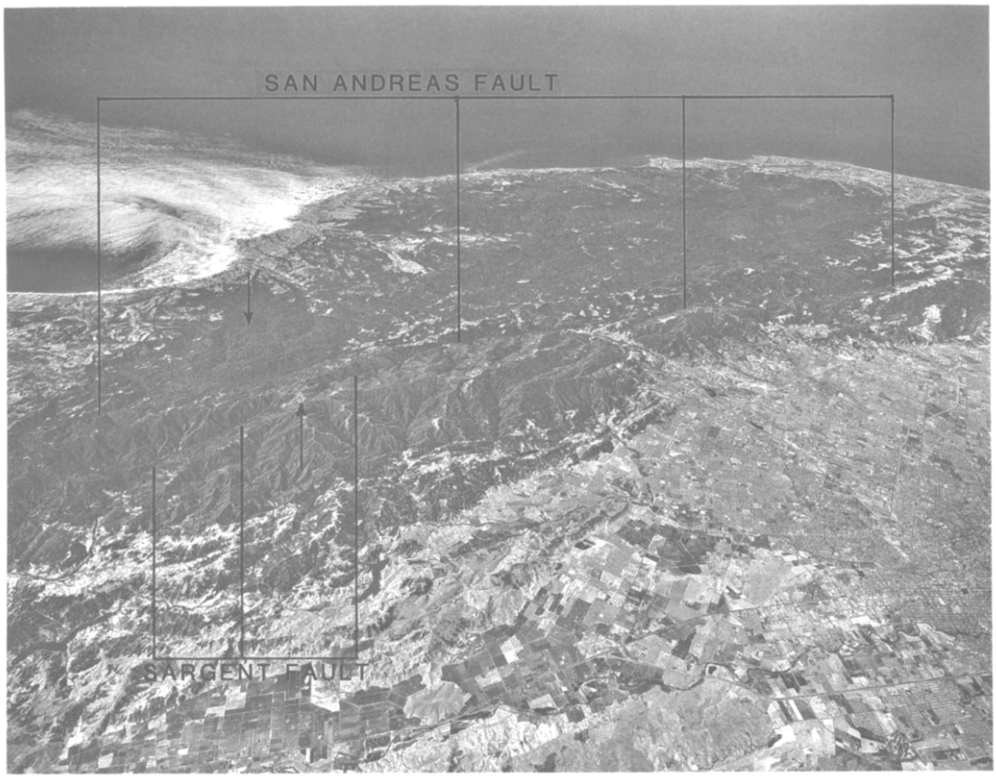

FIG. 1. View west across the Santa Clara Valley (foreground), with San Jose at the right margin, and the Santa Cruz Mountains (middleground) to the Pacific Ocean in the distance. Monterey Bay is the partially cloud-covered feature in the upper left with Santa Cruz and surrounding cities on its northern margin. The San Andreas and Sargent faults are each shown at several localities. The mainshock epicenter is shown with the downward-pointing arrow and Loma Prieta peak with the upward-pointing arrow. Frame 071-059R, U.S. Air Force, 17 July 1968.

tionally driven slope failure, with bedding-plane faulting being important at specific localities.

The significant component of reverse slip that accompanied the Loma Prieta earthquake (in a sense to uplift the Santa Cruz Mountains southwest of the San Andreas fault), while not unexpected in this terrane of crustal shortening and vertical tectonics, has raised questions about the legitimacy of the forecast for rupture of the southern Santa Cruz Mountain segment of the San Andreas fault (e.g., Working Group on California Earthquake Probabilities, 1988, 1990) and, indeed, whether the Loma Prieta earthquake actually ruptured the San Andreas fault at all (Segall and Lisowski, 1990; Prentice and Schwartz, this issue). Nevertheless, the Loma Prieta earthquake seems to be slip-predictable in the sense that its ~ 1.5 to 2 m of right-lateral slip is close to what should have accumulated in this region since 1906 (Thatcher, 1990). Valensise and Ward (this issue) note that the infrequent recurrence (300 to 600 years) of Loma Prieta-type earthquakes would explain the marine terraces uplifting along the Santa Cruz coast at their present rates for the last 125,000 years. Vertical tectonics of only this type, however, are inconsistent with uplift of the Santa Cruz Mountains both northeast and southwest of the San Andreas fault.

The pancaked Cypress Street viaduct, the Bay Bridge span failure, the Marina District tragedy, tumbled unreinforced masonry, and splintered homes in the Santa Cruz Mountains, however, are the impressions of the Loma Prieta earthquake that last, of structures destroyed, of lives extinguished, of paradise lost (Fig. 2). Rationalizing the observed damage and destruction in terms of the mainshock ground motion has occupied many scientists and engineers since the earthquake occurred, and the large number of articles in this special issue devoted to these topics reflects this continuing concern. Three issues emerge time and again: the relative strength of ground motion in the San Francisco–Treasure Island–Oakland corridor, where the majority of life and property loss occurred; the strong effect of local site conditions (including nonlinear amplification), especially at sites underlain by young Bay muds and artificial fill; and the importance of ground failure mechanisms in areas of hydraulic fill, most notably at Treasure Island and the Marina District.

Hutchings (this issue) estimates mainshock ground motion at five sites around the Bay area using aftershocks as empirical Green's functions and a range of mainshock source parameters that might have been anticipated in advance. He finds good agreement with the mainshock ground motion as actually recorded at four of these five sites but not at Yerba Buena Island, a rock site, where the observed ground motion is significantly larger than the predicted ground motion. This seems to be true for the entire San Francisco–Treasure Island–Oakland corridor of damage: peak accelerations (Campbell, this issue) and especially peak velocities (Hanks and Brady, this issue) are significantly larger at these distances ($\sim 95 \pm 5$ km) and azimuths ($\sim 334 \pm 5°$) than would be expected from the pre-existing data set for California earthquakes. While Somerville and Yoshimura (1990) have argued that deep crustal reflections are responsible for these anomalously large amplitudes, Campbell (this issue) notes that several other possibilities exist as well, including directivity and radiation pattern, path-dependent attenuation, and systematic differences in local site conditions.

Chin and Aki (this issue) use CALNET magnitude residuals to estimate weak-motion amplification factors at many strong-motion sites in the Bay Area.

FIG. 2. The facade of the home pictured here, high in the Santa Cruz Mountains, looked south across Monterey Bay to the Monterey Peninsula beyond. Failure of this structure occurred in several ways, the result of strong ground motion, possibly topographically amplified, and slope failure. The deck in the lower left of the picture was formerly attached to the house at the first floor level beneath the sliding glass doors just to the left of the chimney well.

They then find, after estimating geometric and anelastic attenuation factors, that their predicted mainshock peak accelerations at $R \leqq 50$ km were consistently larger than those observed at sedimentary sites and smaller than those observed at sites underlain by Franciscan rocks, suggestive of pervasive nonlinear amplification at the sedimentary sites. Darragh and Shakal (this issue) examine strong and weak motion at a soft-soil site (Treasure Island) and find strong evidence for nonlinear amplification of incoming seismic radiation. A stiff-soil site and a sandstone site of the Gilroy array, which recorded the 1979 Coyote Lake and 1984 Morgan Hill earthquakes as well as the Loma Prieta earthquake, did not, however, show significant differences between strong and weak motion. Boatwright *et al.* (this issue) note that strong-motion extrapolations based on aftershock (weak) motions for the Marina District are considerably larger than the mainshock record at Treasure Island, which Hanks and Brady (this issue) argue is the best available surrogate record for the Marina District.

Aftershock studies figure prominently in this special issue, both for site response investigations and as an indication of the mainshock environment. Schwartz and Nelson (this issue) show that $S-P$ times alone can effectively locate aftershocks under sparse station distribution, and Beck and Patton (this issue) use regional recordings of surface waves to determine the focal mechanisms of aftershocks in the $4 \leqq \mathbf{M} \leqq 4.5$ range. Both the distribution of aftershocks and the diversity of their focal mechanisms point to a complicated readjustment of the adjacent upper crust to the mainshock faulting. Hough *et*

al., Boatwright *et al.*, and Fletcher and Boatwright (all this issue) provide source parameter determinations for many Loma Prieta aftershocks.

Frankel *et al.* (this issue) use aftershock recordings from a small-aperture (~ 300 m station-spacing), four-station array in Sunnyvale to study the seismic response of the alluvium-filled Santa Clara valley and the role of surface waves in the seismic shaking of this and other sedimentary basins. McGarr *et al.* (this issue) analyze aftershock records at four sites, one of which is co-located with a strong-motion accelerograph, at San Francisco International Airport. They find amplifications of a factor of 2.5 relative to nearby bedrock sites and also supporting evidence that the *SmS* phase contributed significantly to peak motions along the San Francisco Peninsula. With small-aperture arrays deployed in the Santa Cruz Mountains, Bonamassa and Vidale (this issue) show that site response has a strong azimuthal dependence and that the shear-wave polarization as well as spectral amplitudes of ground motion are affected by the local site geology. These results will greatly complicate the development of simple site-characterization procedures for use, say, in earthquake hazards assessments.

The Marina District holds a special place in the Loma Prieta earthquake consciousness. It is the latest chapter in San Francisco's long and sad history of recognizing the special problems of the seismic response of young Bay muds and artificial fill only after earthquakes occur, in 1865, 1868, 1906, and again in 1989. It is a reminder, too, that neither are the educated and affluent immune from the effects of earthquakes, although it remains to be seen what this politically active and powerful group of residents will extract from their local, state, and federal governments in the way of earthquake hazards abatement. Finally, the damage and destruction in the Marina District is a case study for the profession in the great diversity and complexity of the relationships between earthquake ground motion and resulting damage (Hanks and Brady, this issue). Bonilla (this issue) describes the natural geologic deposits underlying the Marina District, the historical development of the filled areas, and the effects of the 1868 and 1906 earthquakes in the Marina District area, such as it existed at those times. Boatwright *et al.* (this issue) find that weak-motion amplification relative to Fort Mason is surprisingly uniform at five sites throughout the Marina District, irrespective of the artificial fill boundaries. Because no ground-motion recording device existed in the Marina District at the time of the Loma Prieta earthquake, however, considerable uncertainty surrounds estimates of the amplitude, frequency content, and duration of the mainshock ground motion there.

Clearer associations between ground motion and damage exist for the Cypress Street viaduct. Both Miranda and Bertero (this issue) and Krawinkler *et al.* (this issue) demonstrate that any one of the three closest mainshock ground-motion time histories would suffice to drive one or more of the viaduct bent types to failure. Hanks and Brady (this issue), however, show that there is some difficulty in relating strong ground motion to weak ground motion recorded in the vicinity of the Cypress Street viaduct. Şafak and Çelebi (this issue) analyze the dynamic response of two well-instrumented high-rise structures (the Transamerica Building in San Francisco and the Pacific Park Plaza Building in Emeryville) to the Loma Prieta earthquake, illustrating how system-identification techniques can be used to infer global dynamic response characteristics of complex structural systems. In one of the more practically useful papers ever

published in the *Bulletin*, Shepherd and Delos-Santos (this issue) present an experimental investigation of the performance of retrofitted cripple walls and show how inexpensive and straightforward modifications to existing homes can substantially reduce their vulnerability to earthquake shaking.

This special issue concludes with two papers that deal with earthquake response issues. Thiel *et al.* describe the response of various California state agencies, as of the spring of 1991, to the Governor's Executive Order (D-86-90) based on the findings of The Governor's Board of Inquiry on the 1989 Loma Prieta Earthquake (Housner, 1990). Durkin *et al.* investigate injuries and emergency medical response to the Loma Prieta earthquake, with a case study of emergency medical care in Santa Cruz County.

The Loma Prieta earthquake and its aftershocks offer the community of earthquake scientists and engineers a long research agenda into the causes and effects of earthquakes that will require a decade or more of study to fulfill. Just as importantly, the Loma Prieta earthquake raises questions and issues that cannot be settled with existing data sets. Certainly, the Loma Prieta earthquake is a reminder that earthquakes do not have to occur where we want them to occur or forecast them to occur and that our understanding of how and why earthquakes occur and recur, even along and near the best studied active crustal fault zone in the world, is rudimentary and incomplete. Because of such problems, Savage (1991) questions the validity of all the principal forecasts of the Working Group on Earthquake Probabilities (1988).

Similarly, we have much to learn about the complex and diverse relationships between strong ground motion and earthquake damage. In the Marina District, for example, the extensive structural damage resulted not just from the amplification of seismic waves through the entire sedimentary column, nor from the permanent ground deformation in the filled areas, nor from the existence of soft first stories, poor foundations, and deteriorated timbers: All of these factors contributed to bringing the Marina District to its knees. In the absence of even one mainshock record from the Marina District, however, we can only guess at the relative importance of each. So, too, even one mainshock record from the San Francisco–Oakland Bay Bridge would have been of great value in determining the motions of this important yet fragile structure leading to failure at Pier E-9.

Four short years after the Mexico City experience in the fall of 1985, the Loma Prieta earthquake reminded us again of the havoc to be wrought by ground motion amplification in soft soils and ground failure in nonengineered fills. Nevertheless, there is considerable uncertainty in how strong motion relates to weak motion and how spectral-domain amplification relates to time-domain amplification. Quantitative understanding of *in situ* nonlinear amplification will require dedicated, three-dimensional experiments operating for a decade or longer to record the required strong and weak motions, as well as extensive drilling efforts and laboratory analysis to determine basin geometry and material properties of the amplifying medium. The possibility of azimuth-dependent amplifications will compound the challenge, already formidable, of meeting the acknowledged need for more correctly allowing for site response in building codes, which presently lump all soil effects into a single site factor.

These issues and activities motivated by the Loma Prieta earthquake promise to make the scientific and engineering bases of earthquake hazards and risk reduction even more complete in the 21st century. Who will care about such

developments, other than the thousand or so scientists and engineers who actually achieve them, is a more interesting matter. The lessons of the Loma Prieta earthquake are many and varied, but few of them are new (e.g., Earthquake Engineering Research Institute, 1986). The effects of earthquake strong ground motion on unreinforced masonry, soft first stories, decayed timbers, bad foundations, hydraulic fill, and young Bay mud hardly qualify as news, especially in San Francisco where these "lessons" had all been learned in 1906 if not before. Indeed, the principal lesson of the Loma Prieta earthquake seems to be that the American public, even in earthquake country, is surprisingly uninformed about even the basics of earthquake occurrence, hazards, and risk; the latest reminder of this is the enormous nonsense, much of it news-media generated, surrounding Iben Browning's bogus prediction for a major earthquake in the New Madrid seismic zone during the first week of December 1990. Until there is a permanent, national consciousness that the hazards from earthquakes are very real and the potential losses very great, it seems inevitable that we shall learn the lessons of 1906 and 1989 yet again.

ACKNOWLEDGMENTS

This Special Issue was commissioned by the Board of Directors of the Seismological Society of America at the annual meeting of the Society in the spring of 1990. We very much appreciate the enthusiasm and effort of the 78 different authors and a like number of reviewers of their papers. D. M. Boore, Editor of the *Bulletin*, and L. Weber of Waverly Press were of great service to us in bringing this Special Issue to fruition. M. Clark brought Figure 1 of this Introduction to our attention, E. Dingle provided the labeling on it, and C. Sullivan prepared the text.

REFERENCES

Beck, S. L. and Patton, H. J. (1991). Inversion of regional surface-wave spectra for source parameters of aftershocks from the Loma Prieta earthquake, *Bull. Seism. Soc. Am.* **81,** 1726–1736.

Beroza, G. C. (1991). Near-source modeling of the Loma Prieta earthquake: evidence for heterogeneous slip and implications for earthquake hazard, *Bull. Seism. Soc. Am.* **81,** 1603–1621.

Boatwright, J., J. B. Fletcher, and T. E. Fumal (1991). A general inversion scheme for source, site, and propagation characteristics using multiply recorded sets of moderate-sized earthquakes, *Bull. Seism. Soc. Am.* **81,** 1754–1782.

Boatwright, J., L. C. Seekins, T. E. Fumal, H.-P. Liu, and C. S. Mueller (1991). Ground motion amplification in the Marina District, *Bull. Seism. Soc. Am.* **81,** 1980–1997.

Bonamassa, O. and J. E. Vidale (1991). Directional site resonances observed from aftershocks of the 18 October 1989 Loma Prieta earthquake, *Bull. Seism. Soc. Am.* **81,** 1945–1957.

Bonilla, M. G. (1991). The Marina District, San Francisco, California: geology, history, and earthquake effects, *Bull. Seism. Soc. Am.* **81,** 1958–1979.

Campbell, K. W. (1991). An empirical analysis of peak horizontal acceleration for the Loma Prieta, California, earthquake of 18 October 1989, *Bull. Seism. Soc. Am.* **81,** 1838–1858.

Chameau, J. L., G. W. Clough, F. Reyna, and J. D. Frost (1991). Liquefaction response of San Francisco Bayshore fills, *Bull. Seism. Soc. Am.* **81,** 1998–2018.

Chin, B.-H. and K. Aki (1991). Simultaneous study of the source, path, and site effects on strong ground motion during the 1989 Loma Prieta earthquake: a preliminary result on pervasive nonlinear site effects, *Bull. Seism. Soc. Am.* **81,** 1859–1884.

Darragh, R. B. and A. F. Shakal (1991). The site response of two rock and soil station pairs to strong and weak ground motion, *Bull. Seism. Soc. Am.* **81,** 1885–1899.

Dietz, L. D. and W. L. Ellsworth (1990). The October 17, 1989, Loma Prieta, California, earthquake and its aftershocks: geometry of the sequence from high-resolution locations, *Geophys. Res. Lett.* **17,** 1417–1420.

Durkin, M. E., C. C. Thiel, Jr., J. E. Schneider, and T. De Vriend (1991). Injuries and emergency medical response in the Loma Prieta earthquake, *Bull. Seism. Soc. Am.* **81,** 2143–2166.

Earthquake Engineering Research Institute (1986). Reducing earthquake hazards: lessons learned from earthquakes, Earthquake Engineering Research Institute 86-02, 208 pp.

Earthquake Engineering Research Institute (1989). Loma Prieta earthquake October 17, 1989 preliminary reconnaissance report, Earthquake Engineering Research Institute 89-03, 51 pp.

Earthquake Engineering Research Institute (1990). Loma Prieta earthquake reconnaissance report, Earthquake Engineering Research Institute 90-01, 448 pp.

Fletcher, J. B. and J. Boatwright (1991). Source parameters of Loma Prieta aftershocks and wave propagation characteristics along the San Francisco Peninsula from a joint inversion of digital seismograms, *Bull. Seism. Soc. Am.* **81,** 1785–1812.

Frankel, A., S. Hough, P. Friberg, and R. Busby (1991). Observations of Loma Prieta aftershocks from a dense array in Sunnyvale, California, *Bull. Seism. Soc. Am.* **81,** 1900–1922.

Hanks, T. C. and A. G. Brady (1991). The Loma Prieta earthquake, ground motion, and damage in Oakland, Treasure Island, and San Francisco, *Bull. Seism. Soc. Am.* **81,** 2019–2047.

Hanks, T. C. and H. Kanamori (1979). A moment magnitude scale, *J. Geophys. Res.* **84,** 2348–2350.

Hartzell, S. H., G. S. Stewart, and C. Mendoza (1991). Comparison of L_1 and L_2 norms in a teleseismic waveform inversion for the slip history of the Loma Prieta, California, earthquake, *Bull. Seism. Soc. Am.* **81,** 1518–1539.

Hough, S. E., L. Seeber, A. Lerner-Lam, J. G. Armbruster, and H. Guo (1991). Empirical Green's function analysis of Loma Prieta aftershocks, *Bull. Seism. Soc. Am.* **81,** 1737–1755.

Housner, G. W. (Chairman) (1990). Competing against time, Report to Governor George Deukmejian from the Governor's Board of Inquiry on the 1989 Loma Prieta earthquake, 264 pp.

Hutchings, L. (1991). "Prediction" of strong ground motion for the 1989 Loma Prieta earthquake using empirical Green's functions, *Bull. Seism. Soc. Am.* **81,** 1813–1837.

Kanamori, H. (1977). The energy released in great earthquakes, *J. Geophys. Res.* **82,** 2981–2987.

Krawinkler, H., A. Nassar, and M. Rahnama (1991). Damage potential of Loma Prieta ground motions, *Bull. Seism. Soc. Am.* **81,** 2048–2069.

Lisowski, M., W. H. Prescott, J. C. Savage, and M. J. Johnston (1990). Geodetic estimate of coseismic slip during the 1989 Loma Prieta, California, earthquake, *Geophys. Res. Lett.* **17,** 1437–1440.

Marshall, G. A., R. S. Stein, and W. Thatcher (1991). Faulting geometry and slip from co-seismic elevation changes: the 18 October 1989, Loma Prieta, California, earthquake, *Bull. Seism. Soc. Am.* **81,** 1660–1693.

McGarr, A., M. Çelebi, E. Sembera, T. Noce, and C. Mueller (1991). Ground motion at the San Francisco International Airport from the Loma Prieta earthquake sequence, 1989, *Bull. Seism. Soc. Am.* **81,** 1923–1944.

McNally, K. and S. N. Ward (1990). The Loma Prieta earthquake of October 17, 1989: introduction to the special issue, *Geophys. Res. Lett.* **17,** 1177.

Miranda, E. and V. V. Bertero (1991). Evaluation of the failure of the Cypress Viaduct in the Loma Prieta earthquake, *Bull. Seism. Soc. Am.* **81,** 2070–2086.

Ponti, D. J. and R. E. Wells (1991). Off-fault ground ruptures in the Santa Cruz Mountains, California: ridge-top spreading versus tectonic extension during the 1989 Loma Prieta earthquake, *Bull. Seism. Soc. Am.* **81,** 1480–1510.

Prentice, C. S. and D. P. Schwartz (1991). Re-evaluation of 1906 surface faulting, geomorphic expression, and seismic hazard along the San Andreas fault in the southern Santa Cruz Mountains, *Bull. Seism. Soc. Am.* **81,** 1424–1479.

Richter, C. F. (1935). An instrumental magnitude scale, *Bull. Seism. Soc. Am.* **25,** 1–32.

Şafak, E. and M. Çelebi (1991). Analyses of recorded responses of two high-rise buildings during the Loma Prieta earthquake of 18 October 1989, *Bull. Seism. Soc. Am.* **81,** 2087–2110.

Savage, J. C. (1991). Criticism of some forecasts of the National Earthquake Prediction Evaluation Council, *Bull. Seism. Soc. Am.* **81,** 862–881.

Schwartz, S. Y. and G. D. Nelson (1991). Loma Prieta aftershock relocation with S–P travel times: effects of 3-D structure and true error estimates, *Bull. Seism. Soc. Am.* **81,** 1705–1727.

Segall, P. and M. Lisowski (1990). Surface displacements in the 1906 San Francisco and 1989 Loma Prieta earthquakes, *Science* **250,** 1241–1244.

Shepherd, R. and E. O. Delos-Santos (1991). An experimental investigation of retrofitted cripple walls, *Bull. Seism. Soc. Am.* **81,** 2111–2126.

Snay, R. A., H. C. Neugebauer, and W. H. Prescott (1991). Horizontal deformation associated with the Loma Prieta earthquake, *Bull. Seism. Soc. Am.* **81,** 1647–1693.

Somerville, P. and J. Yoshimura (1990). The influence of critical Moho reflections on strong ground motions recorded in San Francisco and Oakland during the 1989 Loma Prieta earthquake, *Geophys. Res. Lett.* **17,** 1203–1206.

Steidl, J. H., R. J. Archuleta, and S. H. Hartzell (1991). Rupture history of the 1989 Loma Prieta, California, earthquake, *Bull. Seism. Soc. Am.* **81,** 1573–1602.

Thatcher, W. (1990). 1989 Loma Prieta earthquake: characteristic San Andreas slip or rare event? (abstract), *EOS* **71,** 1447.

Thiel, C. C., Jr., G. W. Housner, and L. T. Tobin (1991). State response to the Loma Prieta earthquake: competing against time, *Bull. Seism. Soc. Am.* **81,** 2127–2142.

Uhrhammer, R. A. and B. A. Bolt (1991). The seismic magnitude of the 1989 Loma Prieta mainshock determined from strong motion records, *Bull. Seism. Soc. Am.* **81,** 1511–1517.

U.S. Geological Survey (1989). Lessons learned from the Loma Prieta, California, earthquake of October 17, 1989, *U.S. Geol. Surv. Circ. 1045*, 48 pp.

U.S. Geological Survey (1990). The Loma Prieta, California, earthquake: an anticipated event, *Science* **247,** 286–293.

Valensise, G. and S. N. Ward (1991). Long-term uplift of the Santa Cruz coastline in response to repeated earthquakes along the San Andreas fault, *Bull. Seism. Soc. Am.* **81,** 1694–1704.

Wald, D. J., D. V. Helmberger, and T. H. Heaton (1991). Rupture model of the 1989 Loma Prieta earthquake from the inversion of strong-motion and broadband teleseismic data, *Bull. Seism. Soc. Am.* **81,** 1540–1572.

Wallace, T. C., A. Velasco, J. Zhang, and T. Lay (1991). A broadband seismological investigation of the 1989 Loma Prieta, California, earthquake: evidence for deep slow slip?, *Bull. Seism. Soc. Am.* **81,** 1622–1646.

Working Group on California Earthquake Probabilities (1988). Probabilities of large earthquakes occurring in California on the San Andreas fault, *U.S. Geol. Surv. Open-File Rept. 88-398*, 62 pp.

Working Group on California Earthquake Probabilities (1990). Probabilities of large earthquakes in the San Francisco Bay region, California, *U.S. Geol. Surv. Circ. 1053*, 51 pp.

U.S. Geological Survey/Stanford University Institute for
Research in Earthquake Engineering and Seismology
Stanford University
Stanford, California 94305

Manuscript received 31 July 1991

Bulletin of the Seismological Society of America, Vol. 81 5, pp. 1945–1957, October 1991

DIRECTIONAL SITE RESONANCES OBSERVED FROM AFTERSHOCKS OF THE 18 OCTOBER 1989 LOMA PRIETA EARTHQUAKE

BY ORNELLA BONAMASSA AND JOHN E. VIDALE

ABSTRACT

Two weeks after the 18 October 1989 Loma Prieta, California, earthquake, 18 three-component digital seismometers were deployed in the epicentral area to form three six-station subarrays. The subarray configuration allowed us to investigate the presence of direction- and frequency-dependent site resonances. We measured the shear-wave polarization from the recordings of 10 aftershocks from the Loma Prieta earthquake.

Our observations show that the site response has a strong azimuthal dependence and that both the shear-wave polarization and the spectral amplitude of the ground motions are affected by site characteristics. In the frequency range from 1 to 18 Hz, the majority of stations examined showed preferred azimuths of ground motion for the scattered waves that did not depend either on the earthquake location or on the polarization of the shear waves expected from the known focal mechanism. The measurements were made from 5-sec windows that included direct and scattered shear waves, which contain the largest amplitude motions in the near-source region and are therefore of most interest to earthquake engineers. However, in the 0- to 2-Hz frequency range, the first pulse of shear waves shows a polarization that is well predicted by the mechanism and location of the earthquake.

The rapid spatial variation of the preferred directions and their corresponding frequencies indicate that geologic structures within a distance of the order of 50 m probably control these site effects. We suggest that the site amplified the motion of scattered waves in one preferred direction, altering the resulting polarization and modulating the spectral amplitude.

INTRODUCTION

The analysis of strong ground motions recorded at various surficial sites (Seed *et al.*, 1976; Campbell, 1981; Joyner and Boore, 1981; Rogers *et al.*, 1984; Kagami *et al.*, 1986) and in boreholes (Haukkson *et al.*, 1987; Malin *et al.*, 1988) shows that near-receiver geology is an important factor in determining the strength of shaking from an earthquake. Spectral analysis of time histories recorded at the same site for Italian earthquakes has shown amplification (or deamplification) in specific frequency bands that is independent of earthquake location and that is not reproduced at neighboring sites (Rovelli *et al.*, 1988). On the basis of observations such as these, the sum of the complex phenomena that take place near the receiver has been termed the *site effect*. Although both source and site effects strongly influence observed spectral amplitudes, it is still possible to distinguish between the two effects (e.g., Andrews, 1984; Castro *et al.*, 1990; Mueller and Bonamassa, manuscript in preparation).

In many cases, flat-layered receiver structure has been useful in explaining observed site amplification (e.g., Seed *et al.*, 1972; Joyner *et al.*, 1976). The amplification of 2-sec energy by lakebed deposits in Mexico City during the 1985 Michoacán earthquake is a dramatic example of the influence of thin low-velocity layers near the Earth's surface (Campillo *et al.*, 1989). Patterns of

amplification and duration of shaking on the surface that require lateral variations in geologic structure (Vidale and Helmberger, 1988), and strong-motion effects of some simple large-scale structures (Vidale *et al.*, 1985; Bard and Gariel, 1986; Kawase and Aki, 1989) have been investigated; however, the importance of near-receiver structures more complicated than horizontal layers has not been previously documented for high-frequency seismic energy.

The aim of our study is to investigate the presence of direction- and frequency-dependent station resonances. Previous work on the 1987 Whittier Narrows, California, earthquake sequence suggests that the *strength* of the shaking at a site partly depends on the focal mechanism (Vidale, 1989), but this study indicates that in many cases the *direction of polarization* of the motion depends on the site geology. We show that in the frequency range from 1 to 20 Hz, some sites have preferred directions of ground motion polarization that do not depend either on the earthquake location or on the polarization of the shear waves expected from the focal mechanism. The most likely explanation for these azimuthal patterns is that particle motion in one direction is amplified compared to the motion in the orthogonal direction. The observations that these amplifications can change on a scale of 25 m and that the preferred directions of motion remain relatively constant through the *S*-wave arrival and coda suggest that these structures are very near the receivers, probably within distances of the order of 50 m. It is of great interest to earthquake engineers whether particular sites are likely to be strongly shaken in particular directions in a given frequency range. Our observations are not explicable by the conventional azimuthally symmetric models of site response.

Data Analysis

The analysis performed in this article is based on data collected with the instruments provided by the IRIS-PASSCAL Loma Prieta Aftershock Project. During the first 2 weeks after the 18 October 1989 Loma Prieta earthquake, 21 stations, each consisting of one Reftek 16-bit digitizer and two L-22 three-component geophones (resonance frequency is 2 Hz), operated in the epicentral region. For the following 3 weeks, nine of these instruments were reconfigured to form three six-station, three-component subarrays (for a total of 18 recording sites) to allow a detailed study of ground motions (see Fig. 1). The geometry of the subarrays was designed to be favorable for the analysis of the spatial and frequency coherence of the shaking. Figure 2 shows the location of the sensors at the ZAYA array whose records we examined in detail in this article.

Ten aftershocks characterized by varying locations and differing focal mechanisms (see Table 1) were selected for analysis. All events have an excellent signal-to-noise ratio and clear initial *P*-wave onsets and were recorded by all six stations installed at the ZAYA array.

This study is focused on the ZAYA site, but a preliminary analysis of data from the two other array sites shows similar levels of site effects at the PREZ array and less severe site effects at the WVRD array. A typical suite of the north–south component seismograms for all six elements of the ZAYA array is shown in Figure 3. It is remarkable that even the instruments spaced only 25 m apart record noticeably different signals.

Our analysis of site effect is based on both the polarization and spectral amplification of shear waves at the stations of the ZAYA array. On each seismogram, a cosine-tapered 5-sec window is applied in order to analyze both

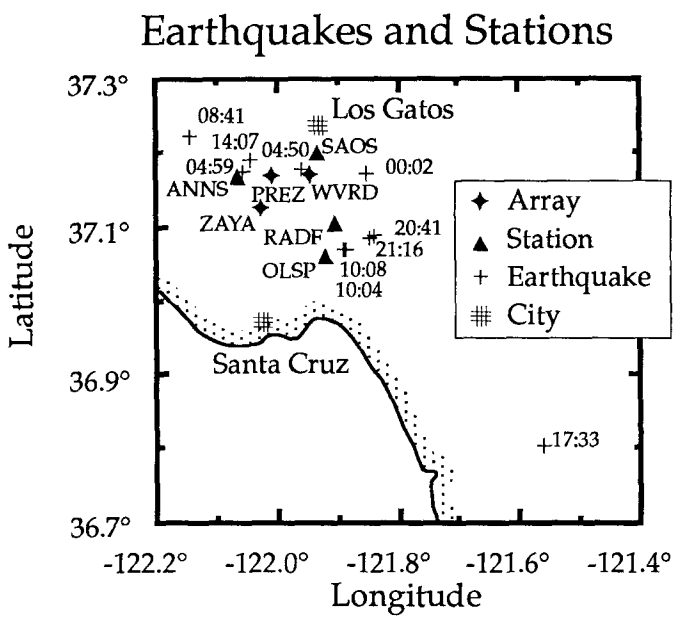

FIG. 1. Map view of the IRIS-PASSCAL stations and earthquake locations used in the analysis. Earthquake locations were obtained from David Oppenheimer (personal comm.).

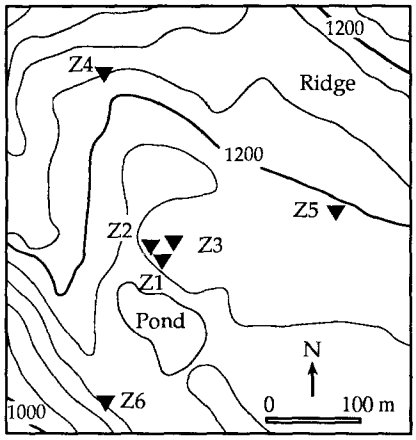

FIG. 2. Location of the six three-component stations comprising the ZAYA array. The array has the geometry of an inner and an outer triangle whose sides are approximately 25 and 300 m, respectively.

direct and scattered shear waves. The use of the 5-sec window for earthquakes having source duration less than 1 sec is justified by the need to study the part of the seismogram that shows the strongest shaking. If strong shaking lasts less than 5 sec, the polarization analysis is weighted by the square of the amplitude of shaking and therefore is dominated by the time intervals that have strong shaking. The spectra used below are an rms of the amplitude spectra of the two horizontal components. For each event, an average spectrum is computed by a logarithmic average of the spectra at all triggered stations, excluding the

TABLE 1

EARTHQUAKE PARAMETERS

Day	Time	Latitude	Longitude	Depth (km)	Δ (km)	Magnitude	Dip Direction*	Dip	Rake
11-14-89	00:02	37°10′	−121°51′	3.7	17	1.9	145°	80°	50°
11-14-89	04:50	37°11′	−121°58′	6.0	7	2.3	215°	40°	130°
11-14-89	08:41	37°13′	−122°09′	8.4	16	2.0	230°	30°	120°
11-14-89	17:33	37°48′	−121°34′	7.1	58	3.1	90°	15°	−130°
11-14-89	20:41	37°05′	−121°50′	5.7	19	2.8	220°	358°	100°
11-14-89	21:16	37°05′	−121°51′	5.6	20	3.4	165°	50°	10°
11-15-89	10:04	37°04′	−121°53′	15.0	15	2.5	275°	40°	−50°
11-15-89	10:08	37°04′	−121°53′	14.8	16	2.3	260°	35°	−50°
11-16-89	04:59	37°11′	−122°03′	10.8	5	2.9	240°	45°	160°
11-16-89	14:07	37°12′	−122°03′	10.5	5	2.4	200°	65°	100°

*The dip direction is the strike direction increased by 90°.
Mechanisms were provided by D. Oppenheimer (personal comm.).

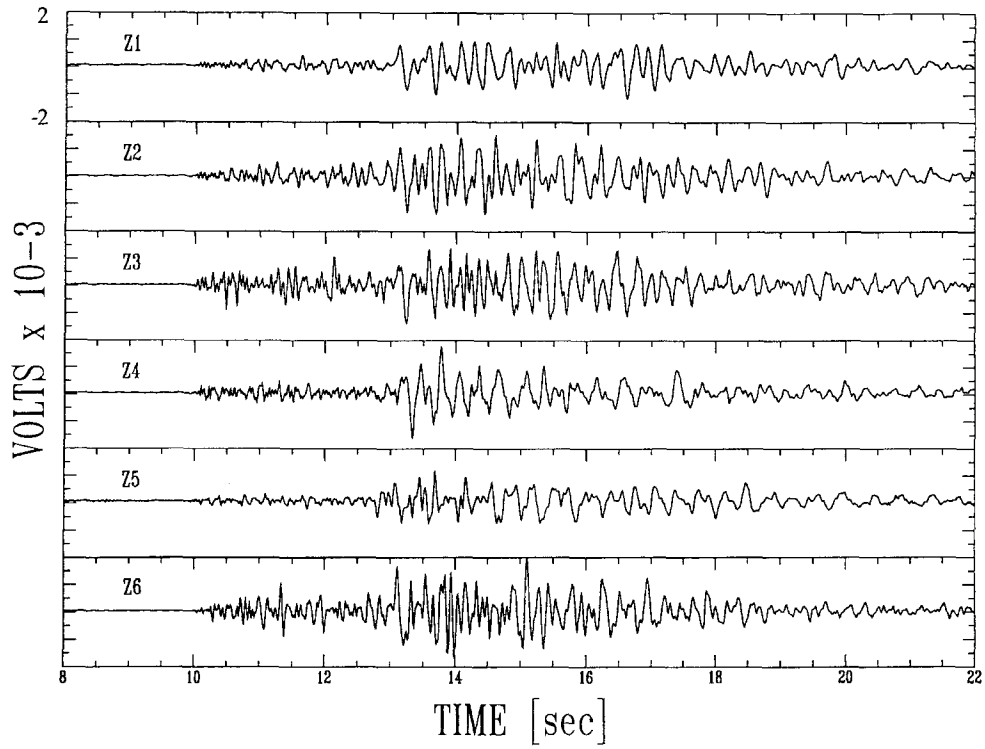

FIG. 3. North-south component seismograms for all six elements of the ZAYA array. The top three seismograms were recorded at the inner sites spaced 25 m apart; however signals are noticeably different.

stations of the ZAYA array. In this way, azimuthal amplitude variations and site effects have been averaged, providing a spectrum characteristic of the event. We did not correct for instrumental response, geometrical spreading, focal mechanism, or attenuation along the path. With logarithmic averaging, geometric spreading corrections would only shift the baseline of the spectra, not

change the patterns shown. Attenuation appears to depend on the path in unpredictable ways; this may be the subject of future studies. We note, however, that some studies have inverted for attenuation (e.g., Castro *et al.*, 1990).

Spectral amplitude ratios are computed between each of ZAYA's six stations and the average event spectrum at frequencies of 1 to 20 Hz. Ratios estimated for each event are averaged for the 10 events considered and are shown in Figure 4. This figure compares the average spectral amplitude of ZAYA's stations to the rest of the network. A value of the ratio equal to one would represent spectral behavior similar to the rest of the stations; in general, some amplification is seen. An increase in the ratio in two distinct frequency ranges is evident: at low frequency between 2 and 7 Hz for all stations, and at high frequency between 13 and 18 Hz for some stations. The amplitude ratios for the inner three elements are similar at 6 Hz and lower frequencies; the outer elements are similar only below 3 Hz.

The primary goal of this analysis is to investigate directional site effects and to determine their consistency and strength. A site effect that introduces a consistent amplification of one component of the motion will be most easily recognizable in a polarization study. Therefore, we have performed a systematic estimate of shear-wave polarization direction at different frequencies for many earthquakes with various locations and mechanisms recorded at the stations of the ZAYA array. Cosine-bell-shaped 2-Hz-wide windows centered from 1 to 20 Hz have been applied in the frequency domain as bandpass filters in overlapping frequency bands. Polarization directions have been estimated from the covariance matrix of the real signal. The eigenvector associated with the largest eigenvalue points in the direction of the largest amount of ground motion: this direction is indicated in this article as the polarization direction (Montalbetti and Kanasewich, 1970; Vidale, 1986). In order to eliminate scattered compressional waves from the analysis of shear-wave polarization, we have estimated

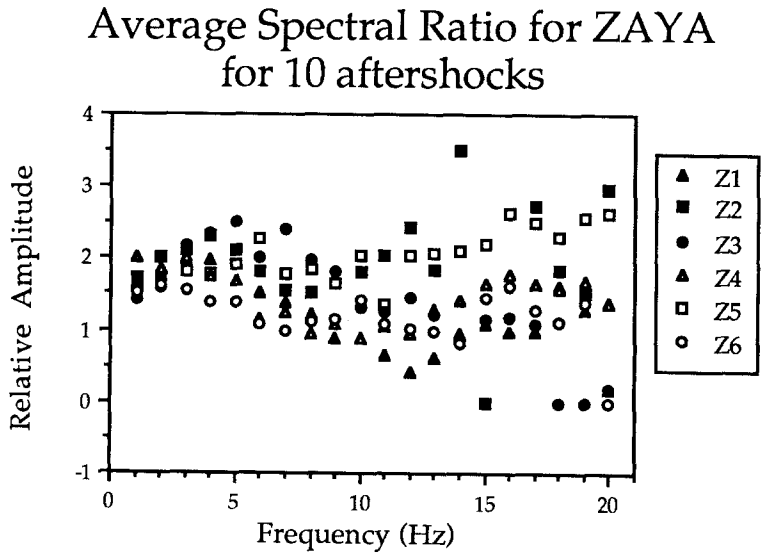

FIG. 4. Average spectral ratios for the six elements of the ZAYA array. Solid symbols are from the inner elements, open symbols from the outer elements.

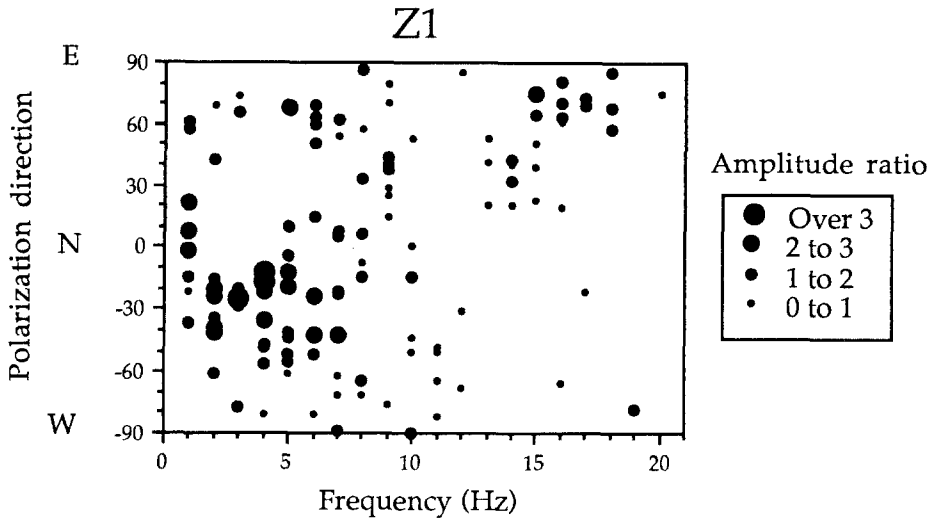

FIG. 5. Direction of strongest polarization plotted against frequency for the station Z1. Data from 10 events are shown. The symbol size is proportional to the amplification relative to the average spectra computed from stations outside the ZAYA array. The polarization has a range of 180°; the range extends from east to west through north. Thus, the polarization direction wraps from the top of the plot to the bottom.

the dip angle of each filtered signal. Data having polarization dips larger than 25° from the horizontal are most likely due to late *P*-wave coda, which we verified by inspecting the time domain records, and have been discarded. This selection has reduced the number of polarization measurements available at frequencies higher than 10 Hz.

RESULTS

The polarization direction versus frequency at station Z1 is shown in Figure 5 for the 10 events analyzed. In the hypothesis that the polarization is controlled exclusively by the focal mechanism at all frequencies, we would expect the polarization to have a certain azimuth at 1 Hz and to maintain that azimuth for all frequency bands. Plotting together the angles estimated for 10 different events for the range of frequencies, we would expect the angle values not to change with frequency for the same site for a given event, with each event showing a different direction of shaking. Instead, we see that in the frequency range from 2 to 5 Hz, most events produce particle motion with an azimuth of about −20° (N20°W) in correspondence with the spectral amplification seen in Figure 4 for this station. The spectral amplification may also be seen in the clustering of the largest symbols near −20° at 22 to 4 Hz. Perhaps some alignment at the azimuth 70° is seen for frequencies from 15 to 18 Hz. The similarity of particle motion directions for the 10 events, despite differences in focal mechanisms, suggests that the geologic structure that is amplifying motion at 2 to 5 Hz is more complicated than a simple stack of flat layers. Our interpretation of Figure 5 is that ground motion at site Z1 in the 2- to 5-Hz range is most prone to strong shaking with an azimuth of −20°, and the particle motion carries little information about the focal mechanism, with the exception of the first 0.5 sec, as noted below.

That this directionality is significant may be seen in Figure 6, which shows the horizontal particle motion of the ground in the passband from 3 to 5 Hz. The ratio of amplitude in the direction of strongest shaking (generally N20°W) to the amplitude in the orthogonal direction ranges from 1.4 to 2.5 and averages 1.8. The ratio of 1.8 in amplitude means a ratio of 3.2 in the energy of shaking, which may be significant to engineers.

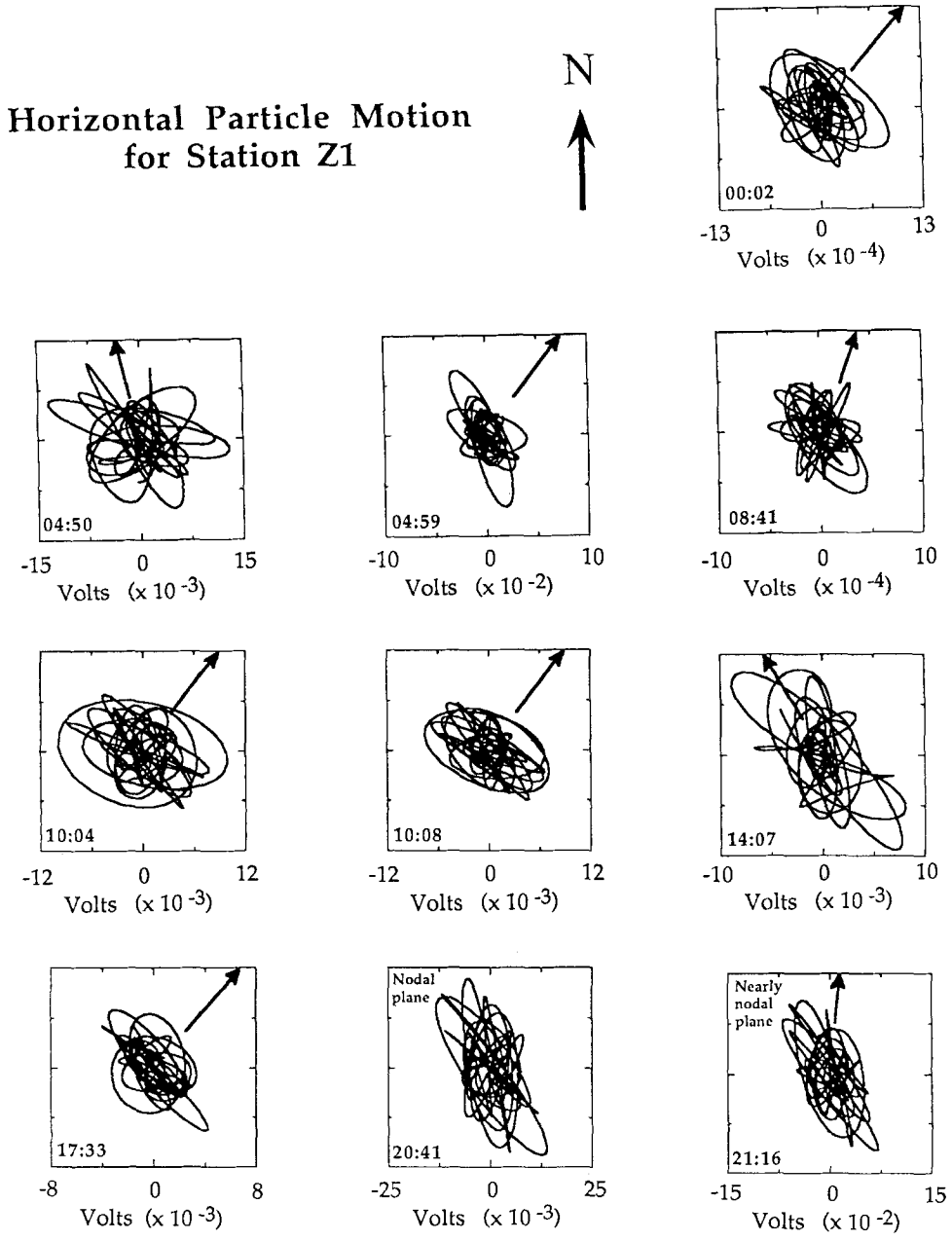

FIG. 6. Horizontal particle motion in a 5-sec window that starts with the shear-wave arrival for station Z1. Data are filtered in the passband from 3 to 5 Hz. The arrows point in the polarization direction predicted by the focal mechanism. The events are specified by hour and minute in the *lower left* corner of each frame.

Four of the six elements in the ZAYA array show strongly preferred *S*-wave particle motion directions in some frequency bands. Plots for station Z2 to Z6 are shown in Figure 7. Station Z2 shows a preferred direction of motion that shifts continuously clockwise from about 0° toward 90° with increasing fre-

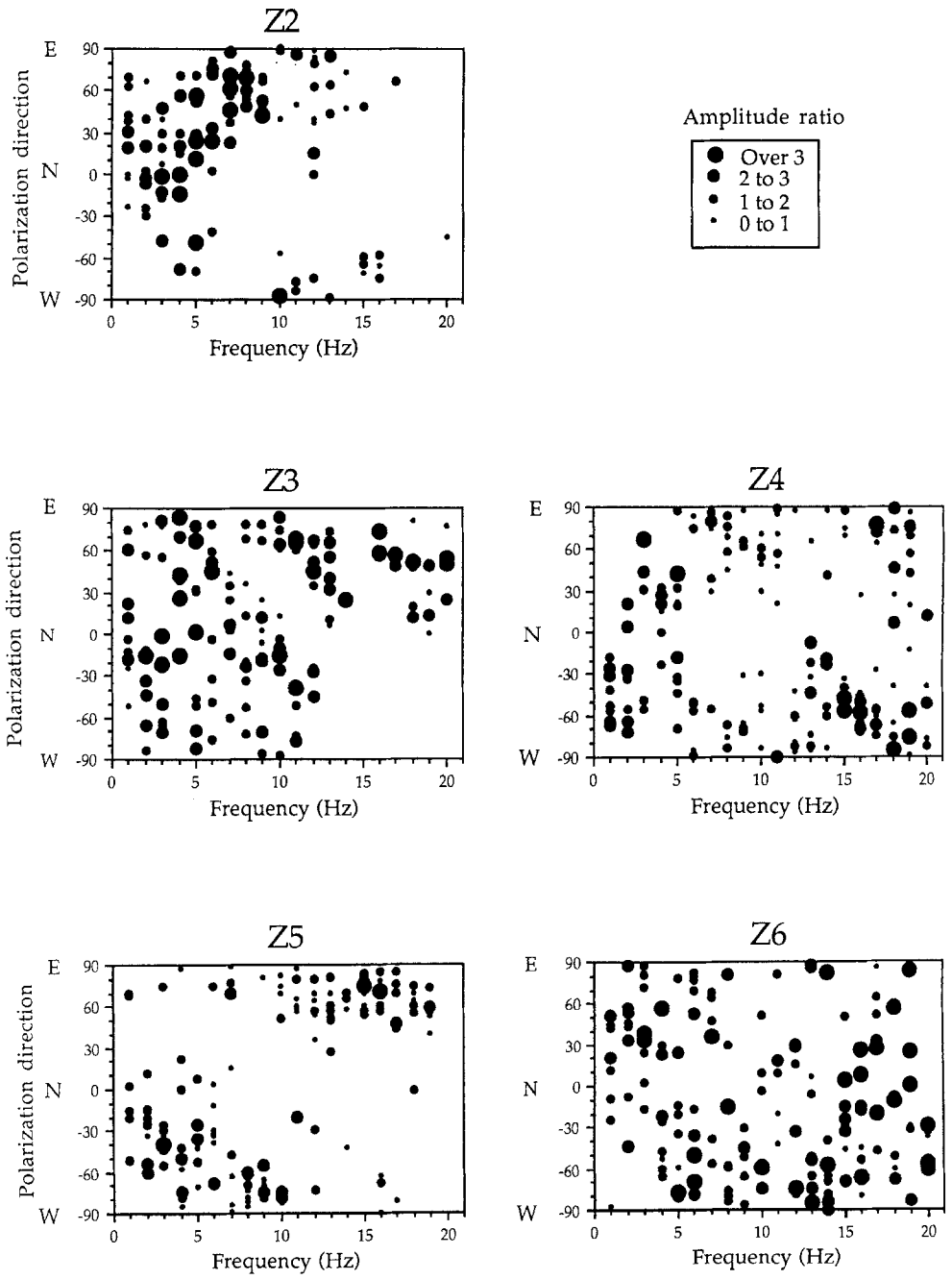

FIG. 7. Direction of strongest polarization plotted against frequency for the stations Z2 to Z6. Data from 10 events are plotted. The symbol size is proportional to the amplification relative to the average spectra computed from stations outside the ZAYA array.

quency. Stations Z3 and Z6 show no strong direction-dependent patterns, however neither do they show agreement with the direction expected from the locations and focal mechanisms. Station Z3 may show the more traditional direction-independent amplification at 3 to 5 Hz, consistent with the expected results from a flat-layered structure. Station Z4 shows motions centered around $-45°$ at 1 Hz and a strong $-60°$ clustering and amplification at 15 Hz. This behavior differs strongly from 1-Hz observations at the inner stations that show a preferred direction for the polarization in the positive range. Thus, the amplitude at 1 Hz is similar across the array, as seen in Figure 4, but the polarization directions at 1 Hz vary, as seen in Figures 5 and 7. Station Z5 shows particle motion orientation that rotates counterclockwise from 0° to $-90°$ in the frequency range from 1 to 10 Hz.

The estimated polarization directions are due to the strongest shaking in the 5-sec windows and apparently carry little information about the source. A closer examination of the seismograms allows us to formulate an interpretation of the observed phenomenon.

Figure 8a shows the seismograms of the event of 14 November 1989 at 00:02 GMT (same event shown in Fig. 3, details are given in Table 1) recorded by the six sensors of the ZAYA array. The top traces are the stack of the recordings shown below. For each sensor, two horizontal components are plotted: the upper trace is in direction of the polarization consistent with the focal mechanism; the lower is in the orthogonal direction. Data have been filtered with a passband of 0 to 2 Hz. The component in the direction of the expected polarization starts with a 0.5-sec pulse, followed by a scattered coda characterized by a lower amplitude. The orthogonal component is quiet at the time of the pulse, but it shows a series of scattered waves in the coda whose amplitude is comparable with the coda on the other component. This phenomenon is evident for all the six sensors, confirming that the polarization direction of the first 0.5-sec pulse is consistent with the polarization direction predicted by the focal mechanism. This initial coherence is expected (see Bernard and Zollo, 1989, for a review; Menke *et al.*, 1990). Figure 8b shows the same data, but bandpass filtered between 3 and 5 Hz, where the directional resonance is observed for station Z1. Various stacking strategies were tried, but the 3- to 5-Hz energy simply does not stack well. As in the previous figure, the first pulse is present in the top seismogram recorded at Z1 and is almost absent in the orthogonal component. The coda, however, shows peak amplitudes larger than in the first 0.5-sec of the signal. This coda can be interpreted as a resonance effect that generates the strongest shaking of the signal and whose directional dependence is evident in the analysis of the polarization.

The focal mechanism can also be observed in the average polarization of the array in the low-frequency passband (0 to 2 Hz). Figure 9 shows the comparison between the polarization direction predicted by the focal mechanism and the polarization direction obtained by averaging the 0- to 2-Hz covariance matrix of the six sites at ZAYA array (Jurkevics, 1988). Aside from the case of observations predicted to be nodal, the agreement between focal mechanism and average array polarization is quite good.

The physical cause of this resonance effect may be topography and surface geology, given the lack of information available about the detailed structure beneath the sensors. The six sensors lie at the two sides of the San Lorenzo syncline in a geologically homogeneous area of Tertiary age. The surface

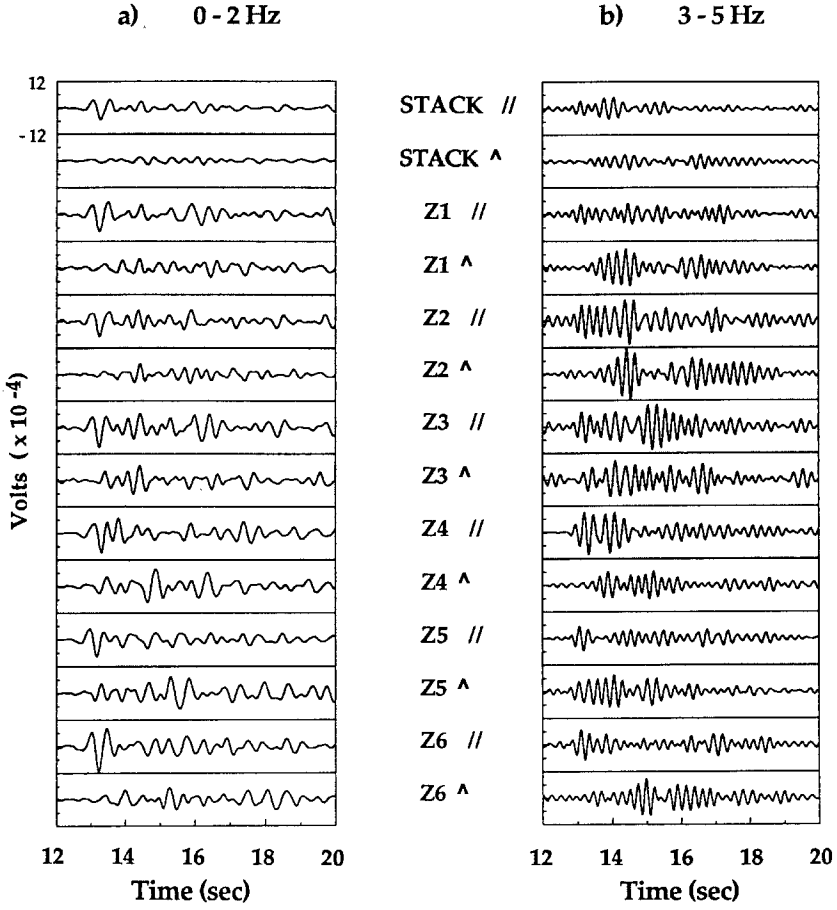

FIG. 8. Data from the 14 November 1989 (00:02 GMT) aftershock. The horizontal component seismograms recorded at the six sites of the ZAYA array have been rotated in the direction of polarization expected from the focal mechanism and in the orthogonal direction. (a) The data have been filtered in the 0- to 2-Hz passband. The *top* two seismograms are the stack of the six two-component data shown below. (b) Same as (a), except that the seismograms have been filtered in the 3- to 5-Hz passband.

geology indicates that the sensors Z1, Z2, Z3, Z4, and Z5 have been buried in Lambert Shale (Marine semi-siliceous shale and siltstone; Saucesian stage, late Miocene), while sensor Z6 is in the slightly older Vaqueros Sandstone (Marine arkosic sandstone; minor siltstone; Saucesian and Zemorrian stages, Brabb and Dibblee, 1979). Surface geology and topography are similar for the three inner sensors, leaving the observed differences unexplained. The sensor Z4, located on a steep slope near a ridge, resonates with directions that are not easily related to topography, while sensor Z6 lies on a steepest ridge and does not show a well-defined site effect. In sum, observations are not easily related to topography, while geology probably plays a significant role.

Figure 10 summarizes our results. For each station, the arrows indicate the direction of polarization and its frequency band. In general, sites that exhibit some directional effect show resonance at low frequency (1 to 3 Hz) in the northwest–southeast direction and at higher frequency in the east-west direc-

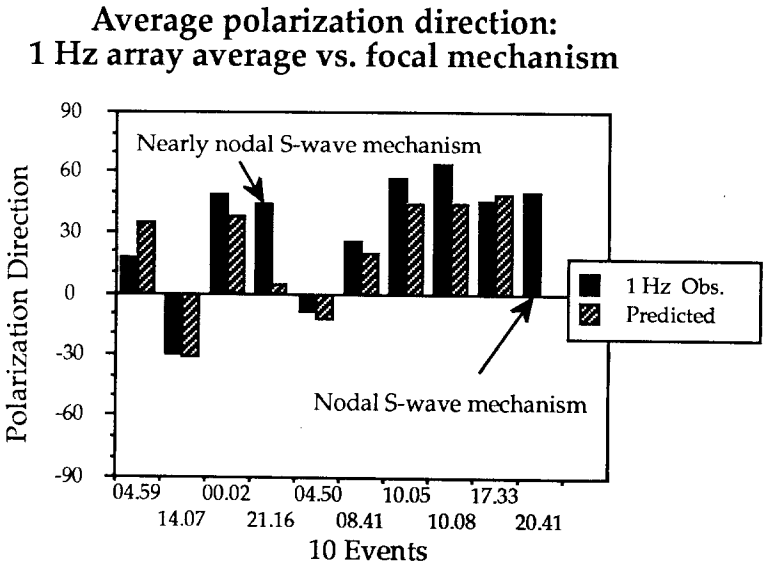

FIG. 9. Comparison between polarization direction predicted by the focal mechanism and the polarization direction obtained by averaging the covariance matrix of the six sites at the ZAYA array in the 0- to 2-Hz band.

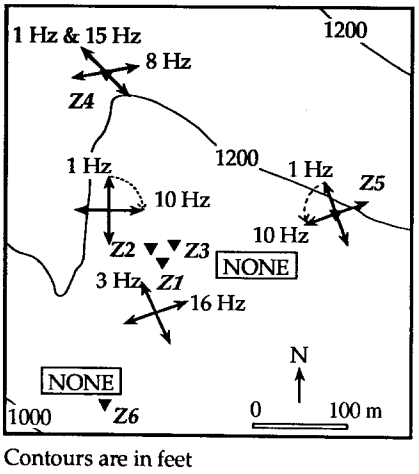

FIG. 10. Map of the ZAYA array displaying a summary of the observed directional resonances. At each site, the arrows indicate direction of the resonance and its frequency band.

tion. We will not attempt to interpret this probably coincidental correlation here.

The most likely explanation for the observed resonance patterns is that particle motion in selected frequency bands is amplified in particular directions compared to motions in other directions. The specific geological structures that cause this amplification are not yet known. The direction of amplified particle motion changes across the inner 25-m triangle of stations, and the preferred directions of motion at each station remain relatively constant through the *S*-wave arrival and coda.

Conclusions

The analysis of 10 events recorded at a small-aperture array of six digital stations has shown that polarization, as well as spectral amplitude of the ground motion, can be affected by site characteristics. Similar directional site resonances have also been noticed by the authors for the 1 October 1987 Whittier Narrows earthquake (Vidale *et al.*, 1991). We suggest that the site may amplify the motion in one preferred direction, leaving the motion in the orthogonal direction unaffected or diminished. This direction-dependent amplification alters the particle motion. However, the first 0.5-sec pulse of the recorded signals often shows a polarization direction consistent with the polarization direction predicted by the focal mechanism. The observation of a directional resonance is new, while site-specific spectral amplifications have previously been widely observed.

The specific geological structures that cause this amplification are not yet known. Lateral gradients in near-surface shear-wave velocity are the most likely cause of these lateral resonances. The observations that these amplifications can change on a scale of 25 m and that the preferred directions of motion remain relatively constant through the *S*-wave arrival and coda suggest that these structures are very near the receivers, probably within a few tens of meters. The predictability of the preferred direction of strong shaking should prove useful to earthquake engineers.

Acknowledgments

We wish to thank all who helped with field operations, especially Susan Schwartz, Aaron A. Velasco, Marino Protti-Quesada (UCSC), Grant Lindley and Keith Dinger (UCSB). We also thank David Oppenheimer (USGS) for providing locations and focal mechanism solutions and IRIS for supplying instrumentation for the field deployment. This material is based upon work supported by the Incorporated Research Institutions for Seismology under their Cooperative Agreement No. EAR 84-19149 with the National Science Foundation.

Support for this work has been provided in part by a grant from the W. M. Keck Foundation, and the Institute of Tectonics, University of California, Santa Cruz. Support has also been provided by the USGS grant number 14-08-0001-G1837. Contribution Number 84 from the Charles F. Richter Seismological Laboratory at the University of California, Santa Cruz.

References

Andrews, J. (1984). Objective determination of source parameters and similarity of earthquakes of different size, in *Earthquake Source Mechanics*, S. Das, J. Boatwright, and C. H. Scholz (Editors) American Geophysical Monograph 37, 259–267.

Bard, P.-Y. and J. C. Gariel (1986). The seismic response of two-dimensional sedimentary deposits with large vertical velocity gradients, *Bull. Seism. Soc. Am.* **76**, 343–60.

Bernard P. and A. Zollo (1989). Inversion of near-source *S* polarization for parameters of double-couple point sources, *Bull. Seism. Soc. Am.* **79**, 1779–1809.

Brabb, E. E. and T. W. Dibblee (1979). Preliminary geologic map of the Castle Rock Ridge quadrangle. Santa Cruz and Santa Clara counties, California, *U. S. Geol. Surv. Open-File Rep.* **79-659**.

Campbell, K. W. (1981). Near-source attenuation of peak horizontal acceleration, *Bull. Seism. Soc. Am.* **71**, 2039–2070.

Campillo, M., J. C. Gariel, K. Aki, and F. J. Sánchez-Sesma (1989). Destructive strong ground motion in Mexico City: source, path and site effects during the great 1985 Michoacán earthquake, *Bull. Seism. Soc. Am.* **79**, 1718–1734.

Castro, R. R., J. G. Anderson, and S. K. Singh (1990). Site response, attenuation and source spectra of *S*-waves along the Guerrero, Mexico subduction zone, *Bull. Seism. Soc. Am.* **80**, 1481–1503.

Haukkson, E., T.-L. Teng, and T. L. Henyey (1987). Results from a 1500 m deep, three-level downhole seismometer array, *Bull. Seism. Soc. Am.*, **77**, 1883–1904.

Joyner, W. B. and D. M. Boore (1981). Peak horizontal acceleration and velocity from strong-motion records from the 1979 Imperial Valley, California earthquake, *Bull. Seism. Soc. Am.*, **47**, 2011-2038.

Joyner, W. B., R. E. Warrick, and A. A. Oliver, III (1976). Analysis of seismograms from a downhole array in sediments near San Francisco Bay, *Bull. Seism. Soc. Am.* **66**, 937-958.

Jurkevics, A. (1988). Polarization analysis of three component array data, *Bull. Seism. Soc. Am.* **78**, 1725-1743.

Kagami, H., S. Okada, K. Shiono, M. Oner, M. Dravinski, and A. K. Mal (1986). Observation of 1-5 second microtremors and their application to earthquake engineering. Part III. A two-dimensional study of site effects in the San Fernando Valley, *Bull. Seism. Soc. Am.* **76**, 1801-1812.

Kawase, H. and K. Aki (1989). A study on the response of a soft basin for incident *S*, *P*, and Rayleigh waves with special reference to the long duration observed in Mexico City, *Bull. Seism. Soc. Am.* **79**, 1361-1382.

Malin, P. E., J. A. Waller, R. D. Borcherdt, E. Cranswick, E. G. Jensen, and N. Van Schaak (1988). Vertical seismic profiling of Oroville microearthquakes: velocity spectra and particle motion as a function of depth, *Bull. Seism. Soc. Am.* **78**, 401-420.

Menke, W., A. L. Lerner-Lam, B. Dubendorff, and J. Pacheco (1990). Polarization and coherence of 5 to 30 Hz seismic wave fields at a hard-rock site and their relevance to velocity heterogeneities in the crust, *Bull. Seism. Soc. Am.* **80**, 430-449.

Montalbetti, J. R. and E. R. Kanasewich (1970). Enhancement of teleseismic body phases with a polarization filter, *Geophys. J. R. Astr. Soc.* **21**, 119-129.

Rogers, A. M., R. D. Borcherdt, P. A. Covington, and D. M. Perkins (1984). A comparative ground response study near Los Angeles using recordings of Nevada nuclear tests and the 1971 San Fernando earthquake, *Bull. Seism. Soc. Am.* **74**, 1925-1949.

Rovelli, A., O. Bonamassa, M. Cocco, M. Di Bona, and S. Mazza (1988). Scaling laws and spectral parameters of the ground motion in active extensional areas in Italy, *Bull. Seism. Soc. Am.* **78**, 530-560.

Seed, H. B., H. Boulton, P. Schnabel, and J. Lysmer (1972). Modification of seismograph records for effects of local soil conditions, *Bull. Seism. Soc. Am.* **62**, 1649-1664.

Seed, H. B., C. Ugas, and J. Lysmer (1976). Site-dependent spectra for earthquake-resistant design, *Bull. Seism. Soc. Am.* **66**, 221-244.

Vidale, J. E. (1986). Complex polarization analysis of particle motion, *Bull. Seism. Soc. Am.* **76**, 1393-1406.

Vidale, J. E. (1989). Influence of focal mechanism on peak accelerations for the Whittier Narrows, California, earthquake and an aftershock, *J. Geophys. Res.* **94**, 9607-9615.

Vidale, J. E., O. Bonamassa, and H. Houston (1991). Directional site resonances observed from the 1 October 1987 Whittier Narrows, California, earthquake and the 4 October aftershock, *Earthquake Spectra* **7**, 107-125.

Vidale, J. E. and D. V. Helmberger (1988). Elastic finite-difference modeling of the 1971 San Fernando, California, earthquake, *Bull. Seism. Soc. Am.* **78**, 122-142.

Vidale, J. E., D. V. Helmberger, and R. W. Clayton (1985). Finite-difference seismograms for *SH* waves, *Bull. Seism. Soc. Am.* **75**, 1765-1782.

Institute of Tectonics
University of California
Santa Cruz, California 95064

Manuscript received 29 July 1990

5

Engineering Characterization of Ground Motion

Yousef Bozorgnia

Kenneth W. Campbell

5.1 Introduction

"The basic data of earthquake engineering are the recordings of ground accelerations during earthquakes. A knowledge of the ground motion is essential to an understanding of the earthquake behavior of structures" (Housner, 1970a). Recorded ground motion time series contain valuable characteristics and information that are used directly, or indirectly, in seismic analysis and design. Parameters such as peak

ground motion values (acceleration, velocity and displacement), measures of the frequency content of the ground motion, duration of strong shaking and various intensity measures play important roles in seismic evaluation of existing facilities and design of new systems.

This chapter presents *engineering* characteristics of strong ground motion. Seismological aspects of ground motion, which are related to the topics presented in this chapter, are covered in Chapter 2. In Section 5.2, we provide a historical perspective of strong-motion recordings and present numerous examples of ground acceleration and velocity time series, followed by a list of the agencies that provide strong ground motion records. In Section 5.3, we discuss the characteristics and applications of various strong-motion *spectra* and their associated parameters. These include Fourier spectra, elastic response spectra, elastic design spectra, drift spectra, inelastic spectra, inelastic design spectra, energy spectra, damage spectra and other parameters such as Housner Spectrum Intensity and Arias Intensity. Strong-motion spectra have widespread applications in probabilistic and deterministic seismic hazard analysis, seismic analysis and design, quantification of damage potential of ground motion, near real-time post-earthquake response, among many others. Discussions about the recent ground motion relations, or *attenuation relations*, used in the 2002 U.S. National Seismic Hazard Maps are presented in Section 5.4. These maps provide the fundamental data for the latest seismic design requirements in the United States. Also presented in Section 5.4 are recent advances on the engineering characteristics of fault rupture directivity, vertical ground motion and hanging wall and footwall effects. In Section 5.5, the methodology and technical reasons behind the representation of the ground motion in the *International Building Code (IBC)*, which includes recent seismic design provisions in the United States, are elaborated. The chapter is concluded with a discussion about the future challenges on characterizing strong ground motion for engineering applications.

5.2 Strong-Motion Recordings

5.2.1 Historical Perspective

After the 1925 Santa Barbara, California earthquake, a program to study strong ground motion was initiated in the United States. In 1932, strong-motion instruments were deployed at selected sites in California, and the first significant strong motions were recorded during the March 10, 1933 Long Beach, California, earthquake (M_w 6.4). In 1940, the M_w 6.9 Imperial Valley, California, earthquake was recorded in the basement of a concrete building located in El Centro. The site was located about 6 km from ground rupture observed during the earthquake. For many years, the El Centro recording was used throughout the world for seismic analysis and design. In recent years, however, several studies have shown that, compared with more recent near-source recordings, the El Centro record has limited damage potential (e.g., Mahin and Bertero, 1981; Bozorgnia and Bertero, 2002). In 1966, at a site located about 80 m from ground rupture associated with the M_w 6.1 Parkfield earthquake in central California, the first strong-motion recording in excess of 0.5 g (g = acceleration of gravity = 981 cm/sec^2) was recorded. There was considerable debate at the time whether or not even higher ground motions were possible.

Near-source recordings in excess of 0.5 g have now become commonplace, and several accelerations exceeding 1 g have been recorded. The largest recording to date (larger than 2 g) is the vertical acceleration obtained during the M_w 6.8 Nahanni earthquake, which occurred in 1985 in a remote area of the Northwest Territories, Canada (Campbell, 2000a). There are now tens of thousands of strong-motion instruments located throughout the world. Several earthquakes have triggered over 50 accelerographs, including the 1971 San Fernando (M_w 6.6), 1984 Morgan Hill (M_w 6.2), 1987 Whittier Narrows (M_w 6.0), 1989 Loma Prieta (M_w 6.9), 1994 Northridge (M_w 6.7), 1995 Hyogo-ken Nanbu (Kobe, M_w 6.9) and 1999 Chi-Chi (M_w 7.6). Dense networks in urban areas form the backbone of recording systems designed to provide a near real-time assessment of ground shaking within minutes after an earthquake to aid in emergency response and post-earthquake applications. For example, in California, TriNet (Wald et al., 1999) and CISN (Lin et al., 2002) automatically generate contour maps (a program called ShakeMap) of basic strong-motion parameters and

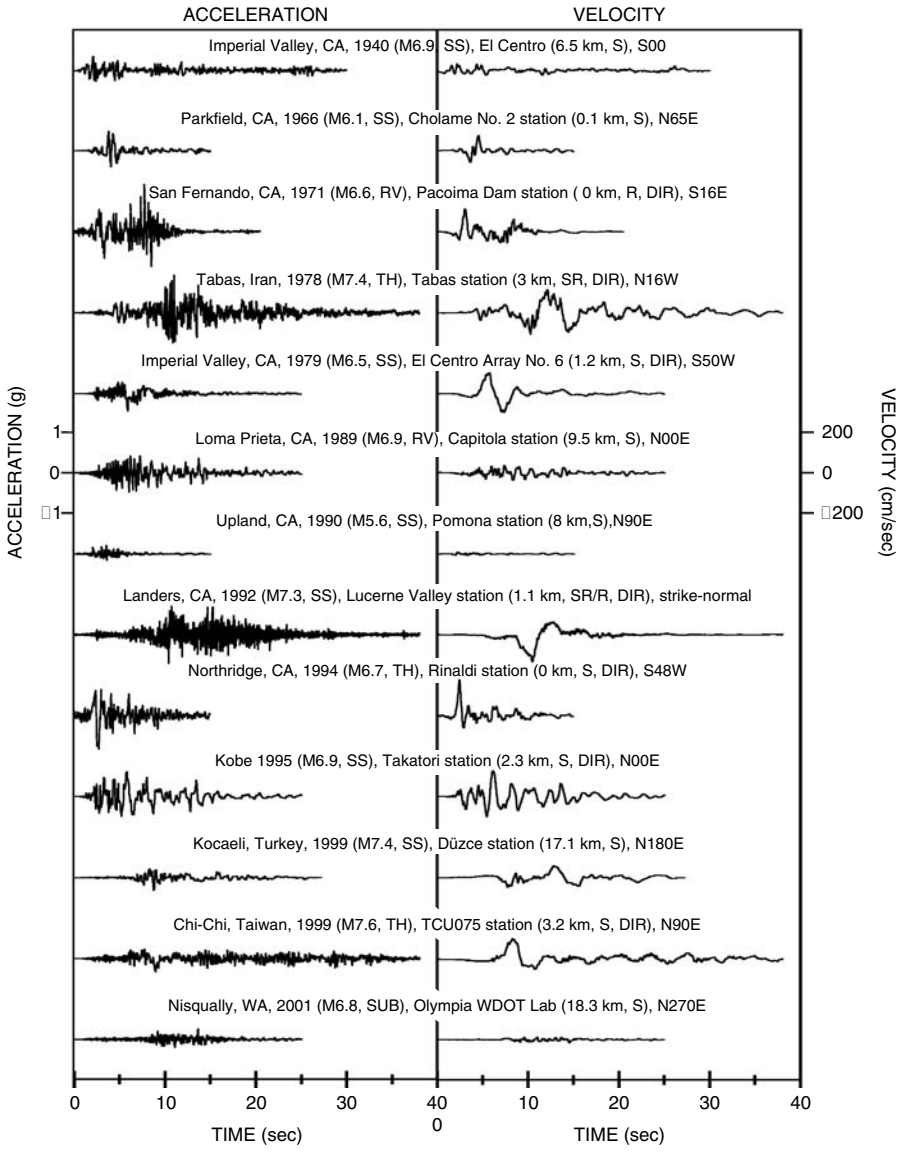

FIGURE 5.1 Selected recorded ground accelerations (plotted at the same scale), and the corresponding ground velocities. SS = strike-slip faulting; RV = reverse faulting; TH = thrust faulting; SUB = subduction intraslab earthquake; S = soil site; R = rock site; SR = soft rock site; DIR = record includes fault rupture directivity effects. Distance measure is from the recording site to surface projection of fault rupture plane (epicentral distance for the Nisqually earthquake).

post them on the Internet in near real-time. Due to their success, similar networks and programs are being developed in different regions of the country as well.

5.2.2 Examples of Acceleration and Velocity Time Series

Ground motions recorded at different sites and in different earthquakes will vary significantly due to several factors, including, but not limited to, earthquake magnitude, faulting mechanism, distance from the recording site to the earthquake source, local site condition, depth of sediments, basin and other wave-focusing effects and source directivity effects. Figure 5.1 presents plots of selected recorded ground

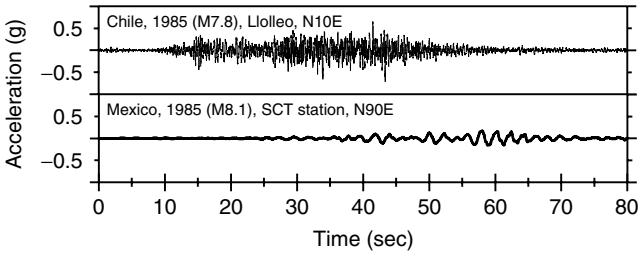

FIGURE 5.2 Ground accelerations recorded during the March 3, 1985 Chile and September 19, 1985 Mexico earthquakes.

accelerations (plotted on the same scale) and the corresponding time variation of the ground velocity. In this figure, the largest peak ground acceleration is 1.17 *g* for the 1971 San Fernando earthquake recorded at Pacoima Dam and the largest peak ground velocity is 178 cm/sec for the 1994 Northridge earthquake at Rinaldi Receiving Station. Special characteristics of the ground motions affected by fault rupture directivity are discussed in Section 5.4.5. In some instances, a large peak velocity may be associated with a so-called fling step displacement pulse. An example of such a case for the 1999 Chi-Chi, Taiwan earthquake is presented in Chapter 2. Depending on various factors, especially earthquake magnitude and local site response, recorded ground motions can have a long duration. Examples of long duration ground motions with repeated cycles of ground oscillations are shown in Figure 5.2 for the 1985 earthquakes in Chile (M_w 7.8) and Mexico (M_w 8.1). Generally, long duration strong motions will have high damage potential. Structural members and systems subjected to repeated cycles of strong motions become increasingly vulnerable (e.g., see experimental studies by Bertero et al., 1977). Hence, duration should also be taken into account in the quantification of damage potential of earthquake ground motion.

5.2.3 Processing Strong-Motion Records

The primary strong-motion recording device used throughout a large region of the United States is the SMA-1 analog mechanical-optical system. SMA-1 instruments are rapidly being replaced by digital accelerographs. Digital instruments extend the dynamic range of strong-motion recordings to accelerations as small as 0.001*g* and to frequencies as high as 50 Hz or greater (Campbell, 2000a). The analog traces of ground motion must be digitized, processed for baseline distortion and instrument response, filtered and integrated to obtain velocity and displacement (see Hudson, 1979; Campbell, 2000a for more details). Ground accelerations recorded by digital instruments also usually need corrections for offset in the acceleration baseline (Boore et al., 2002; USGS, 2002). This correction usually affects only the long period portion of the response spectrum.

Various computer programs can process digitized accelerograms. The United States Geological Survey (USGS) developed *BAP*, strong-motion processing software for personal computers (Converse, 1992), and its mainframe version called *AGRAM*. These programs provide various useful data processing functions. There are also other computer programs that can be used for specific computations using strong-motion records. For example, *SPECEQ* (Nigam and Jennings, 1968; NISEE, 1999) is widely used for the computation of elastic response spectra. Other computer routines are also available through the National Information Service for Earthquake Engineering (NISEE, 1999). Commercially available software packages such as MATLAB® (2002) and Strong Motion Analyst (SMA) (Kinemetrics, 2003) can also be employed for data processing and analyzing recorded ground motion.

5.2.4 Sources of Strong-Motion Records

Various federal, state and local agencies, as well as many universities, operate strong-motion networks. For example, in the United States, the USGS National Strong Motion Program (NSMP) has the responsibility of operating and producing strong-motion networks and data at the federal level. In California, the major source of strong-motion data comes from the California Strong Motion Instrumentation Program (CSMIP) of the

TABLE 5.1 Selected Sources of Strong-Motion Recordings and Their Parameters

Source	Web Site and Reference
California Strong Motion Instrumentation Program (CSMIP)	http://www.consrv.ca.gov/cgs/smip/
California Integrated Seismic Network (CISN)	http://docinet3.consrv.ca.gov/csmip/cisn-edc/default.htm
U.S. Geological Survey (USGS)	http://nsmp.wr.usgs.gov/
U.S. Geological Survey (USGS)	CD ROM of digitized strong-motion accelerograms of North and Central American Earthquakes, 1933–1986 (Seekins et al., 1992; http://nsmp.wr.usgs.gov/cdrom.html)
Consortium of Organizations for Strong-Motion Observation Systems (COSMOS)	http://db.cosmos-eq.org/
'TriNet', and 'ShakeMap'	http://www.trinet.org/ http://earthquake.usgs.gov/shakemap
University of Southern California (USC)	http://www.usc.edu/dept/civil_eng/Earthquake_eng/
US National Geophysical Data Center (NGDC/NOAA)	http://www.ngdc.noaa.gov/seg/hazard/strong.html
Pacific Earthquake Engineering Research (PEER) Center	http://peer.berkeley.edu/smcat/search.html
SAC steel project, strong-motion database	http://nisee.berkeley.edu/data/strong_motion/sacsteel/ground_motions.html
Caltech strong motion database (SMARTS)	Diskettes of selected records (http://www.eerl.caltech.edu/smarts/smarts.html)
Pacific Northwest Seismograph Network (PNSN)	http://www.geophys.washington.edu/SEIS/PNSN/SMO/
European Strong-Motion Database (ESD)	http://www.isesd.hi.is/ESD_Local/frameset.htm
Japan, Kyoshin Net (K-Net); National Research Institute for Earth Science and Disaster Prevention (NIED)	http://www.k-net.bosai.go.jp/
Japan, KiK-Net; National Research Institute for Earth Science and Disaster Prevention (NIED)	http://www.kik.bosai.go.jp/kik/index_en.shtml
Mexico, Guerrero Accelerograph Network	http://www.seismo.unr.edu/ftp/zeng/GUERRERO/guerrero.html
Switzerland, National Strong Motion Network	http://seispc2.ethz.ch/strong_motion/home.jsp
Taiwan, Central Weather Bureau (CWB)	http://www.cwb.gov.tw/V4e/index.htm For the 1999 Chi-Chi earthquake, a CD of strong motion records was also produced by Lee et al. (2001)
Turkey, General Directorate of Disaster Affairs	http://angora.deprem.gov.tr/indexen.htm

California Geological Survey (CGS). Strong-motion recordings and a summary of recorded strong-motion parameters can be obtained from a variety of sources, including those listed in Table 5.1.

5.3 Characteristics of Strong-Motion Spectra

5.3.1 Introduction

Various types of ground-motion parameters and spectra can quantify numerous characteristics of strong ground motion. Ground-motion spectra are used in a wide variety of applications, such as seismic hazard analysis, seismic design, ground motion scaling for analysis and design, quantification of damage potential of recorded motions and performance-based earthquake engineering.

Some of the strong-motion parameters and spectra discussed in the following sections are based solely on the recorded free-field ground motion and are, therefore, independent of any structural model and response. Other strong-motion parameters and spectra are based on the *elastic* and *inelastic* response of single-degree-of-freedom (SDF) systems, or other generic models, each excited by the free-field ground motion.

5.3.2 Fourier Spectra

One way to characterize the frequency content of a recorded ground motion is to represent the ground motion in the frequency domain through its Fourier spectrum. The Fourier transform of the ground acceleration time series, $a_g(t)$, is defined as

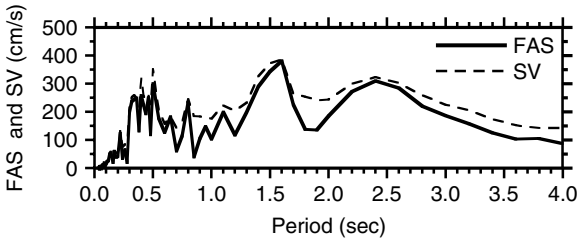

FIGURE 5.3 Fourier amplitude spectrum (FAS) and zero-damped spectral velocity (SV) of the ground acceleration recorded at Sylmar County Hospital (NS component) during the 1994 Northridge, California, earthquake.

$$F(\omega) = \int_0^{T_0} a_g(t) e^{-iwt} dt \tag{5.1}$$

where $F(\omega)$ is the Fourier transform of the ground acceleration, ω is circular frequency (rad/sec), T_0 is time duration and $i = (-1)^{1/2}$. Given the Fourier spectrum, $F(\omega)$, the time series $a_g(t)$ can be recovered through the inverse Fourier transform

$$a_g(t) = \frac{1}{2\pi} \int_{-\infty}^{\infty} F(\omega) e^{i\omega t} d\,\omega \tag{5.2}$$

Equation 5.1 can be rewritten as

$$F(\omega) = \underbrace{\int_0^{T_0} a_g(t) \cos \omega t \, dt}_{=C(\omega)} - i \underbrace{\int_0^{T_0} a_g(t) \sin \omega t \, dt}_{=S(\omega)} \tag{5.3}$$

where, it is evident that $F(\omega)$ is a complex-valued function, which can be represented by its amplitude (modulus) and a phase angle. The amplitude of $F(\omega)$, called the Fourier amplitude spectrum, $FAS(\omega)$, and the phase of $F(\omega)$, called the Fourier phase spectrum, $\Phi(\omega)$, are calculated by (e.g., Clough and Penzien, 1993; Hudson, 1979)

$$FAS(\omega) = \sqrt{C^2(\omega) + S^2(\omega)} \tag{5.4a}$$

$$\Phi(\omega) = -\tan^{-1}\left[S(\omega)/C(\omega)\right] \tag{5.4b}$$

Given a digitized, or digitally recorded, ground acceleration time series, the computation of the Fourier spectrum is usually performed by a discrete Fourier transform and fast Fourier transform (FFT) technique (Clough and Penzien, 1993; Humar, 1990; Press et al., 1992). Various computer programs can be employed to calculate $FAS(\omega)$, usually shortened to FAS, including BAP (Seekins et al., 1992) and MATLAB (2002). Slightly different definitions of the Fourier transform may be used in different computer programs; thus, care should be taken in interpreting the output results.The FAS of the processed ground accelerations are usually published by the various recording agencies. An example of published FAS is shown in Figure 5.3 for the north–south component of the ground acceleration recorded during the 1994 Northridge earthquake at the Sylmar County Hospital. In this figure, the FAS is plotted versus period ($=2\pi/\omega$). Spectral velocity (SV) is also plotted in this figure for comparison. The definition and characteristics of SV are provided in Section 5.3.3.

Ground motion is either recorded digitally or digitized (sampled) in the time domain. Therefore, there is a limit on the amount of short- and long-period information that can be extracted from it. The shortest

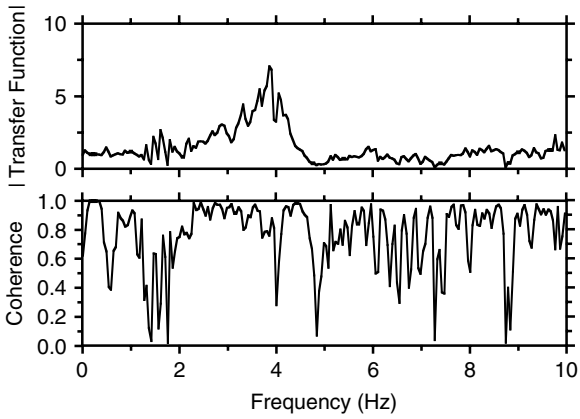

FIGURE 5.4 Example of a transfer function and coherence between the vertical accelerations recorded at the roof and base of a 14-story steel building located in El Segundo, California, during the Northridge, California, earthquake. (Adapted from Bozorgnia et al. (1998). Vertical response of twelve structures recorded during the Northridge earthquake. *Earthquake Spectra*, 14, 411–432.)

period that can be represented by the Fourier spectrum is referred to as the *Nyquist* period, which is two times the time digitization (or sampling) interval of the ground motion (Humar, 1990; Takahashi et al., 1972). For example, if the interval of digitization of an acceleration record is 0.02 sec, the shortest period in the Fourier spectrum of the record is 0.04 sec. In the computation of the FAS using the discrete Fourier transform, the frequency resolution, (that is, the shortest frequency interval at which the FAS can be computed) is inversely proportional to the record length (Humar, 1990). This is a practical limit on the frequency resolution of the Fourier spectrum.

Applications of Fourier spectra are widespread in earthquake engineering and seismology and serve as the fundamental means of examining the frequency content of recorded ground motion or structural response. Also, other functions commonly used in spectral analysis techniques are dependent on Fourier spectra. These functions include the power spectral density function (or autospectrum) as well as the cross-spectrum, coherence function and transfer function between two motions recorded at different locations. Definitions and details of these functions can be found in Bendat and Piersol (1980). Two of these functions are mentioned herein. The Power spectral density (PSD) function can be computed as FAS^2/T_0. In practice, however, there are different methods to reduce the variance of the computed PSD (e.g., see the signal processing toolbox of MATLAB). The coherence function between two recorded motions, x(t) and y(t), is defined as

$$\gamma_{xy}^2 = \left|S_{xy}\right|^2 \Big/ \left(S_{xx}S_{yy}\right) \tag{5.5}$$

where $|S_{xy}|$ is the amplitude of the cross-spectrum of x(t) and y(t), and S_{xx} and S_{yy} are their PSD functions. In Equation 5.5, all the terms are functions of frequency. A high value of coherence at a given frequency indicates that the two recorded signals are highly correlated at that frequency. In structural earthquake engineering, coherence, cross-spectra and transfer functions can be used to examine the recorded structural response (e.g., Celebi, 1993). Examples of a transfer function (TF) and coherence function are presented in Figure 5.4 for a pair of vertical motions recorded at the roof and base of a 14-story steel building (Bozorgnia et al., 1998). The TF may be used to identify the natural frequencies of the system and the correlation of the motions at a given frequency can be examined through the coherence function. For example, using Figure 5.4, a frequency of about 3.9 Hz can be identified as the vertical natural frequency of the system, which also corresponds to a high coherence, that is, the roof and base vertical motions are strongly correlated at that frequency. There are also various applications of Fourier spectra

and their related functions in engineering seismology. For example, Abrahamson et al. (1991) used the complex-valued coherency function to study the spatial variation of ground motion (see Chapter 2). Another important application of Fourier spectra in engineering seismology is its use in the so-called stochastic method which is used to estimate ground motion from fundamental seismological parameters in areas where there are an insufficient number of strong-motion recordings (e.g., Campbell, 2003d; Boore, 2003). These stochastic motions are then used to develop attenuation relations for these areas. Fourier spectra are also used in site-response studies, such as those done with one-dimensional, vertically propagating seismic-wave analysis.

5.3.3 Elastic Response Spectra

5.3.3.1 Definitions and Examples

The concept of elastic response spectrum was introduced by Maurice A. Biot (Biot 1933, 1934, 1941; see also Bozorgnia, 2003; and Chapter 1). The technique is now a fundamental method in earthquake engineering (Housner 1941; Housner et al., 1953; Hudson, 1962). The elastic response spectrum represents the maximum response (over time) of a linear elastic SDF system versus its natural period (or frequency) when excited by a ground acceleration time history. The natural period, T (sec), of the SDF system is related to the circular frequency, ω (rad/sec), and cyclic frequency, f (cycles/sec or Hz), through the expression

$$\omega = \sqrt{(k/m)} = 2\,\pi\, f = 2\,\pi/T \tag{5.6}$$

where k and m are the stiffness and mass of the system, respectively. The SDF system can have different values of damping ratio, usually specified as a percentage of the critical damping (e.g., see Chopra, 2001). The response quantity of the SDF system can be one of the following:

S_d = maximum deformation of the SDF system relative to the ground
SV = maximum velocity of the SDF system relative to the ground
SA = maximum absolute (total) acceleration of the SDF system
S_v (or PSV) = pseudo-velocity = ωS_d
S_a (or PSA) = pseudo-acceleration = $\omega^2 S_d$

For response spectra, the absolute values of these quantities are used. The maximum elastic restoring force (or the base shear) in the SDF system is

$$F_e = k\, S_d = m\, \omega^2 S_d = m\, S_a \tag{5.7}$$

The elastic *seismic coefficient*, a term commonly used in earthquake-resistant design, is defined as

$$C_e = F_e/w = S_a/g \tag{5.8}$$

where w is the weight of the system and g is the acceleration of gravity. Because of their physical interpretations and practical applications, S_v and S_a are the preferred choices by earthquake engineers as opposed to SV and SA. Examples of S_a, S_v and S_d response spectra are presented in Figure 5.5 for a 5% damped SDF system subjected to the ground motion recorded at the Rinaldi Receiving Station during the 1994 Northridge earthquake.

Applications of response spectra are extensive in earthquake engineering, including its use in the characterization of ground motion and in the elastic dynamic structural analysis by the modal superposition method (Clough and Penzien, 1993; Chopra, 2001).

It is evident from the definition of the response spectrum as compared with the FAS that the response spectrum, in a sense, combines the characteristics of the ground motion excitation and the response of the structure (Hudson, 1962). It thus brings together under one representation the major parameters of

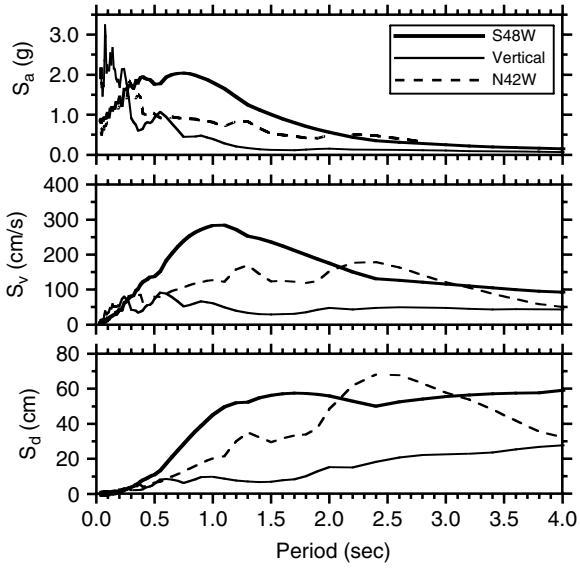

FIGURE 5.5 Elastic pseudo-acceleration (S_a), pseudo-velocity (S_v), and relative displacement (S_d) response spectra for 5% damping for the ground motion recorded at the Rinaldi Receiving Station during the1994 Northridge, California, earthquake.

interest to the earthquake engineer. It can be shown (Hudson, 1979), as is also evident from Figure 5.3, that the FAS ordinates (of acceleration records) are less than, or equal to, the undamped SV ordinates.

The difference between S_v and SV and between S_a and SA are generally negligible for most of the typical period and damping ranges of engineering interest (Hudson, 1962). For zero damping (an undamped system), S_a = SA but $S_v \neq$ SV (Hudson, 1979). At very long periods (for example, for very flexible structures), the absolute (or total) deformation of the mass will become very small and consequently the relative deformation of the mass with respect to the ground will approach the ground displacement. Therefore, at very long periods, S_d will approach the peak ground displacement; SV will approach the peak ground velocity; and SA will approach zero. However, for the same case (very long periods), S_v and S_a both approach zero. Thus, at long periods, there is a considerable difference between SV and S_v (Hudson, 1979). At very short periods, (for example, very stiff structures), the relative deformation of the mass with respect to the ground will be very small; therefore, the total acceleration of the mass will approach the ground acceleration. Hence, SA and S_a approach the peak ground acceleration (PGA) for all damping ratios.

By definition, elastic response spectra are for *linear elastic systems* and unless they are modified appropriately, they will not include features of inelastic structural response. For the same reason, elastic response spectra do not include the cumulative damage due to the number of inelastic cycles of structural deformations and the cumulative damage due to the foreshocks, the main shock and the aftershocks. A function that does include these cumulative effects is the hysteretic energy spectrum (see Section 5.3.8).

5.3.3.2 Effects of Damping on Response Spectra

The effect of damping on response spectra is to reduce the spectral ordinates; however, the amount of this reduction depends on various factors, including the period of the structure and the frequency content of the ground motion. Because of the basic characteristics of response spectra at very short and very long periods, viscous damping does not have much influence in these period ranges. In the intermediate period range, however, damping has its greatest effect on the response reduction. Figure 5.6 shows response spectra of the Rinaldi Receiving Station (S48W component) record for various damping ratios. Approximate procedures to scale an elastic design spectrum for different damping values are presented in Section 5.3.4.

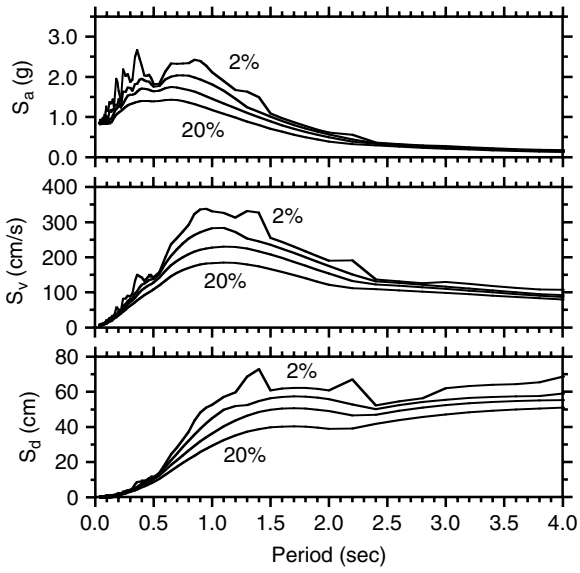

FIGURE 5.6 Elastic pseudo-acceleration (S_a), pseudo-velocity (S_v) and relative displacement (S_d) response spectra for 2, 5, 10 and 20% damping for the ground motion recorded at Rinaldi Receiving Station (S48W component) during the 1994 Northridge, California, earthquake.

5.3.3.3 Scaling of Response Spectra with PGA

As mentioned before, at very short periods, the spectral acceleration approaches the peak ground acceleration (PGA). PGA has been traditionally widely used by earthquake engineers to characterize the severity of ground motion. In practice, however, the importance of PGA alone to quantify the damage potential of the recorded ground motion may have been overemphasized. It should be noted that scaling of the entire amplitude of a ground acceleration time history results in scaling of its elastic response spectrum over the entire period range. However, a single high acceleration spike in a record, resulting in a spurious PGA, is not necessarily associated with high spectral ordinates over the entire period range and, hence, it does not necessarily represent a high damage potential of this ground motion. This is demonstrated in Figure 5.7. In this figure the response spectrum of the recorded motion at Düzce (EW component) during the August 17, 1999 Kocaeli, Turkey, earthquake is plotted. Also shown in this figure is the response spectrum in which time history has been altered by increasing the amplitude of the peak acceleration pulse by a factor of 2. Similarly, the response spectra for the original and the altered records of the El Centro ground motion are also plotted in Figure 5.7(c). It should be noted that in these cases, the entire time history is not scaled but only the amplitude at the peak spike is increased. It is evident from Figure 5.7 that from a practical point of view, an increase in the amplitude of the acceleration pulse of the time history mainly affects the short-period (high frequency) range of the response spectrum.

5.3.3.4 Response Spectra in Near Real-Time

Elastic response spectra of recorded ground motions are usually published by the recording agencies for 0, 2, 5, 10 and 20% damping ratios. Also, following an earthquake in the United States, in near real-time, maps of spatial distributions of elastic spectral accelerations of the recorded ground motions at selected periods are generated by TriNet (Wald et al., 1999) and CISN (Lin, et al., 2002) (see also Chapter 2). Called ShakeMaps, these maps are automatically generated and posted on the Internet for various post-earthquake applications. Although originally these maps were developed for Southern California, ShakeMap has been or is being implemented for many other regions of the United States, including Northern California, Utah and the Pacific Northwest. The current list of available regions and ShakeMaps are accessible on the Internet at http://earthquake.usgs.gov/shakemap/

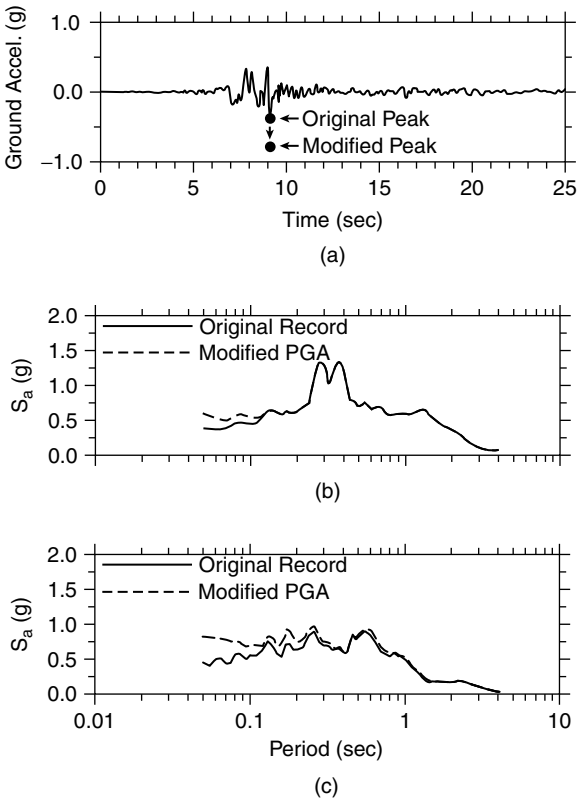

FIGURE 5.7 (a) Ground acceleration recorded at Düzce (EW component) during the August 17, 1999 Kocaeli, Turkey, earthquake; the original and modified peak accelerations are marked. (b) The corresponding pseudo-acceleration response spectra (S_a) for 5% damping. (c) The response spectrum (5% damping) for the El Centro (NS component) recording from the 1940 Imperial Valley earthquake, and the spectrum for the modified record. The El Centro time history (not shown) was modified in the same manner as in the top figure (a).

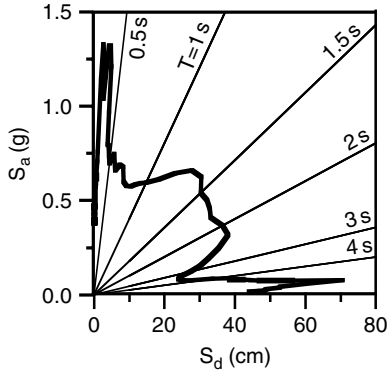

FIGURE 5.8 An acceleration-displacement (AD) diagram, also referred to as an acceleration-displacement response spectrum (ADRS) for 5% damping for the Düzce (EW component) recording of the August 17, 1999 Kocaeli, Turkey, earthquake.

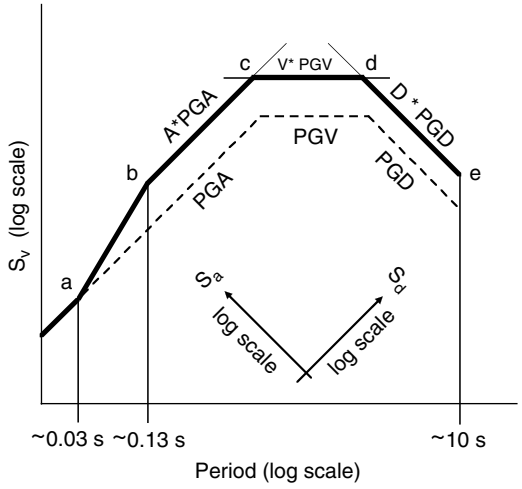

FIGURE 5.9 Elastic horizontal design spectrum according to Newmark and Hall. (Adapted from Chopra and Goel (2001). Direct displacement-based design: use of inelastic vs. elastic design spectra, *Earthquake Spectra*, 17, 47–64.)

5.3.3.5 Different Formats of Response Spectra

The data associated with response spectra can be presented in different formats. The most commonly used format, as mentioned previously and plotted in Figures 5.5 and 5.6, is a plot of the spectral ordinate (acceleration, velocity, or displacement) in linear scale versus natural period or natural frequency (in linear scale). This format is also used in most of the seismic design codes. However, more details of the spectra at shorter periods can be revealed by using a logarithmic scale for the period (Figure 5.7).

Another format for presenting the response spectrum is the acceleration-displacement (AD) diagram, also referred to as the *acceleration-displacement response spectrum* (ADRS). It is a plot of S_a versus S_d with periods represented by lines radiating from the origin. An example of an AD diagram is shown in Figure 5.8. The AD format of the response spectrum has been used by structural engineers for simplified analysis procedures to estimate the deformation demanded by the earthquake ground motion (Freeman, 1995; Chopra and Goel, 1999). The AD format has the visual advantage of being able to overlay the acceleration-displacement demand and the capacity diagrams of a structure on the same plot (see for example, Figure 9.6 in Chapter 9). A disadvantage of the AD diagram is that for long periods the spectral points become close to each other.

The spectra can also be shown in a *tripartite* logarithmic format. In this format, the three response spectra parameters S_a, S_v and S_d are combined such that S_v is on the vertical axis and period is on the horizontal axis, both on a logarithmic scale. S_a can be read off an axis rotated 45° counterclockwise and S_d can be read off an axis rotated 45° clockwise from the vertical axis. Thus, the lines with 45° slopes represent constant S_a lines and the lines with 135° slopes represent constant S_d lines (Figure 5.9). Apparently, this type of paper was first introduced sometime before 1958 by Edward Fisher (Housner, 1997). In recent years, practical applications of the tripartite logarithmic format have been curtailed.

5.3.3.6 Housner Spectrum Intensity

Spectrum intensity (SI) is defined as the area under the pseudo-velocity response spectrum (S_v) over the period range 0.1 to 2.5 sec (Housner, 1952). It is a measure of the intensity of ground shaking for elastic structures. As Housner (1975) states:

> The spectrum intensity is a single number that is a good measure of the intensity of ground shaking as regards its effect on the elastic vibrations of structures. It has, however, been observed that it is not necessarily a good measure of the severity of shaking as indicated by the damage. This was demonstrated, for example, by the 1966 Parkfield, California earthquake where the motion close to

the fault had an unprecedentedly large spectrum intensity but caused very little observed damage. This was attributed to the fact that, although very intense, the strong shaking had a very short duration.

The computed SI at different recording stations can be used to construct a contour map of SI in a geographical area affected by the earthquake (Bozorgnia and Bertero, 2001a). Such a map can be used to examine the spatial distribution of the general intensity of the ground motion that impacts elastic structures.

5.3.4 Elastic Design Spectra

5.3.4.1 Introduction

Whereas a response spectrum is computed for a specific ground motion, for design purposes it is more appropriate to use a design spectrum. A design spectrum is based on a statistical analysis of a collection of numerous spectra of different recorded ground motions in different earthquakes, with possible modifications based on engineering experience. In the history of earthquake engineering, design spectra have been proposed by various engineers. Biot (1941) suggested that: "When we possess a collection of earthquake spectrums at a given location, it is suggested that a simplified envelope should be used as a standard spectrum for the purpose of design in that region." Widely used design spectra were developed by Housner (1970b), Seed et al. (1976), Newmark et al. (1973) and Newmark and Hall (1982). Also, various editions of building codes and seismic design guidelines have recommended design spectra. In Section 5.5, the design spectrum recently recommended in the International Building Code (IBC, 2000) is discussed. In the following sections, two additional examples of design spectra are presented. The first is the design spectrum proposed by Newmark and Hall (1982), which has been used extensively in research and engineering practice, and the second is a design spectrum proposed by FEMA-356 (2000).

5.3.4.2 Newmark-Hall Elastic Design Spectrum

The design spectrum proposed by Newmark and Hall (1982) is schematically plotted in Figure 5.9. This figure is plotted in the format of a tripartite logarithmic plot, the preferred plotting method proposed by these authors for reasons that will become obvious below. The Newmark-Hall procedure to construct an elastic design spectrum is as follows:

1. Estimate peak ground acceleration (PGA), peak ground velocity (PGV) and peak ground displacement (PGD); e.g., using an attenuation relation and relationships between these parameters as discussed below. Draw PGA, PGV and PGD lines on a tripartite logarithmic plot at constant values of S_a, S_v and S_d, respectively (see Figure 5.9).
2. Parallel to the PGA, PGV, and PGD lines, draw another set of lines at values equal to A×PGA, V×PGV and D×PGD, where A, V and D are dynamic amplification factors for acceleration, velocity and displacement, respectively, as specified next. Values of A, V and D for use in developing a median design spectrum (50% probability of nonexceedance of the spectral ordinates), are given in Equation 5.9 and those proposed for use in developing a median plus one standard deviation spectrum (84.1% probability of nonexceedance) are given in Equation 5.10:

$$A = 3.21 - 0.68 \ln \xi; \quad V = 2.31 - 0.41 \ln \xi; \quad D = 1.82 - 0.27 \ln \xi \tag{5.9}$$

$$A = 4.38 - 1.04 \ln \xi; \quad V = 3.38 - 0.67 \ln \xi; \quad D = 2.73 - 0.45 \ln \xi \tag{5.10}$$

   where ξ is the damping ratio in percent (i.e., for 5% damping ratio, $\xi = 5$). Equation 5.10 obviously results in a more conservative design spectrum than Equation 5.9.
3. Approximate periods for corner points *a*, *b* and *e*, are shown in Figure 5.9. Corner points *c* and *d* are the crossing points of the A×PGA, V×PGV and D×PGD lines. In practice, periods for points *c* and *d* fall in ranges of approximately 0.5–0.7 and 3–4 sec, respectively.

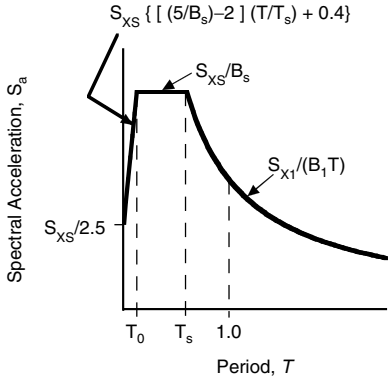

FIGURE 5.10 Elastic horizontal design spectrum recommended by FEMA-356 [2000]. Corner periods are $T_S = (S_{X1}\, B_S) / (S_{XS}\, B_1)$ and $T_0 = 0.2\ T_S$.

4. For periods shorter than about 0.03 sec, the design spectrum follows the constant PGA line.

As mentioned above, the first step in constructing a Newmark-Hall design spectrum is to estimate PGA, PGV and PGD. In practice, however, it may be difficult to accurately estimate PGD. This is, in part, due to its sensitivity to the filtering parameters used to process the acceleration record during double integration. To simplify the construction of the design spectrum, Newmark and Hall (1982) suggested approximate rules to estimate PGV and PGD for a given value of PGA. Based on an analysis of several strong-motion records, they suggested that the ratio of PGV/PGA may be taken as 48 and 36 inches/sec/*g* for competent soil and rock, respectively; and the dimensionless ratio (PGA × PGD)/PGV^2 may be taken as 6 (consistent units should be used in this relation to make it unitless).

5.3.4.3 FEMA-356 Elastic Design Spectrum

According to FEMA-356 (2000), a pre-standard document for seismic rehabilitation of buildings, different levels of ground motion are used to achieve different structural performance levels. Two Basic Safety Earthquake (BSE) levels, BSE-1 and BSE-2 are defined, where the BSE-2 level is a more severe level of ground motion than the BSE-1 level. For example, the basic safety objective achieves the dual goals of (a) life safety structural performance for the BSE-1 ground-motion level; and (b) collapse prevention for the BSE-2 ground-motion level.

The procedure to construct the elastic spectra for the BSE-2 and BSE-1 ground motion levels, is as follows:

1. For the BSE-2 ground motion level, the spectral accelerations S_S (at period of 0.2 sec) and S_1 (at period of 1.0 sec) are obtained using the approved contour maps for the Maximum Considered Earthquake (MCE). These maps can be found on the USGS Internet web site at http://geohazards.cr.usgs.gov/eq/ The MCE ground motion is based on a combination of deterministic and probabilistic estimates and may be interpreted as a "collapse ground motion" (Leyendecker et al., 2000). The details of the characteristics of the MCE ground motion are presented in Section 5.5.
2. S_S and S_1 for the BSE-2 ground-motion level are adjusted for local site conditions. These adjusted spectral accelerations are denoted S_{XS} and S_{X1}. The procedure to adjust the spectral ordinates for local site conditions is similar to that of the IBC (2000) and is outlined in Section 5.5.2.
3. For the BSE-1 ground motion level, the spectral accelerations S_{XS} and S_{X1} are taken as the smaller of the following:
   - The values of S_S and S_1 taken from approved contour maps of spectral accelerations for 10% probability of exceedance in 50 years, adjusted for local site conditions (see Section 5.5.2).
   - 2/3 of the values of the spectral ordinates determined for the BSE-2 ground motion level (step 2, above).

4. Given spectral accelerations S_{XS} and S_{X1}, the elastic horizontal spectra for the BSE-2 and BSE-1 ground motion levels are constructed according to Figure 5.10. In this figure, B_S and B_1 are damping modification factors (or damping coefficients, in FEMA-356 terminology) to modify S_{XS} and S_{X1}, respectively, for damping values other than 5%. The recommended values of B_S and B_1 are given in Table 5.2 A more detailed discussion about the damping modification factors is provided in Section 5.3.4.4. In summary, given S_{XS}, S_{X1}, B_S and B_1, one can determine the corner periods T_s and T_0 (see Figure 5.10), and the design spectrum can be constructed as indicated in the figure. For 5% damping, B_S and B_1 are unity, and the ratio of the peak of the design spectrum over the zero-period acceleration is 2.5. This amplification factor is consistent with the previous editions of the *Uniform Building Code*, e.g., UBC (1994).

TABLE 5.2 Damping Modification Factors[a]

Damping Ratio (%)	Newmark and Hall (1982)[b] Acceleration (A)	Velocity (V)	Displacement (D)	FEMA-356 (2000) B_S	B_1
2	0.77	0.81	0.85	0.80	0.80
5	1.00	1.00	1.00	1.00	1.00
10	1.29	1.21	1.16	1.30	1.20
20	1.80	1.53	1.37	1.80	1.50
30	2.36	1.80	1.54	2.30	1.70
40	3.02	2.07	1.68	2.70	1.90
50	3.85	2.34	1.81	3.00	2.00

[a] See also Naeim and Kircher (2001) for more details.
[b] Using Equation 5.9 of this chapter.

5.3.4.4 Modification of Design Spectra for Damping Values

It is common practice to specify a design spectrum for a 5% damping ratio. However, depending on the structural (or fluid) material behavior and the level of ground motion excitation, a design spectrum for other damping values may be needed. For example, a steel liquid storage tank located at a rock site has a damping ratio of 2 to 3% for the horizontal impulsive mode (Whittaker and Jury, 2000). Approximate equivalent viscous damping values for various systems are given, for example, by Newmark and Hall (1982).

An approximate procedure to derive a design spectrum for a damping ratio other than 5% is to *divide* the 5% damped spectral ordinates by a *damping modification factor*. There are different procedures and damping modification factors, including those by Newmark and Hall (1982), Rosenblueth (1980), Idriss (1993), Abrahamson and Silva (1996), FEMA-356 (2000), among others (see also a summary of selected procedures by McGuire et al., 2001). The Newmark and Hall (1982) and FEMA-356 (2000) procedures are presented below.

Equation 5.9 or 5.10 by Newmark and Hall (1982) can be used to compute the damping modification factors. For example, between points *b* and *c* in Figure 5.9, a 2% damped median design spectral ordinate may be approximately derived by dividing the 5% damped median design spectral ordinate by a factor of $(3.21 - 0.68 \ln 5)/(3.21 - 0.68 \ln 2) = 0.77$. The damping modification factors calculated by this procedure are listed in Table 5.2 (Naeim and Kircher, 2001). These modification factors are for adjusting the dynamic amplification factors A, V and D (see Figure 5.9) of the 5% damped spectrum to derive a spectrum for other damping values.

As mentioned previously, FEMA-356 (2000) also recommends damping modification factors B_S and B_1 to scale spectral accelerations at periods of 0.2 and 1.0 sec, respectively (see Figure 5.10). These factors are also listed in Table 5.2. As Naeim and Kircher (2001) have pointed out, for damping ratios less than about 20%, B_S and B_1 are almost the same as those recommended by Newmark and Hall (1982) for the

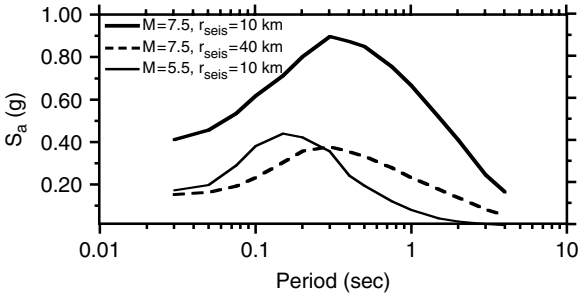

FIGURE 5.11 Pseudo-acceleration (S_a) spectra for the average of the two horizontal components for 5% damping at a stiff soil site and for strike-slip faulting, based on the Campbell and Bozorgnia (2003) ground motion (attenuation) relations. Here r_{seis} is the shortest distance from the site to the seismogenic rupture zone of the fault (see Section 5.4).

acceleration and velocity dynamic amplification factors, respectively. For damping ratios higher than 20%, B_S and B_1 are less than the factors recommended by Newmark and Hall (1982), i.e., the FEMA-356 spectrum becomes more conservative than that proposed by Newmark and Hall. This is due to the decision by code and guideline development groups to choose conservative damping modification factors for design of highly damped systems (Naeim and Kircher, 2001).

It should be noted that the validity of the damping modification factors given in Table 5.2, for response spectra of near-fault ground motions that are dominated by severe long-period pulses has yet to be determined.

5.3.4.5 Scaling a Fixed-Shape Spectrum

In general, the *shape of a smoothed spectrum* is a function of different parameters, including magnitude, source-to-site distance, local site conditions and direction of fault rupture propagation. An example is presented in Figure 5.11. This figure shows horizontal spectral acceleration for 5% damping at a stiff soil site, strike-slip faulting, M_W 5.5 and 7.5 and distances of 10 and 40 km from the seismic source. The spectra are based on statistical analyses of 443 recordings from 36 worldwide shallow earthquakes of magnitude 4.7 to 7.7 (for details, see Campbell and Bozorgnia, 2003). In Figure 5.11, compare, for example, the two spectra for M_W 7.5 and M_W 5.5, both at a distance of 10 km from the source. It is evident that the larger magnitude results in larger spectral ordinates, but more at long periods than at short periods.

In the same figure, compare the spectrum of the M_W 5.5 earthquake at distance of 10 km with that of M_W 7.5 earthquake at a distance of 40 km. These spectra have comparable PGA values (compare the spectra at a very short period). However, the spectrum of the smaller earthquake at smaller distance is richer at short periods than that of the larger earthquake at larger distance.

Therefore, using a fixed spectral shape and scaling it with a single parameter such as PGA to account for the effects of magnitude and other factors, is not conceptually justified. The shape of a design spectrum should take into account the effects of various parameters including magnitude, distance, local site conditions, fault rupture directivity effects, among other factors.

5.3.5 Arias Intensity and Strong-Motion Duration

Arias intensity (I_A) is a ground motion parameter related to the *spectrum* of the energy demanded by a strong-motion record, as defined below. Because I_A is closely related to a widely used definition of strong-motion duration, a discussion of duration is also provided in this section.

The commonly used version of Arias intensity (Arias, 1970) is the sum of total energy per unit weight in a set of undamped elastic SDF systems having frequencies uniformly distributed in the range of zero to infinity, evaluated at the end of the ground motion record. It can be shown (Arias, 1970; Trifunac and Brady, 1975) that the above definition can be translated into the following expression for the Arias Intensity:

$$I_A = (\pi/2g) \int_0^{t_d} [a_g(t)]^2 dt \tag{5.11}$$

where $a_g(t)$ is the ground acceleration, t_d is the total duration of the record and g is the acceleration of gravity.

Influences of source-to-site distance, magnitude and local site condition on I_A have been recently examined. For example, Kayen and Mitchell (1997) examined the correlation of I_A with magnitude and distance for different soil conditions and used the Arias intensity approach to assess the liquefaction potential of soil deposits during earthquakes (see also Chapter 4). Recently, Travasarou et al. (2003) used a larger number of recordings and developed the following attenuation relation for I_A

$$\ln (I_A) = c_1 + c_2 (M_W - 6) + c_3 \ln (M_W / 6) + c_4 \ln (r_{rup}^2 + h^2)^{0.5} + [s_{11} + s_{12} (M_W - 6)] S_C + [s_{21} + s_{22} (M_W - 6)] S_D + f_1 F_N + f_2 F_R \tag{5.12}$$

where I_A is the average Arias intensity (m/s) of the two the horizontal components; M_W is moment magnitude; r_{rup} is the closest distance to the rupture plane (km); h is a fictitious depth term (km) determined by the regression; F_N and F_R are indicator variables for the fault mechanism and are respectively both 0 for strike-slip faults, 1 and 0 for normal faults, and 0 and 1 for reverse or reverse-oblique faults; S_C and S_D are indicator variables for the soil type and are respectively both 0 for site category B, 1 and 0 for site category C, and 0 and 1 for site category D, where B is for competent rock, C is for weathered soft rock and shallow stiff soil, and D is for deep stiff soil. The computed values of the coefficients are as follows: $c_1 = 2.80$, $c_2 = -1.981$, $c_3 = 20.72$, $c_4 = -1.703$, $h = 8.78$, $s_{11} = 0.454$, $s_{12} = 0.101$, $s_{21} = 0.479$, $s_{22} = 0.334$, $f_1 = -0.166$ and $f_2 = 0.512$. The model is applicable for earthquakes with M_w between 4.7 and 7.6. The standard deviation of the random error in the above relationship was found to be a function of the median predicted Arias intensity and soil type. In fact, the error is smaller for soil sites D, larger for soil sites C and the largest for soil sites B.

Travasarou et al. (2003) also found that the average I_A of two horizontal components is insensitive to forward directivity in the near-fault region; however, the Arias intensity in the fault-normal direction was approximately 20% higher and in fault-parallel direction was approximately 20% lower than the average I_A.

Strong-motion duration is an important parameter that may contribute to the performance of structural and geotechnical systems during earthquakes. For example, experimental studies have shown that structural systems and components subjected to cycles of inelastic deformations become more vulnerable due to cumulative damage (e.g., Bertero et al., 1977). This is usually the case if the strong-motion duration is relatively long. Therefore, strong-motion duration may play an important role in assessing the damage potential of earthquake ground motion. The cumulative effects of strong-motion duration are included in hysteretic energy and damage spectra (see Sections 5.3.8 and 5.3.9).

Strong-motion duration can be defined in different ways. A review of various definitions is given by Bommer and Martinez-Pereira (1999). Chapter 2 also provides more discussion about the strong-motion duration. Most commonly used definitions of strong-motion duration are defined below.

Bracketed duration was defined by Bolt (1973) as the elapsed time between the first and last acceleration excursions greater than a given level (e.g., 0.05*g*).

Significant duration is defined based on the time variation of the integral of the square of the ground acceleration time history. This definition is related to the *Arias intensity*, as defined previously, if t_d in Equation 5.11 is replaced with time t; and hence, the result of Equation 5.11 will become a function of time. Two common definitions of the significant duration are the time intervals between 5 and 95% and between 5 and 75% of the integral of the square of the ground acceleration (Trifunac and Brady, 1975; Stewart et al., 2001). An example of the evolution of I_A is presented in Figure 5.12 for the 1978 Tabas, Iran, earthquake (M_S 7.4) recorded at Tabas (N16W component). As marked in this figure, the time interval between 5% and 95% of I_A represents a significant duration of the record. An example of the use of significant duration in engineering practice is the evaluation of seismic slope stability (see Section 4.6.2.3.3 in Chapter 4: Displacement-Based Methods of Analysis).

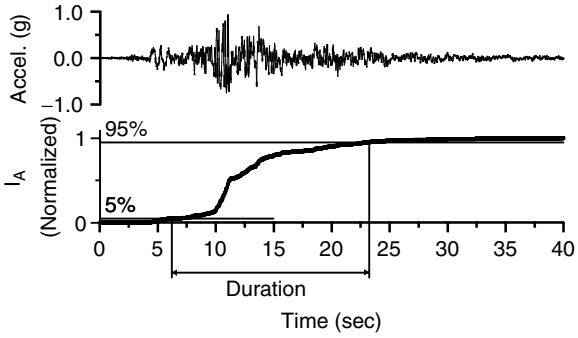

FIGURE 5.12 Ground acceleration of the 1978 Tabas, Iran, earthquake ($M_s = 7.4$) recorded at Tabas (N16W component), and the corresponding evolution of the Arias intensity.

5.3.6 Drift Spectrum

The drift spectrum represents approximately the story drift ratio in multi-story buildings demanded by the ground motion (Iwan, 1997). The formulation is based on the linear elastic response of a uniform continuous cantilevered shear beam model, where interstory drift is computed as the first derivative of the displacement response of the beam model (see also Kim and Collins, 2002). The drift spectrum has been proposed for quantifying the seismic demand on linear elastic systems subjected to near-fault pulse type ground motions. To generate the drift spectrum, ground velocity and displacement time histories are needed as input motions (Iwan, 1997). Hence, accurate processing of the ground motion records, especially for near-fault ground motions, is important for developing a drift spectrum.

The story drift of the shear beam model can be computed at different heights of the model, though it is commonly computed at the base. As an example, Figure 5.13 presents the drift spectrum evaluated at the base of a shear beam model for the Northridge earthquake recorded at Sylmar County Hospital (NS component).

The drift spectrum has the same fundamental limitations as the other linear elastic response parameters, i.e., it does not directly reveal information about inelastic response. Recently, Kim and Collins (2002) have also found that for ground motions that exhibit a permanent ground displacement, the formulation of the drift spectrum predicts residual drift values at the end of the record. This is inconsistent with the linear elastic behavior assumed in developing the model. As a result, Kim and Collins (2002) have proposed improved models for computing drift spectra. However, the improved models do not have the computational simplicity of the original drift spectrum model.

5.3.7 Inelastic Response Spectra

5.3.7.1 Introduction and Definitions

A severe ground motion generally demands large deformations on various structural systems, and inelastic structural response and hysteretic energy dissipation are generally inevitable in typical structures. This fact has been recognized since the early years of earthquake engineering. For example, Biot (1941) realized that a severe ground motion can demand excessively high stresses in an undamped *elastic* structural model; and he concluded:

> Observations of the effect of actual earthquakes indicate that for most structures such high stresses are not reached and this points out the importance of the damping or other causes of stress reduction. Considerable hysteresis damping will set in as soon as the yield point in some part of the building is reached.

For a structure to behave elastically during a severe ground shaking, its strength, in general, must be considerably higher than the minimum requirements recommended in building codes. Therefore, in a major earthquake, many types of structures respond inelastically, and in fact, their survival depends on

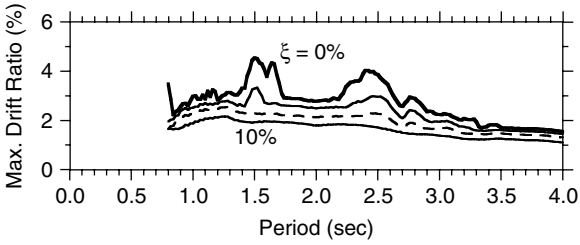

FIGURE 5.13 Drift spectra (elastic) for 0, 2, 5 and 10% damping evaluated at the base of the building model for the Sylmar County Hospital (NS component) recording of the Northridge, California, earthquake.

proper inelastic behavior and hysteretic energy dissipation. Therefore, an *elastic* response spectrum, although a very important concept with widespread applications, has a limited capability to predict structural damage in severe earthquakes. An inelastic response spectrum (IRS) includes some fundamental features of inelastic dynamic behavior.

An IRS represents the maximum response of an inelastic (nonlinear) SDF system versus its initial (elastic) natural period when it is excited by a ground acceleration record. As discussed before, for the computation of an *elastic* response spectrum, only two system parameters must be specified: natural period and damping ratio. For computation of an IRS, in addition to these parameters, the complete force-deformation characteristics of the SDF system must be specified, including its loading, unloading and re-loading behavior. The inelastic force-deformation relationship of the SDF system can be idealized as bilinear, trilinear, stiffness and strength degrading, among others.

One of the traditional parameters used in the IRS as well as in seismic design is the displacement ductility ratio (μ), which is defined as

$$\mu = u_{\max}/u_y \tag{5.13}$$

where u_{max} and u_y are, respectively, the maximum and yield deformations of the SDF system (the deformations are all relative to the ground). By definition, $\mu \leq 1$ indicates an elastic response and $\mu > 1$ indicates inelastic behavior.

In the process of constructing an inelastic spectrum, the following variables are also commonly used in research and practice. Consider a generic force-deformation relationship as shown in Figure 5.14. In this figure, F_y is the equivalent yield strength; F_s is the design strength according to the seismic provisions and F_e is the elastic strength demand if the system were to remain elastic. The relationships among these forces are as follows (Uang and Bertero, 1991; Uang, 1991; FEMA-369, 2001):

$$F_s = F_e/R \tag{5.14a}$$

$$F_y = F_e/R_d \tag{5.14b}$$

$$\Omega = F_y/F_s \tag{5.14c}$$

where, in terms of building code terminology, R is the response modification coefficient to compute the design strength F_s from the elastic design strength F_e (obtained from an elastic design spectrum; see Equation 5.7 and also Section 5.3.4); R_d is the reduction factor due to the available ductility of the system; and Ω represents the system overstrength factor which relates the design strength (F_s) to the equivalent yield strength of the system (F_y). In seismic design, usually $R > 1.0$; thus, structures are designed for forces smaller than demanded for a completely elastic response (FEMA-369, 2001). Values of R, R_d and Ω are dependent on the basic seismic-force-resisting structural system (SEAOC, 1999; IBC, 2000). For example, according to the International Building Code (IBC, 2000), for special steel moment frames R = 8.

5.3.7.2 Different Formats of Inelastic Response Spectra

Inelastic response spectra can be presented in different formats. The most commonly used formats are given below.

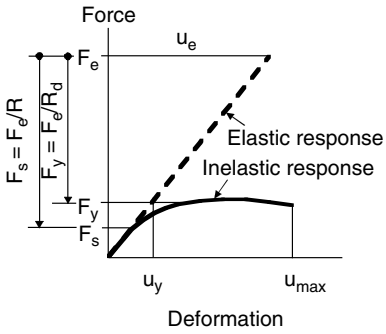

FIGURE 5.14 Elastic and inelastic force-deformation relationships. (Adapted from Uang, C.M. (1991). Establishing R (or R_w) and C_d factors for building seismic provisions. *ASCE Journal of Structural Engineering*, 117, 19–28.)

5.3.7.2.1 Displacement Ductility Spectrum

Given the characteristics of an inelastic SDF system, including its force-deformation relationship with specified yield strength and damping ratio, the IRS can be presented in a plot of the computed (or demanded) displacement ductility (μ) versus the initial elastic period (T). In this format, the yield strength of the SDF system is specified, and the maximum deformation u_{max} and displacement ductility factor μ demanded by the ground motion, are computed. In practice, the equivalent yield strength can be determined either according to the seismic provisions in a building code, i.e., based on a reduced elastic design spectrum, or using the results of a static nonlinear (pushover) analysis.

An example of IRS is plotted in Figure 5.15. The different inelastic spectra in this figure are for a 5% damping ratio and a bilinear force-deformation relationship (i.e., two different linear force-deformation relationships for $u < u_y$ and $u > u_y$) with a post-yield stiffness equal to 1% of the initial elastic stiffness. For Figure 5.15, the yield strength of the system is specified based on the elastic spectrum recommended in the UBC (1994) for soil type S_2 in seismic zone 4, reduced by the factor R_d (see Figures 5.14 and 5.15(a), and Equation 5.14b). Figure 5.15 shows that using a period-independent reduction factor (R_d), can result in large ductility demands, especially at short periods. IRS for other recently recorded near-source ground motions have also been computed by Bozorgnia and Mahin (1998).

Figure 5.16 presents an example of the effects of multiple events on inelastic spectra. Figure 5.16(a) shows the ground acceleration time histories recorded at Düzce during the August 17, 1999 Kocaeli and November 12, 1999 Düzce earthquakes in Turkey. The time history plot includes 10 seconds of zero ground acceleration added in between the recorded ground motions in the two events. Figure 5.16(b) shows displacement ductility spectra of the first and second ground motions independently, as well as the ductility spectrum for the combined acceleration time histories. The inelastic spectra shown in this figure are for an SDF system with 5% damping and an elastic-perfectly-plastic (EPP) force-displacement relationship with yield strength based on the elastic spectrum of UBC (1997) reduced by R_d=3.4. Figure 5.16(b) shows that the displacement ductility spectrum for the combined ground motions is predominated by the November 1999 event and may not necessarily include strong cumulative effects of the first and second events (Bozorgnia and Bertero, 2002). Other parameters such as hysteretic energy include stronger cumulative effects of multiple events (see Section 5.3.8).

5.3.7.2.2 Constant Ductility Spectrum

An IRS can also be presented as a plot of the computed yield strength (F_y) of an SDF system versus its initial elastic period for a given value of ductility (μ). An example of such IRS is plotted in Figure 5.17. To construct such a constant-ductility IRS, first various values of period T and F_y are assumed and the displacement ductility demands are computed. Then, through an interpolation process, the required values of F_y are determined to result in a pre-specified value of displacement ductility ratio. Figure 5.17

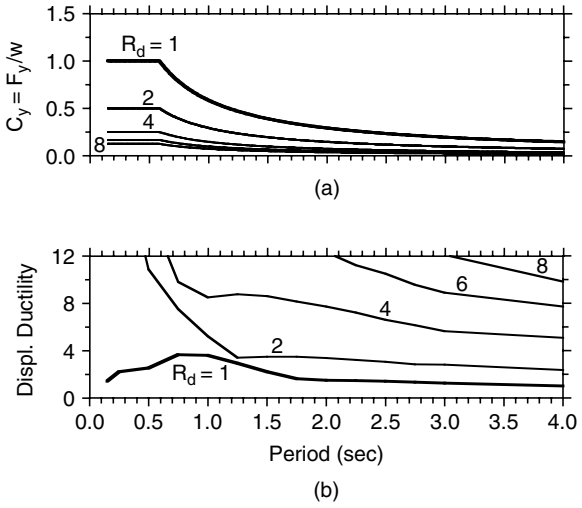

FIGURE 5.15 Given C_y (top figure), the computed inelastic response spectra, in terms of displacement ductility ratios, are plotted (bottom figure). The inelastic response spectra are for the 1994 Northridge, California, earthquake recorded at Rinaldi Receiving Station (S48W component). The SDF system has 5% damping and a bilinear force-deformation relationship.

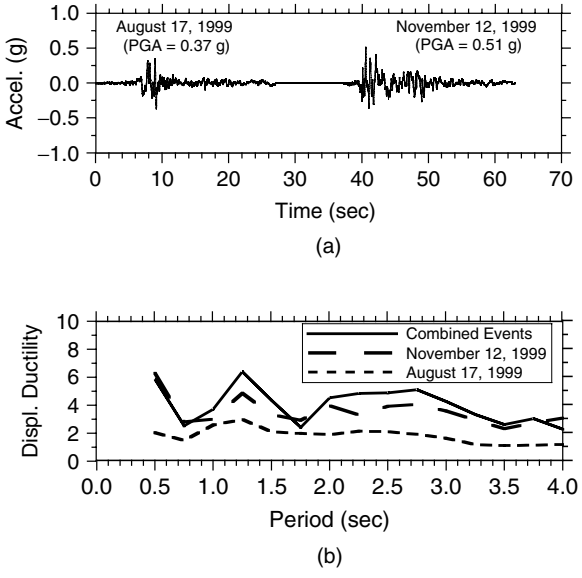

FIGURE 5.16 Ground accelerations (a); and displacement ductility ratio spectra (b); for the Düzce (EW component) recordings of the August 17, 1999 Kocaeli ($M_w = 7.4$) and November 12, 1999 Düzce ($M_w = 7.1$) earthquakes in Turkey.

shows the results of this process for the 1994 Northridge earthquake recorded at Rinaldi Receiving Station. The IRS in this figure are for a 5% damping and a bilinear force-deformation relationship with a post-yield stiffness equal to 1% of the initial elastic stiffness. The curve for $\mu = 1$ corresponds to the elastic response spectrum. It is evident from this figure that for the intermediate period range, if the structural system can provide a moderate ductility, a substantial reduction in the required yield strength (F_y) can be achieved.

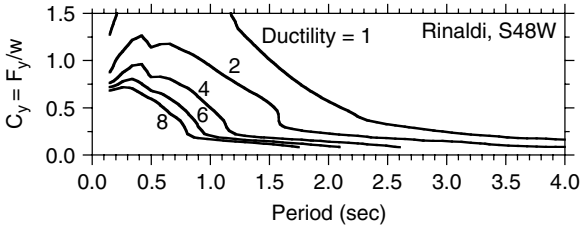

FIGURE 5.17 Constant-ductility inelastic response spectra for the 1994 Northridge, California, earthquake recorded at Rinaldi Receiving Station (S48W component). The SDF system has 5% damping and a bilinear force-deformation relationship.

5.3.7.3 Computer Programs to Construct Inelastic Response Spectra

There are various computer programs with different capabilities to compute inelastic response spectral ordinates. General purpose inelastic dynamic analysis software packages can also be used for this task. Publicly available computer programs for the generation of inelastic response spectra include NONSPEC (Mahin and Lin, 1983); BISPEC (Hachem, 2000); and NSPECTRA (Reinhorn et al., 1999). For example, the results shown in Figures 5.15 and 5.16 were computed using NONSPEC with additional post-processing.

5.3.7.4 Inelastic Design Spectra

Inelastic response spectra are for specific ground motions; however, for general use, smoothed inelastic design spectra may be more applicable. Examples of proposed inelastic design spectra are given below:

5.3.7.4.1 Newmark–Hall Inelastic Design Spectrum

Given the *elastic* design spectrum and assumed (or available) displacement ductility ratio (μ) of an SDF system, an *inelastic* design spectrum is constructed by modifying the elastic design spectrum. The procedure is as follows. The first step is to construct an elastic design spectrum (see Section 5.3.4.2 and Figure 5.9). Consider an elastic-perfectly-plastic (EPP) force-deformation relationship, which is a special case of the bilinear force-deformation relationship with a zero postyield stiffness. The Newmark–Hall procedure to construct an inelastic design spectrum for such a system is summarized in Figure 5.18. In the short period range, the flat portion of the elastic acceleration spectrum is reduced by a factor of $(2\mu - 1)^{0.5}$. This is based on an assumption that the areas under the force-displacement curves for the elastic and inelastic systems are equal (see Figure 5.14). At longer periods, the elastic acceleration design spectrum is reduced by a factor of μ. This is based on an assumption (Newmark and Hall, 1982) that the maximum deformations of the EPP and the elastic systems are approximately the same, i.e., $u_e = u_{max}$ in Figure 5.14. In Figure 5.18, point c' is obtained as the intersection of the flat and decaying portions of the inelastic design spectrum. Thus, given the period and available displacement ductility (μ), and using the inelastic design spectrum (Figure 5.18), the design yield strength (F_y) can be determined.

5.3.7.4.2 Other Inelastic Design Spectra

The process of generating the inelastic design spectrum shown in Figure 5.18 may be further simplified by using a period-independent (constant) reduction factor R_d, instead of using two factors R_{d1} and R_{d2}. This simplified version of constructing an inelastic design spectrum is conceptually similar to the procedure used in various building codes to reduce an elastic design spectrum to determine the strength (base shear) of the system.Other researchers have also proposed to use values for the strength reduction factor R_d as a means to reduce an elastic design spectrum to construct an inelastic design spectrum. For example, Krawinkler and Nassar (1992) proposed the following reduction factor R_d for a bilinear force-deformation relationship:

$$R_d = [c\,(\mu - 1) + 1]^{1/c} \text{ where } c(T, \alpha) = [T^{\,a} / (1 + T^{\,a})] + [b/T] \tag{5.15}$$

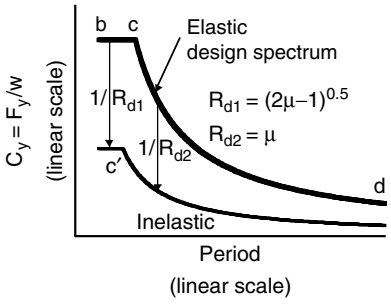

FIGURE 5.18 Inelastic design spectrum according to Newmark and Hall (1982). Points *b*, *c* and *d* correspond to those marked in Figure 5.9. See also Mahin and Bertero (1981).

where T is the natural period and parameters a and b are functions of α (the ratio of post-yield stiffness over initial elastic stiffness). For example, for $\alpha = 0$, the following values are used: $a = 1.0$ and $b = 0.42$. Similarly, for $\alpha = 2\%$, one should use $a = 1.0$ and $b = 0.37$; and for $\alpha = 10\%$, one should use $a = 0.8$ and $b = 0.29$.

Miranda and Bertero (1994) also examined numerous reduction factors previously proposed and concluded that the strength reduction factor is a function of available displacement ductility, period of the system and the site condition. Other recent studies on this subject include that by Vidic et al. (1994). A summary and comparison of some of the recent studies on R_d values have been provided by Chopra and Goel (1999).

5.3.8 Energy Spectra

The *elastic* response spectrum, although an important measure with extensive applications, has limitations in quantifying the damage potential of ground motion. For example, among its other limitations, it does not directly include the effects of inelastic structural response, which are generally associated with damage. Inelastic response spectra, in the form of maximum deformation ductility and inelastic design strength spectra, reveal some fundamental features of inelastic response and structural damage. However, among their other limitations, an IRS does not necessarily reveal information on the cumulative effects of number of cycles of inelastic deformations. The energy spectrum, especially the *hysteretic energy spectrum* defined below, can provide additional important information about the damage potential of the earthquake ground motion related to these cumulative effects.

Seismic input energy to an inelastic SDF system (E_I) is balanced as follows (Uang and Bertero, 1990; Bertero and Uang, 1992)

$$E_I = E_H + E_K + E_S + E_\xi \tag{5.16}$$

where E_H, E_K, E_S and E_ξ are irrecoverable dissipated hysteretic energy, kinetic energy, recoverable elastic strain energy and dissipated viscous damping energy, respectively. The absorbed energy E_A is given by

$$E_A = E_H + E_S = \int F\, du \tag{5.17}$$

where F is the restoring force and u is the deformation response (relative to the ground) of the mass of the SDF system. Hysteretic energy (E_H) is the amount of energy the structure must dissipate through inelastic nonlinear response. If the structure can dissipate the hysteretic energy demanded by the earthquake, it will survive without collapsing. If the structure remains elastic, i.e., no significant damage is expected, E_H will be zero. In general, a high hysteretic energy demanded by the ground motion is an indication of a high degree of damage. The details of the time history of the inelastic deformation can

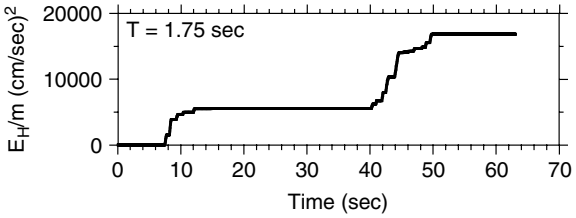

FIGURE 5.19 Time variation of hysteretic energy per unit mass at period $T = 1.75$ sec for the ground accelerations recorded at Düzce (EW component) during the August 17, 1999 Kocaeli ($M_w = 7.4$) and November 12, 1999 Düzce ($M_w = 7.1$) earthquakes in Turkey (see Figure 5.16(a) for the input ground motion).

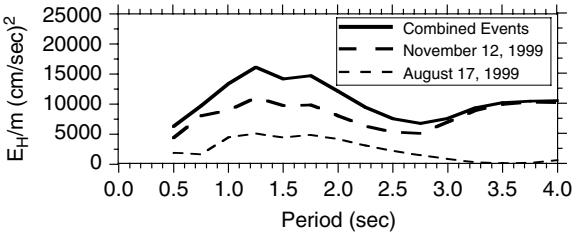

FIGURE 5.20 Hysteretic energy spectra per unit mass for the individual ground motions recorded at Düzce (EW component) during the August 17, 1999 Kocaeli and November 12, 1999 Düzce earthquakes in Turkey, and for the combined ground motion time histories (see Figure 5.16(a) for input time histories).

also play an important role in this process. Hysteretic energy by definition includes the cumulative effects of repeated cycles of inelastic response. Therefore, the cumulative damage effects of strong-motion duration are also included in this parameter.

An example of the time variation of E_H is presented in Figure 5.19 for the ground motions recorded at Düzce during the August and November 1999 earthquakes in Turkey. The characteristics of the inelastic SDF system are the same as those used for Figure 5.16(b). It is evident from Figure 5.19 that E_H includes the cumulative effects of the two events. The hysteretic energy spectrum presents the maximum (over time) of the hysteretic energy for a series of inelastic SDF systems. Figure 5.20 shows E_H spectra per unit mass for the 1999 earthquakes in Turkey recorded at Düzce (see Figure 5.16(a) for the input ground motions). For this figure, the mechanical characteristics of the SDF system are the same as those used for Figure 5.16(b). E_H spectra, such as those shown in Figure 5.20, reveal the cumulative damage potential due to a multiple sequence of ground shakings.

For practical reasons, it is convenient to use a normalized version of E_H. Various versions of normalized E_H have been introduced. For example, Mahin and Bertero (1976, 1981) defined normalized hysteretic energy (NHE) as

$$\text{NHE} = E_H/(F_y\, u_y) \tag{5.18}$$

where F_y and u_y are the yield strength and deformation of the SDF system, respectively (see Figure 5.14). Equivalent hysteretic velocity V_H (Akiyama, 1985; Uang and Bertero, 1988) has also been defined as

$$V_H = (2\, E_H/m)^{1/2} \tag{5.19}$$

where m is the mass of the system.Other recent developments on various forms of energy spectra include the use of energy-based concepts for seismic design and evaluation by Fajfar (1992) and Fajfar and Vidic (1994), the investigation of various normalized energy-based parameters by Bruneau and Wang

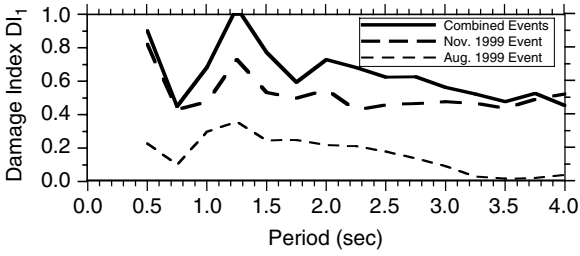

FIGURE 5.21 Damage spectra for the individual ground motions recorded at Düzce (EW component) during the August 17, 1999 Kocaeli and November 12, 1999 Düzce earthquakes in Turkey and for the combined ground motion time histories (see also Figure 5.16(a)).

(1996), the investigation of the use of elastic input energy for seismic hazard analysis by Chapman (1999) and Decanini and Mollaioli (1998), the attenuation of absorbed energy spectra by Chou and Uang (2000) and the presentation of the relationship between elastic input energy spectrum and Fourier amplitude spectrum of the ground acceleration by Ordaz et al. (2003), among others.

5.3.9 Damage Spectra

Structural performance and damage limit states can be quantified by a *damage index* (DI). A well-defined damage index is a normalized quantity that will be zero if the structure remains elastic (i.e., no significant damage is expected) and will be one if there is a potential of failure. Other structural performance states (such as operational, life-safe, near collapse, etc.) correspond to values of DI between zero and one. The *damage spectrum* represents the variation of a damage index over structural period for a series of SDF systems subjected to a ground motion record (Bozorgnia and Bertero 2001a, 2001b, 2003).

A damage spectrum, therefore, can quantify the damage potential of the recorded earthquake ground motion. For example, Bozorgnia and Bertero (2001a, 2001b, 2002, 2003) defined an improved damage spectrum based on a combination of normalized displacement ductility and hysteretic energy spectra for an inelastic SDF system

$$DI_1 = [(1 - \alpha_1)\ (\mu - \mu_e) / (\mu_{mon} - 1)] + \alpha_1\ (E_H/e_{Hmon}) \tag{5.20}$$

where μ ($= u_{max}/u_y$) is displacement ductility ratio; μ_e ($= u_{elastic}/u_y$) is the ratio of the maximum elastic portion of deformation over the yield deformation; μ_{mon} is the displacement ductility capacity of the system under monotonically increasing lateral deformation; E_H is the hysteretic energy demanded by the earthquake ground motion; e_{Hmon} is the hysteretic energy capacity of the system under monotonically increasing lateral deformation; and $0 \le \alpha_1 \le 1$ is a constant. Equation 5.20 is an improved version of the DI_{PA} defined by Park and Ang (1985), which is a widely used damage index (for more details see Bozorgnia and Bertero, 2001b). It can be shown that for an elastic-perfectly-plastic SDF system, e_{Hmon} is related to μ_{mon} and, hence, Equation 5.20 is greatly simplified.

If the system remains elastic (so that $\mu_e = \mu \le 1$ and $E_H = 0$), DI_1 will become zero. On the other hand, under a monotonically increasing lateral deformation, if the maximum displacement demand (u_{max}) reaches the displacement capacity of the structure (u_{mon}), i.e., an indication of failure, DI_1 will be one. Also, it is evident from Equation 5.20 that the normalized displacement ductility and hysteretic energy spectra are special cases of the damage spectrum and that they can be derived by assigning α_1 values of zero and one, respectively (Bozorgnia and Bertero, 2003). Examples of damage spectra are presented in Figure 5.21 for the EW component of the ground motions recorded at Düzce during the 1999 earthquakes in Turkey. The basic characteristics of the inelastic SDF system are the same as those used for Figure 5.16(b), with the following additional parameters: μ_{mon}=8 and α_1=0.29 (Bozorgnia and Bertero, 2002).Other characteristics of damage spectra, including the attenuation of damage spectral ordinates

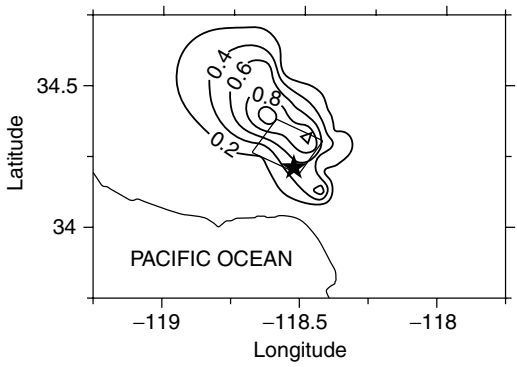

FIGURE 5.22 Distribution of the computed damage spectral ordinate (DI_1) at a 1.0 sec period for the horizontal ground motions recorded in the Northridge, California, earthquake. The epicenter and surface projection of the fault plane are also shown.

with source-to-site distance, have also been examined (see Bozorgnia and Bertero, 2002, 2001b). Following an earthquake, near real-time contour maps of damage spectral ordinates at selected periods can provide useful information on the spatial distribution of damage potential of the recorded ground motions for specified types of structures. Figure 5.22 shows the distribution of the damage spectral ordinate at 1.0 sec period for the horizontal motions recorded during the Northridge earthquake. For this figure, the basic characteristics of the inelastic SDF system are the same as those used in Figure 5.21, except $\mu_{mon} = 12$, $\alpha_1 = 0.27$, and no near-source factors are used. Utilization of an up-to-date inventory of existing structures together with the damage spectra can be used to identify the expected damage or losses for post-earthquake applications.

The damage spectra presented in a format such as that in Figure 5.21 can be used for seismic performance assessment of existing facilities. For performance-based design of new structures, the value of DI (corresponding to the desired performance) can be specified and the structural strength determined. For such applications, it is desirable to construct strength spectra for constant values of DI (Bozorgnia and Bertero, 2002). Figure 5.23 shows an example of such strength spectra for the El Centro (NS component) recording of the 1940 Imperial Valley earthquake. In this figure, consistent with previous results, a zero value for DI corresponds to an elastic spectrum. Also, as expected, the design strength decreases by increasing the value of DI. In the lower range of DI, a moderate increase in the value of DI (i.e., accepting minor damage) results in a significant reduction in the design strength.

5.3.10 Strong-Motion Spectra: A Summary

A wide variety of strong-motion parameters and spectra were discussed in Section 5.3. To give an overall perspective, it is convenient to classify their characteristics using the following categories:

- Parameters that are measures of free-field ground motion or reveal some basic ground motion characteristics, independent of any structural systems and models. These include peak ground motion values (acceleration, velocity and displacement), strong-motion duration and Fourier spectra of the ground motion. Arias intensity, as related to the integral of the square of the ground acceleration time history, falls in this category; however, it belongs also to the next category, as explained below.
- Spectra and parameters that are related to *elastic* response of SDF and continuous shear beam models. These include elastic response spectra, spectrum intensity, elastic design spectra and drift spectrum. The Arias intensity falls also in this category, because, it is defined as the sum of total energy per unit weight in a set of elastic SDF systems. This category includes important spectra and parameters with extensive applications in earthquake engineering. However, such spectra and

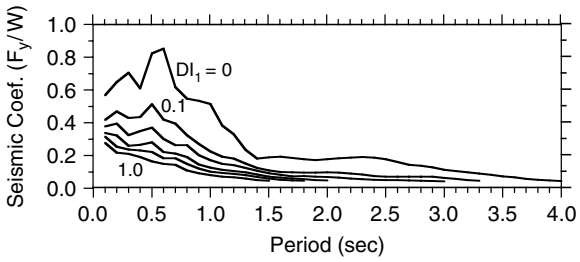

FIGURE 5.23 Strength spectra for constant values of damage index (DI_1= 0, 0.1, 0.2, 0.4, 0.6, 1.0) for an elastic-perfectly-plastic SDF system with 5% damping subjected to the El Centro (NS) recording of the 1940 Imperial Valley, California, earthquake. (From Bozorgnia, Y. and Bertero, V.V., 2002. Improved damage parameters for post-earthquake applications. *Proc. SMIP02 Seminar on Utilization of Strong-Motion Data*, Los Angeles, 61–82.)

parameters do not directly include the effects of amplitude and number of cycles of *inelastic* structural deformations (which are generally associated with damage), unless such effects are approximately and indirectly included.

- *Inelastic* response spectra in the form of maximum displacement ductility and strength spectra (for constant values of ductility) are based on maximum response of inelastic SDF systems. The inelastic spectra reveal some fundamental features of inelastic response and structural damage. However, they do not necessarily include the cumulative effects of number of cycles of inelastic response.
- Energy spectra, especially the *hysteretic energy spectrum*, can provide additional important information about the damage potential of the earthquake ground motion related to the cumulative damage effects. Hysteretic energy spectrum represents the dissipated hysteretic energy (due to yielding) in an *inelastic* SDF system. It includes the cumulative effects of cycles of inelastic response and strong-motion duration. For practical engineering applications, it is more convenient to normalize the demanded hysteretic energy spectra with respect to a measure of energy dissipation capacity of the system.
- Damage spectra represent variation of a damage index for an *inelastic* SDF system versus period. A well-defined damage spectrum will be zero if the response remains elastic and will be one if there is a potential of failure. Other structural performance states (such as operational, life-safe, near collapse, etc.) correspond to values of the damage spectral ordinates between zero and one. This makes the damage spectrum a promising tool for performance-based damage assessment of existing structures and performance-based design of new structures. If in the formulation of damage spectrum, cumulative parameters such as hysteretic energy are included, the damage spectrum would be influenced by the cumulative effects of strong-motion duration.

It is evident that there are some, but not total, overlaps in the information revealed by the various spectra discussed herein. Also, some types of spectra are simpler than others, requiring less input information and simpler computations. Besides their simplicity, however, their reliable applicable ranges must not be overlooked.

5.4 Ground Motion (Attenuation) Relations

5.4.1 Introduction

An essential element in both deterministic and probabilistic seismic hazard analyses is the ability to estimate strong ground motion from a specified set of seismological parameters. This estimation is carried out using a ground motion relation, or what engineers commonly refer to as an attenuation relation. A ground motion relation is a mathematical equation (i.e., a model) that relates a given strong-motion parameter to one or more parameters of the earthquake source, wave propagation path and local site

conditions, collectively referred to as seismological parameters. These parameters are discussed at length below, but first it is useful to examine the mathematical structure and seismological basis of the ground motion relation itself.

The ground motion relation, in its most basic form, can be described by a mathematical equation of the form

$$\ln Y = c_1 + c_2 M - c_3 \ln R - c_4 R + \varepsilon \tag{5.21}$$

where $\ln Y$ is the natural logarithm of the strong-motion parameter of interest, M is earthquake magnitude, R is source-to-site distance or a term involving this distance and ε is a random error term with a mean of zero and a standard deviation of $\sigma_{\ln Y}$. The mathematical form of Equation 5.21 can be traced back to the basic principles of earthquake seismology (Richter, 1958; Lay and Wallace, 1995). The term $c_2 M$ is consistent with the definition of earthquake magnitude as a logarithmic measure of the amplitude of ground motion. The term $-c_3 \ln R$ is consistent with the geometric spreading of the seismic wave front as it propagates away from the earthquake source. The parameter c_3 will vary with distance depending on the seismic wave type, such as whether it is a direct (body) wave or a surface wave and the effect of crustal structure, such as critical reflections off the base of the crust. The term $-c_4 R$ is consistent with the anelastic attenuation of seismic waves caused by material damping and scattering as they propagate through the crust. In practice (e.g., see Section 5.4.4.2), ground motion relations are more complex than implied by Equation 5.21. This additional complexity is needed to account for the effects of near-source behavior, faulting mechanism, local site conditions, source directivity and radiation pattern, the hanging-wall and footwall and tectonic environment. Figure 5.24 shows a typical example of a ground motion relation for peak ground acceleration (PGA).

The discussion in this chapter is limited to those ground motion relations that are used in the most recent (2002) update of the USGS national seismic hazard maps (Frankel et al., 2002). Even though these maps will not find their way into the building codes for several years, the ground motion relations on which they are based will be adopted in engineering practice almost immediately. Because of space limitations, only three of these ground motion relations are provided in equation form (see Section 5.4.4.2). The remainder of the relations are presented in Appendix A to this section that is posted on the accompanying Internet web site of the book. The discussion in this chapter is focused on providing guidance on the use of these relations and a description of how they were applied in the development of the 2002 USGS hazard maps. Other more broadly based compilations are given by Campbell (2003a, 2003b, 2003d).

5.4.2 Model Parameters

5.4.2.1 Ground Motion Parameters

Strong motion parameters typically used in engineering practice can be classified as either time-domain or frequency-domain. PGA and PGV are the most common examples of time-domain parameters. They represent the maximum absolute amplitude of the ground motion measured from a recorded or synthetic time history. PGD is another, albeit, less used peak-domain parameter. The most common frequency-domain parameters are S_a, S_v and S_d response spectral ordinates, which are related to one another through the relationships given in Section 5.3.3.1.

5.4.2.2 Earthquake Magnitude

Earthquake magnitude is used to quantify the size of an earthquake. There are many different scales that are used to define magnitude (see also Chapter 2), but all of the ground motion relations discussed in this chapter use moment magnitude (designated M_W in this chapter but alternatively denoted **M** by many seismologists). By definition, M_W is related to seismic moment, M_0, a measure of the seismic energy radiated by an earthquake, by the formula (Kanamori, 1978; Hanks and Kanamori, 1979)

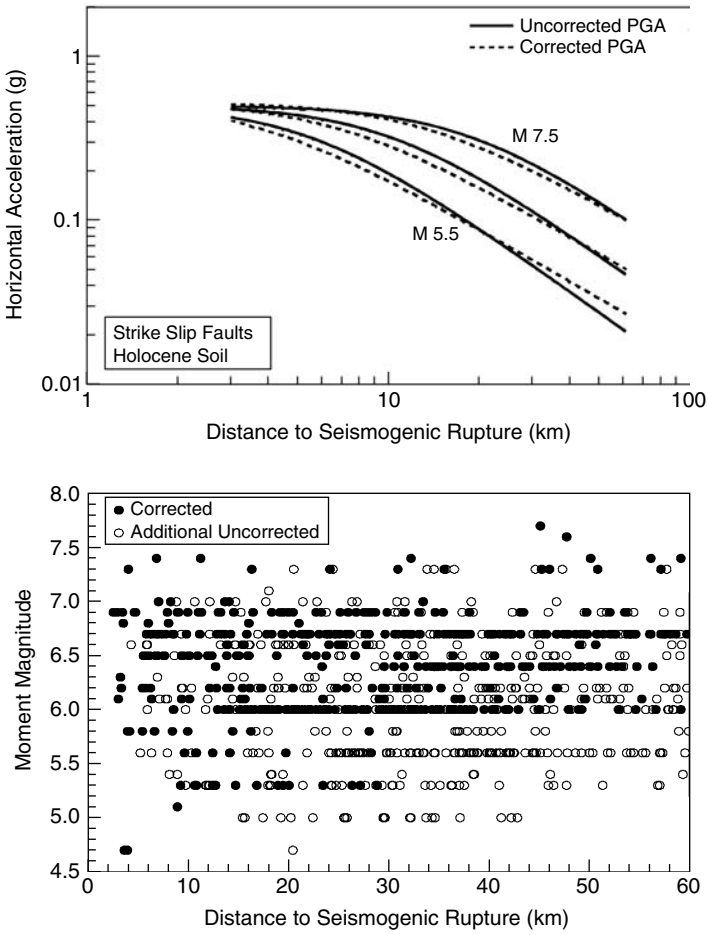

FIGURE 5.24 Example PGA ground motion relation (top) and its associated database (bottom). Uncorrected recordings refer to analog or digital acceleration time histories that have not been processed and, therefore, can only provide estimates of PGA. Corrected recordings refer to acceleration time histories that have been processed to derive velocity and displacement time histories, response spectra, and Fourier amplitude spectra. (From Bozorgnia, Y., Campbell, K.W. and Niazi, M. (1999). Vertical ground motion: characteristics, relationship with horizontal component, and building-code implications. *Proceedings, SMIP99 Seminar on Utilization of Strong-Motion Data*, San Francisco, California, 23–49.)

$$M_W = \frac{2}{3}\log M_0 - 10.7 \tag{5.22}$$

where $M_0 = \mu A_f \overline{D}$ or $2\mu E_S/\Delta\sigma$, μ is the shear modulus of the crust in the source region, A_f is the fault rupture area, $\overline{D}$ is the average displacement over the fault rupture plane, $\Delta\sigma$ is the average static stress drop over the fault rupture plane and E_S is the radiated seismic energy. The definition based on $A_f\overline{D}$ allows M_0 to be derived from geological faulting parameters that are easily observed in the field, at least for large surface-rupturing earthquakes. The definition based on $E_S/\Delta\sigma$ allows M_0 to be derived from instrumental measurements routinely obtained from seismological networks.

5.4.2.3 Source-to-Site Distance

Source-to-site distance is used to characterize the diminution of ground motion in terms of both geometric and anelastic attenuation, as it propagates away from the earthquake source. Distance measures

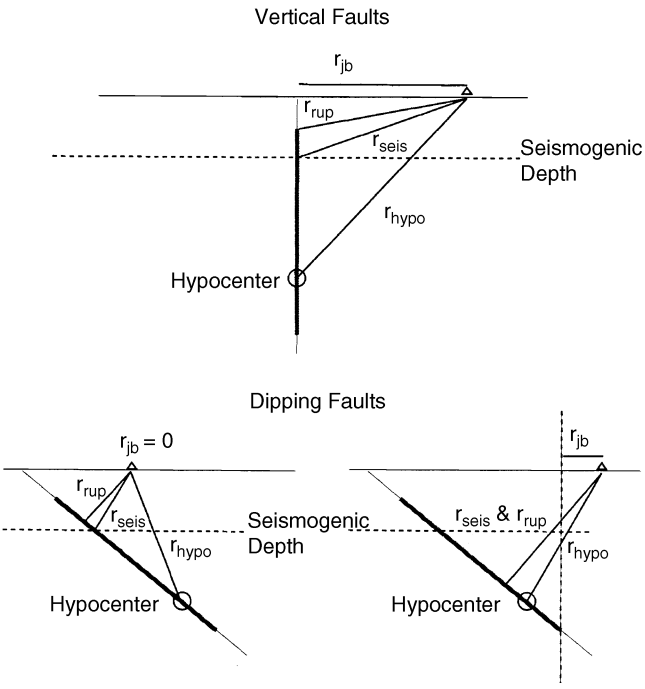

FIGURE 5.25 Relationship between distance measures used in the development of the ground motion relations. *(* From Abrahamson, N.A. and Shedlock, K.M. (1997). Overview. *Seismological Research Letters*, 68, 9–23.)

can be grouped into two broad classes depending on whether they treat the earthquake as a point source or as a finite source. Point-source distance measures include epicentral distance, r_{epi}, and hypocentral distance, r_{hypo}, where

$$r_{hypo} = \sqrt{r_{epi}^2 + h_{hypo}^2} \tag{5.23}$$

and h_{hypo} is the focal (hypocentral) depth of the earthquake. Generally speaking, r_{epi} and r_{hypo} are poor measures of distance for earthquakes with large rupture areas (i.e., large magnitudes). They are primarily used for characterizing distances from small earthquakes that can be reasonably represented by a point source. Experience has shown that ground motion relations that use point-source measures should not be used to estimate ground motions close to large earthquakes unless some approximate adjustment is made to account for finite-faulting effects.

The three finite-source distance measures used in the ground motion relations presented in this chapter are the closest horizontal distance to the vertical projection of the fault rupture plane, r_{jb}, the closest distance to the fault rupture plane, r_{rup} and the closest distance to the seismogenic part of the fault rupture plane, r_{seis}. The definition of r_{seis} assumes that fault rupture within the near-surface sediments or shallow fault gouge is non-seismogenic and not of engineering interest. These distance measures are schematically defined in Figure 5.25. Although r_{jb} is reasonably easy to estimate for a future (e.g., Design) earthquake, the distance measures r_{rup} and r_{seis} are not so easily determined, particularly when the earthquake is not expected to rupture the entire seismogenic width of the crust. In such cases, it is important to take into account the expected depth to the top of the fault rupture plane. If rupture-specific information is not available, the average depth to the top of the inferred fault rupture plane, d_{rup}, or to the seismogenic part of this plane, d_{seis}, can be calculated from (Campbell, 2000b)

$$d_i = \begin{cases} \frac{1}{2}\left[H_{top} + H_{bot} - W\sin(\delta)\right] & d_i \geq H_i \\ H_i & \text{otherwise} \end{cases} \tag{5.24}$$

where the subscript i is equal to rup or seis depending on the distance measure of interest, H_{bot} is the depth to the bottom of the seismogenic part of the crust, H_{top} is the depth to the top of the fault, H_{seis} is the depth to the top of the seismogenic part of the fault, δ is the dip of the fault, and W is the down-dip width of the fault rupture plane. There are many relationships that can be used to calculate W, but one often used in engineering practice is given by Wells and Coppersmith (1994)

$$\log W = -1.01 + 0.32 M_W \tag{5.25}$$

where W is measured in kilometers and the standard deviation of $\log W$ is 0.15.

Campbell (1997) recommends restricting the seismogenic depth used to calculate r_{seis} to $H_{seis} \geq 3$ km, even when the fault ruptures above this depth. This recommendation is based on several factors, including: (1) observations of aftershock distributions and background seismicity, (2) slip distributions on fault rupture planes derived from earthquake modeling studies and (3) an independent assessment of the depth of seismogenic faulting by Marone and Scholz (1988).

Many of the ground motion relations discussed in this chapter include near-source distance terms that account for the widely held belief that short-period strong-motion parameters should become less dependent on magnitude, i.e., they should saturate, close to the causative fault. Most engineers and seismologists consider such behavior to be an accepted behavior of near-fault ground motion. The ground motion relation shown in Figure 5.24 exhibits such behavior at short distances.

5.4.2.4 Faulting Mechanism

The faulting mechanism, or style of faulting, of an earthquake characterizes the direction of slip on the fault plane, seismologically defined as the rake (Lay and Wallace, 1995). Rake is a continuous variable representing the angle between the direction of slip on the fault plane and the orientation of the fault on the Earth's surface (its strike). Rake has not been used directly in any ground motion relation. Instead, the faulting mechanism has been classified in terms of two or more faulting categories. These categories are typically defined as strike slip, reverse and normal. The values of rake that correspond to these categories are 0° for pure left-lateral strike-slip faulting, 180° for pure right-lateral strike-slip faulting, 90° for pure reverse faulting and 270° for pure normal faulting (Lay and Wallace, 1995). Alternatively, some seismologists use a rake of –90° to define pure normal faulting. Thrust faulting is a special case of reverse faulting in which the dip of the rupture plane is shallow, typically less than 45°. A combination of strike-slip and either reverse or normal faulting (oblique faulting) has a rake that falls between those given above. It has been common practice in the past to put strike-slip and normal-faulting events into a single strike-slip category. However, a recent study by Spudich et al. (1999) suggests that normal-faulting events, or for that matter strike-slip events in an extensional tectonic regime, might have lower ground motions than other types of shallow crustal earthquakes. All of the ground motion relations discussed in this chapter predict higher ground motions for reverse and reverse-oblique earthquakes than for strike-slip and normal earthquakes.

A great deal of interest has been generated in blind thrust faults by seismologists and engineers after unusually large ground motions were observed during the 1987 Whittier Narrows, California, the 1988 Saguenay, Canada and the 1994 Northridge, California, earthquakes. Whether similarly high ground motions can be expected from all future blind thrust earthquakes is at present speculative. However, it cannot be ruled out, considering the current limited observational database. The higher ground motions observed during blind thrust earthquakes have been found to correspond to higher-than-average stress

drops. More theoretical and empirical studies will be needed before there is a clear understanding why these three earthquakes produced such high stress drops and how such events might be predicted in the future. The Campbell and Bozorgnia (2003) ground motion relation is the only one discussed in this chapter that includes differences between reverse and thrust events. This relation predicts higher short-period ground motions for thrust events as would be expected if these differences were due to higher stress drops.

5.4.2.5 Local Site Conditions

Local site conditions describe the type of deposits that lie beneath the site. They are usually described in terms of surface or near-surface geology, shear-wave velocity and sediment depth. The latter two descriptions are preferred because they represent physical quantities that can be related directly to the dynamic response of the underlying geological deposits. Traditionally, local site conditions have been classified as soil or rock. Many ground motion relations discussed in this chapter still use this simple classification. However, Boore et al. (1997), Rodriguez-Marek et al. (2001), Campbell and Bozorgnia (2003) and Stewart et al. (2003) have clearly demonstrated the importance of a more refined site classification scheme in the prediction of near-source ground motion. Park and Elrick (1998) and Wills and Silva (1998) have also shown that a more refined geological classification appears to be warranted based on measured shear-wave velocities in various geological units in California.

There are typically two methods for classifying a site in terms of shear-wave velocity, here denoted V_S. The first is the average value of V_S in the top 30 m (100 ft) of the deposit, referred to here as 30-m velocity, V_{30}. The second is the average value of V_S over a depth equal to a quarter-wavelength of a ground-motion parameter of specified period or frequency, referred to here as effective velocity. The 1997 edition of the *Uniform Building Code* (UBC) and the 2000 edition of the *International Building Code* (IBC) use the 30-m velocity as the primary basis for defining National Earthquake Hazard Reduction Program (NEHRP) site categories and their associated site factors that are used to adjust design ground motions for local site effects (Table 5.3; see also Chapter 4). Other properties of the soil profile such as standard penetration resistance, unconfined shear strength and depth of soft soil are also used to define the NEHRP site class, but these properties are not listed in Table 5.3, see also Chapter 4. The California Geological Survey (Wills et al., 2000) modified the NEHRP site classification scheme to incorporate boundary site categories, which they used for the purpose of developing a site conditions map for California (Table 5.3; see also Chapter 4). The 30-m velocity is calculated from the formula

$$V_{30} = \sum_{i=1}^{n} d_i \Big/ \sum_{i=1}^{n} (d_i / V_{Si}) \tag{5.26}$$

where d_i is the thickness and V_{Si} is the shear-wave velocity of the ith soil layer. Progressively deeper soil layers are used until the summation in the numerator of Equation 5.26 equals 30 m (100 ft). Boore et al. (1997) developed the only ground motion relation discussed in this chapter that uses V_{30} as a site parameter. However, Choi and Stewart (2003) and Stewart et al. (2003) developed nonlinear site factors for NEHRP site categories B through E that can be used with the ground motion relations of Abrahamson and Silva (1997), Sadigh et al. (1997) and Campbell and Bozorgnia (2003).The NEHRP site categories proposed by the California Geological Survey (CGS) were defined by relating measured values of V_{30} to mapped geological units in California. However, the CGS defined overlapping velocity ranges for their site categories that make their use difficult in practice. For site categories E through BC, the CGS defines nominal values of V_{30} (Table 5.3) in the GIS version of the California site-conditions map that avoids the ambiguity in estimating V_{30} knowing the site category. The CGS assigns a nominal 30-m velocity value of 1000 m/sec to NEHRP B, although the writers prefer the nominal value given in Table 5.3, which is listed as 1130 m/sec, the midpoint of the velocity range that defines this category. Because of the overlapping velocity ranges, an ambiguity arises when attempting to assign a particular site to a CGS site category when 30-m velocity is known. Because there is no consensus on how this should be done, a non-overlapping

TABLE 5.3 Definition of NEHRP Site Classes Based on Shear-Wave Velocity

NEHRP Site Class[a]			30-m Velocity, V_{30} (m/sec)		
Code	CGS	Soil Profile Name	Code	Cgs[b]	Nominal[c]
A	A	Hard rock	≥1500	≥1695	1890
—	AB	A-B boundary		1315–1695	1500
B	B	Rock	760–1500	945–1315	1130
—	BC	B-C boundary	–	660–945	760
C	C	Very dense soil and soft rock	360–760	460–660	560
—	CD	C-D boundary	–	315–460	360
D	D	Stiff soil	180–360	225–315	270
—	DE	D-E boundary	–	165–225	180
E	E	Soft soil	<180	<165	150

[a] National Earthquake Hazard Reduction Program (NEHRP) site class definitions: Code, as defined in the 1997 *Uniform Building Code* (UBC) and the 2000 *International Building Code* (IBC); CGS, as defined by the California Geological Survey (Wills et al., 2000) and extended by the writers to include A and AB site classes.

[b] Approximate ranges of V_{30} proposed by the writers to use in assigning CGS NEHRP site-classes when V_{30} is known.

[c] Single best estimate of V_{30} to use for each NEHRP site class when no other information is available.

range of V_{30} values is proposed and listed in Table 5.3. However, because there is no unique way of defining these ranges, the user must apply his or her own judgment in deciding what CGS site category should be used to correspond to a specific value of V_{30}. The values listed in Table 5.3 are meant to be used only as a guide. There is no such ambiguity in the range of 30-m velocity for the code-based NEHRP site categories. However, there is an ambiguity in defining a nominal value for the first and last building-code categories, which are defined by inequalities in V_{30}. In this case, a reasonable estimate of the nominal value of V_{30} based on published sources is provided in Table 5.3. The value for soft soil (E) is that given for intertidal mud by Wills and Silva (1998). The value for hard rock (A) is that reported by Savy et al. (1987) for older sedimentary rock sites in the eastern United States.

Joyner et al. (1981) proposed effective velocity as a site parameter, which is related to the non-resonant amplification produced as a result of the energy conservation of seismic waves that propagate vertically upward through a deposit of gradually changing velocity. This parameter is defined as the average velocity from the surface to a depth corresponding to a quarter-wavelength of a strong-motion parameter of specified period or frequency. Effective velocity can be calculated from Equation 5.26 by summing to a depth corresponding to a quarter-wavelength rather than to 30 m. This depth is given by the equation (Boore, 2003)

$$D_{1/4}(f) = \sum_{i=1}^{n} d_i \tag{5.27}$$

where $T = 1/f$ is the period of interest. Progressively deeper soil layers are used in the above summation until the equality $\sum_{i=1}^{n} d_i / V_{Si} = T/4$ is achieved. Effective velocity is used to calculate site amplification factors using the stochastic method (Boore, 2003). This is important because several of the Eastern North America (ENA) ground motion relations discussed in this chapter were developed using this method.

Sediment or basin depth is the depth to the basement-rock horizon beneath the site. Basement rock is a geological term that is used to describe the more resistant, generally crystalline rock that lies beneath layers or irregular deposits of younger, relatively deformed sedimentary rock. This parameter is not generally used in engineering practice and is not included in any of the ground motion relations discussed in this chapter. First proposed empirically over several decades ago, its importance has been recently

recognized by several seismologists. For example, based on empirical and theoretical considerations, Joyner (2000) found that long-period spectral amplifications predicted from the sediment-depth term given in Campbell (1997, 2000b) were similar to those derived from the effects of traveling surface waves generated at the edge of the Los Angeles basin. Lee and Anderson (2000), Field (2000) and Field and the SCEC Phase III Working Group (2000) found that sediment depth could be used to approximately account for the modeled 3-D response of the Los Angeles basin. Rodriguez-Marek et al. (2001) found that the depth to bedrock with $V_S \geq 760$ m/sec was an important parameter in estimating site response from the 1989 Loma Prieta and 1994 Northridge, California, earthquakes. Campbell and Bozorgnia (2003) evaluated sediment depth as a parameter in their ground motion relation and also found it to be important, especially at long periods. However, they chose not to include it in their relation at that time because they found from past experience, e.g., in applications involving the ground motion relation of Campbell (1997, 2000b), that it is often misunderstood and misinterpreted by engineers.

5.4.2.6 Stress Drop

Stress drop, or more correctly dynamic or Brune stress drop (Brune, 1970, 1971), is one of the parameters that controls the high-frequency amplitude of ground motion. It is related to the amount of stress that is relieved at the rupture front during an earthquake. Theoretical studies have shown that higher stress drop results in higher short-period ground motion. None of the ground motion relations discussed in this chapter explicitly include stress drop as a parameter. However, stress drop is one of the parameters that is included in the calculation of ground motion using the stochastic method, which was used to develop several of the ENA ground motion relations discussed in this chapter.

As discussed above, relatively high stress drops are likely to have been the cause of the relatively high ground motions observed during some recent blind thrust earthquakes. On the other hand, low stress drops might have been the cause of the relatively low short-period ground motions observed during the 1999 Chi-Chi (M_w 7.6), Taiwan, earthquake (Tsai and Huang, 2000; Boore, 2001), the 1999 Kocaeli (M_w 7.4), Turkey, earthquake (Anderson, 2000, 2003) and, at least based on preliminary ground motions available at the time this book went to press, the 2002 Denali (M_w 7.9), Alaska, earthquake. The observation of relatively low short-period ground motions during the Chi-Chi earthquake is particularly significant because it is a large thrust earthquake, which had been expected from previous empirical and theoretical studies to have relatively large ground motion. This earthquake did, however, have relatively large ground motion on the hanging wall of the rupture plane and relatively large PGV and long-period S_a as had been expected. The relatively low stress drops implied for the Taiwan, Turkey and Alaska earthquakes could be a result of large total slip on the causative faults (Anderson, 2003) or large surface ruptures (Somerville, 2000). More study will be needed to better understand the phenomena that might have contributed to these low ground motions. If these earthquakes are found to be typical of similar large earthquakes worldwide, the implication is that the current ground motion relations might be overpredicting short-period ground motions from large earthquakes, something that has been suggested from observations of precariously balanced rocks near great earthquakes on the San Andreas fault (Brune, 1999).

5.4.2.7 Hanging-Wall and Footwall Effects

Generally speaking, the hanging wall is that portion of the crust that lies above the rupture plane of a dipping fault and the footwall is that portion of the crust that lies below this plane. Sites located on the hanging wall of a reverse or thrust fault generally exhibit higher-than-average ground motion. The hanging-wall effect is probably caused by a combination of radiation pattern, source directivity, decoupling of the hanging-wall and footwall during rupture propagation and the entrapment of seismic waves within the hanging-wall wedge of the crust (that portion between the rupture plane and the Earth's surface). Theoretical ground-motion modeling has consistently shown that higher ground motion can be expected on the hanging wall of reverse and thrust faults and that lower ground motion can be expected on the footwall of such faults (Anderson, 2003; Brune 2001). This is consistent with the observation of shattered rock on the hanging wall of thrust faults in Southern California and the lack of such shattered

rock and the presence of precariously balanced rocks on the footwall of at least two thrust faults in this same region (Brune, 2001). It is also consistent with observed ground motion from the 1994 Northridge earthquake (Abrahamson and Somerville, 1996) and the 1999 Chi-Chi earthquake (Shin et al., 2000). Two of the ground motion relations discussed in this chapter include a hanging-wall term (Abrahamson and Silva, 1997; Campbell and Bozorgnia, 2003).

5.4.2.8 Tectonic Environment

Tectonic environment refers to the state of stress and the seismological properties of the crust. It has a significant impact on the amplitude and attenuation of strong ground motion. It has traditionally been classified into four basic types for the purpose of estimating strong ground motion: (1) shallow crustal earthquakes in a tectonically active region, (2) shallow crustal earthquakes in a tectonically stable region, (3) intermediate-depth earthquakes (also known as Wadati-Benioff or intraslab earthquakes) within the down-going crustal plate of a subduction zone and (4) earthquakes along the seismogenic interface of the down-going and overriding crustal plates of a subduction zone. The shallow crustal environment can be further subdivided into compressional and extensional regimes. Each of these tectonic environments is represented by at least one of the ground motion relations discussed in this chapter.

A detailed discussion of the different tectonic environments and their global distribution is provided by Moores and Twiss (1995). A shallow crustal environment refers to the seismogenic part of the crust, which generally varies from 10 to 30 km in thickness, depending on the region. A tectonically active environment is one in which large earthquakes are relatively frequent and tectonic deformation is relatively large. It is usually located in the vicinity of tectonic plate margins. Such regions are typically characterized by relatively low stress drops and relatively high anelastic attenuation. A tectonically stable environment is one in which large earthquakes are relatively infrequent and tectonic deformation is relatively small. It is usually located away from plate margins in an intraplate region characterized by very old continental crust. Such regions are typically characterized by relatively high stress drops and relatively low anelastic attenuation. Johnston (1996) presents a series of maps that show the geographic distribution of tectonically active and tectonically stable continental regions worldwide. A compressional regime is one in which the crust is undergoing shortening. It is typically associated with relatively high stress drops. An extensional regime is one in which the crust is undergoing lengthening and is typically associated with relatively low stress drops. Zoback (1992) presents a stress map that shows the geographic distribution of compressional and extensional regimes worldwide.

A subduction zone is a region in which one tectonic plate (usually oceanic crust) thrusts beneath, or is *subducted* by, another tectonic plate (usually continental crust). Subduction interface earthquakes, some of which are the largest in the world, occur along the seismogenic boundary of the subducting and overriding plates. Depending on the age of the subducting plate, this interface occurs to depths ranging anywhere from 20 to 50 km. So-called Wadati-Benioff, or intraslab, earthquakes occur within the subducting plate below the subduction interface zone as it descends into the Earth's mantle.

5.4.3 Analysis Methods

5.4.3.1 Strong Motion Database

In regions where strong-motion recordings are abundant, ground motion relations are developed from statistical regression analysis. This requires a suitable strong-motion database. Engineering estimates of ground motion are intended to provide estimates of ground motion on level ground in the free field, unaffected by any man-made or natural structures, or what engineers refer to as soil-structure interaction effects. This means that these recordings should not be located on or near a large structure, in an area of strong topographic relief, or below the ground surface. All of these situations have been shown to significantly modify free-field ground motion in some situations. Although it is generally agreed upon that non-free-field recordings should be excluded from a strong-motion database, there is no consensus on what constitutes such a recording. Furthermore, because the majority of the available recordings were obtained in or near a man-made structure, it is impossible to restrict the database to truly free-field

recordings without restricting their number to the point where a statistical analysis might not be meaningful. All of the empirical ground motion relations discussed in this chapter have attempted to screen out non-free-field recordings to some degree, albeit using different and sometimes conflicting criteria. A recent study by Stewart (2000) will help in providing a more quantitative basis for identifying such recordings in the future.

Stewart (2000) evaluated the conditions for which recordings obtained at the foundation of a structure can be expected to provide a reasonably unbiased estimate of free-field ground motion with minimal uncertainty. He found that variations between spectral accelerations recorded in the free field and those recorded on a nearby building foundation correlated well with dimensionless parameters that strongly influence kinematic and inertial soil-structure interaction phenomena, such as embedment ratio, dimensionless frequency (the product of wave frequency and foundation radius normalized by soil shear-wave velocity) and structure-to-soil stiffness ratio. Stewart also found that low frequency components of spectral acceleration recorded on shallow foundations provide reasonable estimates of free-field ground motion. However, such was not the case for PGA or, in some cases, even PGV.

Stochastic, theoretical and hybrid empirical (semi-theoretical) analysis methods are typically used to develop a synthetic strong-motion database in areas where there are an insufficient number of strong-motion recordings. These synthetic data are used to develop a ground motion relation in much the same manner that actual data are used. The stochastic method uses a stochastic representation of the ground motion, shaped by simple seismological models of the source spectrum and propagation path and a mathematical representation of the response of an SDF oscillator, to derive a set of synthetic strong-motion parameters for a desired set of magnitudes and distances (Campbell, 2003a, 2003b, 2003d; Boore, 2003). One of the important aspects of the stochastic method is whether a single-corner or a double-corner source spectrum is used (Atkinson and Boore, 1998), because the latter results in relatively low mid-to-long period ground motions compared to the one-corner source spectrum. Of the five ENA ground motion relations discussed in this chapter, three were developed using the stochastic method (Atkinson and Boore, 1995, 1997; Frankel et al., 1996; Toro et al., 1997) and, of these, only the Atkinson and Boore relation was based on the two-corner source spectrum. The theoretical method uses kinematic or dynamic dislocation models of the earthquake rupture process, together with empirical or theoretical Greens functions and seismic ray theory, to develop synthetic strong-motion parameters. Because of its greater complexity, only one of the ENA ground motion relations discussed in this chapter used the theoretical method (in this case the kinematic approach) in its derivation (Somerville et al., 2001). Because it has only recently gained the interest of seismologists, only one of the ENA ground motion relations (Campbell, 2001, 2003c) was developed using the hybrid empirical method. This method uses the stochastic method to adjust empirical ground motion relations developed for one region, in this case Western North America (WNA), to estimate synthetic strong-motion parameters in another region, in this case ENA, where there are a limited number of strong-motion recordings. These adjustments take into account differences in the earthquake source, wave propagation and site-response characteristics between the two regions.

5.4.3.2 Regression Analysis

Whether developed from recorded or synthetic ground motion data, all ground motion relations are derived using a statistical fitting procedure known as regression analysis (e.g., Draper and Smith, 1981). Regression analysis is used to determine the best estimate of the coefficients in the relation (e.g., the coefficients c_1 through c_4 in Equation 5.21) using any number of statistical fitting procedures, such as least squares or maximum likelihood. Three different methods were used to develop the ground motion relations discussed in this chapter: (1) weighted nonlinear least-squares regression; (2) two-step least squares regression and (3) random-effects regression. Each of these methods has its own strengths and weaknesses; however, they all attempt to mitigate the bias introduced by the uneven distribution of recordings with respect to magnitude, distance and other seismological parameters. An advantage of the latter two methods is that they provide a direct estimate of the intra-earthquake and inter-earthquake

components of randomness, although these components can be derived, albeit indirectly, using the first method as well.

5.4.3.3 Predicted Value

Because the predicted value from Equation 5.21 is the logarithm of *Y*, this prediction represents the mean value of $\ln Y$, or what is referred to statistically as the median (50th-percentile) value of *Y*. By definition, the median value is exceeded by 50% of the underlying observations. The $100\times(1-\alpha)$-percentile estimate of the mean of n_0 future observations of $\ln Y$ is statistically given by the formula (Draper and Smith, 1981)

$$\ln Y_{1-\alpha} = \ln Y + t_{\nu}(\alpha)\sqrt{\frac{\sigma_{\ln Y}^2}{n_0} + \sigma_{\overline{\ln Y}}^2} \tag{5.28}$$

where $t_{\nu}(\alpha)$ is the Student's *t*-statistic for an exceedance probability of α and for $\nu = n - p$ degrees of freedom (this statistic is widely available in statistic books), $\sigma_{\overline{\ln Y}}$ is the standard error of the mean value of $\ln Y$ (a measure of modeling uncertainty) and $\sigma_{\ln Y}$ is the standard error of regression (a measure of randomness). The standard error of regression is given by

$$\sigma_{\ln Y} = \sqrt{\frac{1}{n-p}\sum_{i=1}^{n}\left(\ln Y_i - \overline{\ln Y_i}\right)^2} \tag{5.29}$$

where *n* is the number of recordings, *p* is the number of regression coefficients, $\ln Y_i$ is the *i*th recorded value, and $\overline{\ln Y_i}$ is the *i*th predicted value. The $100\times(1-\alpha)$-percentile estimate of a single future observation of $\ln Y$, the most common application of Equation 5.28, is calculated by setting $n_0 = 1$.

It is common engineering practice to calculate the $100\times(1-\alpha)$-percentile estimate of a single future value of $\overline{\ln Y_i}$ by setting $\sigma_{\overline{\ln Y}} = 0$ and replacing the *t*-statistic with the standard normal variable, *z*. These assumptions reduce Equation 5.28 to its more commonly used form

$$\ln Y_{1-\alpha} = \ln Y + z_{\alpha}\sigma_{\ln Y} \tag{5.30}$$

where z_{α} is the standard normal variable for an exceedance probability of α (this variable is widely available in statistics books). Although statistically incorrect, results using Equation 5.30 are not significantly different from those using Equation 5.28 unless the predicted value is derived from an extrapolation of the regression equation or from a regression equation that is based on very few recordings. In the first case, the value of $\sigma_{\overline{\ln Y}}$ is non-negligible and, in the second case, the *z*-statistic is inaccurate. When Equation 5.30 is used to predict ground motion, it is engineering practice to account for epistemic uncertainty by using several ground motion (attenuation) relations to predict $\ln Y$. However, even such practice will not necessarily account for all of the epistemic uncertainty inherent in the estimation of ground motion.

5.4.4 Ground Motion (Attenuation) Relations Used by USGS

5.4.4.1 General Description

All ground motion relations have certain limitations. These limitations stem from issues that arise during their development, such as the number and distribution of recordings, the data selection criteria, the selection of a functional form, the theoretical assumptions and the choice of seismological parameters used to define the source, path and site effects. It is dangerous to assume that any engineering model can be extrapolated beyond its data, theoretical assumptions, or geographic region of applicability and still provide a reliable estimate of ground motion. In fact, some of the ground motion relations presented in this and the next section have specific caveats regarding their use, which are noted when known.

However, these caveats are often ignored in seismic hazard analysis for practical reasons. Such is the case in the development of the 1996 and 2002 USGS national seismic hazard maps.

The shallow crustal ground motion relations used in the 2002 USGS hazard maps are segregated into two tectonic regions: WNA and ENA. WNA is further segregated into extensional, compressional and subduction regimes. The division between WNA and ENA has traditionally been taken as 105° W. Longitude. A somewhat more detailed definition of this boundary has been proposed by Frankel et al. (1996, 2000, 2002). Because ENA is tectonically stable, earthquakes in this region are typically associated with higher stress drops and lower anelastic attenuation, resulting in higher ground motion at short periods and large distances.

The USGS used four ground motion relations for compressional regimes in WNA; namely, Abrahamson and Silva (1997), Boore et al. (1997), Sadigh et al. (1997) and Campbell and Bozorgnia (2003). Although not specifically used in the development of the hazard maps, the Sadigh et al. (1993) ground motion relation is presented along with these authors' 1997 relation because it is widely used in engineering practice to predict the vertical component of ground motion for rock sites. For extensional regimes in WNA, the USGS used the above four ground motion relations, each evaluated for strike-slip and normal faulting (see discussion below) along with the Spudich et al. (1999) relation. All of these relations were developed from regression analyses of strong-motion recordings using the empirical method. The USGS used five ground motion relations for ENA; namely, Atkinson and Boore (1995, 1997), Frankel et al. (1996), Toro et al. (1997), Somerville et al. (2001) and Campbell (2001, 2003c). All of these relations were developed from regression analyses of synthetic strong-motion parameters calculated using either the stochastic, theoretical (kinematic), or hybrid empirical method and are, therefore, non-empirical. The Atkinson and Boore relation was updated by D. Boore to represent the NEHRP B-C Boundary site condition.

Great interface earthquakes of M_W 8.3 and 9.0 on the Cascadia Subduction Zone (Cascadia S. Z.) dominate the seismic hazard along the western coasts of Oregon and Washington. The USGS used two ground motion relations for modeling subduction interface events; namely, Youngs et al. (1997) and Sadigh et al. (1997). The Youngs et al. relation was evaluated for interface events and the Sadigh et al. relation for reverse-faulting events (see discussion below). The hypocentral depth was fixed at 20 km when evaluating the Youngs et al. relation. Weights for each relation are defined as a function of distance so that the Youngs et al. And Sadigh et al. relations have equal weight at relatively close distances and the Youngs et al. relation has 100% weight at relatively larger distances. The USGS used a constant distance range of 70 ± 15 km for the M_W 8.3 event and 60 ± 15 km for the M_W 9.0 event, independent of period, to define the distance range over which the weights were linearly varied. However, in reality, this range is period dependent. The maximum magnitude that is allowed in the Sadigh et al. relation is 8.5, so M_W was set to this value for the M_W 9.0 event. The USGS used the Youngs et al. relation and two versions of a new relation developed by Atkinson and Boore (2003), both evaluated for intraslab conditions, for intermediate-depth (Wadati-Benioff) events associated with the Cascadia S. Z. The hypocentral depth used in the Youngs et al. relation and the depth to the top of faulting used to estimate r_{rup} in both relations was fixed at 50 km.

Table 5.4 lists relevant information concerning the ground motion relations that were used in the development of the 2002 USGS hazard maps. This information includes the subregion in which they were applied, the weight assigned to them for the given subregion, whether they predict the vertical component of ground motion (V) in addition to the average horizontal component (H), the range of periods for which they are applicable, the seismological parameters that are included in each, and the range of magnitudes and distances for which they are considered valid. In parentheses, beneath the region designation, is a description of the method that was used to develop each relation. For the WNA relations, the subregion indicates whether they were used for compressional and extensional regimes. The extensional regime includes the Basin and Range province, which generally extends from the eastern front of the Cascade and Sierra Nevada Mountains to the western front of the Rocky and Wasatch Mountains. This regime includes eastern California (including Imperial Valley), eastern Oregon, eastern Washington, southern Idaho, western Utah, Arizona, Nevada and New Mexico (Frankel et al., 2002). For the ENA

relations, the subregion indicates whether they were used for faults and for background seismicity (also known as gridded or smoothed seismicity). Explicitly modeled ENA faults include those responsible for the 1811–1812 New Madrid sequence and the 1876 Charleston earthquake. Background seismicity can have a maximum magnitude as large as M_W 7.5; nevertheless, the USGS did not use the Somerville et al. (2001) relation for such earthquakes, even though the authors of the relation recommend its use for events of $M_W \geq 6$. The model parameters enclosed in parentheses are the alternative symbols used to describe the ground motion relations presented in the Appendix A provided on the accompanying Internet site and in Campbell (2003a, 2003b, 2003d). This alternative notation was used to provide a consistent set of notation among the different ground motion relations.

Among the ENA models, only those of Somerville et al. (2001) and Campbell (2001, 2003c) explicitly include near-source scaling characteristics. The others, because they are based on point-source seismological models, require their distance measures to be modified or capped to give realistic ground-motion estimates at near-source distances. In the development of the USGS hazard maps, the hypocentral distance used by Atkinson and Boore (1995, 1997) and Frankel et al. (1996) was replaced by the closest distance to the surface projection of faulting, r_{jb}, as suggested by Boore (2003). Furthermore, a fictitious depth was used to force the relation to asymptotically approach a limiting amplitude at short distances, similar to those relations that use a finite-fault distance measure. In addition, absolute amplitude caps were applied to both the median estimates and the upper tails of the aleatory distributions of PGA and selected spectral accelerations in ENA (Table 5.5). All of the ground-motion aleatory distributions (the random distribution of ground motion about the median), including those for the WNA and Cascadia S. Z., were truncated at ±3 standard deviations in the probabilistic seismic hazard analysis. Two fictitious depths, 5 and 10 km, were used to limit near-source ground motions computed from the point-source ground motion relations, depending on whether the source was modeled as background seismicity or finite faulting, respectively. The depth of 5 km used for background seismicity was also used with those ground motion relations that use the fault-distance measures r_{rup} and r_{seis} (Table 5.4).

Table 5.6 lists the faulting categories used in each of the WNA ground motion relations. These categories are defined in terms of the rake and the values of the faulting mechanism (style-of-faulting) parameters used in each relation, according to the alternative notation used in the Appendix A published on the accompanying Internet site and in Campbell (2003a, 2003b, 2003d). The rake is an important parameter because it corresponds to a physically meaningful quantity of the earthquake source — the orientation of slip on the fault — that ultimately determines the focal mechanism of the earthquake. The faulting mechanism parameter is a convenient way of statistically describing the effects of the rake on the predicted ground motion in the regression analysis. Only the WNA ground motion relations include a faulting mechanism parameter. However, some of these relations either do not specify the range of rakes that correspond to a given faulting category or give an incomplete description of these rakes. The values of rake included in Table 5.6 were determined based on discussions with the authors of the relations. The faulting categories given in italics are those used in the development of the 2002 USGS hazard maps. For purposes of developing these maps, all faults were placed into one of three faulting categories, characterized as strike slip, normal, or reverse. Reverse-oblique faulting was placed into the reverse-faulting category. Although Spudich et al. (1999) distinguished between strike slip and normal faulting, they found no significant difference in the two and, as a result, did not include a faulting mechanism parameter in their ground motion relation. The Sadigh et al. (1997) relation was evaluated for reverse faulting when used for estimating ground motions for Cascadia S. Z. interface events. In addition to a faulting mechanism parameter, the Abrahamson and Silva (1997) and Campbell and Bozorgnia (2003) ground motion relations include a hanging-wall term. However, the USGS evaluated the Abrahamson and Silva relation for hanging-wall effects only for reverse faults and for sites located directly over the rupture plane or its horizontal extension, a restriction not imposed by the authors. The USGS did not attempt to apply a more general hanging-wall model, such as that described by Campbell (2003a, 2003b, 2003d), to all of the relations. Nor did they attempt to apply a general source directivity term to any of the ground motion relations, such as that described in Section 5.4.5.3. Such a directivity term is often used in engineering practice.

TABLE 5.4 Ground Motion Relations Used in the 2002 USGS National Seismic Hazard Maps

Ground Motion Relation	Region	Subregion	Weight	Comp	Periods	Model Parameters[b]	Validity
Abrahamson and Silva (1997)	WNA (Empirical)	Compressional Extensional	0.250 0.200	H, V	PGA, 0.02 – 5.0	M (M_W), r_{rup}, F, S (S_{Soil}), HW, $\widehat{\text{pga}}_{\text{rock}}$ (A_{Rock})	$5.0 \le M_W \le 8.0$, $r_{rup} \le 100$ km
Boore et al. (1997)	WNA (Empirical)	Compressional Extensional	0.250 0.200	H	PGA, 0.10 – 2.0	M (M_W), r_{jb}, b_{1ss} (c_{1s}), b_{1rs} (c_{1r}), b_{1all} (c_{1u}), V_S (V_{30})	$5.5 \le M_W \le 7.5$, $r_{jb} \le 80$ km
Campbell and Bozorgnia (2003)	WNA (Empirical)	Compressional Extensional	0.250 0.200	H, V	PGA, 0.05 – 4.0	M_W, r_{seis}, r_{jb}, F_{RV}, F_{TH}, S_{VFS}, S_{SR}, S_{FR}, HW	$4.7 \le M_W \le 8.0$, $r_{rup} \le 100$ km
Sadigh et al. (1993, 1997)	WNA (Empirical)	Compressional Extensional	0.250 0.200	H, V	PGA, 0.07 – 4.0	M (M_W), r_{rup}, (F), (S_{Soil})	$4.0 \le M_W \le 8.0$, $r_{rup} \le 100$ km
Spudich et al. (1999)	WNA (Empirical)	Extensional	0.200	H	PGA, 0.10 – 2.0	M (M_W), r_{jb}, Γ (S_{Soil})	$5.0 \le M_W \le 7.7$, $r_{jb} \le 100$ km
Atkinson and Boore (1995, 1997)	ENA (Stochastic)	Background Faults	0.286 0.250	H	PGA, 0.10 – 1.0	M (M_W), r_{hypo}, (S_{Deep})	$4.0 \le M_W \le 8.2$, $10 \le r_{hypo} \le 1000$ km[c]
Campbell (2001, 2003c)	ENA (Hybrid Empirical)	Background Faults	0.143 0.125	H	PGA, 0.02 – 4.0	M_W, r_{rup}	$5.0 \le M_W \le 8.2$, $r_{rup} \le 1000$ km
Frankel et al. (1996)	ENA (Stochastic)	Background Faults	0.286 0.250	H	PGA, 0.1 – 2.0	M (M_W), R (r_{hypo})	$4.4 \le M_W \le 8.2$, $10 \le r_{hypo} \le 1000$ km
Toro et al. (1997)	ENA (Stochastic)	Background Faults	0.286 0.250	H	PGA, 0.03 – 2.0	M (M_W), r_{jb}	$4.5 \le M_W \le 8.0$, $1 \le r_{jb} \le 500$ km
Somerville et al. (2001)	ENA (Kinematic)	Faults	0.125	H, V	PGA, 0.04 – 4.0	M (M_W), r (r_{jb})	$6.0 \le M_W \le 7.5$, $r_{jb} \le 500$ km
Youngs et al. (1997)	Cascadia S. Z. (Empirical)	Interface Intraslab	0.5 – 1[a] 0.500	H	PGA, 0.08 – 3.0	M (M_W), r_{rup}, H (h_{hypo}), Z_T (z_t), (S_{Soil})	$5.0 \le M_W \le 8.2$, $10 \le r_{rup} \le 500$ km
Sadigh et al. (1997)	Cascadia S. Z. (Empirical)	Interface	0.5 – 0[a]	H	PGA, 0.08 – 3.0	M (M_W), r_{rup}, (F), (S_{Soil})	$4.0 \le M_W \le 8.0$, $r_{rup} \le 100$ km
Atkinson and Boore (2003)	Cascadia S. Z. (Empirical)	Intraslab: Global Intraslab: Cascadia	0.250 0.250	H	PGA, 0.04 – 3.0	M (M_W), D_{fault} (r_{rup}), h (h_{hypo}), sl ($f_3(A_B)$), PGA_{rx}, S_C, S_D, S_E	$5.5 \le M_W \le 8.3$, $10 \le r_{rup} \le 300$ km

[a] Weights linearly range between values shown from r_{rup} = 55–85 km for the M_W = 8.3 scenario and from r_{rup} = 45–75 km for the M_W = 9.0 scenario.

[b] Parameters in parentheses are alternative notation used in this chapter.

[c] Limits increased by D. Boore (personal communication, 2002) for use in the 2002 USGS national seismic hazard maps.

TABLE 5.5 ENA Ground Motion Caps and NEHRP B-C Boundary Adjustment Factors

Period (sec)	Ground Motion Caps (g)[a]		Adjustment Factors
	Median	Upper Tail	
PGA	1.5	3.0	1.52
0.1	3.0	6.0	1.74
0.2	3.0	6.0	1.76
0.3	3.0	6.0	1.72
0.5	3.0	6.0	1.58
1.0	—	—	1.34
2.0	—	—	1.20

[a]Caps are applied after applying the adjustment factors.

TABLE 5.6 Faulting Mechanism Categories Used in the WNA and Cascadia Subduction Zone Ground Motion Relations

Ground Motion Relation	Faulting Category [a]	F	F_{RV}	F_{TH}	Rake, λ [b]
Abrahamson and Silva (1997)	*Strike slip*	0	—	—	0–30°, 150–210°, 330–360°
	Normal	0	—	—	210–330°
	Reverse-oblique	0.5	—	—	30–60°, 120–150°
	Reverse	1.0	—	—	60–120°
	Unknown, random	0.5	—	—	Unknown or random rake
Boore et al. (1997)	*Strike slip*	c_{1s}	—	—	0–30°, 150–210°, 330–360°
	Normal	c_{1s}	—	—	210–330°
	Reverse	c_{1r}	—	—	30–150°
	Unknown, random	c_{1u}	—	—	Unknown or random rake
Campbell and Bozorgnia (2003)	*Strike slip*	—	0	0	0–22.5°, 157.5–202.5°, 337.5–360°
	Normal	—	0	0	202.5–337.5°
	Reverse	—	1.0	0	22.5–157.5° ($\delta > 45°$)
	Thrust	—	0	1.0	22.5–157.5° ($\delta \leq 45°$)
	Reverse or Thrust	—	0.5	0.5	Unknown or random dip
	Unknown, random	—	0.25	0.25	Unknown or random rake
Sadigh et al. (1993, 1997) WNA	*Strike slip*	0	—	—	0–45°, 135–225°, 315–360°
	Normal	0	—	—	225–315°
	Reverse	1.0	—	—	45–135°
	Unknown, random	0.5	—	—	Unknown or random rake
Sadigh et al. (1993, 1997) (Cascadia S. Z. interface)	Strike slip	0	—	—	0–45°, 135–225°, 315–360°
	Normal	0	—	—	225–315°
	Reverse	1.0	—	—	45–135°
	Unknown, random	0.5	—	—	Unknown or random rake
Spudich et al. (1999)	Strike slip	—	—	—	0–45°, 135–225°, 315–360°
	Normal	—	—	—	225–315°

[a] Faulting categories used in the 2002 USGS national seismic hazard maps are given in italics.
[b] Based on the convention of Lay and Wallace (1995).

Table 5.7 lists the site categories used in each of the ground motion relations. These categories are defined in terms of the values of the specified site parameters, which in turn are approximately related to an average or preferred value of 30-m velocity and a corresponding NEHRP site category. Two sets of NEHRP site categories are given, one originally defined for use in the building codes and one defined by the CGS (Wills et al., 2000), which differ from the former in the specific use of boundary site categories (see Section 5.4.2.5 and Table 5.3). The CGS's NEHRP classification has been extended to include the A and A-B boundary site categories in Table 5.7 for applications outside of California. The site parameters are given in terms of the alternative notation used in the Appendix A published on the accompanying Internet site and in

TABLE 5.7 Site Categories Used in the Ground Motion Relations

Ground Motion Relation	Site Category[a]	Site Parameter									V_{30} (m/s)[b]	NEHRP Site Class		Adjustment Factors for BC[c]
		S_{soil}	S_{VFS}	S_{SR}	S_{FR}	S_{deep}	S_C	S_D	S_E	V_{30}		Code	CGS	
Abrahamson and Silva (1997)	*Generic rock*	0	—	—	—	—	—	—	—	—	620	C	C	1.0
	Generic soil	1.0	—	—	—	—	—	—	—	—	310	D	D	—
Boore et al. (1997)	*30-m velocity*	—	—	—	—	—	—	—	—	760	All	All	All	1.0
Campbell and Bozorgnia (2003)	Firm soil	—	0	0	0	—	—	—	—	—	298	D	D	—
	Very firm soil	—	1.0	0	0	—	—	—	—	—	368	C	CD	—
	Soft rock	—	0	1.0	0	—	—	—	—	—	421	C	CD	—
	Firm rock	—	0	0	1.0	—	—	—	—	—	830	B	BC	—
	Generic rock	—	0	0.5	0.5	—	—	—	—	—	620	C	C	Exp(0.204 c6)
	Generic soil	—	0.25	0	0	—	—	—	—	—	310	D	D	—
Sadigh et al. (1997)	*Generic rock*	0	—	—	—	—	—	—	—	—	620	C	C	1.0
	Generic soil	1.0	—	—	—	—	—	—	—	—	310	D	D	—
Spudich et al. (1999)	Generic rock	0	—	—	—	—	—	—	—	—	760	B	BC	1.0
	Generic soil	1.0	—	—	—	—	—	—	—	—	310	D	D	—
Atkinson and Boore (1995, 1997)	Very hard rock	—	—	—	—	0	—	—	—	—	2800	A	A	—
	Firm rock (BC)[d]	—	—	—	—	—	—	—	—	—	760	B	BC	1.0
	Deep stiff soil	—	—	—	—	1.0	—	—	—	—	500	C	C	—
Campbell (2001, 2003c)	*Very hard rock*	—	—	—	—	—	—	—	—	—	2800	A	A	See Table 5.5
Frankel et al. (1996)	*Firm rock (BC)*	—	—	—	—	—	—	—	—	—	760	B	BC	1.0
Toro et al. (1997)	*Very hard rock*	—	—	—	—	—	—	—	—	—	2800	A	A	See Table 5.5
Somerville et al. (2001)	*Very hard rock*	—	—	—	—	—	—	—	—	—	2800	A	A	See Table 5.5
Youngs et al. (1997)	*Generic rock*	0	—	—	—	—	—	—	—	—	620	C	C	1.0
	Generic soil	1.0	—	—	—	—	—	—	—	—	310	D	D	—
Sadigh et al. (1997)	*Generic rock*	0	—	—	—	—	—	—	—	—	620	C	C	1.0
	Generic soil	1.0	—	—	—	—	—	—	—	—	310	D	D	—
Atkinson and Boore (2003)	NEHRP B	—	—	—	—	—	0	0	0	—	1130	B	B	—
	NEHRP BC[e]	—	—	—	—	—	0.5	0	0	—	760	B	BC	1.0
	NEHRP C	—	—	—	—	—	1.0	0	0	—	560	C	C	—
	NEHRP D	—	—	—	—	—	0	1.0	0	—	270	D	D	—
	NEHRP E	—	—	—	—	—	0	0	1.0	—	150	E	E	—

[a] Site categories used in the 2002 USGS national seismic hazard maps to evaluate the ground motion relations for the NEHRP B-C boundary are given in Italics. [b]Value of V_{30} that best represents the given site category in the judgment of the writers. [c]Additional multiplicative factors used by the USGS to adjust ground motions to the B-C boundary (V_{30} = 760 m/sec) in the 2002 USGS national seismic hazard maps: Campbell and Bozorgnia (2003) adjustments are based on the site term of Boore et al. (1997), where the coefficient c_6, denoted b_v by Boore et al. Is the period-dependent regression coefficient given in the Supplement on the accompanying Internet site and in the compilations of Campbell (2003a, 2003b, 2003d); Adjustment factors for very hard rock are from Frankel et al. (1996) and are listed in Table 5.5. [d] Category added by D. Boore (personal communication, 2002) for use in 2002 USGS national seismic hazard maps. [e]Recommended by G. Atkinson (personal communication, 2002) for use in 2002 USGS national seismic hazard maps.

Campbell (2003a, 2003b, 2003d). They can be related to the site parameters originally defined by the authors of the relations using Table 5.4. The relationship between each site category and V_{30} is admittedly crude, but useful, because V_{30} is the only site parameter that corresponds to a physically quantifiable attribute of a profile's site-response characteristics. For those ENA ground motion relations listed in Table 5.7 that predict ground motion on very hard rock ($V_{30} = 2800$ m/sec), the USGS adjusted them to the NEHRP B-C boundary ($V_{30} = 760$ m/sec) using the adjustment factors given in Table 5.5 (Frankel et al. 1996, 2000, 2002).

The specific site categories used by the USGS to evaluate the WNA ground motion relations for the NEHRP B-C Boundary are, in some cases, inconsistent with the estimated values of V_{30} that correspond to these site categories. This apparent bias was introduced either at the suggestion of the authors of the relations or by default (e.g., when there was insufficient evidence to the contrary [Frankel et al. 2002]). At least in one case, the coauthors themselves disagree as to an appropriate value of V_{30}. For example, W. Silva (personal communication, 2002) believes that the average value of V_{30} is around 510 m/sec for sites classified as generic rock in the Abrahamson and Silva (1997) ground motion relation; whereas, N. Abrahamson (personal communication, 2002) believes that this value lies somewhere between 510 and 760 m/sec, the value assumed by the USGS at his suggestion. B. Youngs (personal communication, 2002) believes that the average value of V_{30} for sites classified as generic rock in the Sadigh et al (1993, 1997) ground motion relations is in the upper range that defines NEHRP C, much less than the 760 m/sec value assumed by the USGS at his suggestion. An independent assessment by Choi and Stewart (2003) indicates that the lower V_{30} values originally recommended by W. Silva and B. Youngs appear to be consistent with the generic rock sites used by both the Abrahamson and Silva (1997) and Sadigh et al (1993, 1997) relations. Because of this controversy, unless there is evidence to the contrary, the average value of V_{30} for generic soil and generic rock should be taken as 310 and 620 m/sec, respectively (Table 5.7), consistent with the recommendation of Boore and Joyner (1997). There is a project currently under way by the Pacific Engineering Research Center (PEER) Lifelines Program (http://peer.berkeley.edu) that will hopefully resolve the ambiguities noted above. The purpose of that project is to compile a comprehensive strong-motion database and to have several WNA ground-motion experts, including those listed in Table 5.4, develop the next generation of WNA ground motion relations. These new relations will redefine the state-of-the-practice and will no doubt be used in future updates of the USGS hazard maps.

5.4.4.2 Example Relations for WNA, ENA and Cascadia S. Z.

It is not possible to present the equations for all of the ground motion relations used in the 2002 USGS hazard maps discussed in this chapter. Instead, three relations representing the three major tectonic environments in the United States are presented. These are the Campbell and Bozorgnia (2003) relation, representing WNA, the Campbell (2001, 2003c) relation, representing ENA and the Youngs et al. (1997) relation, representing Cascadia S. Z interface and intraslab events. The remaining ground motion relations are given in Appendix A of this chapter on the accompanying Internet site and are discussed extensively in Campbell (2003a, 2003b, 2003d).

The WNA ground motion relation of Campbell and Bozorgnia (2003) is given by the equation

$$\ln Y = c_1 + f_1(M_W) + f_2(M_W, r_{seis}, S) + f_3(F) + f_4(S) + f_5(HW, M_W, r_{seis}) \tag{5.31}$$

where magnitude scaling is given by the function

$$f_1(M_W) = c_2 M_W + c_3 (8.5 - M_W)^2 , \tag{5.32}$$

distance scaling and near-source (nonlinear) site response is given by the functions

$$f_2(M_W, r_{seis}, S) = c_4 \ln R , \tag{5.33}$$

$$R = \sqrt{r_{seis}^2 + g(S)^2\left(\exp[c_5 M_W + c_6(8.5 - M_W)^2]\right)^2}\,, \tag{5.34}$$

$$g(S) = c_7 + c_8(S_{VFS} + S_{SR}) + c_9 S_{FR}\,, \tag{5.35}$$

the effects of faulting mechanism are given by the function

$$f_3(F) = c_{10}F_{RV} + c_{11}F_{TH}\,, \tag{5.36}$$

far-source (linear) site response is given by the function

$$f_4(S) = c_{12}S_{VFS} + c_{13}S_{SR} + c_{14}S_{FR}\,, \tag{5.37}$$

and hanging-wall effects are given by the functions

$$f_5(HW, M_W, r_{seis}) = HW\, f_3(F) f_{HW}(M_W) f_{HW}(r_{seis})\,, \tag{5.38}$$

$$HW = \begin{cases} 0 & r_{jb} \geq 5 \text{ km or } \delta > 70^\circ \\ (S_{VFS} + S_{SR} + S_{FR})(5 - r_{jb})/5 & r_{jb} < 5 \text{ km and } \delta \leq 70^\circ \end{cases} \tag{5.39}$$

$$f_{HW}(M_W) = \begin{cases} 0 & M_W < 5.5 \\ M_W - 5.5 & 5.5 \leq M_W \leq 6.5 \\ 1 & M_W > 6.5 \end{cases}, \tag{5.40}$$

$$f_{HW}(r_{seis}) = \begin{cases} c_{15}(r_{seis}/8) & r_{seis} < 8 \text{ km} \\ c_{15} & r_{seis} \geq 8 \text{ km} \end{cases}. \tag{5.41}$$

In these equations, Y is either the average horizontal or vertical component of PGA or 5%-damped S_a (g), M_W is moment magnitude, r_{seis} is the closest distance to the seismogenic part of the rupture plane (km) and r_{jb} is the closest distance to the surface projection of the rupture plane (km). The faulting mechanism parameters, F_{RV} and F_{TH}, are defined in Table 5.6 and the site parameters, S_{VFS}, S_{SR} and S_{FR}, are defined in Table 5.7. The hanging-wall parameter, HW, which quantifies the geometric and associated effects related to the hanging wall, evaluates to zero for firm soil site conditions, for $r_{jb} \geq 5$ km, or for a fault dipping greater than 70°. A more detailed definition of these parameters can be found in Section 5.4.2

The standard deviation of $\ln Y$ is defined as a function of magnitude according to the expression

$$\sigma_{\ln Y} = \begin{cases} c_{16} - 0.07M_W & M_W < 7.4 \\ c_{16} - 0.518 & M_W \geq 7.4 \end{cases}, \tag{5.42}$$

or as a function of PGA according to the expression

$$\sigma_{\ln Y} = \begin{cases} c_{17} + 0.351 & \text{PGA} \le 0.07g \\ c_{17} - 0.132 \ln \text{PGA} & 0.07g < \text{PGA} < 0.25g \\ c_{17} + 0.183 & \text{PGA} \ge 0.25g \end{cases} . \tag{5.43}$$

The magnitude-dependent version of the standard deviation was used in the development of the 2002 USGS hazard maps. The authors of the relation, however, prefer the PGA-dependent version. The regression coefficients of this ground motion relation are listed in Table 5.8. The relation is considered to be valid for $4.7 \le M_W \le 8.0$ and $r_{seis} \le 100$ km. Guidance on setting the faulting mechanism and site parameters is given in Tables 5.6 and 5.7. Figure 5.26 compares the spectral accelerations predicted by this relation with those predicted by the other WNA relations listed in Table 5.4.

The ENA ground motion relation of Campbell (2001, 2003c) is given by the equation

$$\ln Y = c_1 + f_1(M_W) + f_2(M_W, r_{rup}) + f_3(r_{rup}) \tag{5.44}$$

where magnitude scaling is given by the function

$$f_1(M_W) = c_2 M_W + c_3 (8.5 - M_W)^2 , \tag{5.45}$$

and distance scaling is given by the functions

$$f_2(M_W, r_{rup}) = c_4 \ln R + (c_5 + c_6 M_W) r_{rup} , \tag{5.46}$$

$$R = \sqrt{r_{rup}^2 + [c_7 \exp(c_8 M_W)]^2} , \tag{5.47}$$

$$f_3(r_{rup}) = \begin{cases} 0 & r_{rup} \le 70 \text{ km} \\ c_9 (\ln r_{rup} - \ln 70) & 70 < r_{rup} \le 130 \text{ km} \\ c_9 (\ln r_{rup} - \ln 70) + c_{10} (\ln r_{rup} - \ln 130) & r_{rup} > 130 \text{ km} \end{cases} . \tag{5.48}$$

The standard deviation of $\ln Y$ is defined as a function of magnitude according to the expression

$$\sigma_{\ln Y} = \begin{cases} c_{11} + c_{12} M_W & M_W < 7.16 \\ c_{13} & M_W \ge 7.16 \end{cases} . \tag{5.49}$$

In these equations, Y is the average horizontal component of PGA or 5%-damped S_a (g), r_{rup} is the closest distance to the rupture plane (km), and all of the other parameters are as defined previously. The regression coefficients of this relation are listed in Table 5.9. The relation is considered to be valid for $5.0 \le M_W \le 8.2$ and $0 \le r_{rup} \le 1000$ km, but the WNA empirical database on which it is based is restricted to earthquakes up to about magnitude 7.5 and distances up to about 100 km. The relation can be realistically extrapolated to larger magnitudes and distances because of its physically based functional form and its seismologically constrained geometric and anelastic attenuation. The relation predicts ground motion for very hard rock typical of glacially scoured cratonic shield areas of ENA (Table 5.7). Figure 5.27 compares the spectral accelerations predicted by this relation with those predicted by the other ENA relations listed in Table 5.4.

The subduction-zone ground motion relation of Youngs et al. (1997) is given by the equation

TABLE 5.8 Coefficients for the WNA Ground Motion Relation

T (s)	c_1	c_2	c_3	c_4	c_5	c_6	c_7	c_8	c_9	c_{10}	c_{11}	c_{12}	c_{13}	c_{14}	c_{15}	c_{16}	c_{17}
Average Horizontal Component																	
PGA	–4.033	0.812	0.036	–1.061	0.766	0.034	0.041	–0.005	–0.018	0.343	0.351	–0.123	–0.138	–0.289	0.370	0.920	0.219
0.05	–3.740	0.812	0.036	–1.121	0.724	0.032	0.058	–0.004	–0.028	0.302	0.362	–0.140	–0.158	–0.205	0.370	0.940	0.239
0.075	–3.076	0.812	0.050	–1.252	0.648	0.040	0.121	–0.005	–0.051	0.243	0.333	–0.150	–0.196	–0.208	0.370	0.952	0.251
0.10	–2.661	0.812	0.060	–1.308	0.621	0.046	0.166	–0.009	–0.068	0.224	0.313	–0.146	–0.253	–0.258	0.370	0.958	0.257
0.15	–2.270	0.812	0.041	–1.324	0.613	0.031	0.212	–0.033	–0.081	0.318	0.344	–0.176	–0.267	–0.284	0.370	0.974	0.273
0.20	–2.771	0.812	0.030	–1.153	0.704	0.026	0.098	–0.014	–0.038	0.296	0.342	–0.148	–0.183	–0.359	0.370	0.981	0.280
0.30	–2.999	0.812	0.007	–1.080	0.752	0.007	0.059	–0.007	–0.022	0.359	0.385	–0.162	–0.157	–0.585	0.370	0.984	0.283
0.40	–3.511	0.812	–0.015	–0.964	0.842	–0.016	0.024	–0.002	–0.005	0.379	0.438	–0.078	–0.129	–0.557	0.370	0.987	0.286
0.50	–3.556	0.812	–0.035	–0.964	0.842	–0.036	0.023	–0.002	–0.004	0.406	0.479	–0.122	–0.130	–0.701	0.370	0.990	0.289
0.75	–3.709	0.812	–0.071	–0.964	0.842	–0.074	0.021	–0.002	–0.002	0.347	0.419	–0.108	–0.124	–0.796	0.331	1.021	0.320
1.0	–3.867	0.812	–0.101	–0.964	0.842	–0.105	0.019	0	0	0.329	0.338	–0.073	–0.072	–0.858	0.281	1.021	0.320
1.5	–4.093	0.812	–0.150	–0.964	0.842	–0.155	0.019	0	0	0.217	0.188	–0.079	–0.056	–0.954	0.210	1.021	0.320
2.0	–4.311	0.812	–0.180	–0.964	0.842	–0.187	0.019	0	0	0.060	0.064	–0.124	–0.116	–0.916	0.160	1.021	0.320
3.0	–4.817	0.812	–0.193	–0.964	0.842	–0.200	0.019	0	0	–0.079	0.021	–0.154	–0.117	–0.873	0.089	1.021	0.320
4.0	–5.211	0.812	–0.202	–0.964	0.842	–0.209	0.019	0	0	–0.061	0.057	–0.054	–0.261	–0.889	0.039	1.021	0.320
Vertical Component																	
PGA	–3.108	0.756	0	–1.287	0.587	0	0.142	0.046	–0.040	0.253	0.173	–0.135	–0.138	–0.256	0.630	0.975	0.274
0.05	–1.918	0.756	0	–1.517	0.498	0	0.309	0.069	–0.023	0.058	0.100	–0.195	–0.274	–0.219	0.630	1.031	0.330
0.075	–1.504	0.756	0	–1.551	0.487	0	0.343	0.083	0.000	0.135	0.182	–0.224	–0.303	–0.263	0.630	1.031	0.330
0.10	–1.672	0.756	0	–1.473	0.513	0	0.282	0.062	0.001	0.168	0.210	–0.198	–0.275	–0.252	0.630	1.031	0.330
0.15	–2.323	0.756	0	–1.280	0.591	0	0.171	0.045	0.008	0.223	0.238	–0.170	–0.175	–0.270	0.630	1.031	0.330
0.20	–2.998	0.756	0	–1.131	0.668	0	0.089	0.028	0.004	0.234	0.256	–0.098	–0.041	–0.311	0.571	1.031	0.330
0.30	–3.721	0.756	0.007	–1.028	0.736	0.007	0.050	0.010	0.004	0.249	0.328	–0.026	0.082	–0.265	0.488	1.031	0.330
0.40	–4.536	0.756	–0.015	–0.812	0.931	–0.018	0.012	0	0	0.299	0.317	–0.017	0.022	–0.257	0.428	1.031	0.330
0.50	–4.651	0.756	–0.035	–0.812	0.931	–0.043	0.012	0	0	0.243	0.354	–0.020	0.092	–0.293	0.383	1.031	0.330
0.75	–4.903	0.756	–0.071	–0.812	0.931	–0.087	0.012	0	0	0.295	0.418	0.078	0.091	–0.349	0.299	1.031	0.330
1.0	–4.950	0.756	–0.101	–0.812	0.931	–0.124	0.012	0	0	0.266	0.315	0.043	0.101	–0.481	0.240	1.031	0.330
1.5	–5.073	0.756	–0.150	–0.812	0.931	–0.184	0.012	0	0	0.171	0.211	–0.038	–0.018	–0.518	0.240	1.031	0.330
2.0	–5.292	0.756	–0.180	–0.812	0.931	–0.222	0.012	0	0	0.114	0.115	0.033	–0.022	–0.503	0.240	1.031	0.330
3.0	–5.748	0.756	–0.193	–0.812	0.931	–0.238	0.012	0	0	0.179	0.159	–0.010	–0.047	–0.539	0.240	1.031	0.330
4.0	–6.042	0.756	–0.202	–0.812	0.931	–0.248	0.012	0	0	0.237	0.134	–0.059	–0.267	–0.606	0.240	1.031	0.330

Source: Adapted from Campbell, K.W. and Bozorgnia, Y. (2003). Updated near-source ground motion (attenuation) relations for the horizontal and vertical components of PGA and acceleration response spectra. *Bulletin of the Seismological Society of America*, 93, 314–331.

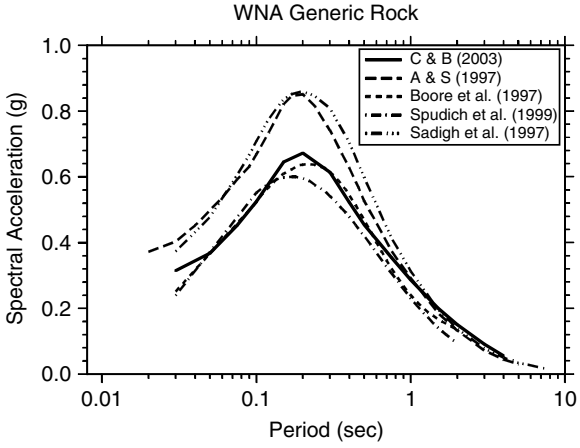

FIGURE 5.26 Comparison of 5%-damped pseudo-acceleration (S_a) response spectra predicted by the *WNA ground motion relations* listed in Table 5.4. The relations are evaluated for $M_W = 7$, $r_{jb} = r_{rup} = 10$ km, $r_{seis} = 10.4$ km ($d_s = 3$ km), strike-slip faulting, and generic rock site conditions (see Tables 5.6 and 5.7). PGA is plotted at 0.03-sec period. A & S (1997) refers to Abrahamson and Silva (1997) and C & B (2003) refers to Campbell and Bozorgnia (2003).

TABLE 5.9 Coefficients for the ENA Ground Motion Relation

T(s)	c_1	c_2	c_3	c_4	c_5	c_6	c_7	c_8	c_9	c_{10}	c_{11}	c_{12}	c_{13}
0.01	0.0305	0.633	–0.0427	–1.591	–0.00428	0.000483	0.683	0.416	1.140	–0.873	1.030	–0.0860	0.414
0.02	1.3535	0.630	–0.0404	–1.787	–0.00388	0.000497	1.020	0.363	0.851	–0.715	1.030	–0.0860	0.414
0.03	1.1860	0.622	–0.0362	–1.691	–0.00367	0.000501	0.922	0.376	0.759	–0.922	1.030	–0.0860	0.414
0.05	0.3736	0.616	–0.0353	–1.469	–0.00378	0.000500	0.630	0.423	0.771	–1.239	1.042	–0.0838	0.443
0.075	–0.0395	0.615	–0.0353	–1.383	–0.00421	0.000486	0.491	0.463	0.955	–1.349	1.052	–0.0838	0.453
0.10	–0.1475	0.613	–0.0353	–1.369	–0.00454	0.000460	0.484	0.467	1.096	–1.284	1.059	–0.0838	0.460
0.15	–0.1901	0.616	–0.0478	–1.368	–0.00473	0.000393	0.461	0.478	1.239	–1.079	1.068	–0.0838	0.469
0.20	–0.4328	0.617	–0.0586	–1.320	–0.00460	0.000337	0.399	0.493	1.250	–0.928	1.077	–0.0838	0.478
0.30	–0.6906	0.609	–0.0786	–1.280	–0.00414	0.000263	0.349	0.502	1.241	–0.753	1.081	–0.0838	0.482
0.50	–0.5907	0.534	–0.1379	–1.216	–0.00341	0.000194	0.318	0.503	1.166	–0.606	1.098	–0.0824	0.508
0.75	–0.5429	0.480	–0.1806	–1.184	–0.00288	0.000160	0.304	0.504	1.110	–0.526	1.105	–0.0806	0.528
1.0	–0.6104	0.451	–0.2090	–1.158	–0.00255	0.000141	0.299	0.503	1.067	–0.482	1.110	–0.0793	0.543
1.5	–0.9666	0.441	–0.2405	–1.135	–0.00213	0.000119	0.304	0.500	1.029	–0.438	1.099	–0.0771	0.547
2.0	–1.4306	0.459	–0.2552	–1.124	–0.00187	0.000103	0.310	0.499	1.015	–0.417	1.093	–0.0758	0.551
3.0	–2.2331	0.492	–0.2646	–1.121	–0.00154	0.000084	0.310	0.499	1.014	–0.393	1.090	–0.0737	0.562
4.0	–2.7975	0.507	–0.2738	–1.119	–0.00135	0.000074	0.294	0.506	1.018	–0.386	1.092	–0.0722	0.575

Source: Adapted from Campbell, K.W. (2001). Development of semi-empirical attenuation relationships for CEUS. U.S. Geological Survey, *Award 01HQGR0011*, final report; and from Campbell, K.W. (2003). Prediction of strong ground motion using the hybrid empirical method and its use in the development of ground motion (attenuation) relations in eastern North America. *Bulletin of the Seismological Society of America*, 93, 1012–1033.

$$\ln Y = c_1 + f_1(M_W) + f_2(M_W, r_{rup}, h_{hypo}) + f_3(z_T) \tag{5.50}$$

where magnitude scaling is given by the function

$$f_1(M_W) = c_2 M_W + c_3 (10 - M_W)^3 , \tag{5.51}$$

distance and depth scaling are given by the functions

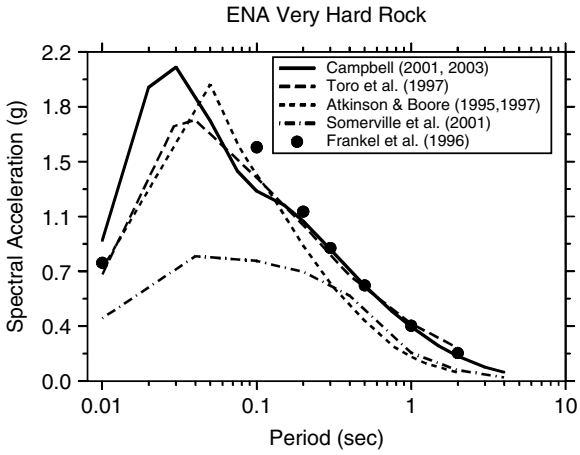

FIGURE 5.27 Comparison of 5%-damped pseudo-acceleration (S_a) response spectra predicted by the *ENA ground motion relations* listed in Table 5.4. The relations are evaluated for $M_W = 7$, $r_{jb} = r_{rup} = 10$ km, $r_{hypo} = 14.1$ km ($h_{hypo} = 10$ km), and very hard rock site conditions (see Tables 5.6 and 5.7). PGA is plotted at 0.01 sec period. The values of PGA and spectral acceleration predicted by the Frankel et al. (1996) relation are divided by the factors given in Table 5.5 to adjust them from firm rock to very hard rock site conditions. The Frankel et al. relation is plotted as single spectral ordinates to emphasize the lack of spectral ordinates below 0.1 sec.

$$f_2(M_W, r_{rup}, h_{hypo}) = c_4 \ln R + c_5 h_{hypo}\,, \tag{5.52}$$

$$R = r_{rup} + c_6 \exp(c_7 M_W)\,, \tag{5.53}$$

and the type of event (interface or intraslab) is given by the function

$$f_3(z_T) = c_8 z_T. \tag{5.54}$$

The standard deviation is given as a function of magnitude according to the expression

$$\sigma_{\ln Y} = \begin{cases} c_9 + c_{10} M_W & M_W \le 8.0 \\ c_{11} & M_W > 8.0 \end{cases}. \tag{5.55}$$

In these equations, Y is the average horizontal component of PGA or 5%-damped S_a (g), h_{hypo} is focal depth (km), $z_T = 0$ for subduction interface events and 1 for subduction intraslab (intermediate-depth or Wadati-Benioff) events, and all of the other parameters are as defined previously. The regression coefficients of this relation are listed in Table 5.10. The authors of the relation do not explicitly state the range of magnitudes and distances for which they considered the relation to be valid, but the database is constrained to $5.0 \le M_W \le 8.2$ and $10 \le r_{rup} \le 500$ km. Nonetheless, the relation is used to evaluate ground motions for a M_W 9.0 earthquake on the Cascadia S. Z. in the 2002 USGS hazard maps. Figure 5.28 compares the spectral accelerations predicted by this relation with those predicted by the other subduction-zone relations listed in Table 5.4.

5.4.5 Effects of Near-Fault Directivity

5.4.5.1 Introduction

Under certain conditions, ground motions recorded at stations located near faults can exhibit two special characteristics: (a) fault rupture directivity or directivity pulse; and (b) a fling step (see Chapter 2). The fault rupture directivity can be either forward or backward. Forward rupture directivity occurs when the

TABLE 5.10 Coefficients for the Subduction-Zone Ground Motion Relation

T(s)	c_1	c_2	c_3	c_4	c_5	c_6	c_7	c_8	c_9	c_{10}	c_{11}
					Generic rock						
PGA	0.2418	1.414	0	–2.552	0.00617	1.7818	0.554	0.3846	1.45	–0.1	0.650
0.075	1.5168	1.414	0	–2.707	0.00617	1.7818	0.554	0.3846	1.45	–0.1	0.650
0.1	1.4298	1.414	–0.0011	–2.655	0.00617	1.7818	0.554	0.3846	1.45	–0.1	0.650
0.2	0.9638	1.414	–0.0027	–2.528	0.00617	1.7818	0.554	0.3846	1.45	–0.1	0.650
0.3	0.4878	1.414	–0.0036	–2.454	0.00617	1.7818	0.554	0.3846	1.45	–0.1	0.650
0.4	0.1268	1.414	–0.0043	–2.401	0.00617	1.7818	0.554	0.3846	1.45	–0.1	0.650
0.5	–0.1582	1.414	–0.0048	–2.360	0.00617	1.7818	0.554	0.3846	1.45	–0.1	0.650
0.75	–0.9072	1.414	–0.0057	–2.286	0.00617	1.7818	0.554	0.3846	1.45	–0.1	0.650
1.0	–1.4942	1.414	–0.0064	–2.234	0.00617	1.7818	0.554	0.3846	1.45	–0.1	0.650
1.5	–2.3922	1.414	–0.0073	–2.160	0.00617	1.7818	0.554	0.3846	1.50	–0.1	0.700
2.0	–3.0862	1.414	–0.0080	–2.107	0.00617	1.7818	0.554	0.3846	1.55	–0.1	0.750
3.0	–4.2692	1.414	–0.0089	–2.033	0.00617	1.7818	0.554	0.3846	1.65	–0.1	0.850
					Generic soil						
PGA	–0.6687	1.438	0	–2.329	0.00648	1.097	0.617	0.3648	1.45	–0.1	0.650
0.075	1.7313	1.438	–0.0019	–2.697	0.00648	1.097	0.617	0.3648	1.45	–0.1	0.650
0.1	1.8473	1.438	–0.0019	–2.697	0.00648	1.097	0.617	0.3648	1.45	–0.1	0.650
0.2	0.8803	1.438	–0.0019	–2.464	0.00648	1.097	0.617	0.3648	1.45	–0.1	0.650
0.3	0.1243	1.438	–0.0020	–2.327	0.00648	1.097	0.617	0.3648	1.45	–0.1	0.650
0.4	–0.5247	1.438	–0.0020	–2.230	0.00648	1.097	0.617	0.3648	1.45	–0.1	0.650
0.5	–1.1067	1.438	–0.0035	–2.140	0.00648	1.097	0.617	0.3648	1.45	–0.1	0.650
0.75	–2.3727	1.438	–0.0048	–1.952	0.00648	1.097	0.617	0.3648	1.45	–0.1	0.650
1.0	–3.5387	1.438	–0.0066	–1.785	0.00648	1.097	0.617	0.3648	1.45	–0.1	0.650
1.5	–5.7697	1.438	–0.0114	–1.470	0.00648	1.097	0.617	0.3648	1.50	–0.1	0.700
2.0	–7.1017	1.438	–0.0164	–1.290	0.00648	1.097	0.617	0.3648	1.55	–0.1	0.750
3.0	–7.3407	1.438	–0.0221	–1.347	0.00648	1.097	0.617	0.3648	1.65	–0.1	0.850
4.0	–8.2867	1.438	–0.0235	–1.272	0.00648	1.097	0.617	0.3648	1.65	–0.1	0.850

Source: Adapted from Youngs, R.R., Chiou, S.J., Silva, W.J. and Humphrey, J.R. (1997). Strong ground motion attenuation relationships for subduction zone earthquakes. *Seismological Research Letters*, 68, 58–73.

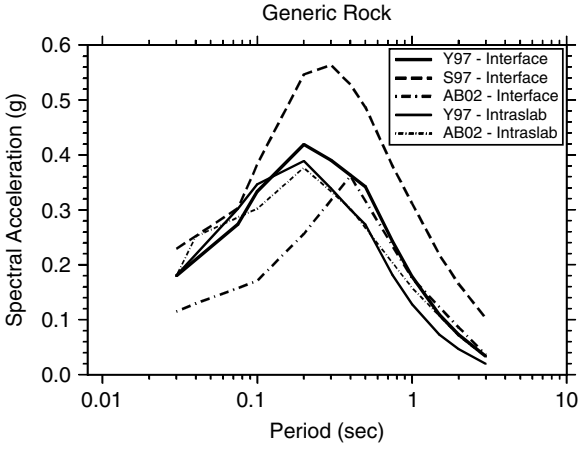

FIGURE 5.28 Comparison of 5%-damped pseudo-acceleration (S_a) response spectra predicted by the *subduction-zone ground motion relations* listed in Table 5.4. The relations are evaluated for M_W = 8.5, r_{rup} = 50 km, and h_{hypo} = 15 km for interface events (z_T = 0) and M_W =7, r_{rup} = 50 km, and h_{hypo} = 50 km for intraslab events (z_T = 1) for generic rock site conditions (see Tables 5.6 and 5.7). PGA is plotted at 0.03 sec period. Y97 refers to Youngs et al. (1997), S97 refers to Sadigh et al. (1997), evaluated for a reverse faulting mechanism, and AB02 refers to Atkinson and Boore (2003).

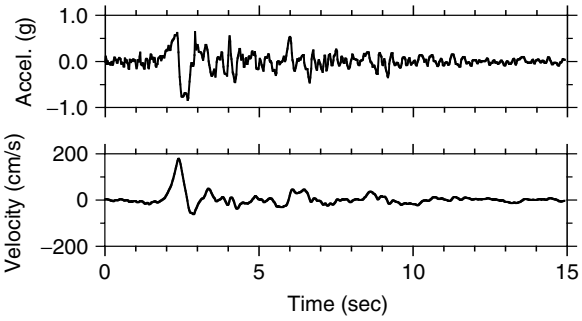

FIGURE 5.29 Recorded ground acceleration, and the computed velocity, from the 1994 Northridge, California, earthquake, Rinaldi Receiving Station (S48W component).

rupture front propagates toward the site and the direction of slip on the fault is aligned with the site (Somerville et al. 1997). Backward directivity occurs when rupture propagates away from the site. Forward directivity will cause a large long-period pulse on the strike-normal component of ground motion. The fling step occurs on the ground displacement component parallel to the fault slip direction and is associated with a permanent displacement of the ground (see Chapter 2).

Near-fault directivity pulses have been observed in numerous earthquakes, most notably the 1971 San Fernando, 1978 Tabas, 1992 Landers, 1994 Northridge, 1995 Kobe, 1999 Kocaeli and 1999 Chi-Chi events. The structural damage potential of such near-fault long-period pulses was first revealed by Bertero et al. (1978) and subsequently confirmed by recorded motions in other earthquakes (e.g., Anderson and Bertero, 1987; Hall et al. 1995; Bozorgnia and Mahin, 1998; Alavi and Krawinkler, 2001). Figure 5.29 shows an example of a strong near-fault pulse recorded in the 1994 Northridge earthquake at Rinaldi Receiving Station (CIT-SMART, 1996). It is evident from this figure that the pulse is associated with a very large ground velocity.

A seismological overview of source directivity and radiation pattern is given in Section 5.4.5.2 (see Chapter 2 for more details). In subsequent sections, the proposed modification of ground motion relations to include fault rupture directivity effects is presented and a brief discussion about engineering implications of near-fault records is provided.

5.4.5.2 Seismological Overview of Source Directivity and Radiation Pattern

Radiation pattern is the geographic asymmetry of the ground motion caused by the fault-rupture process. It is closely related to faulting mechanism. The radiation pattern can be perturbed by source directivity, which causes an increase or decrease in the ground motion as a result of the propagation of the rupture, analogous to the Doppler effect in sound. Ground-motion amplitudes in the forward direction of rupture propagation are increased while those in the backward direction are decreased as a result of source directivity. This effect is particularly important during unilateral faulting. The general concept of radiation pattern and source directivity is shown schematically in Figure 5.30. Source directivity has its largest positive effect on the long-period horizontal ground-motion component that is oriented perpendicular or normal to the rupture plane (the fault-normal or strike-normal component). A schematic showing the radiation pattern for a vertical strike-slip fault and its effect on the fault-normal and fault-parallel components of near-fault ground displacement is shown in Figure 5.31.

Source directivity is a well-known seismological property (Lay and Wallace, 1995) and has been observed or proposed as a factor in controlling the azimuthal dependence of strong ground motion during several past earthquakes (see discussions by Campbell, 2003a, 2003b, 2003d).

5.4.5.3 Modification of Ground Motion Relations for Source Directivity

Source directivity was not used directly in the development of the ground motion relations presented in Section 5.4.4. However, Somerville et al. (1997) and Abrahamson (2000) have developed a simple empir-

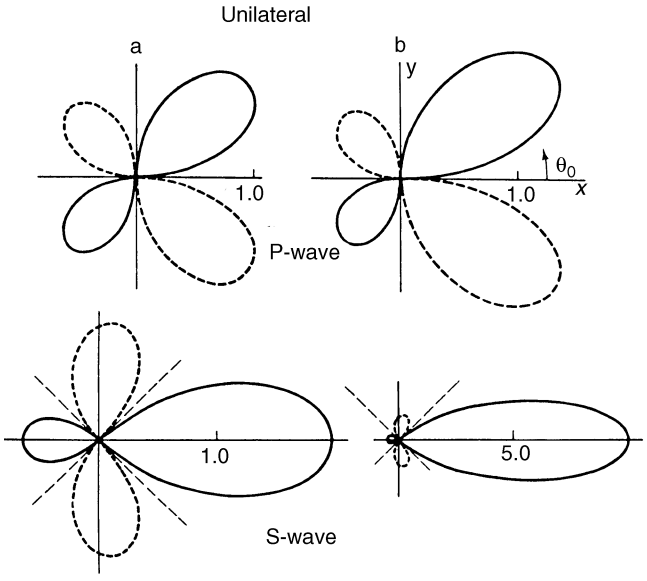

FIGURE 5.30 Radiation pattern showing the variability of compressional and horizontal shear-wave amplitude for a fault rupture propagating from left to right. The diagrams on the left are for a rupture propagation velocity of 0.5 times the shear-wave velocity of the crust and those on the right are for a rupture propagation velocity of 0.9 times the shear-wave velocity of the crust. The amplitude of the lobes represents the relative amplitude of ground motion. The larger lobes are an indication of rupture directivity. Rupture directivity increases with increasing rupture velocity (From Lay, T. and Wallace, T.C. (1995). *Modern Global Seismology*. Academic Press, San Diego. With permission.)

ically based engineering model that can be used to estimate the effects of source directivity and radiation pattern on the prediction of the fault-normal and fault-parallel components of spectral acceleration. Somerville et al. (1997) also provide a list of near-source time histories that contain significant directivity and other near-source effects that can be used in engineering practice.

It should be noted that Somerville (2000) suggests that the simple empirical models proposed by Somerville et al. (1997) and Abrahamson (2000) might be too simplistic. He has found that the near-fault directivity effects observed in recent earthquakes, including the 1999 Chi-Chi and 1999 Kocaeli events, appear to manifest themselves as narrow-band pulses, whose period increases with increasing magnitude. This increase in period with magnitude can actually lead to lower values of spectral acceleration at mid periods ($T \approx 1$ sec) for events of $M_W > 7\frac{1}{4}$. This observation is inconsistent with the assumption of monotonically increasing spectral amplitudes with magnitude that is the basis for the simple engineering model. However, the directivity pulse model needs more development before it can be used in engineering practice. Until then, the simple engineering model of Somerville et al. (1997) and Abrahamson (2000) presented below can be used to estimate rupture directivity effects.

Somerville et al. (1997) found that rupture directivity effects cause spatial variations in the radiation pattern, as well as differences between the fault-normal and fault-parallel components of horizontal ground motion. These effects are significant at periods of 0.6 sec and greater and generally increase in size with increasing period. Abrahamson (2000) found that there were several aspects of the spatial component of the Somerville et al. (1997) rupture directivity model that needed to be modified to make it more generally applicable for engineering practice, such as in probabilistic seismic hazard analysis (PSHA).

The proposed model for incorporating source directivity effects is given by

$$\ln Y_{Dir} = \ln Y + f_1(DR, \xi)T(r_{rup})T(M_W) + f_2(r_{rup}, M_W, \xi) \tag{5.56}$$

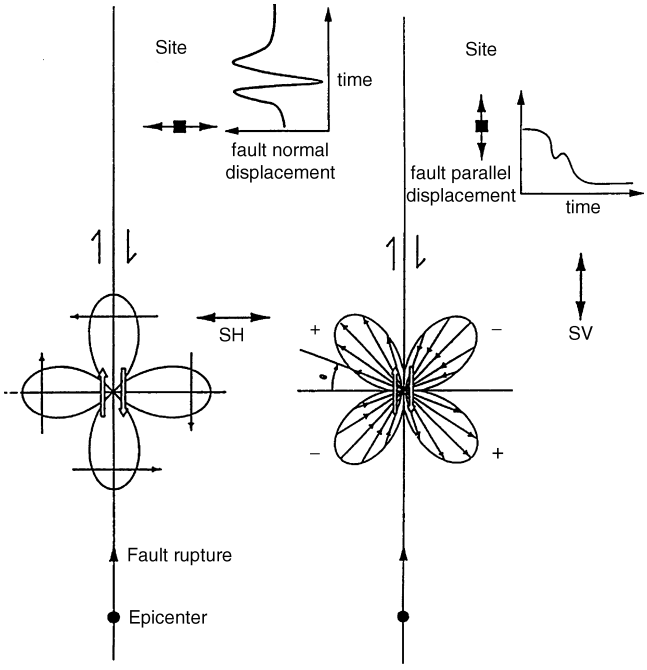

FIGURE 5.31 Radiation pattern for a vertical strike-slip fault showing its effect on the fault-normal and fault-parallel components of near-fault ground displacement. (From Somerville, P.G., Smith, N.F., Graves, R.W. and Abrahamson, N.A. (1997). Modification of empirical strong ground motion attenuation relations to include the amplitude and duration effects of rupture directivity. *Seismological Research Letters*, 68, 199–222.)

where Y is the average horizontal component of PGA or spectral acceleration with average directivity effects and Y_{Dir} is the value of Y with these effects explicitly taken into account, and where, for strike-slip faulting,

$$f_1(DR,\xi)=\begin{cases} c_1+1.88c_2(s/L)\cos(\theta) & \text{for } s/L\le 0.4 \\ c_1+0.75c_2\cos(\theta) & \text{for } s/L>0.4 \end{cases} \tag{5.57}$$

For dip-slip faulting,
$$f_1(DR,\xi)=c_1+c_2(d/W)\cos\phi \tag{5.58}$$

and where

$$f_2(r_{rup},M_W,\xi)=\begin{cases} \dfrac{1}{2}(\cos 2\xi)[c_3+c_4\ln(r_{rup}+1)+c_5(M_W-6)] & \text{for fault-normal} \\ -\dfrac{1}{2}(\cos 2\xi)[c_3+c_4\ln(r_{rup}+1)+c_5(M_W-6)] & \text{for fault-parallel} \\ 0 & \text{for } \xi\ge 45^\circ \end{cases} \tag{5.59}$$

$$T(r_{rup}) = \begin{cases} 1 & \text{for } r_{rup} \le 30 \text{ km} \\ 1-(r_{rup}-30)/30 & \text{for } 30 < r_{rup} < 60 \text{ km} \\ 0 & \text{for } r_{rup} \ge 60 \text{ km} \end{cases} \tag{5.60}$$

$$T(M_W) = \begin{cases} 1 & \text{for } M_W \ge 6.5 \\ 1-(6.5-M_W)/0.5 & \text{for } 6.0 < M_W < 6.5 \\ 0 & \text{for } M_W \le 6.0 \end{cases} \tag{5.61}$$

The standard deviation of the predicted strong-motion parameter when directivity effects are taken into account is calculated from the expression.

$$\sigma_{\ln Y,Dir} = \sigma_{\ln Y} - 0.05 c_2 / 1.333 \tag{5.62}$$

where $\sigma_{\ln Y,Dir}$ is the standard deviation of $\ln Y_{Dir}$ and $\sigma_{\ln Y}$ is the standard deviation of $\ln Y$.

In these equations, r_{rup} is the closest distance to the fault rupture plane (km); the length and width ratios, $DR = s/L$ and d/W, are defined as the fraction of fault rupture length, L, and fault rupture width, W, that ruptures toward the site for strike-slip faults and dip-slip faults, respectively, and $\xi = \theta$ and ϕ are the azimuth and zenith angles between the fault rupture plane and the ray path to the site for strike-slip and dip-slip faults, respectively. These parameters are defined schematically in Figure 5.32

The regression coefficients for the Somerville et al. (1997) and Abrahamson (2000) rupture directivity model are listed in Table 5.11. Note that in this table the values of c_1 and c_2 depend on the faulting

TABLE 5.11 Coefficients for the Source Directivity Model

	Strike Slip		Dip Slip				
T(s)	c_1	c_2	c_1	c_2	c_3	c_4	c_5
0.6	0	0	0	0	0.027	–0.0069	0
0.7	—	—	—	—	0.050	–0.0127	0
0.75	–0.084	0.185	–0.045	0.008	0.061	–0.0155	0
0.8	—	—	—	—	0.070	–0.0178	0
0.9	—	—	—	—	0.088	–0.0220	0
1.0	–0.192	0.423	–0.104	0.178	0.104	–0.0255	0
1.5	–0.344	0.759	–0.186	0.318	0.164	–0.0490	0.034
2.0	–0.452	0.998	–0.245	0.418	0.207	–0.0613	0.059
2.5	—	—	—	—	0.280	–0.0816	0.078
3.0	–0.605	1.333	–0.327	0.559	0.353	–0.1007	0.093
3.5	—	—	—	—	0.415	–0.1172	0.106
4.0	–0.713	1.571	–0.386	0.659	0.456	–0.1282	0.118
4.5	—	—	—	—	0.462	–0.1307	0.128
5.0	–0.797	1.757	–0.431	0.737	0.450	–0.1269	0.137
6.0	—	—	—	—	0.424	–0.1223	0.152

Source: Adapted from Somerville, P.G., Smith, N.F., Graves, R.W. and Abrahamson, N.A. (1997). Modification of empirical strong ground motion attenuation relations to include the amplitude and duration effects of rupture directivity. *Seismological Research Letters*, 68, 199–222; and from Abrahamson, N.A. (2000). Effects of rupture directivity on probabilistic seismic hazard analysis. *Proceedings, 6th International Conference on Seismic Zonation*, Palm Springs, California, 6 p.

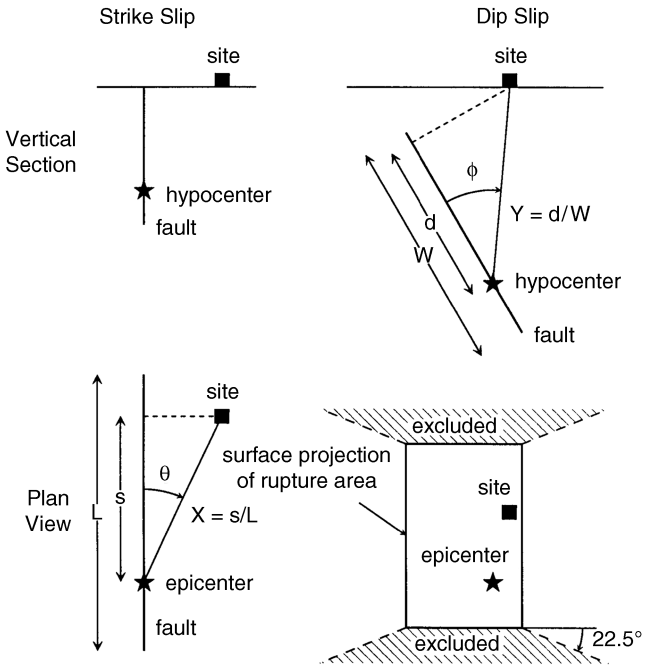

FIGURE 5.32 Definition of fault-rupture directivity parameters used in the engineering model of source directivity effects. (From Somerville, P.G., Smith, N.F., Graves, R.W., and Abrahamson, N.A. (1997). Modification of empirical strong ground motion attenuation relations to include the amplitude and duration effects of rupture directivity. *Seismological Research Letters*, 68, 199–222.)

mechanism, where dip slip is a generic term for reverse, thrust and normal faulting. According to this model, maximum spatial directivity effects for strike-slip faulting occur when $(s/L)\cos\theta = 0.4$, $M_W \geq 6.5$, and $r_{rup} \leq 30$ km and can result in an increase of up to 68% in the average horizontal component of 5-sec spectral acceleration. Minimum spatial directivity effects occur at this same period when $r_{rup} \leq 30$, $M_W \leq 6$, or $r_{rup} \geq 60$ km and can result in a 55% reduction in spectral acceleration. Maximum and minimum spatial directivity effects are smaller for dip-slip faulting for the same magnitudes, distances, and period, or about +36% when $(d/W)\cos(\phi) = 1$ and −35% when $(d/W)\cos(\phi) = 0$. Maximum fault-normal and fault-parallel effects occur at large magnitudes and long periods when $\theta = \phi = 0$. At 5 seconds, these effects can result in an increase of up to 39% in the fault-normal component of spectral acceleration and a decrease of up to 28% in the fault-parallel component of spectral acceleration when $M_W = 7.5$ and $r_{rup} = 0$ km. Because the spatial and fault-normal directivity effects are multiplicative, the total maximum positive directivity effects at 5 seconds can approach a factor of 2.3 for strike-slip faulting and a factor of 1.9 for dip-slip faulting.

5.4.5.4 Engineering Implications of Near-Fault Ground Motions

Fault rupture directivity pulses have important practical implications for the seismic design and analysis of civil engineering facilities. These near-fault pulses can cause very large inelastic deformation demands on a structure. For example, Figure 5.15(b) shows large displacement ductility demands over a relatively wide period range for the near-fault ground motion recorded at the Rinaldi Receiving Station from the Northridge earthquake. The effects of near-fault pulses on structures have been discussed by numerous investigators, including Bertero et al. (1978, 1999); Mahin and Bertero (1981); Anderson and Bertero (1987, 2002); Challa and Hall (1994); Iwan (1994, 1997); Hall et al. (1995); Bozorgnia and Mahin (1998); Malhotra (1999); Alavi and Krawinkler (2001); among others.

Pre-1997 editions of the *Uniform Building Code* (e.g., UBC, 1994) did not have provisions covering near-source effects for fixed-base structures. In fact, fixed-base structures located in the same seismic

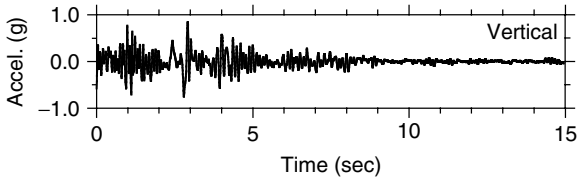

FIGURE 5.33 Vertical ground acceleration recorded in the 1994 Northridge, California, earthquake at Rinaldi Receiving Station.

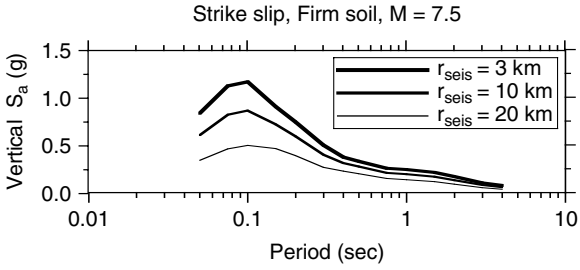

FIGURE 5.34 Median vertical acceleration response spectra for 5% damping and distances from seismogenic faulting of 3, 10, and 20 km. (Adapted from Campbell, K.W. and Bozorgnia, Y. (2003). Updated near-source ground motion (attenuation) relations for the horizontal and vertical components of PGA and acceleration response spectra. *Bulletin of the Seismological Society of America*, 93, 314–331.)

zone, with the same site category, were assigned the same elastic design spectrum, regardless of their proximity to active faults. If one wanted to take these effects into account, the only alternative was to develop a site-specific design spectrum. In the 1997 edition of the UBC, near-source factors were introduced in the main body of the code to increase the design base shear (or strength) of structures located within 15 km of active faults. The near-source elastic design spectra in the 1997 UBC are generally compatible with the average of the two horizontal components; however, this code does not specifically address the larger ground motion expected for the strike-normal component (Somerville, 1998).

A recent U.S. seismic code, the *International Building Code* (IBC, 2000), does not explicitly have near-source factors, because the artificial truncation of ground motion in a seismic zone is not a feature of this code, and the design spectral ordinates attain high values in the vicinity of seismic sources that are judged capable of generating large earthquakes (UBC-IBC Structural, 2000; see also Section 5.5). However, the 1996 USGS hazard maps, which are the basis for the seismic provisions in the 2000 IBC, as well as the 2002 USGS hazard maps do not specifically include directivity effects (Frankel et al. 2002). Therefore, these effects are only accounted for in an average sense through somewhat higher near-fault ground motions and standard deviations at longer periods represented by the ground motion relations used in the probabilistic seismic hazard analysis.

5.4.6 Vertical Ground Motion

Characteristics of the vertical component of ground motion are significantly different than those of the horizontal component. This is clearly evident in the recorded ground acceleration time histories. Compare, for example, the vertical ground acceleration recorded at Rinaldi Receiving Station during the Northridge earthquake (Figure 5.33) with that of the horizontal component recorded at this same station (Figure 5.29). It is evident from this comparison that the vertical component is richer in high frequency content than the horizontal component. This results in high vertical response spectral ordinates at short periods (Figure 5.5). Other examples of vertical response spectra are plotted in Figure 5.34. This figure presents the median vertical response spectra for an earthquake of M_W 7.5 at distances of 3, 10 and 20

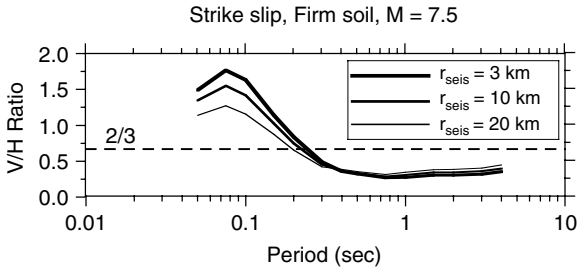

FIGURE 5.35 Vertical-to-horizontal (V/H) spectral ratio for 5% damping and distances from seismogenic faulting of 3, 10 and 20 km. (Adapted from Campbell, K.W. and Bozorgnia, Y. (2003). Updated near-source ground motion (attenuation) relations for the horizontal and vertical components of PGA and acceleration response spectra. *Bulletin of the Seismological Society of America*, 93, 314–331.)

km from the seismogenic part of the causative fault for a firm soil site, approximately equivalent to NEHRP soil category D (Campbell and Bozorgnia, 2003). As this figure shows, vertical spectral acceleration can be high at short periods, especially at sites close to the fault. Other empirical models have shown similar behavior for soil sites.

High vertical spectral acceleration at short periods can affect structural systems and components that have short *vertical* natural periods. In fact, vertical structural periods are generally short, as have been measured, identified, or computed by a number of investigators. For example, based on the recorded structural response of twelve instrumented structures, Bozorgnia et al. (1995a, 1998) identified a range of 0.075 to 0.26 sec for vertical natural periods of several structural systems and components. Another example is the study by Collier and Elnashai (2001), who analyzed a four-story reinforced concrete frame building of typical 1960s European construction and computed a vertical fundamental period of about 0.07 sec.

In recent years, analyses of hundreds of vertical ground motions recorded worldwide have identified distinct characteristics for the vertical component and its relationship to horizontal components (e.g., Niazi and Bozorgnia, 1989, 1991, 1992; Bozorgnia et al.,1995b, 1996, 1999; Watabe et al. 1990; Silva, 1997; Amirbekian and Bolt, 1998; Darragh et al. 1999; Ambraseys and Douglas, 2000; Beresnev et al. 2002; Bozorgnia and Campbell, 2004).

The vertical-to-horizontal (V/H) spectral ratio is a strong function of natural period, source-to-site distance, and local site conditions. Bozorgnia et al. (1999) showed that the behavior of the V/H spectral ratio with distance is different for firm soil (NEHRP soil category D) than for stiffer soil and rock sites. For firm soil sites close to active faults, V/H spectral ratios can easily exceed unity, approaching a factor of 1.8 or greater at short periods. Some examples of V/H spectral ratios predicted from the ground motion relations of Campbell and Bozorgnia (2003) for distances of 3, 10 and 20 km are plotted in Figure 5.35. It is evident from this figure that a period-independent ratio of 2/3 is a grossly unconservative approximation of the V/H spectral ratio at short periods, and is a relatively conservative approximation at long periods (see also Bozorgnia et al. 1999, and Bozorgnia and Campbell, 2004 for more details). Therefore, using the period-independent ratio of 2/3 to derive a vertical spectrum from a horizontal spectrum, as suggested in some engineering guidelines (e.g., Section 1.6.1.5.2 of FEMA-356, 2000) is not justified, especially at firm soil sites located near active faults.

Investigators (e.g., Silva, 1997; Amirbekian and Bolt, 1998) have offered seismological explanations for the observed dependence of the V/H spectral ratio on distance and local site conditions. For example, Amirbekian and Bolt (1998) concluded that the high-amplitude and high-frequency vertical accelerations that are observed on near-source accelerograms are most likely generated by the conversion of shear-waves to compressional waves within the transition zone between the underlying bedrock and the overlying softer sedimentary layers. Recently, based on analysis of five significant earthquakes in California, Beresnev et al. (2002) found that SV-waves dominate vertical motions at periods longer than about 0.1 sec; and at shorter periods, P-waves may become a significant contributor to the vertical motions.

5.5 Ground Motion Representation in the *International Building Code*

5.5.1 Introduction

Compared to previous editions of the *Uniform Building Code* (UBC, 1994, 1997), the *International Building Code* (IBC, 2000) includes major revisions in the characterization of ground motion for seismic design in the United States. It is intended to serve as a single code for the entire country, which comprises very different seismic regions. The challenge is to define a design earthquake that results in a uniform seismic safety margin for these different seismic provinces.

The main steps involved in developing the seismic design spectra in the IBC (2000), FEMA-368 (2001) and SEI/ASCE 7-02 (ASCE, 2002) are as follows:

- Given the site location, spectral accelerations at 0.2 sec and 1.0 sec are obtained from a set of published contour maps. These maps represent the maximum considered earthquake (MCE) ground motion (see Section 5.5.2). The MCE spectral accelerations are adjusted for local site effects (see Section 5.5.2).
- The MCE ground motion may be interpreted as a "collapse ground motion" (Leyendecker et al. 2000). For seismic *design*, the soil-adjusted MCE spectral ordinates are multiplied by a factor of 2/3 (see Section 5.5.3).
- The seismic design spectrum is constructed given the design spectral ordinates at 0.2 and 1.0 sec (see Section 5.5.3).

In the following sections, the main concepts behind the MCE ground motion are summarized, followed by the details of the steps in constructing the design spectrum.

5.5.2 Maximum Considered Earthquake (MCE)

"The most severe earthquake effects considered" in the IBC is what is referred to as the maximum considered earthquake, or MCE. This acronym is different than, and should not be confused with, a similar one traditionally used to represent the maximum capable earthquake or the maximum credible earthquake used in some previous publications and regulations. The MCE ground motion is quantified by the MCE maps published as part of the IBC. These maps are based on a combination of the results of probabilistic and deterministic estimates of ground motion. The background and concepts behind the MCE and the design spectrum in the IBC are discussed next.

5.5.2.1 Probabilistic Seismic Hazard Maps of the United States

The USGS has carried out comprehensive probabilistic seismic hazard analyses of the entire United States (see Frankel et al. 1996, 2000, 2002 for more details). There are hazard maps for different spectral ordinates and for different mean return periods. The return periods include 475 years (corresponding to 10% probability of exceedance in 50 years; abbreviated as 10% in 50 years) and 2475 years (corresponding to 2% probability of exceedance in 50 years, or 2% in 50 years). The latest USGS hazard maps, which were the 2002 edition at the time this chapter was written, can be found at the USGS Internet web site http://geohazards.cr.usgs.gov/eq/. These maps are updated approximately every three years.

The USGS hazard maps have quantitatively revealed important differences between the ground motion characteristics in different regions of the United States. For example, they have shown that the difference between the ground motions for 10% in 50 years and 2% in 50 years in the western United States is typically less than the difference between these two ground motion levels in the central and eastern United States (Leyendecker et al., 2000). Figure 5.36 presents an example of such a difference. For a site in San Francisco, California, the ratio of spectral accelerations for 2% in 50 years over that of 10% in 50 years is around 1.5; whereas, the ratio is greater than 4.4 at Charleston, South Carolina. The significance of this observation, as related to the definition of the design spectrum in the IBC, is elaborated in the following discussion about the structural seismic safety margin.

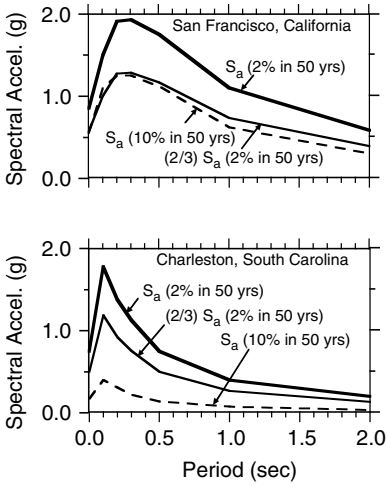

FIGURE 5.36 Uniform hazard response spectra for 2% and 10% probability of exceedance in 50 years for San Francisco, California, and Charleston, South Carolina. For comparison, two thirds of the 2% in 50 years spectra are also plotted. (Adapted from Leyendecker, E.V., Hunt, R.J., Frankel, A.D. and Rukstales, K.S. (2000). Development of maximum considered earthquake ground motion maps. *Earthquake Spectra*, 16, 21–40.)

5.5.2.2 Structural Seismic Safety Margin

The Seismic Design Procedures Group (SDPG), a committee of engineers and earth scientists, examined the safety margin against collapse of conventionally designed structures. The SDPG concluded that "the collective opinion of the SDPG was that the seismic margin contained in the 1997 NEHRP Provisions provides, as a minimum, a margin of about 1.5 times the design earthquake ground motion. In other words, if a structure is subjected to a ground motion 1.5 times the design level, the structure should have a low likelihood of collapse. The SDPG recognized that quantification of this margin is dependent on the type of structure, detailing requirements, etc., but the 1.5 factor was considered a conservative judgment appropriate for structures designed in accordance with the 1997 NEHRP Provisions." (Leyendecker et al. 2000).

Considering a desire to prevent collapse if a relatively rare but high level of ground motion associated with a 2% in 50 year probability were to occur, and taking into account the approximate minimum seismic margin of 1.5 against collapse, the IBC generally defines design ground motion as 1/1.5 (=2/3) times the 2% in 50 year ground motion. There are, however, important exceptions to this rule, especially near active faults in coastal California, as explained below. Referring to Figure 5.36, it is evident that for a site in San Francisco, 2/3 times the uniform hazard spectrum for 2% in 50 years is generally comparable to the traditional design spectrum for 10% in 50 years. However, for Charleston, 2/3 times the spectrum for 2% in 50 years is higher than that for 10% in 50 years (Leyendecker et al., 2000). Therefore, the IBC design philosophy accounts, to some extent, for the possibility of a rare but catastrophic earthquake in the eastern United States.

5.5.2.3 Ground Motions in Coastal California

In coastal California, the 2% in 50 year ground motion is generally conservative compared with a spectrum defined as 1.5 times the design ground motion recommended in the recent editions of the UBC. The 1.5 factor is the approximate seismic margin used by the SDPG to bring the design ground motion to the MCE level. Considering this comparison, as well as the observed performance of structures in coastal California in recent earthquakes, the SDPG defined the MCE as the 2% in 50 year ground motion only until it reaches 1.5 times the basic ground motion corresponding to Seismic Zone 4 in the UBC. The limits on the probabilistically defined ground motion value are sometimes referred to as plateaus (Leyendecker et al. 2000). Specifically, these plateaus are quantified by two spectral accelerations:

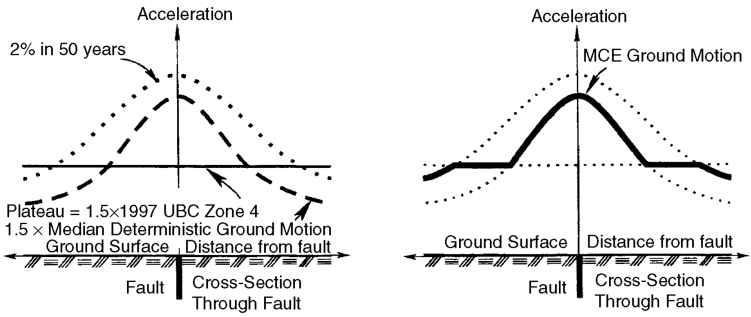

FIGURE 5.37 Procedure to integrate probabilistic and deterministic ground motions to obtain the *Maximum Considered Earthquake* (MCE) ground motion. (From Leyendecker, E.V., Hunt, R.J., Frankel, A.D., and Rukstales, K.S. (2000). Development of maximum considered earthquake ground motion maps. *Earthquake Spectra*, 16, 21–40.)

1.5*g* for a spectral acceleration at 0.2 sec and 0.6*g* for a spectral acceleration at 1.0 sec. These values include the 1.5 scale factor.

Above the plateau, the ground motion is specified according to 1.5 times the median deterministic ground motions derived from the ground motion relations that were used to develop the probabilistic values. However, the deterministic values are not used unless they are *less than* the probabilistic values. The procedure to integrate the probabilistic and deterministic values to obtain the MCE ground motion is illustrated in Figure 5.37. Besides being the seismic margin, the scale factor of 1.5 also is an approximate factor to scale up the median ground-motion value to the median plus one standard deviation value, or 84th percentile. For example, in the ground motion relation developed by Campbell and Bozorgnia (2003), the median plus one standard deviation value of the horizontal spectral acceleration at 1.0 sec can be obtained by multiplying the median spectral acceleration by a factor of 1.65 when PGA $\geq 0.25\ g$.

Close to active faults, defining the design earthquake ground motion based on the median deterministic value is also consistent with the concept of the Near-Source Factors introduced in the 1997 UBC (Kircher, 1999). In the 1997 UBC the introduction of Near-Source Factors became necessary in view of the artificial truncation of peak ground acceleration at 0.4 *g* in Seismic Zone 4. In the IBC, these factors are not found because the design ground motions can attain high values in the vicinity of the active faults (UBC-IBC Structural, 2000). It should be noted, however, that the current MCE maps do not include fault rupture directivity effects (Frankel et al. 2002); so in the fault-normal direction these near-fault deterministic ground motions would even be higher if these effects were taken into account (see Section 5.4.5).

5.5.2.4 MCE Maps

The MCE ground motion, as defined above, is quantified by two sets of contour maps of elastic spectral accelerations. Given the site location, the spectral accelerations at short structural period (0.2 sec), S_S, and at 1.0-sec period, S_1, are obtained from these MCE maps. The maps are printed in the IBC and can also be found at the USGS Internet web site http://geohazards.cr.usgs.gov/eq/. The spectral accelerations are for a 5% damping ratio. The period of 0.2 sec was chosen to represent S_S because in the central and eastern United States the spectral acceleration at 0.2 sec is larger than that at 0.3 sec and better quantifies the larger short-period frequency content in this region. In the western United States, there is little difference between the spectral accelerations at 0.2 and 0.3 sec (e.g., Figure 5.36).

5.5.2.5 Adjustment for Local Site Conditions

The reference site condition for the MCE maps is firm rock with a nominal average shear-wave velocity of 760 m/sec in the top 30 m of the site profile (Frankel et al. 1996, 2000, 2002). This corresponds to the boundary of NEHRP site categories B and C as defined in the IBC. For other site conditions, the MCE ground motions are adjusted by using the site coefficients F_a and F_v specified in IBC Tables 1615.1.2(1) and 1615.1.2(2), respectively (for FEMA-368, use FEMA Tables 4.1.2.4a and 4.1.2.4b, respectively; for

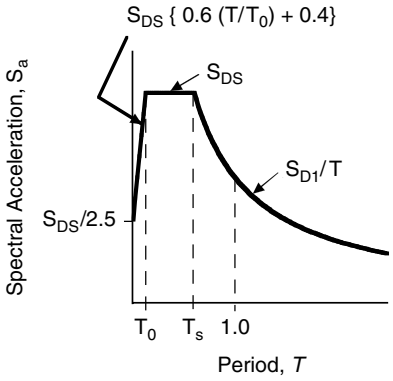

FIGURE 5.38 Elastic design spectrum in the IBC (2000) and FEMA-368 (2001) for 5% damping. Corner periods are $T_S = S_{D1}/S_{DS}$ and $T_0 = 0.2\ T_S$.

SEI/ASCE 7-02, use ASCE Tables 9.4.1.2.4a and 9.4.1.2.4b, respectively). The details of the site categories are discussed in Chapter 4 (see also Table 5.3). Given the site coefficients F_a and F_v, the site-adjusted spectral ordinates S_{MS} (at 0.2-sec period) and S_{M1} (at 1.0-sec period) are defined as

$$S_{MS} = F_a S_S \tag{5.63}$$

$$S_{M1} = F_v S_1 \tag{5.64}$$

These site-adjusted values are used to construct the design spectra, as explained below.

5.5.3 Design Spectra in the IBC

The MCE ground motion may be interpreted as a "collapse ground motion" (Leyendecker et al. 2000). Thus, the actual ground motion used in seismic design is lower than this level. In the IBC, the design ground motion is quantified by two spectral accelerations: S_{DS}, the design spectral acceleration at 0.2 sec, and S_{D1}, the design spectral acceleration at 1.0 sec. These elastic design spectral accelerations are defined as

$$S_{DS} = (2/3)\ S_{MS} \tag{5.65}$$

$$S_{D1} = (2/3)\ S_{M1} \tag{5.66}$$

Given the design spectral accelerations, S_{DS} and S_{D1}, the 5% damped general elastic design spectrum is constructed according to Figure 5.38.

It should be noted that, by comparing the design spectrum in Figure 5.38 to that given in FEMA-356 (2000) as shown in Figure 5.10, the IBC design spectrum can be derived from the FEMA-356 spectrum by assigning a 5% damping ratio (i.e., $B_S = B_1 = 1.0$) and setting $S_{XS} = S_{DS}$ and $S_{X1} = S_{D1}$.

5.5.4 Site-Specific Ground Motion in the IBC

The IBC allows for the development of MCE response spectrum using site-specific methods in lieu of one developed using the general procedure described in Section 5.5.3 of this chapter. Such a study must account for the regional seismicity and geology; the expected recurrence rates and maximum magnitudes of events on known faults and source zones; the locations of the site with respect to these faults and source zones; near-source effects, if any; and the characteristics of the subsurface site conditions. In general, the MCE gound motion is defined as the 2% in 50 year site-specific ground motion. However, if either the 2% in 50 year 0.2-sec or 1.0-sec spectral acceleration exceeds the deterministic limits given in Figure 5.39, the MCE gound motion is taken as the lesser of the probabilistic MCE ground motion or 1.5 times the deterministic site-specific median ground motion resulting from a characteristic earth-

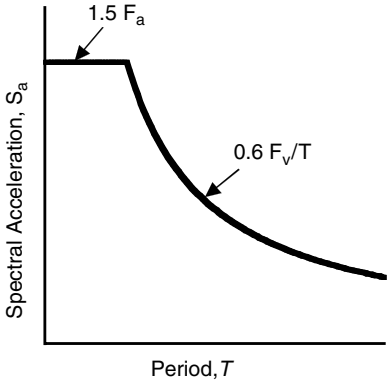

FIGURE 5.39 Deterministic limit on the site-specific MCE response spectrum.

quake on any known active fault in the region, but shall not be taken as less than the deterministic limit given in Figure 5.39. The site-specific design spectrum is the larger of 2/3 of the site-specific MCE spectrum or 80% of the general design spectrum described in Section 5.5.3 of this chapter.

5.6 Future Challenges

As indicated in this chapter, in recent years there have been significant advances in the engineering characterization of strong ground motion. There are, however, numerous exciting challenges confronting earth scientists and earthquake engineers concerning the characterization of ground motion for engineering applications. These challenges include, but are certainly not limited to, the following:

5.6.1 Development of the Next Generation of Ground Motion (Attenuation) Relations

The next generation of ground motion relations will need to be applicable to a wider range of magnitudes and distances than existing relations so it will not be necessary to extrapolate them beyond their range of applicability as is currently done in engineering practice. These future relations will also need to incorporate finer distinctions in site categories (e.g., Hard rock, soft rock, very stiff soil, stiff soil and soft soil; instead of simply soil and rock) or directly use the average shear-wave velocity in the top 30 m of the site profile as defined in recent building codes to better account for site effects. Additionally, future ground motion relations will need to systematically include near-fault directivity effects, hanging wall and footwall effects, sediment depth and other parameters that are used in one or more of the currently available ground motion relations. There are ongoing research efforts to systematically develop such next generation ground motion relations that are expected to take a major step towards obtaining these goals.

5.6.2 Better Understanding and Modeling of Fault Rupture Directivity and Fling

Currently used wide-band modifications of ground motion relations to develop elastic response spectra need to be enhanced to include the observed narrow-band characteristics of near-fault pulses. The observed period of such pulses increases with magnitude. Such a characteristic needs to be reliably modeled and included in the engineering prediction of ground motion. Also, there is a need to reliably quantify and simplify the effects of fault rupture directivity and fling for the design of civil engineering facilities.

5.6.3 Inclusion of the Directivity Effects in Probabilistic Hazard Analysis

In the United States, the 1996 and 2002 national seismic hazard maps that provide the fundamental data for seismic design, do not include fault rupture directivity effects. The hazard analysis for sites located near active faults should incorporate such effects, once the wide-band versus narrow-band issues regarding near-fault pulses are resolved. Inclusion of such effects can have important consequences on the seismic design of civil engineering systems.

5.6.4 Near Real-Time Spatial Distribution of Damage Potential of Ground Motions

Currently, after an earthquake, maps of various traditional ground-motion parameters, including elastic spectral ordinates, are automatically generated in near real-time and posted on the Internet. For rapid performance-based damage assessment of structures, the currently mapped parameters need to be supplemented with other damage-related parameters, for example, strong-motion duration and damage indices. For practical near real-time post-earthquake damage and loss assessments, it would also be desirable to combine the mapped spatial distributions of these ground-motion and damage parameters with an inventory of the existing structural and lifeline facilities.

5.6.5 Vertical Design Spectra

In recent years the understanding of the near-source characteristics of vertical ground motion has greatly advanced. These characteristics will need to be reliably simplified and translated into simple rules for developing vertical design spectra.

5.6.6 Ground-Motion Parameters for Performance-Based Earthquake Engineering

There is a need to identify and predict improved and more reliable ground-motion parameters for performance-based earthquake engineering. Such parameters should be comprehensive enough to include the effects of various important seismological parameters such as magnitude, source-to-site-distance, faulting mechanism and other characteristics. This will require an even greater degree of interaction among earth scientists and engineers than has been achieved in the past.

5.6.7 Modeling Cumulative Damage Potential of Earthquake Ground Motions

Cumulative damage potential of ground motions in foreshocks, the main shock, aftershocks and multiple events needs to be modeled and reliably simplified for practical applications.

Acknowledgments

We would like to recognize the constructive comments of Prof. V.V. Bertero, Prof. C.M. Uang, Prof. J.P. Stewart, Dr. M. Hachem and T. Travasarou, which are greatly appreciated. We would also like to recognize all of the researchers and practicing engineers and seismologists, past and present, without whose work this chapter would not have been possible.

Glossary

Anelastic attenuation — The diminution of ground motion with distance from the source due to material damping and scattering of waves from inhomogeneities in the crust.

Attenuation relation — An equation or tabulation used to estimate a strong-motion parameter from one or more seismological parameters; also known as a ground motion relation.

Basement rock — The more resistant, generally crystalline rock that lies beneath layers or irregular deposits of younger, relatively deformed sedimentary rock.

Critical reflection — The incidence angle below which the ground-motion ray is completely reflected off a layer of higher wave velocity.

Damage spectrum — A plot of variation of a damage index for an inelastic single-degree-of-freedom (SDF) system versus undamped natural period or frequency, when excited by a specified ground motion time history.

Epicenter — The point on the Earth's surface directly above the hypocenter.

Faulting mechanism — The type or style of faulting defined by the direction of slip on the fault rupture plane; usually referred to by such terms as strike slip, reverse, thrust, normal or oblique.

Focus — See hypocenter.

Footwall — That portion of the crust that lies below the fault or fault rupture plane.

Frequency — The reciprocal of period – that is, the number of cycles of oscillation per unit of time (e.g., One second). Usually measured in terms of hertz (1 Hz = 1 cycle per second).

Geometric attenuation — The diminution of ground motion with distance from the source as the area of the wave front expands.

Ground motion — The vibration of the ground in the time or frequency domain measured by a seismometer that records acceleration, velocity or displacement, or an estimate of this vibration or a ground-motion parameter that characterizes this vibration.

Ground motion relation — Same as attenuation relation.

Hanging wall — That portion of the crust that lies above the fault or fault rupture plane.

Hypocenter — The point within the Earth where the earthquake rupture begins (see also focus).

Hysteretic energy spectrum — A plot of the maximum hysteretic energy (due to yielding) in an inelastic SDF system versus undamped natural period or frequency, subjected to a specified ground motion time history at its base.

Inelastic response spectrum — A plot of the maximum response of an inelastic SDF system versus undamped natural period or frequency, subjected to a specified ground motion time history at its base.

Local site conditions — A qualitative or quantitative description of the material properties of the soil and sedimentary rock layers above basement rock.

Magnitude — An instrumental or seismological measure of an earthquake's size proportional to the logarithm of the amplitude or energy of ground motion.

Maximum Considered Earthquake (MCE) — The most severe earthquake effects considered in the *International Building Code* (IBC) and other recent U.S. codes and standards.

Natural frequency — The reciprocal of natural period.

Natural period — The period of an oscillator or structure during free (i.e., unforced) vibration.

Period — The duration of time (e.g., number of seconds) required to complete one oscillation.

Radiation pattern — A geometric description of the amplitude of ground motion and the sense of initial motion at the source which for shear waves has a low-order symmetry that can be used to infer the faulting mechanism.

Rake angle — The angle between the direction of slip on the fault rupture plane and the fault strike.

Response spectrum (elastic) — A plot of the maximum response of a viscously damped linear elastic SDF system versus undamped natural period or frequency, when subjected to a specified ground motion time history at its base.

Seismogenic — That part of the Earth's crust that is capable of generating ground motion at periods of engineering interest, usually 10 sec or less.

Seismological parameter — A parameter used to characterize a seismological property of the earthquake source, the propagation medium, or the response of the materials beneath the site.

Shear-wave velocity — The speed at which shear waves travel through a material; shear waves are waves whose amplitude is perpendicular to the direction of propagation and are the most potentially damaging to man-made structures.

Source directivity — The azimuthal perturbation of the radiation pattern due to rupture propagation on the fault in which the amplitude increases in the direction of rupture and decreases in the opposite direction.

Stress drop — The amount of stress released at the rupture front during an earthquake.

Strike — The orientation of a fault on the Earth's surface, usually measured clockwise from north.

Strong ground motion — Ground motion having the potential to cause measurable damage to a structure's architectural or structural components; usually associated with a PGA of 0.05*g* or greater.

Strong-motion parameter — A parameter characterizing the amplitude of strong ground motion in the time domain (time-domain parameter) or the frequency domain (frequency-domain parameter).

Time history — A data set, usually composed of one vertical and two orthogonal horizontal components, describing a strong-motion parameter (such as ground acceleration) as a function of time.

Tectonic environment — The type of tectonic deformation that occurs in a region; usually described by such terms as active, stable, compressional, extensional or subduction.

List of Symbols

Ground Motion Parameters

PGA	Peak ground acceleration (g)
PGV	Peak ground velocity (cm/sec)
PGD	Peak ground displacement (cm)
SA	Maximum absolute (total) acceleration of SDF system
SV	Maximum velocity of SDF system relative to the ground
S_d	Maximum deformation of an elastic SDF system relative to the ground
S_v	PSV = Pseudo-velocity = ωS_d
S_a	PSA = Pseudo-acceleration = $\omega^2 S_d$
Y	Peak ground motion (generic)
Y_{Dir}	Peak ground motion (generic) including rupture directivity effects
$\sigma_{\ln Y}$	Standard deviation of ln Y
$\sigma_{\ln Y,Dir}$	Standard deviation of ln Y_{Dir} (i.e., when directivity effects are included)

Magnitude Parameters

m_{Lg}	Lg-wave magnitude used in eastern United States (equivalent to m_N in Canada)
M	Earthquake magnitude (generic)
M_S	Surface-wave magnitude
M_W	Moment magnitude (equivalent to **M**)

Distance Parameters

r_{epi}	Epicentral distance (km)
r_{hypo}	Hypocentral distance (km)
r_{jb}	Closest distance to the surface projection of the rupture plane (km)
r_{rup}	Closest distance to the rupture plane (km)
r_{seis}	Closest distance to the seismogenic part of the rupture plane (km)
R	Distance to the earthquake source (generic)

Depth Parameters

d_{rup} Average depth to top of the rupture plane (km)
d_{seis} Average depth to top of the seismogenic part of the rupture plane (km)
h_{hypo} Hypocentral depth (also focal depth) (km)
H_{bot} Depth to the bottom of the seismogenic part of the fault (km)
H_{top} Depth to the top of the fault (km)
H_{seis} Depth to the top of the seismogenic part of the fault (km)

Faulting Mechanism Parameters

F Indicator variable for the type or style of faulting
F_{RV} Indicator variable for reverse faulting ($\delta > 45°$) in Campbell and Bozorgnia model
F_{TH} Indicator variable for thrust faulting ($\delta \leq 45°$) in Campbell and Bozorgnia model
W Down-dip width of the fault rupture plane (km)
λ Rake (direction of slip vector on the fault plane):
0°, pure left-lateral faulting
90°, pure reverse faulting
180°, pure right-lateral faulting
270° or –90°, pure normal faulting

Site Parameters

S_C Indicator variable for very dense soil and soft rock in building code site class
S_D Indicator variable for stiff soil in building code site class
S_E Indicator variable for soft soil in building code site class
S_{VFS} Indicator variable for very firm soil in Campbell and Bozorgnia site class
S_{SR} Indicator variable for soft rock in Campbell and Bozorgnia site class
S_{FR} Indicator variable for firm rock in Campbell and Bozorgnia site class
S_{Deep} Indicator variable for deep stiff soil in eastern North America
S_{Soil} Indicator variable for generic soil in western North America
V_{30} Average value of V_S in the top 30 m (100 ft) of a site profile
V_S Shear-wave velocity (generic)

Hanging-Wall Parameters

HW Indicator variable for a site located on the hanging wall of the rupture plane

Source Directivity Parameters

d Effective rupture width for estimating directivity effects for dip-slip faults
DR Fraction of fault rupture length (s/L) or width (d/W) rupturing towards a site
L Length of the fault rupture plane
s Effective rupture length for estimating directivity effects for strike-slip faults
ϕ Zenith angle between fault rupture plane and ray path to a site for dip-slip faults
θ Azimuth angle between rupture plane and ray path to a site for strike-slip faults

Generic Inelastic Systems and Seismic Code Parameters

F_e Maximum restoring force if the system were to remain elastic
F_y Equivalent yield strength
u_{max} Maximum deformation of the inelastic SDF system
u_y Yield deformation of the inelastic SDF system

μ	Displacement ductility ratio = u_{max}/u_y
R	Response modification coefficient
S_S	Mapped MCE spectral acceleration (5% damping) at a period of 0.2 sec
S_1	Mapped MCE spectral acceleration (5% damping) at a period of 1.0 sec
S_{MS}	MCE spectral acceleration (5% damping) at a period of 0.2 sec, adjusted for site effects
S_{M1}	MCE spectral acceleration (5% damping) at a period of 1.0 sec, adjusted for site effects
S_{DS}	Design spectral acceleration (5% damping) at a period of 0.2 sec
S_{D1}	Design spectral acceleration (5% damping) at a period of 1.0 sec

Miscellaneous Parameters

f	Seismic wave or oscillator frequency (1/T, Hz)
g	fraction of gravity (980.6550 cm/sec^2)
T	Wave or oscillator period (1/f, sec)
z_T	Indicator variable for subduction interface and intraslab events
δ	Angle of the fault plane with respect to the Earth's surface (dip angle)

References

Abrahamson, N.A. (2000). Effects of rupture directivity on probabilistic seismic hazard analysis. *Proceedings, 6th International Conference on Seismic Zonation*, Palm Springs, California, 6 p.

Abrahamson, N.A. and Somerville, P.G. (1996). Effects of the hanging wall and footwall on ground motions recorded during the Northridge earthquake, *Bulletin of the Seismological Society of America*, 86, S93–S99.

Abrahamson, N.A. and Silva, W.J. (1996). Empirical ground motion models. *Report* submitted to Brookhaven National Laboratory.

Abrahamson, N.A. and Silva, W.J. (1997). Empirical response spectral attenuation relations for shallow crustal earthquakes. *Seismological Research Letters*, 68, 94–127.

Abrahamson, N.A., Schneider, J.F. and Stepp, J.C. (1991). Empirical spatial coherency functions for applications to soil-structure interaction analysis. *Earthquake Spectra*, 7, 1–27.

Akiyama, H. (1985). *Earthquake-Resistant Limit-State Design of Buildings*. University of Tokyo Press, Tokyo.

Alavi, B. and Krawinkler, H. (2001). Effects of near-fault ground motions on frame structures. *Report No. 138,* The John A. Blume Earthquake Engineering Center, Stanford University.

Ambraseys, N. and Douglas, J. (2000).Reappraisal of the effect of vertical ground motions on response. *Report ESEE 00-4,* Imperial College of Science, Technology and Medicine, London.

American Society of Civil Engineers (2002). Minimum design loads for buildings and other structures. *SEI/ASCE 7-02*, Reston, Virginia.

Amirbekian, R.V. and Bolt, B.A. (1998). Spectral comparison of vertical and horizontal seismic strong ground motions in alluvial basins. *Earthquake Spectra,* 14, 573–595.

Anderson, J.C. and Bertero, V.V. (1987). Uncertainties in establishing design earthquakes. *ASCE Journal of Structural Engineering*, 113, 1709–1724.

Anderson, J.C. and Bertero, V.V. (2003). Performance improvement of tall steel buildings subjected to pulse-type ground motions. *Proceedings, 7th U.S. National Conference on Earthquake Engineering*, Boston.

Anderson, J.G. (2000). Expected shape of regressions for ground motion parameters on rock. *Bulletin of the Seismological Society of America*, 90, S43–S52.

Anderson, J.G. (2003). Strong motion seismology. In *International Handbook of Earthquake and Engineering Seismology*, Part B, Ed. W.H.K. Lee, H. Kanamori, P.C. Jennings and C. Kisslinger, Academic Press, London.

Arias, A. (1970). A measure of earthquake intensity. In *Seismic Design for Nuclear Power Plants*, Ed. R.J. Hansen, MIT Press, Cambridge, Massachusetts.

Atkinson, G.M. and Boore, D.M. (1995). New ground motion relations for eastern North America. *Bulletin of the Seismological Society of America*, 85, 17–30.

Atkinson, G.M. and Boore, D.M. (1997). Some comparisons between recent ground motion relations. *Seismological Research Letters*, 68, 24–40.

Atkinson, G.M. and Boore, D.M. (1998). Evaluation of models for earthquake source spectra in eastern North America. *Bulletin of the Seismological Society of America*, 88, 917–934.

Atkinson, G.M. and Boore, D.M. (2003). Empirical ground-motion relations for subduction zone earthquakes and their application to Cascadia and other regions. *Bulletin of the Seismological Society of America*, 93, 1703–1729.

Bendat, J.S. and Piersol, A.G. (1980). *Engineering Applications of Correlation and Spectral Analysis*. John Wiley & Sons, New York.

Beresnev, I.A., Nightengale, A.M. and Silva, W.J. (2002). Properties of vertical ground motions. *Bulletin of the Seismological Society of America*, 92, 3152-3164.

Bertero, V.V. and Uang, C.M. (1992). Issues and future directions in the use of an energy approach for seismic-resistant design of structures, In *Nonlinear Seismic Analysis and Design of Reinforced Concrete Buildings*, Ed. P. Fajfar and H. Krawinkler, 3–22.

Bertero, V.V., Anderson, J.C. and Sasani, M. (1999). Impulse earthquake ground motions: A historical and critical review. *Proceedings, ASCE 1999 Structures Congress*, New Orleans, 91–94.

Bertero, V.V., Mahin, S.A. and Herrera, R.A. (1978). Aseismic design implications of near-fault San Fernando earthquake records. *Earthquake Engineering and Structural Dynamics*, 6, 31–42.

Bertero, V.V., Popov, E.P., Wang, T.Y. and Vallenas, J. (1977). Seismic design implications of hysteretic behavior of reinforced concrete structural walls, *Proceedings, 6th World Conference on Earthquake Engineering*, Vol. II, India,1898–1904.

Biot, M.A. (1933). Theory of elastic systems vibrating under transient impulse with an application to earthquake-proof buildings. *Proceedings, National Academy of Sciences*, 19, 262–268.

Biot, M.A. (1934). Theory of vibration of buildings during earthquake. *Zeitschrifr für angewandte Mathematik und Mechanik*, 14, 213–223.

Biot, M.A. (1941). A mechanical analyzer for the prediction of earthquake stresses. *Bulletin of the Seismological Society of America*, 31, 151–171.

Bolt, B.A. (1973). Duration of strong ground motion. *Proceedings*, *5th World Conference on Earthquake Engineering*, Rome, 1304–1313.

Bommer, J.J. and Martinez-Pereira, A. (1999). The effective duration of earthquake strong motion. *Journal of Earthquake Engineering*, 3, 127–172.

Boore, D.M. (2001). Comparisons of ground motions from the 1999 Chi-Chi Earthquake with empirical predictions largely based on data from California. *Bulletin of the Seismological Society of America*, 91, 1212–1217.

Boore, D.M. (2003). Prediction of ground motion using the stochastic method. *Pure and Applied Geophysics,* 160, 635–676.

Boore, D.M. and Joyner, W.B. (1997). Site amplification for generic rock sites. *Bulletin of the Seismological Society of America*, 87, 327–341.

Boore, D.M., Joyner, W.B. and Fumal, T.E. (1997). Equations for estimating horizontal response spectra and peak acceleration from western North American earthquakes: A summary of recent work. *Seismological Research Letters*, 68, 128–153.

Boore, D.M., Stephens, C.D. and Joyner, W.B. (2002). Comments on baseline correction of digital strong-motion data: Examples from the 1999 Hector Mine, California, earthquake. *Bulletin of Seismological Society of America*, 92, 1543–1560.

Bozorgnia, Y. (2003). An introduction to the classic paper: A mechanical analyzer for the prediction of earthquake stresses, by Maurice Biot. *Seismological Research Letters*, 74, 312.

Bozorgnia, Y. and Bertero, V.V. (2001a). Evaluation of damage potential of recorded earthquake ground motion. *Seismological Research Letters*, 72, 233.

Bozorgnia, Y. and Bertero, V.V. (2001b). Improved shaking and damage parameters for post-earthquake applications. *Proceedings, SMIP01 Seminar on Utilization of Strong-Motion Data*, Los Angeles, 1–22.

Bozorgnia, Y. and Bertero, V.V. (2002). Improved damage parameters for post-earthquake applications. *Proc. SMIP02 Seminar on Utilization of Strong-Motion Data*, Los Angeles, 61–82.

Bozorgnia, Y. and Bertero, V.V. (2003). Damage spectra: Characteristics and applications to seismic risk reduction. *ASCE Journal of Structural Engineering*, 129.

Bozorgnia, Y. and Campbell, K.W. (2004). The vertical-to-horizontal response spectral ratio and tentative procedures for developing simplified V/H and vertical design spectra. *Journal of Earthquake Engineering*, 8, 175–207.

Bozorgnia, Y. and Mahin, S.A. (1998). Ductility and strength demands of near-fault ground motions of the Northridge earthquake. *Proceedings, 6th U.S. National Conference on Earthquake Engineering*, Seattle, Washington.

Bozorgnia, Y., Campbell, K.W. and Niazi, M. (1999). Vertical ground motion: Characteristics, relationship with horizontal component, and building-code implications. *Proceedings*, *SMIP99 Seminar on Utilization of Strong-Motion Data*, San Francisco, 23–49.

Bozorgnia, Y., Mahin, S.A. and Brady, A.G. (1995a). Vertical responses of twelve instrumented structures recorded during the Northridge earthquake. *Report,* Earthquake Engineering Research Institute (EERI), Oakland, California, 275 p.

Bozorgnia, Y., Niazi, M. and Campbell, K.W. (1995b). Characteristics of free-field vertical ground motion during the Northridge earthquake. *Earthquake Spectra*, 11, 515–525.

Bozorgnia, Y., Mahin, S.A. and Brady, A.G. (1998). Vertical response of twelve structures recorded during the Northridge earthquake. *Earthquake Spectra*, 14, 411–432.

Bozorgnia, Y., Niazi, M. and Campbell, K.W. (1996). Relationship between vertical and horizontal ground motion for the Northridge earthquake. *Proceedings, 11th World Conference on Earthquake Engineering,* Acapulco, Mexico.

Brune, J. (1970). Tectonic stress and the spectra of seismic shear waves. *Journal of Geophysical Research*, 75, 4997–5009.

Brune, J. (1971). Correction: Tectonic stress and the spectra of seismic shear waves. *Journal of Geophysical Research*, 76, 5002.

Brune, J.N. (1999). Precarious rocks along the Mojave section of the San Andreas fault, California: Constraints on ground motion from great earthquakes. *Seismological Research Letters*, 70, 29–33.

Brune, J.N. (2001). Shattered rock and precarious rock evidence for strong asymmetry in ground motions during thrust faulting. *Bulletin of the Seismological Society of America*, 91, 441–447.

Bruneau, M. and Wang, N. (1996). Normalized energy-based methods to predict the seismic ductile response of SDOF structures. *Engineering Structures*, 18, 13-28.

Campbell, K.W. (1997). Empirical near-source attenuation relationships for horizontal and vertical components of peak ground acceleration, peak ground velocity, and pseudo-absolute acceleration response spectra. *Seismological Research Letters*, 68, 154–179.

Campbell, K.W. (2000a). Engineering seismology. In *Encyclopedia of Physical Science and Technology,* 3rd ed., Academic Press, San Diego.

Campbell, K.W. (2000b). Erratum: Empirical near-source attenuation relationships for horizontal and vertical components of peak ground acceleration, peak ground velocity, and pseudo-absolute acceleration response spectra. *Seismological Research Letters*, 71, 353–355.

Campbell, K.W. (2001). Development of semi-empirical attenuation relationships for CEUS. *Report to the U.S. Geological Survey, Award 01HQGR0011*, final report.

Campbell, K.W. (2003a). Strong motion attenuation relations. In *International Handbook of Earthquake and Engineering Seismology*, Part B, Ed. W.H.K. Lee, H. Kanamori, P.C. Jennings and C. Kisslinger, Academic Press, London.

Campbell, K.W. (2003b). A contemporary guide to strong motion attenuation relations. In *International Handbook of Earthquake and Engineering Seismology*, Handbook CD, Eds. W.H.K. Lee, H. Kanamori, P.C. Jennings and C. Kisslinger, Academic Press, London.

Campbell, K.W. (2003c). Prediction of strong ground motion using the hybrid empirical method and its use in the development of ground motion (attenuation) relations in eastern North America, *Bulletin of the Seismological Society of America*, 93, 1012–1033.

Campbell, K.W. (2003d). Engineering models of strong ground motion. In *Earthquake Engineering Handbook*, Ed. W.F. Chen and C. Scawthorn, CRC Press, Boca Raton, Florida.

Campbell, K.W. and Bozorgnia, Y. (2003). Updated near-source ground motion (attenuation) relations for the horizontal and vertical components of peak ground acceleration and acceleration response spectra. *Bulletin of the Seismological Society of America,* 93, 314–331.

Celebi, M. (1993). Seismic response of eccentrically braced tall building. *ASCE Journal of Structural Engineering*, 119, 1188–1205.

Challa, V.R.M. and Hall, J.F. (1994). Earthquake collapse analysis of steel frames. *Earthquake Engineering and Structural Dynamics*, 23, 1199–1218.

Chapman, M.C. (1999). On the use of elastic input energy for seismic hazard analysis. *Earthquake Spectra*, 15, 607–635.

Choi, Y. and Stewart, J.P. (2003). Nonlinear site amplification as a function of 30 M shear wave velocity. *Earthquake Spectra*, in press.

Chopra, A.K. (2001). *Dynamics of Structures: Theory and Applications to Earthquake Engineering*. 2nd ed., Prentice Hall, Upper Saddle River, New Jersey.

Chopra, A.K. and Goel, R.K. (1999). Capacity-demand-diagram method based on inelastic design spectrum. *Earthquake Spectra*, 15, 637–656.

Chopra, A.K. and Goel, R.K. (2001) Direct displacement-based design: Use of inelastic vs. Elastic design spectra. *Earthquake Spectra*, 17, 47–64.

Chou, C.C. and Uang, C. M. (2000). Establishing absorbed energy spectra — an attenuation approach. *Engineering and Structural Dynamics,* 29, 1441–1455.

CIT-SMARTS (1996). Caltech strong motion accelerogram record transfer system. Report and computer disks, Earthquake Engineering Research Laboratory, California Institute of Technology, http://www.eerl.caltech.edu/smarts/smarts.html.

Clough, R.W. and Penzien, J. (1993). *Dynamics of Structures*. 2nd ed., McGraw-Hill, New York.

Collier, C.J. and Elnashai, A.S. (2001). A procedure for combining vertical and horizontal seismic action effects. *Journal of Earthquake Engineering*, 5, 521–539.

Converse, A.M. (1992). BAP, basic strong-motion accelerogram processing software. *U.S. Geological Survey Open-File Report 92-296A*.

Darragh, R., Silva, W.J. and Gregor, N. (1999). Bay Bridge downhole array analyses. *Report* submitted to Earth Mechanics, Inc., Fountain Valley, California.

Decanini, L.D. and Mollaioli, F. (1998). Formulation of elastic earthquake input energy spectra. *Earthquake Engineering and Structural Dynamics*, 27, 1503–1522.

Draper, N.R. and Smith, H. (1981). *Applied Regression Analysis*. 2nd ed., John Wiley & Sons, New York.

Fajfar, P. (1992). Equivalent ductility factors, taking into account low-cycle fatigue. *Earthquake Engineering and Structural Dynamics*, 21, 837–848.

Fajfar, P. and Vidic, T. (1994). Consistent inelastic design spectra: Hysteretic and input energy. *Earthquake Engineering and Structural Dynamics*, 23, 523–537.

Federal Emergency Management Agency (2000). Prestandard and commentary for the seismic rehabilitation of buildings. *FEMA-356,* Washington, D.C.

Federal Emergency Management Agency (2001). 2000 Edition NEHRP recommended provisions for seismic regulations for new buildings and other structures, Part 1, Provisions. *FEMA-368,* Washington, D.C.

Federal Emergency Management Agency (2001). 2000 Edition NEHRP recommended provisions for seismic regulations for new buildings and other structures, Part 2, Commentary. *FEMA-369,* Washington, D.C.

Field, E.H. (2000). A modified ground-motion attenuation relationship for Southern California that accounts for detailed site classification and a basin-depth effect. *Bulletin of the Seismological Society of America*, 90, S209–S221.

Field, E.H. and the SCEC Phase III Working Group (2000). Accounting for site effects in probabilistic seismic hazard analyses of Southern California: Overview of the SCEC Phase III report. *Bulletin of the Seismological Society of America*, 90, S1–S31.

Frankel, A., Mueller, C., Barnhard, T., Perkins, D., Leyendecker, E., Dickman, N., Hanson, S. And Hopper, M. (1996). National seismic hazard maps: Documentation June 1996, *U.S. Geological Survey Open-File Rept. 96-532.*

Frankel, A.D., Mueller, C.S., Barnhard, T.P., Leyendecker, E.V., Wesson, R.L., Harmsen, S.C., Klein, F.W., Perkins, D.M., Dickman, N.C., Hanson, S.L. and Hopper, M.G. (2000). USGS national seismic hazard maps. *Earthquake Spectra*, 16, 1-19.

Frankel, A.D., Petersen, M.D., Mueller, C.S., Haller, K.M., Wheeler, R.L., Leyendecker, E.V.,Wesson, R.L., Harmsen, S.C., Cramer, C.H., Perkins, D.M. and Rukstales, K.S. (2002). Documentation for the 2002 update of the national seismic hazard maps. *U.S. Geological Survey Open-File Rept. 02-420*.

Freeman, S.A. (1995). A review of practical approximate inelastic seismic design procedures for new and existing buildings. *Proceedings, 64th Annual Convention of the Structural Engineers Association of California*, Indian Wells, California, 311–331.

Hachem, M.M. (2000). *Bispec*. Http://www.ce.berkeley.edu/~hachem/bispec/index.html

Hall, J.F., Heaton, T.H., Halling, M.W. and Wald, D.J. (1995).Near-source ground motion and its effects on flexible buildings. *Earthquake Spectra*, 11, 569–605.

Hanks, T.C. and Kanamori, H. (1979). A moment-magnitude scale, *Journal of Geophysical Research*, 84, 2348–2350.

Housner, G.W. (1941). Calculating the response of an oscillator to arbitrary ground motion. *Bulletin of the Seismological Society of America*, 31, 143–149.

Housner, G.W. (1952). Spectrum intensities of strong-motion earthquakes. *Proceedings*, *Symposium on Earthquake and Blast Effects on Structures*, Eds. C.M. Duke and M. Feigen, Los Angeles, 21–36.

Housner, G.W. (1970a). Strong ground motion. In *Earthquake Engineering*, Ed. R.L.Wiegel, Prentice-Hall, Upper Saddle River, New Jersey.

Housner, G.W. (1970b). Design spectrum. In *Earthquake Engineering*, Ed. R.L. Wiegel, Prentice-Hall, Upper Saddle River, New Jersey.

Housner, G.W. (1975). Measures of severity of earthquake ground shaking. *Proceedings, U.S. National Conference on Earthquake Engineering*, Ann Arbor, Michigan, 25–33.

Housner, G.W. (1997). Connections: The EERI oral history. Stanley Scott, Interviewer, Earthquake Engineering Research Institute (EERI), Oakland, California.

Housner, G.W., Martel, R.R. and Alford, J.L. (1953). Spectrum analysis of strong-motion earthquakes. *Bulletin of the Seismological Society of America*, 43, 49–71.

Hudson, D.E. (1962). Some problems in the application of spectrum techniques to strong-motion earthquake analysis. *Bulletin of Seismological Society of America*, 52, 417–430.

Hudson, D.E. (1979). *Reading and Interpreting Strong Motion Accelerograms.* Monograph, Earthquake Engineering Research Institute, Berkeley, California.

Humar, J.L. (1990). *Dynamics of Structures*. Prentice-Hall, Upper Saddle River, New Jersey.

IBC (2000). *International Building Code,* International Code Council, Falls Church, Virginia.

Idriss, I.M. (1993). Procedures for selecting earthquake ground motions at rock sites. *NIST GCR 93-625*, National Institute of Standards and Technology.

Iwan, W.D. (1994). Near-field considerations in specification of seismic design motions for structures. *Proceedings, 10th European Conference on Earthquake Engineering*, 1, 257–267.

Iwan, W.D. (1997). Drift spectrum: Measure of demand for earthquake ground motions. *ASCE Journal of Structural Engineering*, 123, 397–404.

Johnston, A.C. (1996). Seismic moment assessment of earthquakes in stable continental regions, I. Instrumental seismicity. *Geophysical Journal International*, 124, 381–414.

Joyner, W.B. (2000). Strong motion from surface waves in deep sedimentary basins. *Bulletin of the Seismological Society of America*, 90, S95–S112.

Joyner, W.B., Warrick, R.E. and Fumal, T.E. (1981). The effect of Quaternary alluvium on strong ground motion in the Coyote Lake, California, earthquake of 1979. *Bulletin of the Seismological Society of America*, 71, 1333–1349.

Kanamori, H. (1978). Quantification of earthquakes, *Nature*, 271, 411–414.

Kayen, R.E. and Mitchell, J.K. (1997). Assessment of liquefaction potential during earthquakes by Arias intensity. *ASCE Journal of Geotechnical And Geoenvironmental Engineering*, 123, 1162–1174.

Kim, J., and Collins, K.R. (2002). Closer look at the drift demand spectrum. *ASCE Journal of Structural Engineering*, 123, 942–945.

Kinemetrics (2003). Strong Motion Analyst (SMA), software package, Kinemetrics, Inc., Pasadena, California.

Kircher, C.A. (1999). United States building code approach to variations in regional seismicity. *1999 Annual Meeting of the New Zealand Society of Earthquake Engineering*, Rotorua, New Zealand.

Krawinkler, H. and Nassar, A.A. (1992). Seismic design based on ductility and cumulative damage demands and capacities. In *Nonlinear Seismic Analysis and Design of Reinforced Concrete Buildings*, Eds. Fajfar and Krawinkler, Elsevier Applied Science, New York.

Lay, T. and Wallace, T.C. (1995). *Modern Global Seismology*. Academic Press, San Diego.

Lee, W.H.K., Shin, T.C, Kuo, K.W., Chen, K.C. and Wu, C.F. (2001). Data files from CWB free-field strong-motion data from the 21 September Chi-Chi, Taiwan, earthquake. *Bulletin of Seismological Society of America*, 91, 1390.

Lee, Y. and Anderson, J.G. (2000). Potential for improving ground-motion relations in southern California by incorporating various site parameters. *Bulletin of the Seismological Society of America*, 90, S170–S186.

Leyendecker, E.V., Hunt, R.J., Frankel, A.D., and Rukstales, K.S. (2000). Development of maximum considered ground motion maps. *Earthquake Spectra*, 16, 21–40.

Lin, K.W., Shakal, A., Huang, M., Stephens, C. and Savage, W. (2002). Dissemination of strong-motion data via Internet quick report and Internet data report at the CISN engineering data center. *Proceedings, SMIP02 Seminar on Utilization of Strong-Motion Data*, Los Angeles, 115–126.

Mahin, S.A. and Bertero, V.V. (1976). Problems in establishing and predicting ductility in aseismic design. *Proceedings, International Symposium on Earthquake Structural Engineering*, St. Louis, Missouri, 613–628.

Mahin, S.A. and Bertero, V.V. (1981). An evaluation of inelastic seismic design spectra. *ASCE Journal of Structural Division*, 107, 1777–1795.

Mahin, S.A. and Lin, J. (1983). Construction of inelastic response spectra for single-degree-of-freedom systems. *UCB/EERC-83/17*, Earthquake Engineering Research Center, University of California, Berkeley.

Malhotra, P.K. (1999). Response of buildings to near-field pulse-like ground motions. *Earthquake Engineering and Structural Dynamics*, 28, 1309–1326.

Marone, C. and Scholz, C.H. (1988). The depth of seismic faulting and the upper transition from stable to unstable slip regimes. *Geophysical Research Letters*, 15, 621–624.

MATLAB (2002). Product of The Mathworks, Inc., Natick, Massachusetts.

McGuire, R.K., Silva, W.J. and Costantino, C.J. (2001). Technical basis for revision of regulatory guidance on design ground motions: hazard- and risk-consistent ground motion spectra guidelines. *NUREG/CR-6728,* U.S. Nuclear Regulatory Commission, Washington, DC.

Miranda, E. and Bertero, V.V. (1994). Evaluation of strength reduction factors for earthquake-resistant design. *Earthquake Spectra*, 10, 357–379.

Moores, E.M. and Twiss, R.J. (1995). *Tectonics*. W.H. Freeman and Company, New York.

Naeim, F. and Kircher, C.A. (2001). On the damping adjustment factors for earthquake response spectra. *The Structural Design of Tall Buildings*, 10, 361–369.

Newmark, N.M. and Hall, W.J. (1982). *Earthquake Spectra and Design*. Monograph, Earthquake Engineering Research Institute, Berkeley, California.

Newmark, N.M., Blume, J.A. and Kapur, K.K. (1973). Seismic design spectra for nuclear power plants. *ASCE Journal of Power Division*, 99, 287–303.

Niazi, M. and Bozorgnia, Y. (1989). Behavior of vertical ground motion parameters in the near-field. *Seismological Research Letters*, 60, 4.

Niazi, M. and Bozorgnia, Y. (1991). Behavior of near-source peak vertical and horizontal ground motions over SMART-1 array, Taiwan. *Bulletin of the Seismological Society of America*, 81, 715–732.

Niazi, M. and Bozorgnia, Y. (1992). Behavior of near-source vertical and horizontal response spectra at SMART-1 array, Taiwan. *Earthquake Engineering and Structural Dynamics*, 21, 37–50.

Nigam, N.C. and Jennings, P.C. (1968). Digital calculation of response spectra from strong-motion earthquake records. Earthquake Engineering Research Laboratory, California Institute of Technology, Pasadena.

NISEE (1999). *National Information Service for Earthquake Engineering Software Library*, University of California, Berkeley.

Ordaz, M., Huerta, B. and Reinoso, E. (2003). Exact computation of input-energy spectra from Fourier amplitude spectra. *Earthquake Engineering and Structural Dynamics*, 32, 597–605.

Park, S. and Elrick, S. (1998). Predictions of shear-wave velocities in Southern California using surface geology. *Bulletin of the Seismological Society of America*, 88, 677–685.

Park, Y.J. and Ang, A.H.S. (1985). Mechanistic seismic damage model for reinforced concrete. *ASCE Journal of Structural Engineering*, 111, 722–739.

Press, W.H., Teukolsky, S.A., Vetterling, W.T., and Flannery, B.P. (1992). *Numerical Recipes in C, the Art of Scientific Computing*. 2nd ed., Cambridge University Press, Cambridge, United Kingdom.

Reinhorn, A.M., Barron, R., Valles, R.E. and Sivaselvan, M.V. (1999). NSPECTRA: Nonlinear analysis program for inelastic spectra with degradation and deterioration of structural systems. Department of Civil, Structural, and Environmental Engineering, State University of New York at Buffalo, http://civil.eng.buffalo.edu/nspectra/

Richter, C.F. (1958). *Elementary Seismology*. W.H. Freeman and Company, San Francisco.

Rodriguez-Marek, A., Bray, J.D. and Abrahamson, N.A. (2001). An empirical geotechnical seismic site response procedure. *Earthquake Spectra*, 17, 65–87.

Rosenblueth, E. (1980). Characteristics of earthquakes. In *Design of Earthquake Resistant Structures*, Ed. E. Rosenblueth, John Wiley & Sons, New York.

Sadigh, K., Chang, C.Y., Abrahamson, N.A., Chiou, S.J. and Power, M.S. (1993). Specification of long-period ground motions: Updated attenuation relationships for rock site conditions and adjustment factors for near-fault effects. *Proceedings, ATC-17-1 Seminar on Seismic Isolation, Passive Energy Dissipation, and Active Control*, San Francisco, 1, 11–23.

Sadigh, K., Chang, C.Y., Egan, J.A., Makdisi, F. and Youngs, R.R. (1997). Attenuation relationships for shallow crustal earthquakes based on California strong motion data. *Seismological Research Letters*, 68, 180–189.

Savy, J.B., Bernreuter, D.L. and Chen, J.C. (1987). A methodology to correct for effect of the local site characteristics in seismic hazard analyses In *Ground Motion and Engineering Seismology*, Ed. A.S. Cakmak, Elsevier, Amsterdam, 243–255.

SEAOC (1999). *Recommended Lateral Force Requirements and Commentary*, 7th ed., Seismology Committee, Structural Engineers Association of California.

Seed, H.B., Ugas, C. and Lysmer, J. (1976). Site-dependent spectra for earthquake-resistant design. *Bulletin of the Seismological Society of America*, 66, 221–243.

Seekins, L.C., Brady, A.G., Carpenter, C. and Brown, N. (1992). Digitized strong-motion accelerograms of North and Central American Earthquakes 1933-1986. CD-ROM, *U.S. Geological Survey Digital Data Series (DDS) #7*.

Shin, T.C., Kuo, K.W., Lee, W.H.K., Teng. T.L. and Tsai, Y.B. (2000). A preliminary report on the 1999 Chi-Chi (Taiwan) earthquake. *Seismological Research Letters*, 71, 24–30.

Silva, W. (1997). Characteristics of vertical strong ground motions for applications to engineering design. *NCEER-97-0010,* National Center for Earthquake Engineering Research, Buffalo, New York.

Somerville, P. (1998). Development of an improved representation of near-fault ground motions. *Proceedings, SMIP98 Seminar on Utilization of Strong-Motion Data*, Oakland, California, 1–20.

Somerville, P. (2000). New developments in seismic hazard estimation. *Proceedings, 6th International Conference on Seismic Zonation*, Palm Springs, California, 25 p.

Somerville, P., Collins, N., Abrahamson, N, Graves, R. And Saikia, C. (2001). Ground motion attenuation relations for the central and eastern United States. *U.S. Geological Survey*, *Award 99HQGR0098,* final report.

Somerville, P.G., Smith, N.F., Graves, R.W. and Abrahamson, N.A. (1997). Modification of empirical strong ground motion attenuation relations to include the amplitude and duration effects of rupture directivity. *Seismological Research Letters*, 68, 199–222.

Spudich, P., Joyner, W.B., Lindh, A.G., Boore, D.M., Margaris, B.M. and Fletcher, J.B. (1999). SEA99: A revised ground motion prediction relation for use in extensional tectonic regimes. *Bulletin of the Seismological Society of America*, 89, 1156–1170.

Stewart, J.P. (2000). Variations between foundation-level and free-field earthquake ground motions. *Earthquake Spectra*, 16, 511–532.

Stewart, J.P., Chiou, S. J., Bray, J.D., Graves, R.W., Somerville, P.G. and Abrahamson. N.A. (2001). Ground motion evaluation procedures for performance-based design. *PEER 2001/09*, Pacific Earthquake Engineering Research Center, University of California, Berkeley.

Stewart, J.P., Liu, A.H. and Choi, Y. (2003). Amplification factors for spectral acceleration in tectonically active regions. *Bulletin of Seismological Society of America*, 93, 332–352.

Takahashi, Y., Rabins, M.J. and Auslander, D.M. (1972). *Control and Dynamic Systems*. Addison-Wesley Publishing Co., Reading, Massachusetts.

Toro, G.R., Abrahamson, N.A. and Schneider, J.F. (1997). Model of strong ground motions from earthquakes in central and eastern North America: Best estimates and uncertainties. *Seismological Research Letters*, 68, 41–57.

Travasarou, T., Bray, J.D. and Abrahamson, N.A. (2003). Empirical attenuation relationship for Arias intensity. *Earthquake Engineering and Structural Dynamics*, 32, 1133–1155.

Trifunac, M.D. and Brady, A.G. (1975). A study on the duration of strong earthquake ground motion. *Bulletin of Seismological Society of America*, 65, 581–626.

Tsai, Y.B. and Huang, M.W. (2000). Strong ground motion characteristics of the Chi-Chi, Taiwan earthquake of September 21, 1999. *Earthquake Engineering and Engineering Seismology*, 2, 1–21.

Uang, C.M. (1991). Establishing R (or R_w) and C_d factors for building seismic provisions. *ASCE Journal of Structural Engineering*, 117, 19–28.

Uang, C.M. and Bertero, V.V. (1988). Implications of recorded earthquake ground motions on seismic design of building structures. UCB/EERC-88/13, Earthquake Engineering Research Center, University of California, Berkeley.

Uang, C.M. and Bertero, V.V. (1991). UBC seismic serviceability regulations: Critical review. *ASCE Journal of Structural Engineering*, 117, 2055–2968.

Uang, C.M. and Bertero, V.V. (1990). Evaluation of seismic energy in structures. *Earthquake Engineering and Structural Dynamics,* 19, 77–90.

UBC (1994). *Uniform Building Code* 1994 ed., Vol. 2, International Conference of Building Officials, Whittier, California.

UBC (1997). *Uniform Building Code.* 1997 ed., Vol. 2, International Conference of Building Officials, Whittier, California.

UBC-IBC Structural (2000*). UBC-IBC Structural Comparison and Cross Reference (1997-2000).* International Conference of Building Officials, Whittier, California.

United States Geological Survey (2002). Notes on the processing of digitally recorded data. Http://nsmp.wr.usgs.gov/processing.html#notes

Vidic, T., Fajfar, P. and Fischinger, M. (1994). Consistent inelastic design spectra: Strength and displacement. *Earthquake Engineering and Structural Dynamics*, 23, 507–521.

Wald, D.J., Quitoriano, V., Heaton, T.H., Kanamori, H., Scrivner, C.W. and Worden, C.B. (1999). TriNet "shakemaps": Rapid generation of peak ground motion and intensity maps for earthquakes in southern California. *Earthquake Spectra*, 15, 537–555.

Watabe, M., Tohido, M., Chiba, O. and Fukuzawa, R. (1990). Peak accelerations and response spectra of vertical strong motions from near-field records in USA. *Proceedings, 8th Japan Earthquake Engineering Symposium*, 1, 301–306.

Wells, D.L. and Coppersmith, K.J. (1994). New empirical relationships among magnitude, rupture length, rupture width, rupture area, and surface displacement. *Bulletin of the Seismological Society of America*, 84, 974–1002.

Whittaker, D. and Jury, R.D. (2000). Seismic design loads for storage tanks. *Proceedings, 12th World Conference on Earthquake Engineering*, Paper No. 2376, Auckland, New Zealand.

Wills, C.J. and Silva, W. (1998). Shear-wave velocity characteristics of geologic units in California. *Earthquake Spectra*, 14, 533–556.

Wills, C.J., Petersen, M., Bryant, W.A., Reichle, M., Saucedo, G.J., Tan, S., Taylor, G. and Treiman, J. (2000). A site-conditions map for California based on geology and shear-wave velocity. *Bulletin of the Seismological Society of America*, 90, S187–S208.

Youngs, R.R., Chiou, S.J., Silva, W.J. and Humphrey, J.R. (1997). Strong ground motion attenuation relationships for subduction zone earthquakes. *Seismological Research Letters*, 68, 58–73.

Zoback, M.L. (1992). First- and second-order patterns of stress in the lithosphere: The world stress map project. *Journal of Geophysical Research*, 97, 11,703–11,728.

CyberShake

From SCECpedia

CyberShake is a SCEC research project that is working to develop a physics-based computational approach to probabilistic seismic hazard analysis (PSHA). The CyberShake approach uses full 3D wave propagation simulations to forecast ground motions that will be produced by specific ruptures which is expected to produced significantly more accurate estimates for many sites than commonly used empirical-based ground motion decay attenuation relationships.

Contents

Physics-based Probabilistic Seismic Hazard Analysis

SCEC's CyberShake project utilizes 3D simulations and finite-fault rupture descriptions to compute deterministic (scenario-based) and probabilistic seismic hazard in Southern California. Computational demands are intense, requiring parallel algorithms and high throughput workflows. Long period effects such as coupling of directivity and basin response that cannot be captured with standard approaches are clearly evident in the recently completed CyberShake 1.0 hazard map. Moreover, CyberShake allows for rapid recomputation of the hazard map to reflect short-term probability variations provided by operational earthquake forecasting. Going beyond traditional hazard analysis, event-specific phenomena can also be identified and analyzed through examination of the individual ground motion waveforms. This process highlights the importance of key elements in the Earthquake Rupture Forecast that are required by the simulation approach, including magnitude-rupture area scaling, aleatory and epistemic magnitude variability and spatio-temporal rupture characterization.

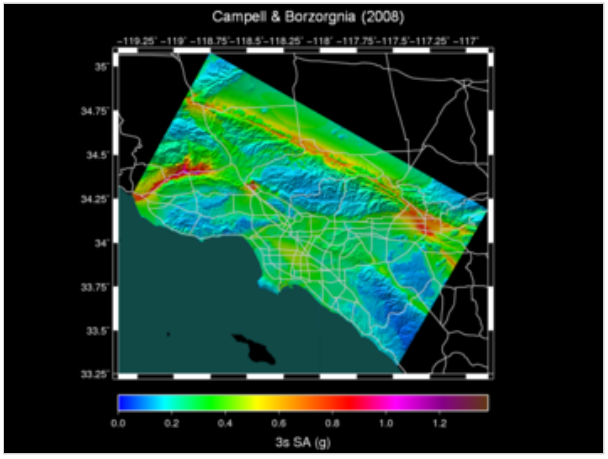

Fig 1: UCERF2.0-based seismic hazard map using Campbell and Bezorgnia (2008) Ground Motion Prediction Equation

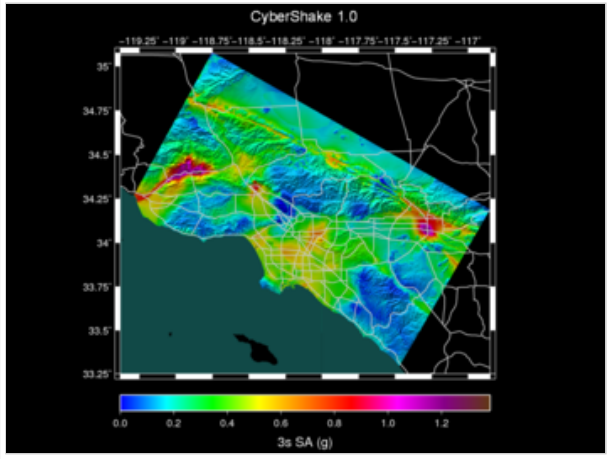

Fig 2: CyberShake results using C & B as background model.

Computational PSHA

CyberShake is a computationally intensive way to improve standard probabilistic seismic hazard analysis. The CyberShake method for calculating long-term seismic hazard analysis is not yet the standard method for calculating long-term seismic hazards in the United States. The CyberShake computational technique has not been possible until recent improvements in 3D earth models, in 3D wave propagation software, in HPC computational resources, in large-scale workflows and data management. SCEC geoscientists are leading the scientific verification and validation of the CyberShake computational approach and SCEC/CME computer scientists are leading development of computational tools and techniques needed to implement the CyberShake calculations at the necessary scale. The

Fig 3: Seismic hazard maps showing difference between four official GMPE's.

CyberShake computational approach improves on standard PSHA calculations in a number of ways including:

1. Wave propagation simulations more accurately describe the distribution of ground motions than the currently used ground motion prediction equations [GMPE].
2. Wave propagation simulations provide good estimates of both ground motion amplitude as well as ground motion duration. Ground motion duration is not available from empirical peak ground motion methods.

Fig 4: Integrated Cybershake with each of the four official GMPE's.

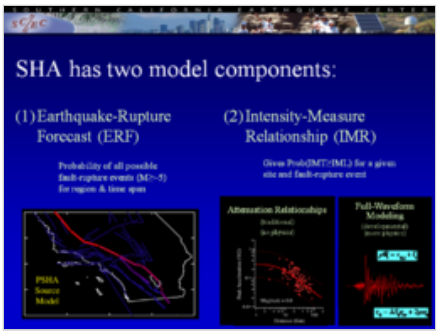

Fig 5: SCEC scientific software models probabilistic seismic hazard calculations using two main types of computational models (1) earthquake rupture forecasts and (2) intensity measure relationships. SCEC's OpenSHA software implementing earthquake rupture forecast models (including UCERF2.0 and planned UCERF3.0) and attenuation relationships. SCEC's CyberShake Project implements the most-advanced, and computationally-expensive, physics-based, full waveform modeling-based PSHA calculations.

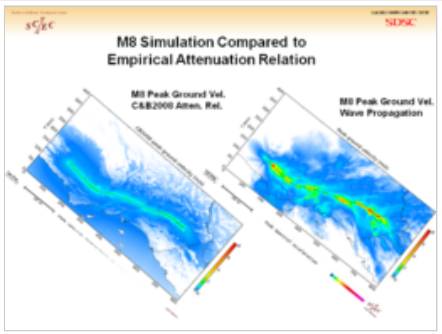

Fig 6: These two maps show how the distribution of ground motions differ between wave propagation simulations and GMPE, even when the distribution of ground motion by distances is quite similar.

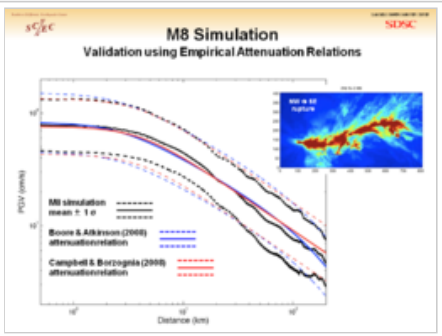

Fig 7: Ground Motion prediction equations and wave propagation simulations show similar distribution of peak ground motion by distance. However, the wave propagation simulation distribution shows significantly more realistic distribution reflecting directivity and basin structure response.

CyberShake Seismic Hazard Model Calculations

CyberShake calculations are performed using a number of different input confirmations, and computational software. SCEC reseachers define a calculation of interest as a Study. To qualify as a Study, the calculation needs to be clearly defined so we can calculate the types and volume of output data.

As of April 2013, we are moving the CyberShake Study numbering scheme to a Year.Month format based on date the simulations are started.

- CyberShake Study 16.8
- CyberShake Study 15.12
- CyberShake Study 15.4
- CyberShake Study 14.2

- CyberShake Study 13.4

Earlier CyberShake number Study numbers, not based on dates, are shown below.

- CyberShake Study 2.2
- CyberShake 2.0
- CyberShake 1.5
- CyberShake 1.4
- CyberShake 1.3
- CyberShake 1.2
- CyberShake 1.1
- CyberShake 1.0

Here is a comparison of CyberShake studies.

- Comparison of CyberShake Studies

CyberShake Curves

- 1 Hz CyberShake Curves
- Comparison Curves
- Hybrid Deterministic/Stochastic Curves
- Fall 2011 Production Run Curves

Related Entries

- CyberShake Central California
- 2016 CyberShake database migration
- CyberShake output data formats
- CyberShake Source Filtering
- High Frequency CyberShake
- UCVM
- UCERF3.0
- CyberShake Workplan
- CyberShake SmartMap
- CyberShake Workflows
- CyberShake Computational Estimates
- UCERF3.0
- CyberShake SmartMap
- CyberShake Testing
  - Testing Parameters
- CyberShake Status
- CyberShake PBR
- SEISM Project
- Geoinformatics Project
- Accessing CyberShake Seismograms
- First CyberShake Allocation Request (2005) (http://hypocenter.usc.edu/research/CyberShake/SCEC_PSHA_TeraGrid_Allocation_Request.pdf)

References

- Graves, R., Jordan, T. H., Callaghan, S., Deelman, E., Field, E. H., Juve, G., Kesselman, C., Maechling, P., Mehta, G., Okaya, D., Small, P., Vahi, K. (2010), CyberShake: A Physics-Based Seismic Hazard Model for Southern California, Pure and Applied Geophysics, Accepted for Publication March, 2010
- Graves, R., S. Callaghan, E. Deelman, E. Field, N. Gupta, T. H. Jordan, G. Juve, C. Kesselman, P. Maechling, G. Mehta, D. Meyers, D. Okaya and K. Vahi (2008) Physics Based Probabilistic Seismic Hazard Calculations for Southern California,14th World Conference on Earthquake Engineering, October, 2008, Beijing China
- The SCEC CyberShake Project: A Computational Platform for Full Waveform Seismic Hazard Analysis Robert Graves (USGS), Scott Callaghan (USC), Patrick Small (USC), Gaurang Mehta (USC), Kevin Milner (USC), Gideon Juve (USC), Karan Vahi (USC), Edward Field (USGS), Ewa Deelman (USC/ISI), David Okaya (USC), Philip Maechling (USC), Thomas H. Jordan (USC) - SSA April 2011

- Cui, Y., Poyraz, E., Callaghan, S., Maechling, P., Chen, P. and Jordan, T. H., Accelerating CyberShake Calculations on XE6/XK7 Platforms of Blue Waters, Blue Waters and XSEDE Extreme Scaling Workshop 2013, August 15-16, Boulder, 2013.

See Also

- Main Page
- SCEC Home Page (http://www.scec.org)

CyberShake Data Request

From SCECpedia

CyberShake Data Request Web Site is a first stage in automating CyberShake data requests. The variety of CyberShake data products is growing, so we propose to develop a web site that will help user request CyberShake data. We will use current CyberShake data requests to try out the proposed data request system. The goal of this first system is to generate a well defined data request. For now, we will continue to process the data requests manually, but will look to automating the retrieval if useful.

Contents

Prototype CyberShake Data Request Site

- CyberShake Data Request Site Prototype (https://scec.usc.edu/it/CyberShake_Data_Request).

General Workflow

At a SCEC URL, the user is presented with a series of choices that selects some subset of all our CyberShake data products. The user makes all the choices and presses send and the web page generates a data request specification that someone can then processes and post. The user can check on the status of their request while waiting.

Initially, the user can select from an official CyberShake Study (13.4, 2.2, or 1.0) and then select the map from which the results should be retrieved (e.g. RWG CVM-S). The user can then select the sites from which they would like the results, either visually via a map or textually via a table. Should they wish to have results from the whole map, there is the option to "select all" the sites. After this, the user is presented with a list of the possible data products that the system can retrieve. We are developing support for the following data products:

1. Maps
2. Hazard Curves
3. Seismograms
4. Peak Amplitudes

5. List of Ruptures and Disaggregation

Upon selecting the data product desired, filling out their e-mail and name, the system then proceeds to perform the necessary computations to serve that request. When it is finished, the system notifies the user via e-mail and a download link is provided.

The system was designed with the following use cases in mind.

Use Case 1

User would like the Graves-Pitarka CVM-S hazard map from CyberShake Study 13.4. User can go to the site, select 13.4, Graves-Pitarka CVM-S, all sites, with data product of map. The system will then calculate and return that map.

Use Case 2

User would like the hazard curve for USC from the Graves-Pitarka CVM-S map from CyberShake Study 13.4. User can go to site, select 13.4, Graves-Pitarka CVM-S, site USC only, and then select hazard curve. The system will generate the hazard curve and notify the user.

Use Case 3

User would like to see visual seismograms available for USC from the AWP CVM-H map from CyberShake Study 13.4. User can go to the site, select 13.4, AWP CVM-H, site USC, and then select seismograms as the data product. The system will generate images and return all applicable seismograms in PNG format.

Use Case 4

User would like to get a list of the top 20 sources that contribute to the hazard at USC from the Study 13.4 AWP CVM-S map. User can go to the site, select 13.4 , AWP CVM-S, site USC, and then select rupture list as the data product, sorted by top contributors.

Use Case 5

User would like to get a list of the peak amplitudes for given periods at USC from the Study 13.4 AWP CVM-H map. User can go to the site, select 13.4, AWP CVM-H, site USC, and then select the data product of peak amplitudes.

XML Document

When the front-end steps are completed a XML document is generated. The format of this XML document is:

```
<datarequest>
   <first_name>John</first_name>
   <last_name>Doe</last_name>
   <email>john.doe@usc.edu</email>
   <study>CyberShake 13.4</study>
   <map>AWP CVM-S</map>
```

```
  <sites>
    <site>USC</site>
  </sites>
  <ruptures>none</ruptures>
  <product>
    <name>Hazard Curves</name>
    <format>log-linear</format>
    ...
  </product>
</datarequest>
```

This is then used by the backend processor, described below, to finalize and fulfill the request.

Backend Workflow

The backend is comprised of three components:

1. csdrs.py
2. requestprocessor.py
3. Separate Python scripts for each data product (e.g. map.py, peakamps.py, etc.)

csdrs.py is an interface Python script allowing for the following functionality:

1. List requests (state) - get a list of all requests in the system matching state.
2. Submit request (request XML) - submits request XML to be parsed by requestprocessor.py, returns a request ID
3. Cancel request (request ID) - halts processing on request ID
4. Status of request (request ID) - gets the status of a particular request ID

When a job is submitted, it spawns a new requestprocessor.py and records the id of that thread (for canceling a request). Requestprocessor.py is intended to be a background process and takes an XML document as input.

User Choices CyberShake Data Sets

Initial User Choices of data sets available:

1. CyberShake 1.0 Map
2. CyberShake 2.2 Map
3. CyberShake 13.4 Map

Other User Choices of data sets:

1. All sites rupture generator 2.X
2. All sites with new rupture generator 3.x
3. PBR sites
4. 10Hz sites
5. CVM-H sites

User Choices Output Formats

Data products output formats (user-define options):

1. Maps (POE@IMT or IMT@POE)
2. Curves (IMT duration POE)
3. Rupture Sets (ERF, Rupture Generator version, Site of Interest)
4. Seismograms (site name, simulation id)
5. Amplitudes (site name, rupture set, imt)
6. ERF Information (erf)
7. Velocity Profiles (site, cvm, sgt)
8. Single Component Hazard curves (site, rotation angle, imt)

Progress

The CyberShake data request system is presently being worked on and is currently in the pre-alpha stage. Presently, we have the following features:

1. Select from CyberShake studies or from a combination of rupture forecasts, SGT generators, rupture generators, velocity models, and frequencies
2. Select sites from a visual (on Google Maps) list of sites as well as a standard row-based one
3. Filter sites based off of categories (e.g. precarious rocks, broadband sites, etc.)
4. Select relevant data products and configure options for them
5. Generates well-formed XML document for either human or machine use
6. Administrative panel to see requests and update links for download
7. Check on status of request via web interface

Related Entries

- CyberShake
- CME Project

Waveform Data
Earthquake Parametric Data
Special Data Sets
SCEDC Citation Policy

Downloads

Special Data Sets

3D Velocity Model for Southern California

Purpose

The purpose of the Three-Dimensional Community Velocity Model for Southern California is to provide a unified reference model for the several areas of research that depend of the subsurface velocity structure in their analysis. These include strong motion modeling, seismicity location, and tomographic velocity modeling. It is also hoped that the geologic community will find the basin models useful because they are based on structures and interfaces that are largely derived from geologic structure models. The deeper sediment velocities themselves are obtained from empirical relationships that take into account age of the formation and depth of burial. The coefficients of these relationships are calibrated to sonic logs taken from boreholes in the region. Shallow sediment velocities are taken from geotechnical borehole measurements. Hardrock velocities are based on tomographic studies.

Use, Documentation and Models

The velocity models are a Fortran code and associated files that are downloaded, compiled, and run locally. The user queries the models by creating an input file of latitude, longitude, and depth values, and the model returns Vp, Vs, and density at each of those points. Some web based interfaces to handle model queries have been developed and are available from the SCEC Community Modeling Environment.

The Community Velocity Model has been released in progressive versions. It is now in version 4. It is recommended to use version 4 over previous versions.

Version 4

Version 4 is based on Version 3 with the following differences:

- San Bernardino Valley: A new San Bernardino Valley basement is based on recent USGS inversion of gravity data confirmed by comparison to a seismic reflection line. The new model features a deep trough in the central valley, in contrast to the previous flat-bottomed valley model. The new basement joins smoothly to the relatively shallow Chino basin to the west.
- Salton Trough: A new model is motivated by the needs of TeraShake simulations of southern San Andreas fault events. Depth to basement is defined by a combination of seismic refraction surveys, inversion of gravity observations, surface geology, and boreholes. Sediment velocity-depth gradients depend on the nature of the basement, smoothing merging into deep metasedimentary basement, and having a discontinuity above shallow crystalline basement. The model includes the portion of the Trough south of the international border.
- Vp-density: The new Vp-density relation is based on density measurements from oil well samples in the Los Angeles basin and the San Gabriel Valley, geotechnical boreholes throughout southern California, and 12 oil wells along the LARSE lines. The newly determined Vp-density ratio is constant, in contrast to the old relation. This is true even for low Vp, as defined by the geotechnical data. The new densities are

higher, for a given Vp, than the old. This will tend to lower the Poisson ratio, which will lower Vp/Vs; that is, changing the Vp-density relation produces a new Vs model.

Download Version 4.0 ~7.0 Mbytes
A "readme" file for this model is available (txt)

As part of SCEC's work in producing SCEC Community Velocity Model -Harvard (CVM-H), Community Velocity Model version 4 (CVM-4) was evaluated. To build the CVM-4 meshes, a "bug-fix" version by Geoff Ely at USC was developed.

Download Bug-fix Version 4.0.
Download Bug-fix Version 4.0 md5sum file.

Version 3
Reference: Kohler, M., H. Magistrale, and R. Clayton, 2003, Mantle heterogeneities and the SCEC three-dimensional seismic velocity model version 3, Bulletin Seismological Society of America 93, 757-774.*

Download Version 3.0 ~6.2 Mbytes
A "readme" file for this model is available (txt)

Version 2
Version 2.2 of the SCEC 3D velocity model was released on Sept 7, 2000. This version of the model is a superset of the first version of the model that adds:

- A geotechnical layer on the top of the model basins
- A laterally varying background velocity
- A laterally varying Moho depth
- The Salton Trough

Reference: Magistrale, H., S. Day, R. Clayton, and R. Graves, 2000, The SCEC southern California reference three-dimensional seismic velocity model version 2, Bulletin Seismological Society of America, 90 (6B), S65-S76.*

Download Version 2.2 ~1.7 Mbytes
A "readme" file for this model is available (txt)

Version 1
Version 1 of the 3D velocity model is composed of the following elements:

- Basin Models: Detailed models for the Los Angeles, San Fernando, San Bernardino, and Ventura Basins are included. The models are based on boundaries between significant stratigraphic units. These boundaries are represented by a number of surfaces (depth as a function of lat and lon), which are valid within specified polygonal regions. The lat-lon coordinates of a particular point are used to determine which surfaces apply, and the depth of the point is used to determine which surfaces to interpolate between.
- Background Velocity: A smoothed version of the standard model used to locate earthquakes in southern California is used.
- Moho Depth: A constant depth to Moho of 32 km is used.
- Mantle Velocity: The upper mantle between 32 and 60 km is a gradient from 7.8 to 7.9 km/s, and is constant below 60 km.

Reference: Magistrale, H., K. McLaughlin, and S. Day, 1996, A geology based 3-D velocity model of the Los Angeles basin sediments, Bulletin Seismological Society of America 86, 1161-1166.*

Download Model and Code ~1.5 Mbytes

Previous Meetings:
SCEC Meeting, Oct 1997
CIT Workshop, Nov 1997

* The Version 2 manuscript contains the most complete description. The Version 3 model is the same as Version 2, but with the addition of an upper mantle model.

↑

Selection of Near-Fault Pulse Motions for Use in Design

C.P. Hayden, J.D. Bray, N.A. Abrahamson & A.L. Acevedo-Cabrera
University of California, Berkeley, CA, USA

SUMMARY:
Earthquake ground motions in the near-fault region can have intense, double-sided pulses in the velocity-time series that can be damaging to structures. Velocity pulses often result from the effects of forward-directivity (i.e., rupture propagation toward the site). The relative contribution of pulse-type motions to the overall seismic hazard should be considered when selecting records in a suite of design ground motions for a site in the near-fault region. This study classifies 390 records as pulse or non-pulse motions using a new classification scheme. A straightforward model is developed to estimate the proportion of pulse motions as a function of closest site-to-source distance and the epsilon of the seismic hazard. This proportion can then be used to estimate the number of pulse-type motions to include within a suite of design ground motions for use in time-history analysis to represent properly the relative contribution of pulse motions to the seismic hazard.

Keywords: Ground Motion, Forward-Directivity, Near-Fault, Pulse, Velocity

1. INTRODUCTION

Earthquake records at small site-to-source distances often have different characteristics than those recorded at larger distances. Sites in the near-fault region may be influenced by the effects of forward-directivity (FD: rupture towards the site) or backward-directivity (BD: rupture away from the site). Forward-directivity often results in early arriving, large double-sided pulses in the velocity-time series.

These intense velocity pulse motions can affect adversely the seismic performance of structures (e.g., Anderson and Bertero, 1987; Hall et al., 1995; Alavi and Krawinkler, 2000). The period of the pulse in relation to the fundamental period of the structure also greatly affects structural performance (Anderson and Bertero, 1987). However, these large pulses do not always occur, even for sites located in the FD region. Other near-fault phenomena, including fling-step, basin edge effects, asperities along fault rupture and others, can produce intense pulses in the velocity-time series as well.

When selecting a suite of design motions for time-history analysis, it is the current state of practice in the United States (e.g., ASCE, 2005) that the magnitude, distance and other parameters are similar to those that control the hazard (e.g., obtained by a PSHA disaggregation by distance and magnitude). Unfortunately, there is a lack of guidance on how to include pulse-like motions into a suite of ground motions, even though the unique nonstationary characteristics of pulse-like motions can greatly affect structural performance (e.g., Anderson and Bertero, 1987; Alavi and Krawinkler, 2000). In this study, near-fault ground motions are classified as pulse or non-pulse motions using a new classification scheme. A straightforward equation is developed to estimate the occurrence of pulse motions in the near-fault region. This equation can be used with the results of a standard probabilistic hazard analysis (PSHA) to provide guidance on an appropriate number of pulse type motions to include in a suite for use in dynamic analysis of structures.

2. NEAR-FAULT GROUND MOTIONS

When a fault ruptures toward a site, a rupture velocity that is slightly slower than the shear wave velocity results in the accumulation of seismic energy released during rupture (Somerville et al., 1997). This generally results in a large, double-sided pulse early in the velocity-time series. An opposite effect is observed in the backward-directivity region, where recordings generally have long durations but low amplitudes.

The radiation pattern of horizontally propagating shear waves (SH) has its maxima aligned along the strike of the fault and the observed pulse is the result of the superposition of these SH waves (Somerville et al., 1997). These SH waves are oriented normal to the fault and as a result the pulse is also oriented normal to the fault plane. Forward-directivity occurs for both strike-slip and dip-slip faults. In the case of strike-slip faults, sites located in the direction of fault rupture and at the end of the fault are typically most influenced by forward-directivity. For dip-slip faults, sites located up-dip of the rupture plane are generally most affected by forward-directivity.

Somerville et al. (1997) identify relatively simple parameters based on source-site geometry that can be used to estimate the effects of directivity on the response spectra, ratio of fault normal to fault parallel spectra, and duration. Later, Abrahamson (2000) recommended decreasing the maximum amount of long period spectral amplification estimated for the effects of FD for strike-slip earthquakes. Spudich and Chiou (2008) derive a more complex model to estimate the spatial variations of ground motions due to the effects of directivity. The Spudich and Chiou (2008) model offers several advantages over the older Somerville et al. (1997) model and estimates approximately half the amplification or deamplification due to directivity compared to the Somerville et al. (1997) model.

Directivity, fling-step, and other possible phenomena contribute to the characteristics of near-fault motions that are often quite distinct from more distant records. The differences are often most apparent in the velocity-time series. Bray and Rodriguez-Marek (2004) identify key parameters in the characterization of forward-directivity pulse motions including amplitude (PGV: peak ground velocity), velocity pulse period, and number of significant cycles. The amplitude of a pulse is often much larger than the median PGV as predicted from the Next Generation Attenuation (NGA) ground motion prediction equations (see Abrahamson et al., 2008 for a summary of the NGA models). The period of the pulse is also important to the seismic performance of structures. If the period of the pulse and fundamental period of the structure align, resonance can greatly increase the demands on a structure (Anderson and Bertero, 1987). A large number of significant cycles can be more demanding to a structure. Fortunately, in the case of forward-directivity, often only one or two significant cycles occur. Bray and Rodriguez-Marek (2004) used largely a qualitative classification scheme, based on their judgment, to develop a database of pulse motions likely caused by forward-directivity. This work was updated in Bray et al. (2009).

Recent work by Shahi and Baker (2011) also examines the occurrence of near-fault pulses by using a wavelet transform procedure (Baker, 2007) to extract pulse-like signals from velocity-time series and classify each recording as pulse-like or non-pulse-like. Their algorithm is quantitative but requires subjective thresholds which are unavoidable when classifying ground motions into binary categories. Using this database of pulse and non-pulse motions, they derive a model of the probability of observing a pulse using several parameters. Modifications are made to a traditional PSHA calculation to better account for near-fault ground motion characteristics.

3 PULSE MOTION CLASIFICATION

3.1 Dataset Selection

In this study, a new classification scheme was developed to distinguish pulse motions from non-pulse motions. All ground motion data were from the 2005 NGA dataset (Chiou et al., 2008) used to develop

the NGA West ground motion prediction equations. Records with moment magnitudes greater than 6.0 and closest source-to-site distances (R_{RUP}) less than 30 km were selected to include motions within and just beyond the near-fault region. Distance is an independent parameter in the derived model, and this threshold is not of major importance because beyond 30 km pulse motions are quite rare. Including more distant records in the regression could actually be detrimental to the fit of the model in the near-fault region.

Motions with moment magnitudes less than 6.0 were excluded for a variety of reasons. Events with magnitudes less than around 6.0 are not as likely to produce substantial forward-directivity, and there is also precedent for magnitude thresholds of around 6.0 from previous studies (e.g., Somerville et al. 1997). Larger magnitude events often control the hazard at a site, so excluding smaller events makes the model more applicable to the magnitude range of primary interest. The model was derived using events with magnitudes of 6.0 to slightly below 8.0 and as a result, care should be taken if trying to apply the model to events outside of this range.

Records with missing acceleration-time series for either horizontal component, unknown component orientations, or those not used by Abrahamson and Silva (2008) were excluded from the database in this study. Removing motions that were excluded by Abrahamson and Silva eliminated many inappropriate motions, including those from unrepresentative earthquakes, records taken inside certain types of buildings, duplicated stations and those missing key metadata (see Abrahamson and Silva, 2008b for a more in depth discussion of excluded motions). The Kobe 1995, Port Island (0 m) record (NGA# 1114) was removed as it was influenced by liquefaction. The Landers 1992, Lucerne (NGA# 879) record had two slightly non-orthogonal horizontal components (85 degrees) but for this study they were treated as orthogonal. In total, 29 motions were excluded due to the reasons mentioned. The resulting ground motion database contained 390 records from 35 earthquakes. A complete list of the 390 motions used can be found in Appendix C of NIST (2011). Appendix C of NIST (2011) also contains additional details regarding the proposed near-fault classification scheme and the derived models discussed in this paper.

3.2 Classification Scheme

3.2.1 Summary

This study identifies pulse motions as those with one or two intense cycles of motion in the velocity-time series. The classification scheme is carried out using MATLAB and allows the automatic classification of a large number of records in a short period of time. However, the authors recognize that no classification system is perfect, particularly a relatively simple method for classifying complex velocity-time series which can be extremely complex. For this reason, the authors allowed limited human intervention in the classification scheme if the algorithm did not appear to work well and a defensible reason for making the change was established. These manual modifications did not have a substantial effect on the final result; instead they merely refined the derived equation and provide a more reasonable database of pulse records for use in suites of ground motions (NIST 2011).

There are several key parameters used in the classification scheme, which require discussion. The first is the peak-to-peak velocity (PPV). As shown in Figure 1a, the PPV is the difference between the two peaks in one cycle of motion. PPV is used as a measure of amplitude in this study instead of PGV for several reasons. There are records where the orientation that maximizes the PPV is substantially more pulse-like than the orientation that gives the maximum PGV. The PPV is likely a better indicator of the demands placed on a structure because the PPV can range from slightly more than the PGV(a one-sided pulse) to slightly less than twice the PGV (a double-sided pulse). A double-sided pulse is expected to be more demanding to a structure than a single sided pulse with the same PGV. Additionally, many near-fault pulses are likely caused by forward-directivity and are expected to be double-sided pulses, so using a parameter that captures this phenomenon is desirable.

Another parameter used is the normalized cumulative squared velocity (NCSV). The NCSV at a given time increment is the sum of the squared velocity at each preceding time increment normalized by the

sum of the squared velocity at the end of the record. The NCSV of a record increases from 0% to 100% and increases rapidly during intervals of high velocity relative to the rest of the record. In Figure 1a, the NCSV increases rapidly during the pulse as expected. As a comparison, the NCSV in Figure 1b has a much more gradual increase that is indicative of a non-pulse-like motion. The uses of NCSV and PPV in the classification scheme are discussed later.

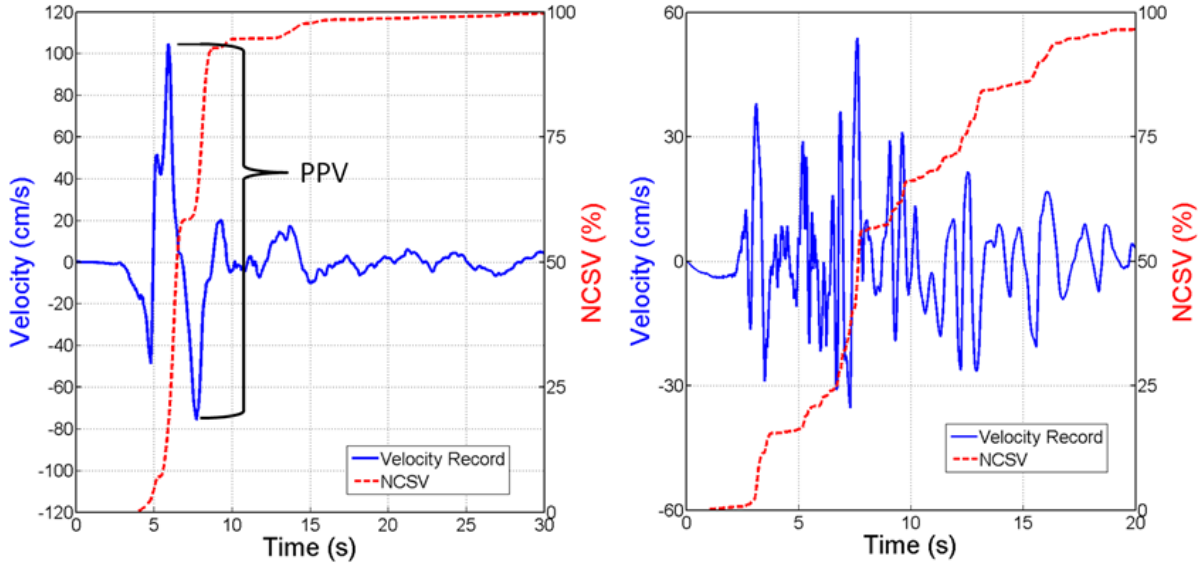

Figure 1. (a) Pulse-like recording of Imperial Valley 1979, El Centro Array #7 (NGA# 182). (b) Non-pulse-like recording of Imperial Valley 1979, Bonds Corner (NGA# 160).

3.2.2 Filtering

Filtering was applied to each time series using a low-pass, 3-pole, causal Butterworth filter to focus on the characteristics of the velocity-time series associated with the primary velocity pulse, which is in the long period range. This filtering also improves the consistency of the classification scheme. The pulse periods in this study varied from less than a second to over 6 seconds, so using a constant cutoff frequency for all records would be inappropriate.

An appropriate cutoff frequency was calculated for each motion. The predominant pulse period was estimated as the period with the largest ratio of the velocity spectra (5% damping) of the record to the median spectral velocity (from the NGA relationships). The record was then filtered using a corner period of one-third of the estimated period. Figure 2 shows an example of estimating the pulse period for the Imperial Valley 1979, Brawley Airport record. The solid line shows the ratio of the two spectra and reaches its maximum at a period of 4.65 seconds. A corner period of 4.65/3 = 1.55 seconds (a frequency of 0.645 Hz) is then used to filter the record. A more complete description of the process can be found in Appendix C of NIST (2011).

3.2.3 PPV pulse identification

The filtered, orthogonal components of the acceleration-time series were integrated to obtain velocity-time series and then rotated through all possible orientations at one degree increments. At each orientation, the largest PPV pulse is identified along with related parameters. The basic steps of the algorithm involve calculating the PPV, finding the number of cycles that have amplitudes exceeding 25% of the PPV (termed “significant cycles”), and calculating the amount the NCSV increases during the PPV pulse (termed NCSV difference). A more detailed process and associated definitions can be found in Appendix C of NIST (2011).

The NCSV difference is a good indicator of the pulse-like nature of a record. If the NCSV increases a large amount during the largest pulse of a record, it indicates that the pulse is substantially larger than

other cycles of motion in the record. The number of half cycles associated with the PPV pulse also indicates how pulse-like a record is. If a large number of half cycles are associated with the PPV pulse, the motion is less pulse-like and more similar to an ordinary motion.

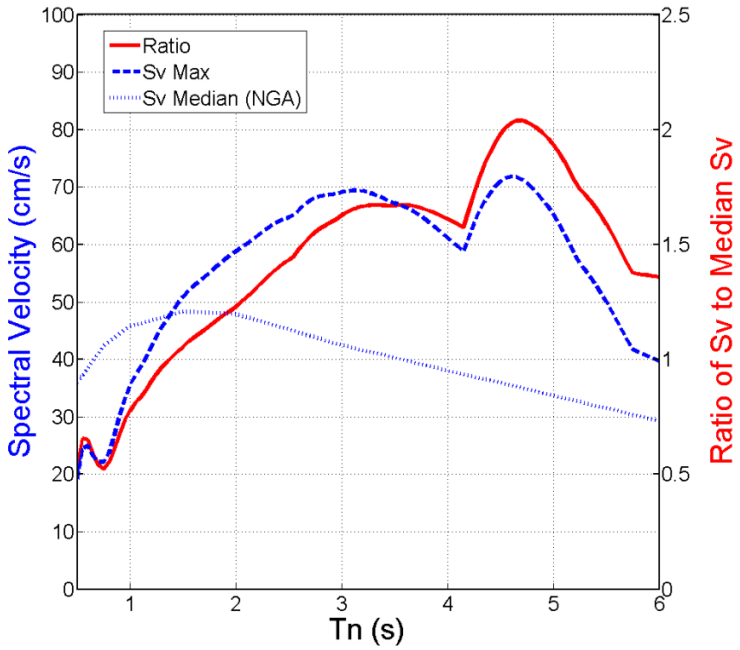

Figure 2. Example of period estimate used for filtering the Imperial Valley 1979, Brawley Airport record (NGA# 161).

3.2.4 Pulse classification score

In developing the classification procedure, the authors found that a composite score of several relevant factors provided a more robust classification method than using any single criterion alone. Additionally, it is also superior to using a series of discriminating thresholds. For example, requiring all pulse motions to have a NCSV difference greater than a set value and a number of significant cycles less than a second specific value will result in some motions being classified as a non-pulse because they were just slightly below the subjective threshold for one factor even though they far exceeded the threshold for the second factor. By scoring each record on two criteria and then combining the scores, a record that would have been just barely below one threshold but far above the second will actually score higher than a less pulse-like motion that happens to only slightly exceed the thresholds for both separate criteria.

The score for each factor ranged from 0% to 100%. In the NCSV difference category, motions with a NCSV difference above 0.7 scored 100%, while motions with an NCSV below 0.5 scored 0%. Motions between 0.5 and 0.7 received a score that transitioned linearly from 0% to 100%. For example, the Brawley Airport record had an NCSV difference of 0.635, so the NCSV score is 68%.
A similar taper was used in the score for number of significant cycles. Records with 1.5 cycles or less scored 100%, those with 2 cycles scored 50% and those with 2.5 or more cycles scored 0%. The Brawley Airport record had only one significant associated cycle, so it scored 100%. Combining the scores from the two factors with equal weighting (50% each) the overall pulse score was: 0.5*68% + 0.5*100% = 84%.

The scoring system described above was partly developed using the existing pulse databases of Shahi and Baker (2011) and Bray and Rodriguez-Marek (2004) to calibrate the scoring scheme. When binning the motions by NCSV or number of cycles and calculating the proportion of motions classified as a pulse of FD by the previous databases, it was clear that this proportion was highly dependent on NCSV or number of significant cycles. Using a logistic regression (appropriate for

binomial data), a similar trend resulted and agreed well with the binned data. As the NCSV difference increased, it was more likely that a given record had been classified as a pulse. As the number of significant cycles increased for a given record, it was less likely to have been classified as a pulse in the two existing classification databases. Several alternate parameters were considered that could also be used to classify pulses, but in this case a relatively simple combination of NCSV difference and number of significant pulses worked well. The specific thresholds and weights of the two categories were also calibrated in part by using these previous classifications.

The 390 motions were sorted by their pulse classification score, and a threshold of 60% in the score was selected by the authors to best mark the transition from pulse to non-pulse motions. Above 60%, most of the motions appeared visually pulse-like and below 60% most records seemed non-pulse-like. Again, in any classification scheme partitioning something as complex as a velocity-time series into binary categories, a subjective threshold is unavoidable. However, by using a threshold in the composite score, the effectiveness of the classification scheme was greatly improved compared to using thresholds on individual parameters.

An additional criterion was added that required motions to have a PPV greater than 25 cm/s to be considered a pulse. This minor requirement substantially improved the classification results, because there are records with low amplitude velocity-time series where a long period signal is picked up by the filtering algorithm, which would result in an unreasonable classification of the motion as being a near-fault pulse. This PPV threshold of 25 cm/s is set sufficiently low that it does not interfere with the classification of legitimate pulses.

Of the 390 records examined in this study, 87 records were classified as being velocity pulse motions, because they had scores greater than 60% required to be considered pulses. The classification scheme was supplemented by a subjective evaluation by the developers, because it was realized that the nuances of a record were not always captured by an automated classification scheme. For this reason, 7 of the 87 records were removed from the pulse category. Additionally, 8 records that did not have scores exceeding 60% were manually added to the pulse category. Thus, with the manual intervention, there were a total of 88 records classified as pulses.

3.2.5 Pulse period

The pulse period of each record was estimated using the same method used to estimate the period of the pulse in the filtering process (Section 3.2.2). The only modification is that the motion is rotated to the max PPV orientation prior to calculating the spectral velocities. The pulse period is the period at which the ratio of the spectral velocity of the PPV pulse to the median spectral velocity from the NGA models is at a maximum. Several other methods of identifying the pulse period were also tested. These included using the period associated with the maximum spectral velocity, the ratio of the spectral velocity of the two orthogonal components, or the zero crossings of the pulse in the velocity-time series. However, these alternate methods did not prove to be as effective. The 88 pulse motions are grouped by the period of the predominant pulse in the velocity-time series and are provided in Appendix C of NIST (2011) along with other characteristics and plots of each pulse time-series. Engineers should select pulse records from the motions listed that cover the period range of interest for the structure being analyzed.

4 PROPORTION OF PULSE MOTIONS

An investigation into the occurrence of pulse motions found that they are more likely to occur when the design ground motions parameter at the selected seismic hazard level is due to a high epsilon value (e.g., the deaggregation of the seismic hazard indicated that the design spectral acceleration at the period of the structure results from an epsilon value greater than one). Additionally, the likelihood of pulse motions occurring increases greatly as the source-to-site distance (R_{RUP}) decreases. These trends are apparent even in the raw data scatter-plot of pulse and non-pulse motions shown in Figure 3.

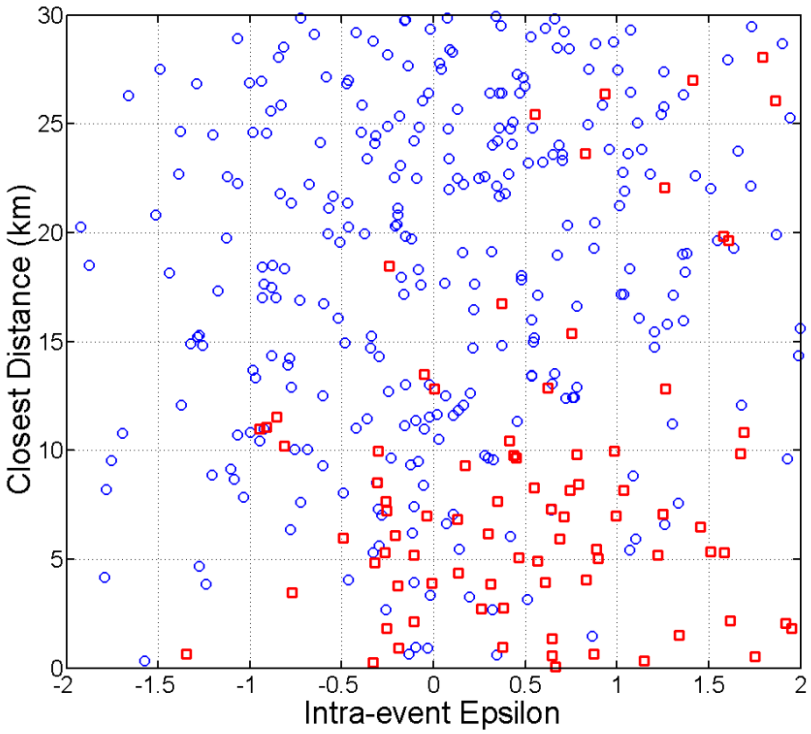

Figure 3. A scatter plot of 390 records with squares indicating motions classified as pulses and circles indicating non-pulse motions.

Intra-event (within-event) epsilon of PGV from Abrahamson and Silva (2008) was used to develop the initial model, but the final model was adjusted to use total epsilon. This was accomplished by normalizing the intra-event residual by the total standard deviation instead of the intra-event standard deviation to obtain an estimate of the mean total epsilon for future earthquakes with random event terms. This total epsilon is consistent with the total epsilon used by the engineer in practice. Therefore, the following relationships can be used directly with total epsilon. It is the recommendation of the developers that the PGV epsilon be used if available. If not available, using the epsilon of the spectral acceleration at the structural period is likely acceptable.

The model developed using logistic regression to capture the dependence of the proportion of pulse motions on epsilon and distance is displayed in Figure 4 for select distances. This figure is simply for visualization. In practice, the engineer should use the following equation with the epsilon (ε) of the design ground motion parameter and closest distance from the site to the source (R in km):

$$Proportion\ of\ Pulse\ Motions = \frac{\exp(0.891 - 0.188 * R + 1.230 * \varepsilon)}{1 + \exp(0.891 - 0.188 * R + 1.230 * \varepsilon)}$$

This relationship may be used by the engineer to estimate the number of ground motions within a suite of records that should be selected from among the 88 identified pulse motions to represent the proper contribution of pulse motions to the seismic hazard. For example, for the case wherein R = 10 km and ε = 1.5 for the 5% damped spectral acceleration at the structural period of 1.2 seconds, the proportion of ground motions that should be pulse motions is 0.70. Thus, for this case, 5 records (i.e., 0.70*7 = 4.9) of a suite of 7 records should be FD-pulse and pulse motions. The presented model can be used with the results of a probabilistic seismic hazard analysis by performing a disaggregation by distance and epsilon and using the values of these two parameters that control the hazard.

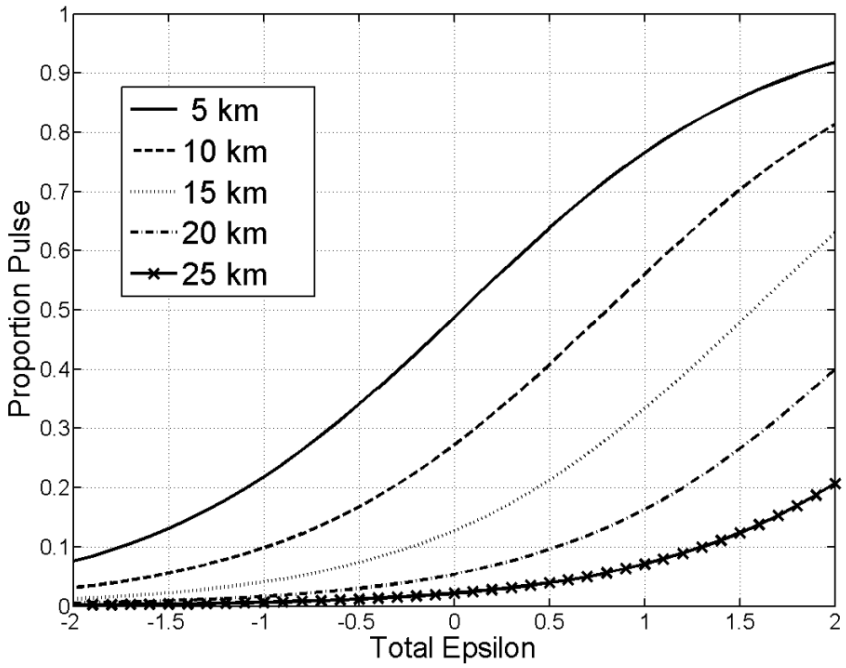

Figure 4. Model for estimating the proportion of pulse motions as a function of epsilon and distance.

The model was developed using pulses of all periods due to the limited data available and several other considerations. This may overestimate the likelihood of pulses when only interested in pulses with a specific period. For example, a pulse with a period of 6 seconds may not have a "pulse-like" effect on a building with a structural period of 1 second. One difficulty in addressing this issue is that there is not a clear transition when a pulse of a given period no longer has a "pulse-like" effect on buildings with varying fundamental periods. For example, a pulse with a period of 3 seconds will have a "pulse-like" effect on structures with periods of around 3 seconds, but it is not clear if will it be "pulse-like" effects on structures with periods of 1.5 seconds. Another issue is that the database is dominated by a few well-recorded earthquakes, most notably Chi-Chi with its aftershocks which make up nearly a third of the 390 records, and the current model gives equal weight to each recording. This is particularly concerning because magnitude has been shown to correlate with pulse period (Bray and Rodriguez-Marek, 2004; Shahi and Baker, 2011). For these reasons it is difficult to determine the proportion of pulses within specific period ranges. These issues warrant additional investigation in the future.

The engineer should select motions that best reflect the period range of interest in the structure being considered. With a limited number of design ground motions in the suite of motions (e.g., a suite of 7 motions is often used in practice and only a portion of these will be pulses), it is important to focus on the period range of interest of the structure. If many ground motions were to be used (e.g., more than 40 or so), then a more comprehensive suite of motions that captures all key earthquake scenarios including a wide range of pulse periods based on the potential near-fault earthquake scenarios could be used. Conventional good practices, such as selecting design motions that best represent the governing earthquake magnitude and distance, should be still followed.

If spectral matching is used, ideally, the motion should be spectrally matched using the concept of a conditional spectrum (Baker, 2011), because pulse motions contain high spectral ordinates within a narrow period range. Thus, spectral ordinates at other periods are likely to be below spectral acceleration values derived from a uniform hazard spectrum. However, traditionally a uniform hazard spectrum is used in earthquake engineering design practice, and for this case, it will be necessary to match the target spectrum over the specified period range (e.g., 0.2T - 1.5T, where T is the fundamental period of vibration of the structure). "Loose" spectral matching should be performed for

pulse-type motions so that the spectral ordinate at the period of the pulse is not larger than about 15% to 30% of the target spectral ordinate at this period and spectral ordinates at periods away from the period of the pulse are not less than about 10% to 20% of the target spectral values at these periods. Finally, the velocity-time series of the matched motion and the seed motion must be inspected to ensure that the nonstationary aspects of the seed motion are preserved in the matching process.

5 CONCLUSIONS

A new quantitative scheme was developed to classify near-fault motions as pulse or non-pulse motions. This scheme involves first filtering the record, calculating several parameters at all orientations, and then scoring motions based on two key ground motion parameters. The scheme was used to automatically classify 390 records with moment magnitudes greater than 6.0 and closest distances (R_{RUP}) less than 30 km. The developers manually reviewed the results and adjusted the classification of a limited number of records, realizing that no numerically based classification procedure would be able to capture all the nuances of a record. In total 88 of the 390 records were classified as pulses.

Using the newly developed pulse database, logistic regression was used to derive an empirical model to estimate the likelihood of occurrence of pulse motions. The equation estimates the proportion of pulse motions as a function of epsilon and closest distance. A disaggregation by distance and epsilon from a probabilistic seismic hazard analysis can help estimate the appropriate values of distance and epsilon for use in the provided equation. Pulse motions are sorted by period in Appendix C of NIST (2011) to facilitate the selection of pulse motions to include in a suite of design earthquake ground motions for time-history analysis.

ACKNOWLEDGEMENT

Financial support was primarily funded by the ATC-82 project through an ATC-CUREE joint venture sponsored by NIST/NEHRP. Additional funding is from a National Science Foundation Graduate Research Fellowship.

REFERENCES

Abrahamson, N.A. (2000). Effects of rupture directivity on probabilistic seismic hazard analysis. *Proceedings, Sixth International Conference on Seismic Zonation*, Palm Springs, CA, Nov. 12-15.

Abrahamson, N., Atkinson, G., Boore, G., Bozorgnia, Y., Campbell, K., Chiou, B., Idriss, I.M., Silva, W., and Youngs, R. (2008). Comparisons of NGA ground-motion relations. *Earthquake Spectra*. **24:1**, 45-66.

Abrahamson, N.A., and Silva, W.J. (2008a). Summary of the Abrahamson and Silva NGA ground-motion relations. *Earthquake Spectra*. **24:1**, 67-97.

Abrahamson, N.A., and Silva, W.J. (2008b). Abrahamson and Silva NGA ground motion relations for the geometric mean horizontal component of peak and spectral ground motion parameters. *Final report prepared for the Pacific Earthquake Engineering Research Center.*

Alavi, B., and Krawinkler, H. (2000), Consideration of near-fault ground motion effects in seismic design. *Proceedings, 12th World Conf. on Earthquake Engineering.*, Auckland, New Zealand.

Anderson, J.C., and Bertero, V.V. Uncertainties in establishing design earthquakes. (1987). *Journal of Structural Engineering*. **113:8**, 1709-1724.

ASCE. (2005). Minimum design loads for buildings and other structures. *ASCE/SEI 7-05*.

Baker, J.W. (2011). Conditional mean spectrum: Tool for ground motion selection. *Journal of Structural Engineering*. **137:3**, 322-331.

Baker, J.W. (2007). Quantitative classification of near-fault ground motions using wavelet analysis. *Bulletin of the Seismological Society of America*. **97:5**, 1486-1501.

Boore, D.M., and Atkinson, G.M. (2008). Ground-motion prediction equations for the average horizontal component of PGA, PGV, and 5% -damped PSA at spectral periods between 0.01 s and 10.0 s. *Earthquake Spectra.* **24:1**, 99-138.

Bray, J.D., and Rodriguez-Marek, A. (2004). Characterization of forward-directivity ground motions in the near-fault region. *Soil Dynamics and Earthquake Engineering.* **24**, 815-828.

Bray, J.D., Rodriguez-Marek, A., and Gillie, J. L. (2009). Design Ground Motions Near Active Faults. *Bulletin of the New Zealand Society for Earthquake Engineering*, 42 (1), March, 8 pp.

Campbell, K.W., and Bozorgnia, Y. (2008). NGA ground motion model for the geometric mean horizontal component of PGA, PGV, PGD and 5% damped linear elastic response spectra for periods ranging from 0.01 to 10s. *Earthquake Spectra.* **24:1**, 139-171.

Chiou, B., Darragh R., Gregor N., and Silva, W. (2008). NGA project strong-motion database, *Earthquake Spectra.* **24:1**, 23-44.

Chiou, B.S.J, and Youngs, R.R. (2008). Chiou-Youngs NGA ground motion relations for the geometric mean horizontal component of peak and spectral ground motion parameters. *Earthquake Spectra.* **24:1**, 173-215.

Hall, J.F., Heaton, T.H., Halling, M.W., and Wald, D.J. (1995). Near-source ground motion and its effects on flexible buildings. *Earthquake Spectra.* **11:4**, 569-605.

NIST. (2011). Selecting and Scaling Earthquake Ground Motions for performing response-history analysis. *Prepared by the NEHRP Consultants Joint Venture for the National Institute of Standards and Technology*.

Shahi, S.K., and Baker, J.W. (2011). An empirically calibrated framework for including the effects of near-fault directivity in probabilistic seismic hazard analysis. *Bulletin of the Seismological Society of America.* **101:2**, 742-755.

Somerville, P.G., Smith, N.F., Graves, R.W., and Abrahamson, N.A. (1997). Modification of empirical strong ground motion attenuation relations to include the amplitude and duration effects of rupture directivity. *Seismological Research Letters*. **68:3**, 199–222.

Spudich, P., and Chiou, B.S.J. (2008). Directivity in NGA earthquake ground motions: Analysis using isochrone theory. *Earthquake Spectra*. **24:1**, 279-298.